Title
Localized States in Dissipative Systems with Spatially Periodic Modulation

Author
Ponedel, Benjamin Charles

Publication Date
2018

Localized States in Dissipative Systems with Spatially Periodic Modulation

by

Benjamin Charles Ponedel

A dissertation submitted in partial satisfaction of the

requirements for the degree of

Doctor of Philosophy

in

Physics

in the

Graduate Division

of the

University of California, Berkeley

Committee in charge:

Professor Edgar Knobloch, Chair
Professor James Sethian
Professor Jonathan Wurtele

Spring 2018

Localized States in Dissipative Systems with Spatially Periodic Modulation

Abstract

Localized States in Dissipative Systems with Spatially Periodic Modulation

by

Benjamin Charles Ponedel

Doctor of Philosophy in Physics

University of California, Berkeley

Professor Edgar Knobloch, Chair

The Ginzburg-Landau equation with spatially periodic parametric forcing is used to study localized states near a weakly subcritical steady-state bifurcation. First the speed and stability of fronts near such a bifurcation are studied without spatial forcing, focusing on the transition between pushed and pulled fronts. Exact nonlinear front solutions are constructed and their stability properties investigated. In some cases, the exact solutions are stable but are not selected from arbitrary small amplitude initial conditions. In other cases, the exact solutions are unstable to modulational instabilities which select a distinct front. Chaotic front dynamics may result and is studied using numerical techniques.

When periodic spatial forcing is added the Ginzburg-Landau equation exhibits bistability between the trivial state and a nontrivial periodic state. It is shown that a family of stationary localized states accumulate near the Maxwell point of the homogeneous problem. Numerical continuation is used to show that under appropriate conditions these localized states are organized within a snakes-and-ladders structure. This phenomenon is named *forced snaking.* The stability properties of these states are determined and it is shown that longer lengthscale forcing leads to stationary trains consisting of a finite number of strongly localized, weakly interacting pulses exhibiting *foliated snaking.*

The phenomenon of forced snaking is not only relevant in dissipative systems and is introduced in the study of gap solitons. These solitons are described by the cubic-quintic Gross-Pitaevskii equation with a spatially periodic potential. The stability of the forced snaking solutions in the gap soliton context is determined. It is shown that multi-pulse solutions of all parities are stabilized when the spatial scale of the periodic forcing is sufficiently large, effectively quenching the self interactions between the pulses. Finally it is shown that the solitons unbind from the potential when subjected to sufficiently large perturbations and a strongly nonlinear theory is derived to capture the dynamics during this transition.

To mother and father.

Contents

List of Figures

List of Tables

Acknowledgments

First I would like to thank my advisor and mentor Professor Edgar Knobloch. Edgar is deeply committed to scientific curiosity, expository clarity, honesty, patience, and has a formidable work ethic. It has been an honor to collaborate with him and I am tremendously grateful for his influence on my overall academic education.

I owe a significant debt of gratitude to Professor James Sethian and Dr. Cédric Beaume for their guidance in my education in the use of numerics. Their influence helped me to see the great value of numerical analysis and permanently changed the way that I approach scientific problems. I would like to extend special thanks to Dr. Beaume for coaching me when I began research and being available for frequent debugging sessions.

I would also like to thank my colleagues and coauthors in the Knobloch Group at Berkeley: Punit Gandhi, Hsien-Ching Kao and Jianbo Xie. They provided me with technical guidance at the start and many informative discussions concerning my research.

I am deeply grateful for the friendships that I have made during graduate school. These have been a source of academic inspiration, very long walks and much needed amusement. I would like to thank Rachel Midori Chin, Eric McVoy Dodds, Zachary Kenneth Fisher, Ryan Joseph Janish, Byungmin Kang, Yi-Chuan Lu, Christopher John Mogni, Tess Eleonora Smidt, Aaron Miklos Strimling Szasz, Sara Rose Tepfer, Ziqi Yan, Albert Yuen and Shudan Zhong.

Finally, I would like to thank my earliest friend Dr. Eric Larson who has been a source of mathematical inspiration to me since elementary school. Eric is always interested in solving math problems no matter how trivial and is thrilled when he can convince others that math is fascinating.

Chapter 1

Introduction

Spontaneous symmetry breaking in physical systems has long been a focal point of modern physics research. In the context of spatially extended systems spontaneous symmetry breaking can manifest when an otherwise isotropic and homogeneous system develops a spatial pattern with a distinctive wave number. Examples of such systems span many fields in physics and include biology [110], fluid dynamics [11], chemical reactions [119], and nonlinear optics [4] to name a few. A mathematical understanding of such phenomena has been one of the primary goals of the pattern formation community for many decades and this dissertation fits into this effort.

Spatial patterns in physical systems frequently develop throughout the spatial domain but may also be confined to compact regions. In the physical context this behavior hearkens to the dynamics of a phase transition in which a local part of the system may initially transition to the new phase after which the transitioned region grows in extent. In the study of pattern formation such localized patterns are known as *localized states* and are of particular interest. In dissipative systems a key element supporting the existence of stable stationary localized states is the simultaneous existence of at least two distinct domain filling

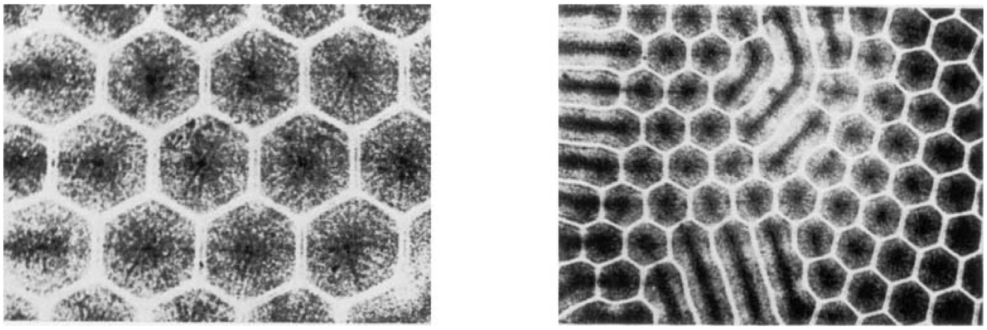

Figure 1.1: (left) Shadowgraph of hexagonal cells formed in Rayleigh-Bénard convection. (right) Transformation of hexagons into a roll pattern. This figure is taken from [129].

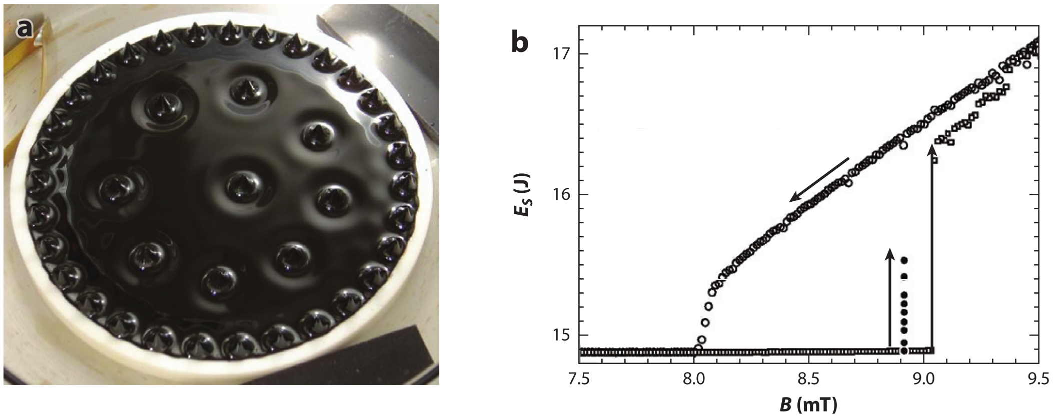

Figure 1.2: (a) A sample of ferrofluid under a strong vertical applied magnetic field. Localized pulses can be seen across the fluid surface. these are generated by finite amplitude localized perturbations at different locations. (b) A bifurcation diagram showing the energy of the surface in response to the applied magnetic field strength. The inset shows the number of peaks that can be observed as a function of the field strength. This figure is taken from [130].

states that are each stable. This permits the pattern in a localized region (state 1) and the base state surrounding it (state 2) both to be stable. This scenario is referred to as *bistability* and arises in systems in which the bifurcation to patterned states is subcritical.

Ferrofluid is a particularly remarkable subcritical dissipative system and offers a striking example of localized states. Ferrofluid is a magnetofluidic colloid made up of particles with definite magnetic dipole moments suspended in a viscous solution. The fluid responds strongly to magnetic fields and when a sufficiently strong uniform field is applied perpendicular to the fluid surface the system enters a subcritical regime. This is pictured in Fig. 1.2. Under the influence of the magnetic field the fluid surface remains stable up to a critical field strength. However, using an external magnet a peak of fluid can be pulled out of the fluid surface which *remains* as a localized lump in the surface when the external magnet is removed. This type of lump creation can be repeated at different locations resulting in beautiful patterns such as the one shown in Fig. 1.2(a). Mathematically the response of the system can be measured by the energy of the surface of the fluid which distinguishes the flat lump-less solution from those with localized lumps. This response is plotted in Fig. 1.2(b) as a function of the magnetic field strength. The localized solutions of this type do not exist everywhere in the subcritical region but it can be shown that they persist in a finite interval [106]. Further details can be found in [130].

As is evident in the case of the ferrofluid the multiplicity and structure of localized states in arbitrary subcritical systems can be very complicated. However, in certain systems the localized states are organized into a systematic bifurcation structure. One example of such a system is doubly-diffusive convection in which a horizontal fluid layer with a dissolved

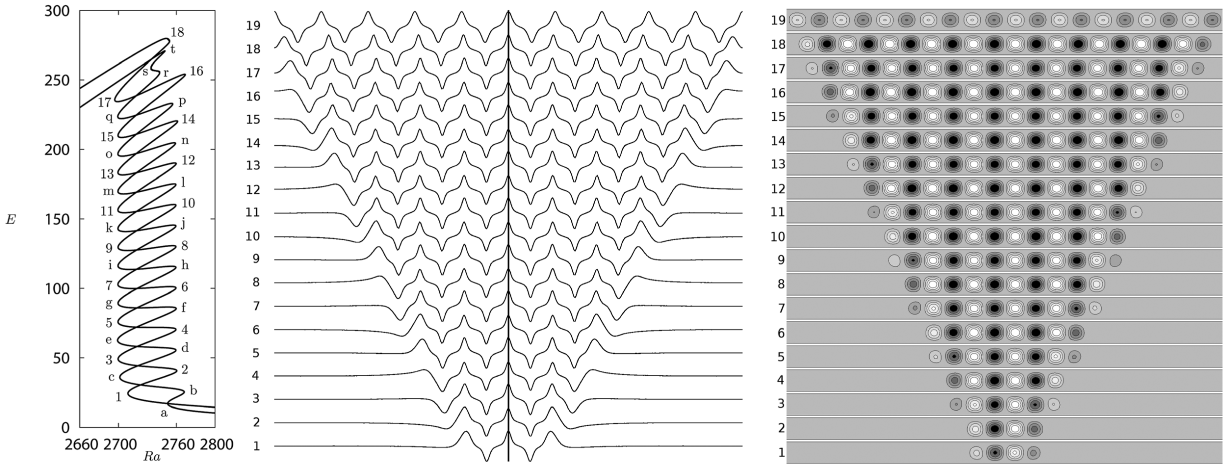

Figure 1.3: Localized states in doubly diffusive convection: a fluid layer with a dissolved solute (like salt) is subject to a a vertical temperature gradient. Convection solutions are computed directly from the Navier-Stokes equations in 2D at Prantl number, $Pr = 1$. (left) Bifurcation diagram for the branches of localized roll solutions as a function of the Rayleigh number, Ra. (center) The dissolved solute concentration integrated vertically over the fluid domain. (right) The stream function associated to the convection solutions. The solution plots correspond to the numbered folds on the bifurcation diagram. This figure is taken from [9].

solute (like salt) is subject to a vertical temperature gradient. This system is subcritical and the trivial conducting state is bistable with a branch of patterned solutions. This pattern takes the form of a series of convection rolls that fill the domain and is pictured (solution number 19) in Fig. 1.3. Because the system is subcritical this pattern is also accompanied by a series of localized states that exist in a subregion of the bistable region. Each of these solutions consists of an integer number of convection rolls surrounded by the trivial conducting solution, also plotted in Fig. 1.3. As a function of the Rayleigh number, Ra, these states are connected to each other as shown in the bifurcation diagram in the left plot. In this structure a solution with n rolls is connected to the solution with $n + 2$ rolls as the solution branch is continued. The oscillatory nature of the bifurcation branches in such a scenario is known as *snaking* and is present in many subcritical physical systems in which one of the bistable states has a definite wave number, which in the present case is related to the roll width.

In order to study the behavior of a subcritical system in which the base state is bistable with a patterned state of definite wave number we consider the limit in which the degree of subcriticality is weak so that a modulation equation can be derived for the amplitude of the patterned state. This model takes the form of the Ginzburg-Landau equation (GLE)

$$A_t = \mu A + A_{xx} + ia_1|A|^2 A_x + ia_2 A^2 \bar{A}_x + |A|^2 A - |A|^4 A \tag{1.1}$$

and is derived in chapter 2. When the underlying system is reflection symmetric and translation invariant Eq. (1.1) is the most general normal form for a weakly subcritical bifurcation. Here A represents the pattern amplitude and all the coefficients (μ, a_1, a_2) are real. Because the amplitude A corresponds to the amplitude of the pattern, patterned states are identified with homogeneous solutions with $|A| \neq 0$. This equation supports solutions that connect the base state (represented by $A = 0$) to the pattern (represented by constant $|A|$) via a continuous solution profile $A(x)$. These composite solutions are known as fronts and can be thought of as the building blocks for localized states. Generically these front solutions travel at constant speed, locally transforming one asymptotic state into the other as in a continuous phase transition. The motion ceases only at a particular μ parameter value known as the Maxwell point where the energy difference between the background and patterned state vanishes. It is here that one might expect to find stable stationary localized states in an interval of parameter values. Unfortunately this is not the case.

The mismatch between Eq. (1.1) and systems such as doubly-diffusive convection stems from the truncation of terms in the normal form calculation. Specifically, in the derivation of Eq. (1.1) terms that couple the pattern envelope, A, to the underlying pattern are pushed to higher order and truncated [40]. The result is that solutions to Eq. (1.1) can be translated freely with respect to the pattern which is not physical. There is a number of possible solutions to this problem. The first is to abandon the amplitude equation derivation and instead study phenomenological models that are not derivable but have coupling between the envelope and pattern by design. The most famous of these is known as the Swift-Hohenberg equation (SHE) and is introduced in chapter 2. This is not the tack adopted here. Instead we promote the principal bifurcation coefficient μ to be a prescribed periodic function of space, $\mu(x)$. This is a natural choice since in the derivation of Eq. (1.1) the coupling between the amplitude and underlying pattern is parametric and the underlying pattern is periodic. In this dissertation we show that this change is sufficient for Eq. (1.1) to support robust localized states that exhibit snaking behavior.

The modification of Eq. (1.1) that we consider here is not only relevant in the context of amplitude equations but is also the model of choice for nonlinear systems that are forced externally by a periodic spatial potential. One such system is the liquid crystal light valve (LCLV) experiment considered in [75, 76] and illustrated in Fig. 1.4. In this experiment a thin film nematic liquid crystal is put into an optical feedback loop in which reflected light from the liquid crystal is fed to a photoconductor behind it. This sets up an electric field in the liquid crystal establishing a feedback mechanism. Periodic light modulation is sent in externally using the light source; this constitutes a spatially periodic potential for the liquid crystal director field. In this context snaking phenomena are observed experimentally and Eq. (1.1) where μ is spatially periodic is the natural model description.

Outline

This dissertation begins with a review of the theoretical framework for the study of pattern formation in chapter 2 and the numerical techniques used here to solve differential equations

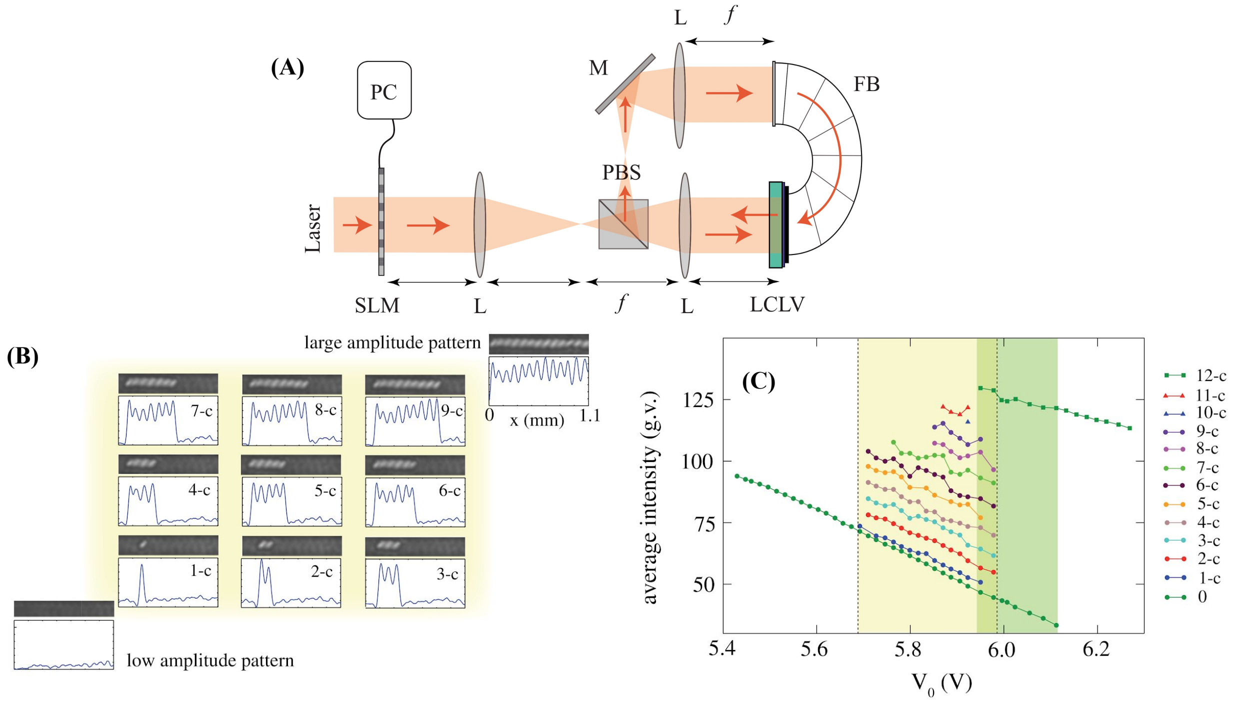

Figure 1.4: (a) The liquid crystal light valve (LCLV) experimental setup. (b) Localized solutions representing two different orientations of the liquid crystal directors are pictured, plotted in terms of their light intensity. (c) A bifurcation diagram for the solutions in (b) is shown in terms of the average externally applied voltage V_0. Solutions lie on parallel bifurcation curves resembling the snaking behavior of stable states. This figure is adapted from [75, 76].

in chapter 3.

Our study of Eq. (1.1) with $\mu = \mu(x)$ in this dissertation is divided into four main components. The first of these involves the homogeneous form of Eq. (1.1) in which μ is constant. As mentioned previously front solutions in this model represent connections between $u \equiv 0$ and the patterned state. These fronts can be glued together like building blocks to form localized states when μ is non-constant. Thus fronts of the homogeneous equation are the key solutions involved in localization in the more general model. In chapter 4 we construct an exact front solution to Eq. (1.1) with full parameter dependence. This front turns out to be uniquely important for localized states in the presence of the potential but also for the dynamics in the homogeneous model. In the remainder of the chapter we study the speed and stability of this front and focus on the transition between the pushed and pulled regimes. In some cases these exact fronts are stable but are not selected from arbitrary small amplitude initial conditions. In other cases, the exact front is unstable to modulational instabilities which select a distinct front. Chaotic front dynamics may also result and are studied using numerical techniques.

The second component of our exposition is the numerical calculation of the bifurcation structure of stationary localized solutions when μ is periodic. This is carried out in chapter 5. We begin by considering the real GLE and set $a_1 = a_2 = 0$. We show that when spatial forcing is included its wavelength is imprinted on the homogeneous states of the unforced equation creating conditions favorable to front pinning and hence spatial localization. We use numerical continuation to show that under appropriate conditions such forcing generates a sequence of localized states organized within a snakes-and-ladders structure centered on the Maxwell point, and refer to this phenomenon as *forced snaking*. We determine the stability properties of these states and show that longer lengthscale forcing leads to stationary trains consisting of a finite number of strongly localized, weakly interacting pulses exhibiting *foliated snaking*.

Chapter 6 connects stationary forced snaking solutions to the dynamics of the full equation. Here we consider the effects of small and large perturbations to the snaking solutions and their resulting dynamics. We specifically focus on a process known as *depinning* where snaking solutions are perturbed in such a way that the fronts bounding the localized pulses begin to propagate. We perform analysis of this procedure by numerical simulation and semi-analytical asymptotic analysis. We close the chapter with an asymptotic calculation to approximate the depinning dynamics using the exact front solution derived in chapter 4.

In the last component of this work, chapter 7, we consider the implications of forced snaking more broadly and study the dynamical behavior of forced snaking solutions in energy conserving systems. The physical systems under consideration are optical and the relevant solutions are known as gap solitons. The governing equations for systems of this type are the Gross-Pitaevskii equations (GPEs) and the forced snaking solutions of chapter 5 for $a_1 = a_2 = 0$ represent gap solitons when the GPE nonlinearity is cubic-quintic. We study the stability of the solutions and specifically show that multi-pulse solutions of all parities are stabilized when the spatial scale of the periodic forcing is sufficiently large (the foliated regime), effectively quenching the self interactions between the pulses. Finally we show that the solitons unbind from the potential when subjected to sufficiently large perturbations and provide a strongly nonlinear theory to capture the dynamics during this transition.

We complete the dissertation with a discussion of the broader context of this work and possible extensions in chapter 8.

Chapter 2

The Mathematical Theory of Pattern Formation

This thesis is concerned with the study of a particular class of partial differential equations (PDEs) used to describe the evolution of spatial patterns in a single spatial dimension. Some of these models can be derived rigorously while others are created heuristically, but all are subject to validation by real world experiments. This chapter is devoted to the exposition of the mathematical background material that governs the aforementioned models.

In the course of this chapter we build up the theory of pattern formation beginning with simple models and ending with the PDEs which we seek to study. The simplest models begin as dynamical systems governing the time evolution of the quantity of interest without any description of spatial dependence. The mathematical theory governing these systems is broadly contained within bifurcation theory for solutions of ordinary differential equations (ODEs) which we present first. Next, spatial dependence is added resulting in a PDE. We discuss the derivation of such PDE models and then proceed to the theory for analysis of their solutions. This analysis is split into: the study of stationary solutions (those with no time dependence) and secondarily their dynamics. The mathematical underpinnings of the former topic are governed by bifurcation theory in terms of so-called “spatial dynamics” while those of the latter are confined to linear eigenvalue problems. Analysis of PDE dynamics beyond linear stability considerations is carried out numerically, the methods for which are discussed in chapter 3.

Finally, since this thesis is concerned primarily with spatially periodically forced systems we close the chapter with a brief review of how spatial periodicity fits into the previous theory. We first introduce periodically forced non-atonomous ODEs and Floquet theory. Next we discuss some of the effects of adding spatially periodic forcing to PDEs.

Some of the topics covered in this chapter date back a century but remain in widespread use in modern research. More comprehensive references on these topics can be found in [74, 77, 79, 90, 98, 100, 152].

2.1 Bifurcation theory

For the purposes of this work we define a dynamical system to be a set of ODEs of the form

$$\dot{\boldsymbol{u}} \equiv \frac{d\boldsymbol{u}}{dt} = \boldsymbol{f}(\boldsymbol{\mu}, \boldsymbol{u}), \tag{2.1}$$

where $\boldsymbol{u} \in \mathbb{R}^n$ represents the dynamical quantity of interest and characterizes the state of the system, $\boldsymbol{\mu} \in \mathbb{R}^p$ represents p distinct scalar control parameters which remain fixed and $\boldsymbol{f} : \mathbb{R}^p \times \mathbb{R}^n \to \mathbb{R}^n$ represents the structure of the system encompassing all of the physical information and dictating how the components of $\boldsymbol{u}$ interact. A *trajectory* of Eq. (2.1) $\boldsymbol{u}(t; \boldsymbol{u}_0)$ is a solution to the equation that passes through $\boldsymbol{u}_0$ at $t = 0$. We typically drop the initial point and write $\boldsymbol{u}(t)$ when the particular starting point is not relevant. We term the set of trajectories generated by the vector field $\boldsymbol{f}$ the *flow* of the dynamical system and denote it by $\phi(\boldsymbol{u}, t)$.

Fixed points

We call a point, $\boldsymbol{u}_0$, in the phase space of Eq. (2.1) a *fixed point* if it satisfies $0 = \boldsymbol{f}(\boldsymbol{\mu}, \boldsymbol{u}_0)$. Trajectories beginning at fixed points remain there for all time. This property is non-generic and it is natural to ask about the behavior of trajectories passing through points nearby $\boldsymbol{u}_0$. This can be studied mathematically by writing $\boldsymbol{u}(t) = \boldsymbol{u}_0 + \epsilon\, \boldsymbol{v}(t)$ where $\epsilon \ll 1$. Making use of Eq. (2.1) $\boldsymbol{v}$ satisfies

$$\dot{\boldsymbol{v}} = D\boldsymbol{f}(\boldsymbol{u}_0)\boldsymbol{v} \tag{2.2}$$

to lowest order in ϵ, i.e. near the fixed point. Here $D\boldsymbol{f}(\boldsymbol{u}_0)$ denotes the Jacobian matrix of the vector field $\boldsymbol{f}$ evaluated at the fixed point $\boldsymbol{u}_0$,

$$[D\boldsymbol{f}(\boldsymbol{u}_0)]_{ij} = \left. \frac{\partial f_i(\boldsymbol{u})}{\partial u_j} \right|_{\boldsymbol{u}=\boldsymbol{u}_0}.$$

In the following we shall implicitly assume the dependence of the Jacobian on the fixed point and write $D\boldsymbol{f}$ for short. Assuming that $D\boldsymbol{f}$ has no repeated eigenvalues the solution of Eq. (2.2) can be written,

$$\boldsymbol{v}(t) = \sum_{i=1}^{n} a_i \boldsymbol{\eta}_i e^{\lambda_i t} \tag{2.3}$$

where $(\lambda_i, \boldsymbol{\eta}_i)$ are eigenvalues and normalized eigenvectors of the matrix $D\boldsymbol{f}$ and $a_i \in \mathbb{R}$ are constants that depend only on the initial value of $\boldsymbol{v}$. In general the eigenvalues of $D\boldsymbol{f}$ may be complex but since $\boldsymbol{f}$ is real-valued they must appear in conjugate pairs. When $D\boldsymbol{f}$ has null eigenvalues the solution Eq. (2.3) may not reflect the dynamics near the fixed point and the situation is more complicated. It is precisely for this case that bifurcation theory was developed.

Fixed points are typically classified by the types of eigenvalues of $D\boldsymbol{f}$. Specifically, the eigenvalues of $D\boldsymbol{f}$ can be partitioned into three distinct types: those with positive real part, negative real part and zero real part. The eigenspaces spanned by eigenvectors associated to eigenvalues in these three categories are referred to as,

$$\begin{aligned} E^s &: \text{the stable subspace} \\ E^u &: \text{the unstable subspace} \\ E^c &: \text{the center subspace.} \end{aligned}$$

These eigenspaces are invariant under the flow of Eq. (2.2). An immediate consequence of this decomposition is that initial conditions beginning in E^s tend towards the fixed point as $t \to \infty$ and those in E^u tend towards the fixed point as $t \to -\infty$. By construction these subspaces partition the ambient space, $\mathbb{R}^n$. In particular, if $\dim(E^j) \equiv n_j$ then $n_s+n_u+n_c = n$.

When E^c is empty the fixed point is referred to as *hyperbolic*. Such fixed points are further grouped into the following categories:

unstable	$n_u > 0$
stable	$n_u = 0$
node	$\Im(\lambda_i) = 0$ for all i, and either $n_u = n$ or $n_s = n$
saddle	$\Im(\lambda_i) = 0$ for all i, and both $n_u > 0$ and $n_s > 0$
focus	at least one pair of eigenvalues has nonzero imaginary parts.

When the center subspace is non-empty classification of the fixed point is more complicated because its stability depends on the nonlinear terms in the equation. Despite this, the special case of a fixed point with a single pair of purely imaginary eigenvalues is referred to simply as a *center* in the context of the linear equation. The inclusion of nonlinear terms could destroy the center.

If $\boldsymbol{f} \in C^r$, the space of functions with continuous derivatives of order $r \in \mathbb{Z}$ then the three subspaces E^s, E^u and E^c may be extended locally into C^r manifolds [152]. Specifically, there exist three manifolds that we denote W^s, W^u and W^c that pass through the fixed point and are tangent to the respective eigensubspace at the fixed point. These three manifolds are correspondingly called the stable, unstable and center manifolds. The manifolds W^s and W^u share the same asymptotic properties as E^s and E^u respectively and all three manifolds are invariant in the sense that any initial condition beginning on one must remain there for all time. While the stable and unstable manifolds are unique the center manifold is not. However, it can be shown that the center manifold is unique to all orders of its Taylor expansion [141].

Trajectories connecting fixed points

If a dynamical system has at least one hyperbolic fixed point $\boldsymbol{u}_0$ then it may also possess a trajectory that approaches that fixed point in both limits $t \to \pm\infty$. This type of trajectory is called a *homoclinic orbit*. This requires that the unstable and stable eigenspaces of $\boldsymbol{u}_0$

both be non-empty. Similarly, a *heteroclinic orbit* is a trajectory that connects two distinct fixed points in the limits $t \to \pm\infty$. Concretely, if such an orbit connects to $\boldsymbol{u}_0$ when $t \to -\infty$ and $\boldsymbol{u}_1$ when $t \to \infty$ then $\boldsymbol{u}_0$ must have a non-empty unstable eigenspace and $\boldsymbol{u}_1$ must have a non-empty stable one. We refer to a chain of heteroclinic orbits that connect a sequence of fixed points as a *heteroclinic cycle*.

Bifurcations of vector fields

Informally speaking, a dynamical system is said to undergo a bifurcation if the flow, ϕ, "qualitatively changes" as the system parameters, $\boldsymbol{\mu}$, are varied. Qualitative changes to the system flow may include the creation of new solutions or changes to solution stability. We term the parameter values for which such changes occur *bifurcation points*. A rigorous mathematical definition of a bifurcation is possible for one-dimensional vector fields but become significantly more complex in higher dimensions. The genericity of a bifurcation is broadly categorized by the number of scalar parameters that must be independently varied in order that the bifurcation occur. We call this number the *codimension* of the bifurcation. Bifurcations that occur in the vicinity of a single fixed point are termed *local bifurcations*, while those that are associated with nonlocal changes to the flow field, such as annihilation of a homoclinic orbit, are termed *global bifurcations*. While global bifurcations are generally difficult to study local bifurcations benefit from a rich mathematical machinery built to understand the behavior of nearby solutions.

Center manifold reduction

Center manifold reduction is a technique used to understand the flow nearby fixed points that are not hyperbolic. If a fixed point is hyperbolic then the Hartman-Grobman theorem guarantees that the flow field near the fixed point is topologically equivalent to the flow determined by Eq. (2.2) [152]. Moreover hyperbolic fixed points are structurally stable, meaning that they remain hyperbolic for small changes in parameters. Thus local bifurcations only occur at non-hyperbolic fixed points, i.e. those with nontrivial center manifolds, W^c.

The flow of initial conditions nearby a non-hyperbolic fixed point occurs on two distinct scales. Initial conditions in W^s or W^u evolve exponentially quickly (see Eq. (2.3)) whereas those in W^c evolve slowly. The fact that initial conditions in W^c have any dynamics at all is due to nonlinear terms whereas in a linear problem initial conditions in E^c will not evolve if all the associated eigenvalues are identically 0. For simplicity suppose that $dim(W^u) = 0$ then as $t \to \infty$ trajectories near the fixed point flow quickly to the center manifold which determines the dynamics on longer timescales. Said another way, after a rapid transient the solution evolves on a slow scale near the center manifold. Although solutions beginning in W^s must remain there for all time, they evolve rapidly to a neighborhood of W^c and adopt dynamics governed by the timescales set on W^c. More precisely, any trajectory of the full system passing through through an initial condition that is sufficiently close to the fixed point asymptotically approaches a trajectory *in the center manifold* [36]. Center manifold reduction exploits this property by reducing the dynamics of the entire space, $\mathbb{R}^n$, to the dynamics near W^c. In the case that W^u is nontrivial a similar understanding of the dynamics results in the opposite asymptotic limit, $t \to -\infty$, for trajectories beginning in W^u. Since W^s and W^u are invariant it suffices to study the case when $dim(W^u) = 0$.

Center manifold reduction proceeds as follows. Assume that the origin is a fixed point of Eq. (2.1) and that $dim(W^u) = 0$. Then after a linear transformation applied to $\boldsymbol{u}$ the dynamical system can be written

$$\begin{aligned} \dot{\boldsymbol{U}} &= A\boldsymbol{U} + f_1(\boldsymbol{U}, \boldsymbol{V}) \\ \dot{\boldsymbol{V}} &= B\boldsymbol{V} + f_2(\boldsymbol{U}, \boldsymbol{V}) \end{aligned} \tag{2.4}$$

where $\boldsymbol{U} \in \mathbb{R}^c$, $\boldsymbol{V} \in \mathbb{R}^s$, the eigenvalues of the matrix A all lie on the imaginary axis, the eigenvalues of the matrix B all have a negative real part and f_k are nonlinear functions of $(\boldsymbol{U}, \boldsymbol{V})$. The Center Manifold Theorem [36] guarantees that near the origin the manifold W^c can be represented as

$$W^c = \{(\boldsymbol{U}, \boldsymbol{V}) \,|\, \boldsymbol{V} = h(\boldsymbol{U}), h(0) = 0, Dh(0) = 0\}.$$

Furthermore the function h is determined by requiring consistency of Eqs. (2.4) after setting $\boldsymbol{V} = h(\boldsymbol{U})$. This results in the identity

$$Dh(\boldsymbol{U}) \cdot [A\boldsymbol{U} + f_1(\boldsymbol{U}, h(\boldsymbol{U}))] = Bh(\boldsymbol{U}) + f_2(\boldsymbol{U}, h(\boldsymbol{U}))$$

which must be satisfied near the origin. This is typically done by allowing $\boldsymbol{U}$ to take the form of a Taylor series. The ultimate dynamics on the center manifold are then governed by

$$\dot{\boldsymbol{U}} = A\boldsymbol{U} + f_1(\boldsymbol{U}, h(\boldsymbol{U})). \tag{2.5}$$

As mentioned previously, the Taylor series of the center manifold is unique although the center manifold is not [141, 152]. The solutions of this equation occur in $\mathbb{R}^c$ and are thus lower-dimensional than the full dynamical system. Typically the dimension reduction is very significant reducing a high-dimensional system to only a handful of modes.

Normal forms

As a result of center manifold reduction all of the fast "linear" dynamics of the system near the fixed point, which manifest through rapid initial transients, have been projected out leaving nonlinear terms that are critical to the character of the flow. Although the dimension of the system cannot be reduced further it is natural to ask whether there exists a transformation of the coordinates to simplify the remaining nonlinear terms in Eq. (2.5). Performing such transformations is what we refer to as putting the equation into *normal form.* To be precise, we pick nonlinear near identity transformations of the form $\boldsymbol{U} =$

$\tilde{\boldsymbol{U}} + g(\tilde{\boldsymbol{U}})$ that are valid in the vicinity of the origin. Broadly speaking, this procedure is carried out order by order by inserting the Ansatz into Eq. (2.5), Taylor expanding and choosing g to eliminate as many nonlinear terms as possible. Typically this procedure is carried out order by order for polynomial terms of increasing degree: the function g is taken to be a linear combination of all polynomials in the components of U of degree k $\left\{\prod_{j=1}^{k} U_{i(j)}\right\}$, after making the substitution and Taylor expanding all terms of degree k are collected and the coefficients of the terms in g are chosen to eliminate as many as possible. Then the procedure is repeated for terms of order $k+1$. The elimination step involves inverting a linear operator that acts on the space of homogeneous polynomials of degree k and when it is not of full rank some terms cannot be eliminated. Those remaining are termed *resonant*. This linear operator is determined entirely by the polynomial degree k and the matrix, A, in Eq. (2.5), i.e. the linear part of the dynamics. Because resonant terms may appear in a variety of combinations the normal form of an equation is generally speaking not unique.

Unfolding a bifurcation

The techniques discussed previously can be used to maximally simplify the equations of a dynamical system near a nonhyperbolic fixed point but do not deal with the dependence of the fixed point and its eigenvalues on parameters. Including parameters in this simplified description is known as *unfolding* the bifurcation. This is performed by extending the dynamical system to include phantom evolution of the parameters by setting $\dot{\boldsymbol{\mu}} = 0$ for $\boldsymbol{\mu}$ in a neighborhood of the bifurcation point. The number of parameters that must be added equals the codimension of the bifurcation. Performing the same center manifold reduction and normal form calculations on the extended system then automatically includes both the required dynamics and free parameters in a higher-dimensional center manifold.

Infinite-dimensional dynamical systems

Although the techniques mentioned above are quite powerful in the study of finite-dimensional dynamical systems care must be taken when applying similar insights in infinite dimensions. This consideration may seem arcane but is relevant because many PDEs may be thought of as infinite-dimensional dynamical systems by projecting the dynamics onto a countably infinite complete set of basis functions for the spatial domain. It is then tempting to assume that in many cases we might use center manifold reduction to reduce the dynamics of a PDE to finite dimensions! Alas this is typically not possible.

The reason for the complication is the potential accumulation of negative real part eigenvalues on the imaginary axis. Consider an infinite-dimensional dynamical system with a finite number of eigenvalues on the imaginary axis. Applying center manifold reduction naively we would split the system into a fast and slow part. In the finite-dimensional case the separation in timescales allows one to project the fast modes onto the slow ones. This timescale separation is defined by the real part of the eigenvalue closest to the origin that lies to the left of the imaginary axis. In the infinite-dimensional case there is no guarantee that this “closest” eigenvalue is a finite distance from the imaginary axis. In particular, there is frequently a series of eigenvalues that accumulate on it. This destroys the separation of timescales and center manifold reduction breaks down. The theory can be applied in cases where there is a finite barrier (referred to as the *spectral gap*) between the imaginary axis and the negative real part eigenvalues, but they are few and far between.

In the case when reduction is possible there exists a potentially infinite-dimensional center manifold [71]. The setting for such a problem is the system

$$u_t = Lu + R(u)$$

in which u lies in a Banach space, L is a differential linear operator and R is a (possibly differential) nonlinear operator such that $R(0) = \partial_u R(0) = 0$. If the eigenvalues of L satisfy the spectral gap condition then the infinite-dimensional Center Manifold Theorem guarantees that in the neighborhood of $u = 0$ there exists a center manifold that is locally invariant and contains the set of bounded solutions to the full dynamics for all time [71]. Here the generalization of the projection operator to the center eigenmodes is a Dunford integral rather than a matrix. In infinite dimensions a number of additional technical conditions are required that are not relevant to the finite-dimensional case, see [71]. The theorem was first proved in 1964.

When there is no spectral gap and eigenvalues accumulate on the imaginary axis such a reduction is not possible. Nonetheless one can use the method of multiple scales to derive a reduced description of the system using amplitude equations. These equations may be derived in regimes in which there is clear spatial scale separation and in many cases provide an effective description of the full system behavior.

Common bifurcations

To close this section we present a summary of several common bifurcations that appear in this thesis. These are all either co-dimension one or two and are all steady state bifurcations, i.e. they have eigenvalues with zero imaginary part at onset.

The Saddle Node Bifurcation

The saddle-node bifurcation is the simplest bifurcation of codimension one. The bifurcation has a normal form

$$\dot{u} = \mu \pm u^2. \tag{2.6}$$

In the “$-$” case the system has a pair of fixed points $\pm\sqrt{\mu}$ when $\mu > 0$ and none when $\mu < 0$. The bifurcation occurs at $\mu = 0$ where the two fixed points are created. A bifurcation diagram showing this is pictured in Fig. 2.1(a). The stable fixed point is indicated with a solid line, the unstable one with a dashed line and the flow of Eq. (2.6) for initial conditions away from the fixed points is indicated by grey arrows. These arrows are omitted from the diagrams

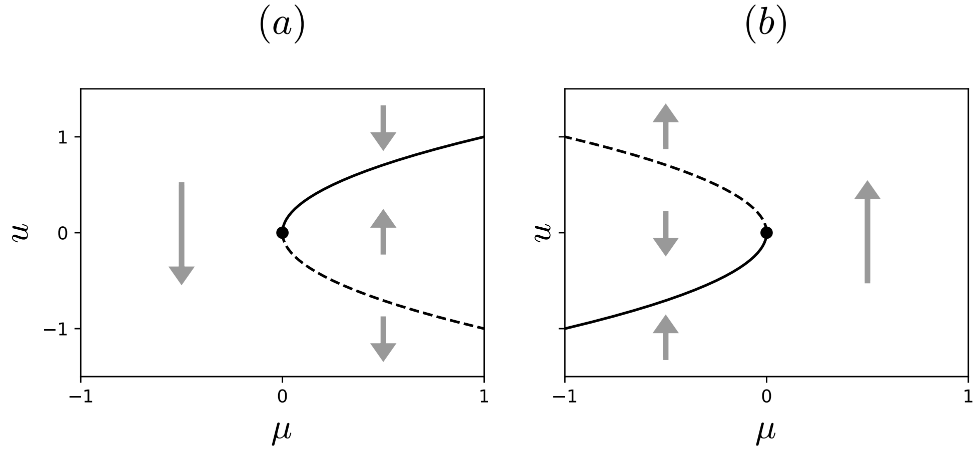

Figure 2.1: Bifurcation diagram for the saddle-node bifurcation: (a) "−" case, (b) "+" case. Solid (dashed) lines indicate stable (unstable) fixed points, the arrows indicate the flow of initial conditions and the bifurcation point is marked with a dot.

in the remainder of this section and solid lines are understood to be attracting while dashed lines are repelling. We refer to the curve $u(\mu)$ of fixed points as a *branch*. Beginning on the upper stable branch as μ is decreased the curve folds over and connects to the lower unstable branch at $\mu = 0$. The bifurcation points on branches exhibiting this behavior (which need not be saddle-nodes) are referred to as *folds*. The "+" case is shown in Fig. 2.1(b). In this case the unstable branch is at higher amplitude and no branches exist for $\mu > 0$.

The Pitchfork Bifurcation

The pitchfork bifurcation has the normal form

$$\dot{u} = \mu u \pm u^3$$

and is generic in systems with $u \to -u$ symmetry. The bifurcation can also occur in non-symmetric systems but is of higher codimension. The bifurcation diagram for the pitchfork is shown in Fig. 2.2. In this case the two possible signs in the normal form are referred to as *subcritical* ("+") and *supercritical* ("−"). In the supercritical case, Fig. 2.2(a), $u = 0$ is the only fixed point for $\mu < 0$ and there are three for $\mu > 0$: $u = 0, \pm\sqrt{\mu}$. The two additional branches are related by the $u \to -u$ symmetry and emerge from the bifurcation point as μ is increased through 0. In the supercritical case these new branches are both stable while $u = 0$ changes stability at the bifurcation point. In contrast for the subcritical case (Fig. 2.2(b)) the extra branches are unstable and exist to the left of the bifurcation point. They annihilate when μ passes through 0 from below.

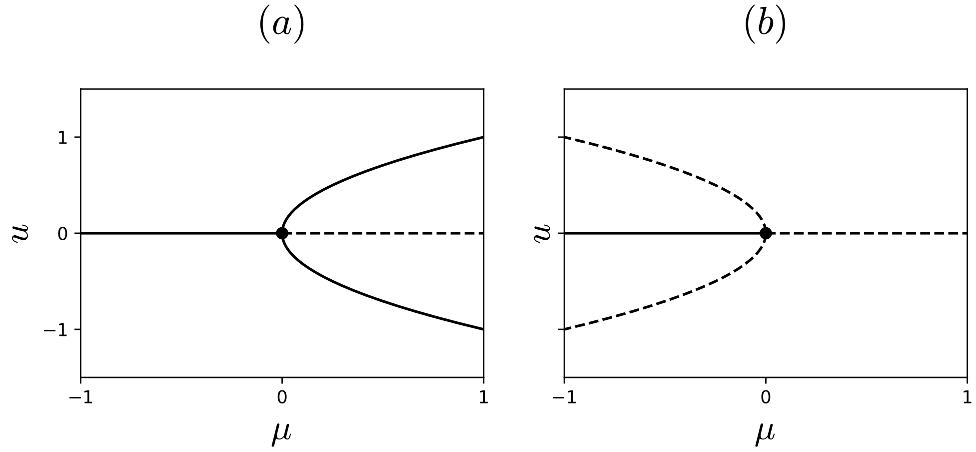

Figure 2.2: Bifurcation diagram for the saddle-node bifurcation: (a) "−" or supercritical case, (b) "+" or subcritical case. Solid (dashed) lines indicate stable (unstable) fixed points and the bifurcation point is marked with a dot.

The Hysteresis (cusp) Bifurcation

The hysteresis bifurcation has a normal form

$$\dot{u} = \mu + \alpha u - u^3$$

and is codimension two. Specifically two scalar parameters must be tuned in order for the bifurcation to occur. Here the bifurcation point occurs when $\mu = \alpha = 0$. For $\alpha < 0$ there is a single fixed point for each $\mu \in \mathbb{R}$ but when $\alpha > 0$ there is an interval of μ values for which there exist three fixed points. In this region the branch resembles an "S" shape and the boundaries of the interval correspond to saddle-nodes in the bifurcation branch. This is shown in Fig. 2.3. In part (a) of the figure we plot the locations of these two saddle-nodes in the (μ, α) plane. The bifurcation point is denoted with a red dot and the dotted lines correspond to slices at fixed α. Each of these slices corresponds to the bifurcation diagram in the (μ, u) plane shown to the right (b). Most of the branch of fixed points is stable except in the $\alpha > 0$ regime where the two saddle nodes bound a branch of unstable fixed points. As can be seen in (b) the two saddle nodes annihilate at the bifurcation point. This occurs in the (μ, α) plane at a cusp point which is the source of the alternative name, *cusp bifurcation*, given to this scenario.

The Necking Bifurcation

The necking bifurcation has the normal form

$$\dot{u} = \mu^2 - \alpha - u^2$$

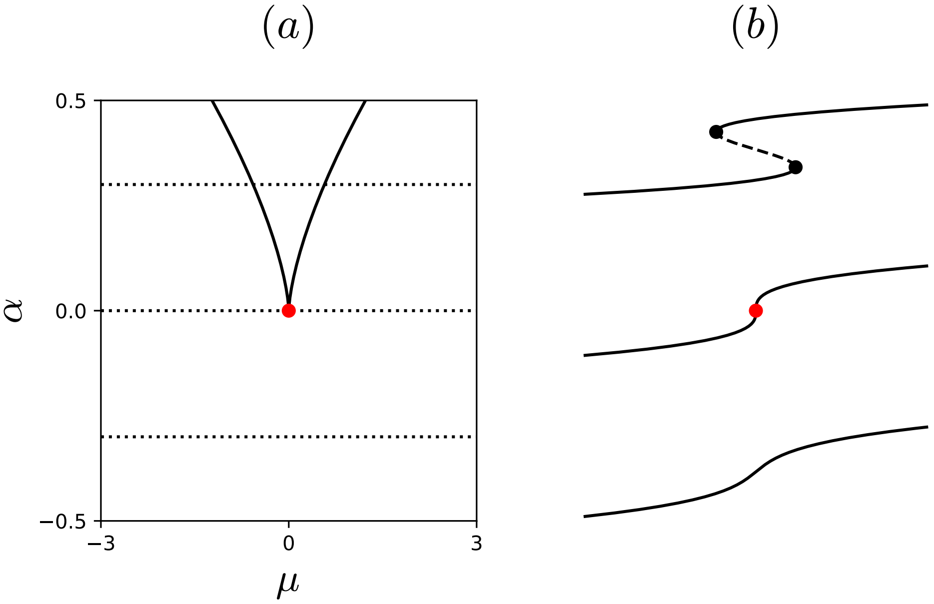

Figure 2.3: Bifurcation diagrams for the hysteresis bifurcation. Plot (a) shows the location of the saddle-nodes in the (μ, α) parameter plane. The bifurcation point is marked with a red dot and the dotted lines denote slices at fixed values of α that correspond to the diagrams in (b) which are plotted offset in the (μ, u) plane. The saddle-nodes are marked with black dots.

and is also of codimension two [128]. The bifurcation point occurs at $\mu = \alpha = 0$. For both $\alpha > 0$ and $\alpha < 0$ there are two separate branches of fixed points. At the bifurcation point these branches coincide. This process can be seen in Fig. 2.4. When $\alpha < 0$ one of the branches is stable while the other unstable and in the $\alpha > 0$ case both branches have a saddle node separating stable and unstable segments. As α passes through 0 from below the two curves of fixed points meet and “pinch” off leaving two saddle-nodes. The locations of these saddle nodes are plotted in the (μ, α) plane in Fig. 2.4(a) and bifurcation curves for fixed values of α in the (μ, u) plane are shown in (b).

The SNIPER Bifurcation

We close this section with a global bifurcation in which a pair of fixed points annihilate to form a periodic orbit. This Saddle-Node Infinite-PERiod bifurcation or *SNIPER bifurcation* [69] is typically written in polar coordinates (r, θ)

$$\dot{r} = r(1 - r^2) \tag{2.7}$$

$$\dot{\theta} = \mu - r\cos(\theta). \tag{2.8}$$

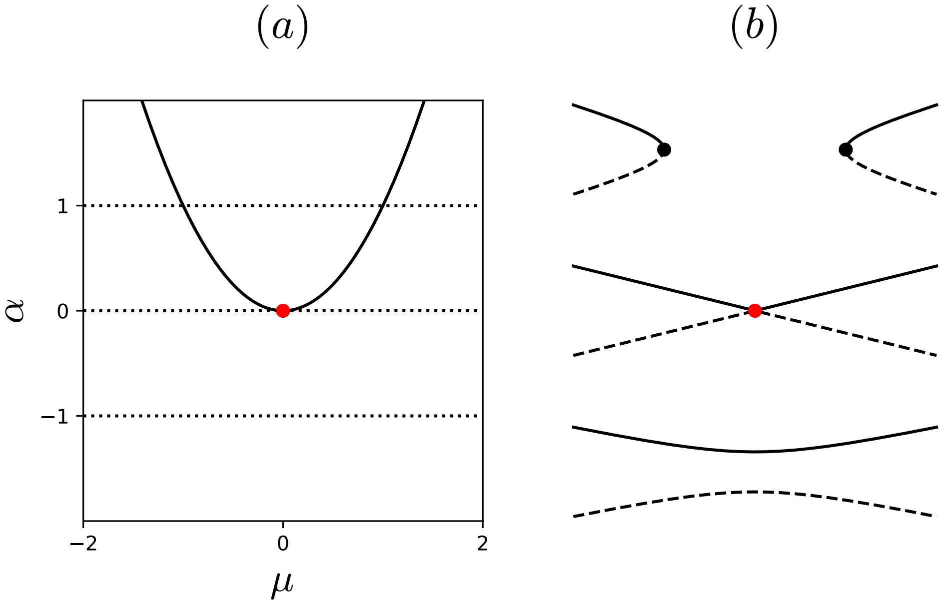

Figure 2.4: Bifurcation diagrams for the necking bifurcation. Plot (a) shows the location of the saddle-nodes in the (μ, α) parameter plane. The bifurcation point is marked with a red dot and the dotted lines denote slices at fixed values of α that correspond to the diagrams in (b) which are plotted offset in the (μ, u) plane. The saddle-nodes are marked with black dots.

Here the radial variable, r, has trivial dynamics. An unstable fixed point at $r = 0$ and stable fixed point at $r = 1$ cause initial conditions to collapse to the unit circle in the radial direction. As a result, the bifurcation can be understood in terms of Eq. (2.8) alone by setting $r = 1$. For $|\mu| < 1$ this equation has a pair of fixed points which are stable and unstable, respectively. In two dimensions one of these points is a saddle and the other is a node. When $\mu = \pm 1$ the bifurcation occurs as the two fixed points annihilate along the unit circle in a saddle-node bifurcation. Without any fixed points, for $|\mu| > 1$ the unit circle is a periodic orbit. The θ-direction of the orbit is positive for bifurcations at $\mu = 1$ and negative if the bifurcation occurs at $\mu = -1$. This process is illustrated in Fig. 2.5.

The SNIPER bifurcation is a global bifurcation. Although it locally involves a saddle-node bifurcation the SNIPER bifurcation creates a finite size periodic orbit. This trajectory leaves the vicinity of the bifurcation point and local analysis of the saddle node cannot detect its presence. The period of the periodic orbit can be computed by integrating Eq. (2.8)

$$T = \frac{1}{2\pi}\int_0^{2\pi} \frac{1}{\mu - r\cos(\theta)}\, d\theta = \frac{1}{\sqrt{\mu^2 - 1}}.$$

As $|\mu| \to 1$ the T diverges as $(|\mu| - 1)^{-\frac{1}{2}}$ which is characteristic of the dynamics near a saddle-node.

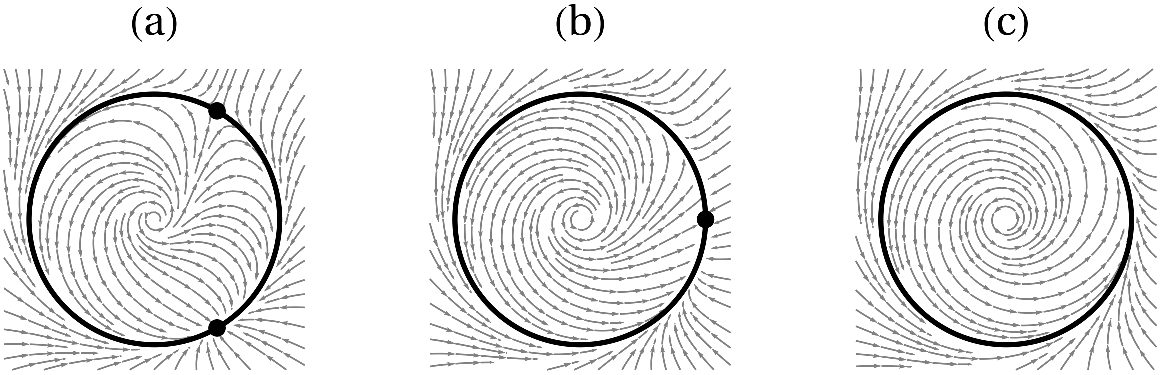

Figure 2.5: Phase space plot for Eqs. (2.7) and (2.8) for increasing values of the parameter: (a) $\mu = 0.5$, (b) $\mu = 1$ and (c) $\mu = 1.5$. The unit circle is shown with a thick black line, fixed points with black dots and the flow with grey arrows. The bifurcation occurs at $\mu = 1$ (b) where the two fixed points collide and annihilate.

2.2 Model equations

This thesis is concerned with the study of spatially extended systems that also exhibit dynamics and thus appropriate models necessarily take the form of PDEs. When we seek to write down a PDE model to describe a physical system we have a specific physical behavior that we wish to capture in mind. In particular we do not attempt to create a "model of everything" but rather try to derive a model that is asymptotically consistent in a particular parameter regime. When such a rigorous derivation is impossible we appeal to principles such as Occam's razor in order to temper the model creation process. Here we have in mind phenomenological examples such as Landau-Ginzburg phase transition models in which few assumptions are made beyond the symmetries that the system possesses and all symmetry allowed terms are included. In this section we explain how these procedures are used to derive the central governing model for the phenomena studied in this thesis and a related model that is not derived but rather proposed by physical reasoning.

Amplitude equations

Consider a spatially extended physical system undergoing a linear instability. Specifically suppose that a system in a single spatial dimension has a linear dispersion relation $\sigma(k, \mu)$ for waves $\epsilon e^{\sigma t + ikx}$ ($\epsilon \ll 1$) such that $\Re(\sigma) > 0$ for some set of wave numbers $\{k_i\}$ (which may be countable or not). Dynamically, initial conditions with small amplitude and a nonzero projection onto the set of unstable modes will grow in amplitude. As this occurs the nonlinear terms in the system will stabilize some Fourier modes and dampen others. Amplitude equations describe the evolution of these Fourier modes. The microscopic equations describing the system need not be known in order to derive an amplitude equation provided that the nature of the linear instability is understood. In this case some parameters of the equation may not be explicitly determined.

Amplitude equations are typically derived using one of two different mathematical theories. These are: the theory of multiple scales and normal form theory. In the multiple scales method applied to a steady state bifurcation one supposes that the solution takes the form

$$u(x,t) = \int_{\mathbb{R}^n} A_k(X,T) e^{ikx} \, dk + c.c. \tag{2.9}$$

where A is the "amplitude" for which we want an equation and X, T are "long"/"slow" space/time scales (we use the term "slow" in the following to refer to both X and T). Because the bifurcation is steady state there is no fast time scale; at a Hopf bifurcation oscillations would also occur on a fast time. These slow scales are obtained by the multiple scales assumption. Typically we let $X = \epsilon^a x$ and $T = \epsilon^b t$ where $a, b > 0$ and then suppose that in the limit $\epsilon \downarrow 0$ the solution varies *independently* on the two scales X and x. Concretely we allow the solution to have the dependence $u = u(X, x, T)$ and perform asymptotic expansions in the limit $\epsilon \downarrow 0$. The amplitude equations result from imposing solvability conditions order by order on the fast scale. In order to use this method one must know the explicit model from which the amplitude equation is to be derived. In this case the resulting asymptotic calculations are straightforward. For example, consider the case of Rayleigh-Bénard convection. Here we seek a description of the behavior near instability of the conducting state and the governing equations are *known* to be Navier-Stokes coupled to the diffusion equation for the temperature field.

If the specific governing model for the problem is not known then normal form theory can be used to derive an amplitude equation nonetheless. Such cases are much more common in the field of pattern formation where soft matter systems undergo identifiable instabilities but do not have known governing equations. Applying normal form theory proceeds initially in a similar manner with the assumption of Eq. (2.9). In particular we make the same multiple scales assumptions but do not explicitly carry out the asymptotic calculation order by order and instead impose symmetry constraints on the possible forms for the nonlinear terms. We include all symmetry allowed terms, i.e. we drop any term that could be eliminated by a transformation of the field as in ODE normal form theory. The multiple scales Ansatz applied to the linear dispersion relation immediately allows us to write down the linear part of the amplitude equation. Since the amplitude equation is derived near the onset of the instability the amplitude of the field is assumed to be small, $A \sim \epsilon^c \tilde{A}$. Once the lowest order symmetry allowed nonlinear terms are determined then c is selected to enforce consistency. Higher order terms are typically dropped formally resulting in a truncated normal form equation. Generically the coefficients of the nonlinear terms are chosen to be $\mathcal{O}(1)$ but specific bifurcations can be studied by allowing particular terms to scale with ϵ. This approach is appealing but can fail when the amplitude equation is nonlocal, see [97].

Derivation of the subcritical Ginzburg-Landau Equation

In this section we derive the main model studied in this thesis: the subcritical cubic-quintic Ginzburg-Landau Equation. In the pattern formation context this equation is derived in the transition regime between sub and supercriticality of the pattern branch. In this case the cubic coefficient is small and fifth order terms are required in order to saturate the nonlinearity.

We seek an amplitude equation to describe the evolution of a one-dimensional system that is unstable to the formation of a patterned state with a particular wave number k_c at the bifurcation point $\mu = 0$ where μ is the control parameter. The dispersion relation for such a system reads

$$\sigma = \mu - (k^2 - k_c^2)^2 + \mathcal{O}[(k^2 - k_c^2)^3] \tag{2.10}$$

The instability occurs for $\mu > 0$ where a set of wave numbers around k_c destabilize. Near the bifurcation consistent scalings are $\sigma = \epsilon^4\tilde{\sigma}$, $\mu = \epsilon^4\tilde{\mu}$ and $k = k_c + \epsilon^2\tilde{k}$ (we drop the tilde). After the multiple scales assumption (Eq. (2.9)) the allowed nonlinear terms are imposed by enforcing the following symmetries: spatial translation, spatial reflection and time translation. To be specific the equation must be equivariant under the following transformations:

$$\begin{aligned}
x \to x+\delta : &\quad A_k(X,T)e^{ikx} \to \left[A_k(X,T)e^{ik\delta}\right]e^{ikx} \\
X \to X+\delta : &\quad A_k(X,T)e^{ikx} \to A_k(X+\delta,T)e^{ikx} \\
x \to -x : &\quad A_k(X,T)e^{ikx} \to A_k(X,T)e^{-ikx} = \overline{\left(\bar{A}_k(X,T)e^{ikx}\right)} \\
X \to -X : &\quad A_k(X,T)e^{ikx} \to A_k(-X,T)e^{ikx} \\
T \to T+\delta : &\quad A_k(X,T)e^{ikx} \to A_k(X,T+\delta)e^{ikx}.
\end{aligned}$$

As A is complex the nonlinear terms at a particular order can be parametrized by polynomial combinations of A, $\bar{A}$ and their spatial derivatives. Supposing $A = \epsilon\tilde{A}$ the lowest order term consistent with the required symmetries is $C_3(X)|A|^2A$. In fact C_3 must be constant due to long scale translation symmetry, real due to spatial reflection symmetry and must be positive in the subcritical regime. Because we seek an equation that describes the transition from sub to supercriticality we then let $C_3 = \epsilon^2\tilde{C}_3$. This is the origin of the term "weakly subcritical" describing this scenario. This choice allows for the inclusion the fifth order terms $C_5|A|^4A$, $ia_1|A|^2A_X$ and $ia_2A^2\bar{A}_X$ in which a_1, a_2 and C_5 are forced to be constant and real. In order that the nonlinear terms saturate C_5 must be negative. This produces a codimension two description of the bifurcation where μ and C_3 are the unfolding parameters. After appropriate rescaling of X, T, A and ϵ the resulting amplitude equation (Eq. (1.1)) may be written,

$$A_t = \mu A + A_{xx} + ia_1|A|^2A_x + ia_2A^2\bar{A}_x + |A|^2A - |A|^4A.$$

where X and T are dropped in favor of their lowercase counterparts.

Past studies of Eq. (1.1) focused mostly on the existence and stability of periodic solutions and coherent structures but a few also examine the well-posedness of the Cauchy problem.

The existence and local stability of rotating wave solutions is treated in [61, 84, 86, 139] while nonlinear stability criteria are provided in [87]. The existence of pulses and fronts was examined in [61], and the persistence of front solutions when the coefficients acquire a small imaginary part was studied in [88]. In the case $a_2 = 0$ a free energy can be defined as follows

$$\mathcal{F}\left(A, \bar{A}\right) = \int_{\mathbb{R}} |A_x|^2 - \mu|A|^2 - \frac{1}{2}|A|^4 + \frac{1}{3}|A|^6 + i\frac{a_1}{4}|A|^2\left(A\bar{A}_x - \bar{A}A_x\right)\,dx$$

so the equation satisfied has gradient structure $A_t = -\frac{\delta\mathcal{F}(A,\bar{A})}{\delta\bar{A}}$. In this case it is known that the energy is bounded from below provided $|a_1| < \frac{4}{\sqrt{3}}$ [86]. This is a necessary condition for well-posedness of solutions of Eq. (1.1) when $a_2 = 0$. In the general case ($a_2 \neq 0$) the condition $|a_1 - a_2| < 2$ is known to be sufficient for global existence of solutions of the Cauchy problem [62]. The same condition is required for the global existence of periodic solutions of Eq. (1.1) and it was suggested though not proved that in this case the bound is sharp [60]. However, the necessary and sufficient condition on the coefficients a_1, a_2 for the global existence of general solutions of Eq. (1.1) remains an open problem.

The Swift-Hohenberg Equation

In this section we discuss a model equation that cannot be derived rigorously but nonetheless has been proposed to describe numerous physical systems with remarkable qualitative agreement. This model is known as the Swift-Hohenberg equation and was first proposed in order to study Rayleigh-Bénard convection [143]. The model takes the form of a partial differential equation for the real-valued order parameter $u(\boldsymbol{x}, t)$

$$u_t = ru - \left(\nabla^2 - k_c^2\right)^2 u - u^3 \tag{2.11}$$

where $\boldsymbol{x} \in \mathbb{R}^2$ and the field u can be thought of as the temperature deviation from the conducting state or the vertical fluid velocity at the mid-plane. This equation has the same linear dispersion relation as Eq. (2.10) and therefore describes systems in which solutions with the wave number k_c have the largest growth rate when $r > 0$. In particular it is tempting to think of Eq. (2.11) as being derived by simply taking the truncation of Eq. (2.10) and attaching an appropriate nonlinearity. However this is not a rigorous procedure and any appropriate spatial scaling in order to justify the dispersion truncation will not yield a differential operator that contains both second and fourth order terms at the same order. On the other hand, despite being phenomenological Eq. (2.11) does respect the desired symmetries of the system, does have a dispersion relation that qualitatively agrees with the physical behavior and does contain fourth order derivatives which are responsible for a plethora of important mathematical properties that we discuss below.

In the context of this thesis we consider a generalized version of the SHE in one dimension that applies to subcritical systems. After appropriate scaling the cubic-quintic SHE can be written

$$u_t = ru - (\partial_{xx} + 1)^2 u + bu^3 - u^5 \tag{2.12}$$

where $u(x,t)$ is real-valued, (r,b) act like unfolding parameters and $x \in \mathbb{R}$. The parameter b measures the degree of subcriticality and the critical wave number has been scaled to $k=1$ (which cannot be done on finite domains). This equation has the Lyapunov functional or "free energy"

$$\mathcal{S}(u) = \frac{1}{2}\int_{\mathbb{R}} ((\partial_{xx}+1)u)^2 - ru^2 - b\frac{u^4}{2} + \frac{u^6}{3}\,dx$$

so that Eq. (2.12) may be written, $u_t = -\frac{\delta\mathcal{S}}{\delta u}$. By differentiating $\mathcal{S}$ this structure yields the simple result that $\frac{d\mathcal{S}}{dt} = -(u_t)^2 \leq 0$ and thus dynamics of the equation evolve in such a way as to minimize the free energy. On a finite size domain this further implies that all initial conditions approach *stationary* minima of $\mathcal{S}$. These stationary solutions to Eq. (2.12) solve a fourth order ODE in the spatial variable which turns out to be a Hamiltonian dynamical system [70]. Specifically, it can be shown that for any solution to the stationary equation the quantity

$$\mathcal{H}(u) = \frac{1-r}{2}u^2 + (u_x)^2 - \frac{1}{2}(u_{xx})^2 + u_x u_{xxx} - b\frac{u^4}{2} + \frac{u^6}{3}$$

is independent of x. In appropriate variables $\mathcal{H}$ serves as the Hamiltonian for the associated dynamical system [70].

In the remainder of this introduction we proceed with the two equations (1.1) and (2.12) hand in hand comparing and contrasting their properties.

2.3 Localization and steady states

A central component of this thesis and the study of pattern formation is the existence of "localized" solutions. Physically speaking these are solutions that exhibit two qualitatively different behaviors in and outside of a compact domain. Stationary localized structures are common in the study of driven dissipative systems and are characterized by a balance of the energy input and dissipation within the structure. Such solutions are thus frequently attractors of the system dynamics and integral to a complete understanding of the possible physical behavior. In this section we discuss the mathematical prerequisites necessary to observe localized stationary solutions and their specific manifestations in equations (1.1) and (2.12).

Spatial dynamics and conditions for localization

The PDE models considered in this thesis are posed in one space dimension and one time dimension and take the form $\boldsymbol{u}_t = \boldsymbol{f}(\boldsymbol{u}, \partial_x, x)$ where ∂_x refers to derivatives of $\boldsymbol{u}$. As a result the stationary solutions solve a set of ODEs in the time-like variable x and all of the previous ODE theory can be applied. This is referred to as *spatial dynamics.* In this paradigm fixed points correspond to spatially constant solutions, homoclinic orbits correspond to pulses and heteroclinic orbits are referred to as fronts. In the context of this thesis we define *localized states* to be the homoclinic and heteroclinic orbits obtained in this spatial dynamics formulation that connect to the fixed point $u \equiv 0$. Although heteroclinic orbits do not decay to the same state biasymptotically, in spatially reflection symmetric problems they can be combined into (potentially non-stationary) heteroclinic cycles that do.

In deriving the necessary criteria for localization to occur there is a natural division between those systems that have autonomous spatial dynamical systems and those that do not. Although any nonautonomous dynamical system can be reduced to an autonomous one by introducing a trivial variable such that $X = x$ and $\dot{X} = 1$, the system no longer has any fixed points. The dichotomy between these two cases is central to the work in this thesis. In particular, this work focuses on localization in the presence of a specific type of non-autonomy when the dependence of $\boldsymbol{f}$ on x is periodic. In order to clearly separate this nonautonomous case from localization in autonomous systems we confine the discussion of periodic nonautonomous problems to section 2.5 and continue here with the added assumption that $\boldsymbol{f}$ has no explicit x dependence.

Consider a one-dimensional system that is spatially reflection-symmetric with steady states described by the autonomous spatial dynamical problem

$$0 = f(u, u_x, u_{xx}, \ldots) \tag{2.13}$$

posed on the real line, $x \in \mathbb{R}$. Furthermore we assume that $(u, u_x, u_{xx}, \ldots) = (0, 0, 0, \ldots) \equiv \mathbf{0}$ is a solution to Eq. (2.13), i.e. $u(x) \equiv 0$ is a fixed point. In the following we derive appropriate conditions under which Eq. (2.13) possesses robust localized states [39]. A dynamical system $\frac{dv}{dx} = h(v)$ with $x \in \mathbb{R}^n$ is said to be reversible if there exists an involution $\mathcal{R} : \mathbb{R}^n \to \mathbb{R}^n$ such that $\frac{d\mathcal{R}(v)}{dx} = h(\mathcal{R}(v))$ [152]. In other words the spatial dynamics on the phase space $\mathcal{R}(\mathbb{R}^n)$ is given by the space reversed vector field. In the problem at hand spatial reflection symmetry implies that Eq. (2.13) is a reversible dynamical system and therefore must be of even dimension. In order for there to exist a solution that is biasymptotic to $\mathbf{0}$ it must be a hyperbolic fixed point. In particular, linearizing Eq. (2.13) about $\mathbf{0}$ yields an equation of the form

$$f_u(\mathbf{0})v + f_{u_x}(\mathbf{0})v_x + f_{u_{xx}}(\mathbf{0})v_{xx} + \ldots = 0$$

where v is small. The eigenvalues associated to the linearization can be determined by setting $v = e^{\lambda x}$ resulting in a characteristic equation that is a polynomial in λ, $\mathcal{P}(\lambda) = 0$. This polynomial is real-valued and thus roots must appear in conjugate pairs. Furthermore, due to reversibility if $\mathcal{P}(\lambda) = 0$ then $-\lambda$ is also a root [152]. Therefore $\mathcal{P}$ is a function of λ^2. In order for the fixed point $\mathbf{0}$ to be hyperbolic one of the roots of $\mathcal{P}$ must be real, the simplest possible case of which is $\mathcal{P}(\lambda) = \lambda^2 - a$. Although such systems may possess homoclinic orbits such solutions are not structurally stable and susceptible to destruction by global bifurcations. As a result such systems do not possess robust localized states and provide a poor model for localization in physical systems. Fortuitously the next simplest case, $\mathcal{P}(\lambda) = \lambda^4 - b\lambda^2 + a$, does support robust localization.

The location of the roots of $\lambda^4 - b\lambda^2 + a$ in the complex plane is pictured in Fig. 2.6 as a function of a and b. Cases in which the roots lie off the imaginary axis potentially enable localization. Of particular note is the curve C_2 which corresponds to a bifurcation in

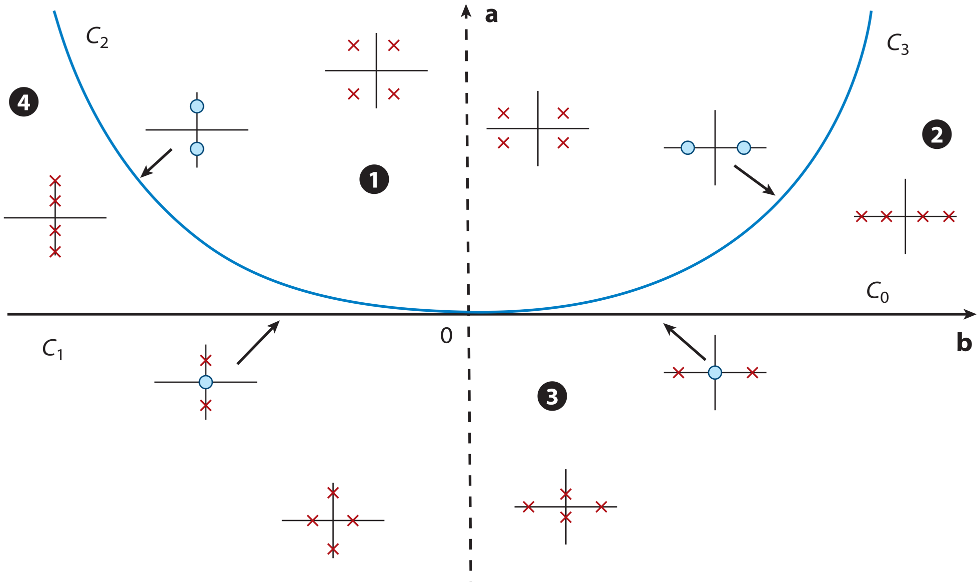

Figure 2.6: The eigenvalues of a fourth order reversible dynamical system with characteristic polynomial $\lambda^4 - b\lambda^2 + a$ are pictured in the (b, a) plane. Four distinct regions of behavior are labeled. The curve C_2 corresponds to the celebrated Hamiltonian-Hopf bifurcation. This figure is adapted from [39, 98].

which the eigenvalues collide on the imaginary axis and then leave it. This is referred to as a Hamiltonian-Hopf bifurcation [65, 82, 154] and is central in systems supporting localized patterned states. It is immediately obvious from its dispersion relation that this bifurcation occurs in the SHE (Eq. (2.12)) as the control parameter r is increased through $r = 0$.

Beyond the hyperbolicity of the fixed point the existence of localized solutions requires the intersection of the unstable and stable manifolds of the fixed point, $\mathbf{0}$. When $n = 4$ and the dynamical system is reversible, as assumed here, the codimension of such an intersection is in many cases reduced. For example when $\mathbf{0}$ has two-dimensional stable and unstable manifolds their intersection is generically codimension one but in reversible systems it is zero. In such a scenario no parameters are required to be set in order to observe such an intersection and thus localized states are robust.

Exact localized solutions of the Ginzburg-Landau Equation

The central tenant of this thesis is the development of stationary localized states in Eq. (1.1). As the equation is second order in space robust solutions of this type do not exist without some modifications which in this work will take the form of a periodic potential. Despite this the basic localized solutions that exist in Eq. (1.1) turn out to be important precursors to the robust solutions described in chapter 5. In fact these solutions can be computed exactly yielding full parameter dependence. Exact solutions to the full version of Eq. (1.1) can be

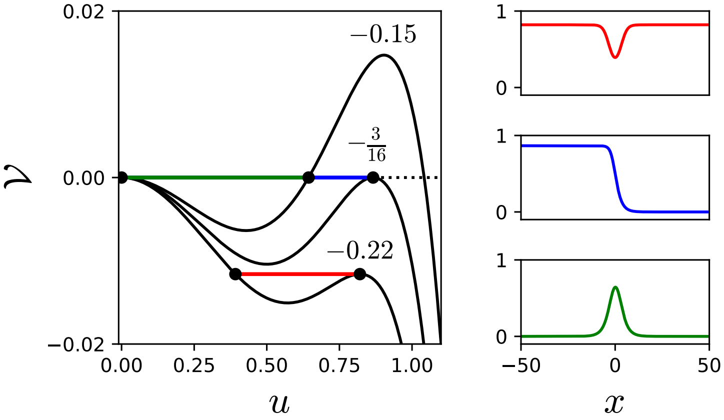

Figure 2.7: The potential $\mathcal{V}(\mu, u)$ is plotted for three distinct values of $\mu = -0.15, -\frac{3}{16}, -0.22$ (black). The three canonical solution types: homoclinic to $u = \sqrt{\frac{3}{4}}$ (red), front between $u = \sqrt{\frac{3}{4}}$ and $u = 0$ (blue) and homoclinic to $u = 0$ (green) are plotted on the potential plot and also to the right as a function of x.

quite complicated and we devote the entirety of chapter 4 to one important case. In this section we illustrate the basic stationary localized solutions by use of the somewhat simpler Ginzburg-Landau equation

$$0 = u_{xx} + \mu u + u^3 - u^5 \tag{2.14}$$

where $\mu \in \mathbb{R}$ and u is real-valued. Solutions of Eq. (2.14) share many qualitative characteristics with those of Eq. (1.1) and are therefore useful in order to understand solutions of the more general equation.

Equation (2.14) is common in physics and is referred to as a "particle in a potential" type problem. Integrating the equation once yields

$$\begin{aligned} E &= \frac{u_x^2}{2} + \mu\frac{u^2}{2} + \frac{u^4}{4} - \frac{u^6}{6} \\ &= \frac{u_x^2}{2} + \mathcal{V}(\mu, u), \end{aligned} \tag{2.15}$$

where E is the first constant of integration and acts as the "total energy" for a particle in the potential $\mathcal{V}$. The solutions of Eq. (2.15) can be understood by way of the potential, which is plotted for three values of μ in Fig. 2.7. For each of the three cases we exhibit one of the canonical solutions to Eq. (2.15). We call these solutions "canonical" because they represent the three generic connections between hyperbolic fixed points in Eq. (2.14).

The equation can be integrated once again in order to recover the spatial dependence of the three types of solutions pictured in Fig. 2.7. Re-arranging Eq. (2.15) produces

$$x - x_0 = \int^u \frac{du}{\sqrt{2E - 2\mathcal{V}(\mu, u)}},$$

where E is selected appropriately based on the desired solution and x_0 is the second constant of integration. The constant x_0 corresponds to the translation symmetry in the problem and is dropped in what follows. Of the three solutions portrayed in Fig. 2.7 only the pulse and front connect to the hyperbolic fixed point $u = 0$. The front only exists at a particular parameter value while the pulse exists over a parameter range. The integration constant E and explicit solutions for these two cases are as follows

$$\begin{array}{llll} \text{Front:} & E = 0 \quad \mu = -\dfrac{3}{16} & ; & u = \dfrac{\sqrt{3}}{\sqrt{e^{-\frac{\sqrt{3}}{2}x} + 4}} \\ \text{Pulse:} & E = 0 \quad -\dfrac{3}{16} < \mu < 0 & ; & u = \dfrac{\sqrt{-3\mu}}{\sqrt{\left(\mu + \frac{3}{16}\right)\varphi^2 + \frac{3}{4}\left(\varphi^{-2} + 1\right)}}, \end{array}$$

where $\varphi = e^{\sqrt{-\mu}x}$.

These basic solutions are in fact members of a much more general family of traveling solutions to Ginzburg-Landau equations. In systems with translation symmetry, solutions like those derived above frequently belong to a set of solutions of the form $u(x, t) = f(x - ct)$ where $c = 0$. In particular by a change of frame to one moving at speed c the governing equation acquires an advective term and then all stationary solutions in the moving frame form a family of traveling solutions in the lab frame parametrized by the frame speed. Because these solutions are non-stationary in the lab frame we delay a discussion of their dynamics to section 2.4 in which dynamical behavior is discussed.

A significant effort has been devoted to solving nonlinear equations for traveling structures exactly and a variety of methods exist for Ginzburg-Landau equations in particular [46, 108, 136]. Chapter 4 is devoted to the application of one such method to Eq. (1.1) in order to derive an exact traveling front solution. This solution turns out to be central to understanding the dynamics of Eq. (1.1) and localization when inhomogeneities are introduced in chapter 5.

Localized snaking solutions of the Swift-Hohenberg Equation

When the SHE has nonlinearities that compete, such as in Eq. (2.12), a branch of periodic solutions (denoted P) may bifurcate from $u = 0$ subcritically creating a region in which both $u = 0$ and a stationary spatially periodic solution are hyperbolic. In Eq. (2.12) the bifurcation occurs at $r = 0$. This structure is shown in Fig. 2.8. In addition to the branch P four branches of localized states, $L_{0,\frac{\pi}{2},\pi,\frac{3\pi}{2}}$, bifurcate out from $u = 0$ at $r = 0$ [32]. These localized states take the form of heteroclinic cycles: $0 \to P \to 0$. Physically this is facilitated by the locking of the fronts bounding the structure to the state P. The solutions on branch L_0 have a maximum at their center and are spatially symmetric whereas those on $L_{\frac{\pi}{2}}$ have a node and are antisymmetric. The branch L_0 ($L_{\frac{\pi}{2}}$) is related to L_π ($L_{\frac{3\pi}{2}}$) by reflection $u \to -u$ which is a symmetry of the system. Because of this curves L_0, L_π (and $L_{\frac{\pi}{2}}, L_{\frac{3\pi}{2}}$) are indistinguishable in Fig. 2.8. The branches of localized states lie on a set of bifurcation curves that oscillate back and forth in a subregion of the subcritical region known as the *pinning region*. This intertwining of the bifurcation curves is the genesis of the name *snaking* for this bifurcation structure.

The localized solutions change significantly as the parameter r is decreased away from the bifurcation point. Near the bifurcation point the branches of localized states that emerge from $u = 0$ have a small amplitude and large spatial extent. As r is reduced they begin to localize and grow in amplitude. Once the central part of the structure nears the amplitude of P the solutions enter the snaking regime. As one follows the bifurcation curves of localized states upwards one passes through folds at either extreme of the pinning region and the solutions grow in spatial extent. This can be seen by tracking the base state at successive folds as the snaking branch is traversed, Fig. 2.8. As the branch is continued from small to large $\|u\|_{L^2}$ the fronts bounding the localized state advance outwards and in so doing add additional half periods of the state P at the edges of the structure. One complete cycle back and forth across the pinning region extends the localized state by a single wavelength, a half on either side. When the problem is posed on $\mathbb{R}$ this snaking process continues ad infinitum.

One important set of additional localized solutions that are present in the pinning region are the so-called “rung states.” These solutions are spatially asymmetric and lie on branches that connect to the symmetric (L_0) and antisymmetric ($L_{\frac{\pi}{2}}$) branches near their folds. These are pictured in Fig. 2.8. These solutions parametrize the transformation of a symmetric solution into an antisymmetric one (and vice versa) by adding a half wavelength of P as r is swept across the pinning region. The presence of these additional rung branches is the cause of name “snakes and ladders” applied to this whole bifurcation structure.

This snaking phenomenon is related to the existence of a special parameter value r for which the free energies of P and $u = 0$ match. This special point is known as the *Maxwell point* by analogy to the Maxwell construction of equilibrium statistical mechanics. In the famous case of a van der Waals gas undergoing a first order phase transition the Maxwell construction is defined by the condition that the Gibbs free energies of the gas and liquid are equal. A similar phenomenon is at work here although the system is not in equilibrium. The free energy of P, $\mathcal{S}(P)$ where the integral is taken over a single period, decreases monotonically through zero as r is increased above the value at the fold along the upper part of the branch (solid line in Fig. 2.8). In particular there exists a value of r such that its energy vanishes matching the free energy of the trivial solution $u = 0$. This Maxwell point value is determined by the joint conditions $\mathcal{S}(P) = 0$ and $\mathcal{H}(P) = 0$ [30, 32]. It is around this point that a finite energy gap (the pinning region) opens in which stationary localized solutions that connect P to $u = 0$ are found. A physical understanding of this phenomenon is that the fronts bounding the structure require a finite energy in order to exceed the local

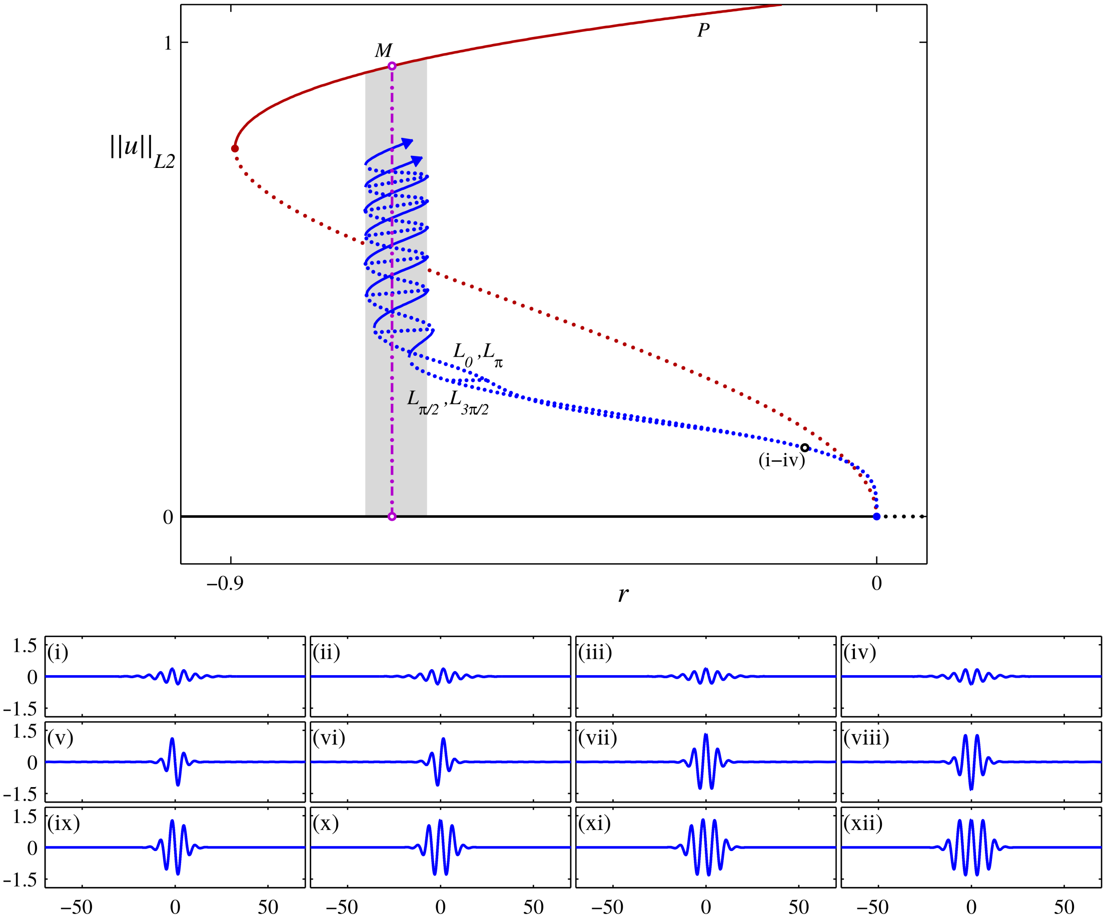

Figure 2.8: Bifurcation diagram showing snaking solutions of Eq. (2.12) for $b = 2$ along with plots of solution profiles below. The solution measure in this bifurcation diagram is the L^2 norm of the solutions. The periodic branch P (red) is pictured bifurcating from $u = 0$ (black) along with the branches $L_{0,\frac{\pi}{2},\pi,\frac{3\pi}{2}}$ (blue). Here the L^2 norm of P is taken over only one period not $\mathbb{R}$. The continuation of the snaking branches is stopped early once inside the pinning region. The pinning region is shaded in grey and the Maxwell point denoted with a vertical magenta line. Bifurcation curves represented with solid (dotted) lines represent solutions that are stable (unstable) in time. This temporal stability analysis is described in section 2.4. This figure is adapted from [30].

pinning potential caused by their interaction with the periodic state [125]. As a result the fronts remain pinned in a finite interval around the Maxwell point.

The size of the pinning region around the Maxwell point depends crucially on the subcriticality parameter b. The snakes and ladders structure in Eq. (2.12) is enabled when $b > 0$ and the primary bifurcation is subcritical. In particular, the structure emerges from the codimension two point $b = 0$, $r = 0$ through a set of hysteresis bifurcations [32]. The width of the pinning region is exponentially thin if $|b| \ll 1$ as a function of b and the snakes and ladders picture is not fully developed until a critical value of b is reached [30, 51].

The snaking structure persists on a finite interval but with some important differences. Firstly with Neumann or Dirichlet boundary conditions the branches of localized states no longer bifurcate from the state $u = 0$ but rather occur a secondary bifurcation on P near $r = 0$. Secondly, as the snaking branches are continued and the localized states grow in extent the domain eventually fills with the periodic state P. This causes the bifurcation curves of localized states to exit the pinning region and either connect to the branch P near but below its fold or other periodic branches. This is not true for Robin boundary conditions for which the the localized branches bifurcate from $u = 0$ at $r = 0$ and there is no periodic branch [113].

2.4 Temporal stability and dynamics

The study of the dynamics of PDEs such as those investigated in this thesis is typically accomplished in two stages. The first stage is to analyze the linear stability properties of the stationary solutions of the PDE, i.e. the evolution of asymptotically small perturbations to stationary solutions. The second stage is to consider perturbations of order one and the asymptotic attractors of the system. Both of these steps are carried out with a combination of analytical and numerical techniques depending on the situation. In this section we discuss the analytical understanding of each of these stages and delay the details of numerics to chapter 3.

The prototypical PDE model considered in this thesis takes the general form $\boldsymbol{u}_t = \boldsymbol{f}(\boldsymbol{u}, \partial_x, x)$. The dynamics of such a PDE are determined by an *initial value problem* posed on a domain $\Omega = \mathbb{R}$ or $[a, b]$ with initial data $\boldsymbol{u}(x, 0) = \boldsymbol{u}_0(x)$ and appropriate spatial boundary conditions. The mathematical formulation of such a problem also involves specifying a function space (a generalization of the dynamical system phase space) in which solutions to the PDE are sought. Such a space is equipped with an inner product and norm, $\|.\|$, which defines a distance in the function space. Our results do not depend critically on the exact choice of this space but a good example to keep in mind for the work here is L^2, the space of square integrable functions. Although the dimension of the PDE phase space is nominally infinite, many of the concepts from dynamical systems theory transfer. In particular stationary solutions generalize the notion of fixed points, and behavior of the PDE with initial data near a given stationary solution is governed by a linearized problem as in the case of finite-dimensional systems.

Linear stability

Similar to the stability for a fixed point of a dynamical system, the linear stability of a stationary solution $\boldsymbol{u}_0(x)$ to a PDE is assessed by letting $\boldsymbol{u}_0(x)+\boldsymbol{u}_1(x,t)$ where $0 < \|\boldsymbol{u}_1(x,0)\| \ll \epsilon$. Then to lowest order $\boldsymbol{u}_1$ solves the linear PDE

$$\boldsymbol{u}_{1t} = \left(\left.\frac{\delta \boldsymbol{f}}{\delta \boldsymbol{u}}\right|_{\boldsymbol{u}=\boldsymbol{u}_0} \right) \boldsymbol{u}_1 \equiv \mathcal{L}(\boldsymbol{u}_1), \tag{2.16}$$

where $\frac{\delta}{\delta \boldsymbol{u}}$ is a Fréchet derivative, at least as long as $\|\boldsymbol{u}_1\|$ remains small. Letting $\boldsymbol{u}_1(x,t) = e^{\sigma t}\tilde{\boldsymbol{u}}_1(x)$ produces a linear eigenvalue problem $\sigma\tilde{\boldsymbol{u}}_1 = \mathcal{L}(\tilde{\boldsymbol{u}}_1)$ for the eigenvalue σ and eigenfunction $\tilde{\boldsymbol{u}}_1$. We refer to the set of eigenvalues $\{\sigma\}$ as the *spectrum* of the linear operator $\mathcal{L}$. Provided that $\|\boldsymbol{u}_1\|$ is small the dynamics of $\boldsymbol{u}_1$ are then completely determined by the spectrum of $\mathcal{L}$. When the spectrum is contained in the left complex half-plane or the imaginary axis, i.e. $\Re[\sigma] \leq 0$ we call the stationary solution stable and otherwise unstable. When such a problem is posed on $\mathbb{R}$ the spectrum is generally the union of two pieces referred to as the *essential spectrum* and the *point spectrum.* The point spectrum of the operator $\mathcal{L}$ is a countable set of isolated eigenvalues while the essential spectrum is characterized by an uncountable set of eigenvalues typically lying on a set of curves in the space $(\Re[\sigma], \Im[\sigma])$.

In the simplest case the spectrum of the linear operator only contains an essential part. This case occurs in the analysis of domain-filling solutions such as those of constant amplitude. Then the linear operator does not typically have spatial dependence and is analogous to the problem of free particles in quantum mechanics. Here the spectrum is typically given by the dispersion relation for Fourier modes and depends continuously on the Fourier wave number k. This picture is significantly more complicated for localized solutions for which the linear operator $\mathcal{L}$ does have spatial dependence and the quantum mechanical analog is the problem of a particle in a potential.

In order to define the essential spectrum $\sigma_{ess}(\mathcal{L})$ and point spectrum $\sigma_{pt}(\mathcal{L})$ rigorously some definitions are required. An operator $\mathcal{L}$ is said to be *Fredholm* if its kernel is finite-dimensional and its range is closed with finite codimension. Motivated by this we define the Fredholm index of an operator by the difference

$$\text{ind}(\mathcal{L}) = \dim[\ker(\mathcal{L})] - \text{codim}[R(\mathcal{L})].$$

Let X be a Banach space and let $\mathcal{L} : D(\mathcal{L}) \subseteq X \to X$ be a closed linear operator with a domain $D(\mathcal{L})$ that is dense in X. Then for $\sigma \in \mathbb{C}$ and I the identity operator if $\sigma I - \mathcal{L}$ is not Fredholm, or $\sigma I - \mathcal{L}$ is Fredholm but $\text{ind}(\sigma I - \mathcal{L}) \neq 0$ then $\sigma \in \sigma_{ess}(\mathcal{L})$. The point spectrum is then defined as the set of eigenvalues not in the essential spectrum, $\sigma_{pt}(\mathcal{L}) = \sigma(\mathcal{L}) \backslash \sigma_{ess}(\mathcal{L})$.

An intuitive understanding of the types of spectrum when $\boldsymbol{u}_0$ is a localized solution is as follows. The essential spectrum in this case contains eigenfunctions associated to the stability of the solution in the spatially asymptotic extremes, $|x| \to \infty$. For localized solutions $\boldsymbol{u} \to 0$ in this limit and the linear operators $\mathcal{L}_{\pm\infty} = \lim_{x\to\pm\infty} \mathcal{L}$ typically become constant coefficient operators. Physically speaking, because the system is homogeneous in these limits its spectrum is given by the dispersion relation for Fourier modes. As a result the associated eigenfunctions, $\boldsymbol{a}_k e^{ikx} + c.c.$, are understood to be valid only in this limit, not localized in space and may individually violate the boundary conditions of the linear problem; this is similar to the free particle problem in quantum mechanics. The essential spectrum is then given by the union of the spectra of $\mathcal{L}_{\pm\infty}$. Point spectra on the other hand correspond to isolated eigenvalues and thus to particular solutions of the linear eigenvalue problem that satisfy the boundary conditions in both asymptotic limits simultaneously, i.e. they are genuine solutions to the spatial ODE. These eigenfunctions are typically spatially localized nearby the base state and frequently reflect symmetries in the system. When an eigenvalue problem is solved numerically all eigenvalues are point eigenvalues but a subset of them converge to the essential spectrum as the number of discretization points increases. This makes identifying point eigenvalues numerically quite subtle.

One of the most important components of an operator's spectrum and eigenspace are eigenfunctions with eigenvalue zero, or *null eigenfunctions.* These eigenfunctions are frequently localized in space. They typically arise in systems that possess continuous symmetries as a consequence of Noether's Theorem. The most celebrated example is known as the Goldstone mode and is the null eigenfunction associated to translation symmetry. Although these zero eigenvalue modes formally do not give rise to dynamics of $\boldsymbol{u}_1$ since $\sigma = 0$, they are in fact relevant to the dynamics of solutions nearby but not at the stationary base state. They dominate the long time behavior of the evolution while modes with larger eigenvalues damp out quickly.

Linear instabilities manifest in a variety of ways depending on how the spectrum of the linear operator enters the right complex half-plane as system parameters are varied. The setting for understanding the onset of linear instability is one in which the PDE has a stable stationary solution that destabilizes as a system parameter is changed. Instabilities corresponding solely to point spectra crossing the imaginary axis are complicated and differ on a case by case basis but those caused by the essential spectrum are better understood. In the following section we consider the case in which the spectrum is parametrized by the dispersion relation for Fourier modes, $\sigma(k)$.

Instability spreading speeds

In many cases when an unstable system is perturbed locally in space the initial perturbation expands throughout the system at finite speed. This speed can be determined directly from the dispersion relation.

Consider a compactly supported initial perturbation of an unstable system with dispersion relation $\sigma(k)$. For simplicity we will also assume that the field of interest $u_1(x,t)$ is scalar. The solution to Eq. (2.16) can be expressed in terms of the Fourier transform $u_1(x,t) = \int_{\mathbb{R}} \hat{u}_1(k) e^{\sigma(k)t - ikx} dk$. Because the system is unstable the perturbation grows in size and extent over time but we assume that because the leading edges of the perturbation are infinitesimal they are described by the linearized problem even as $t \to \infty$. A sketch of this is shown in Fig. 2.9. We define the right flank of the perturbation (a rightward prop-

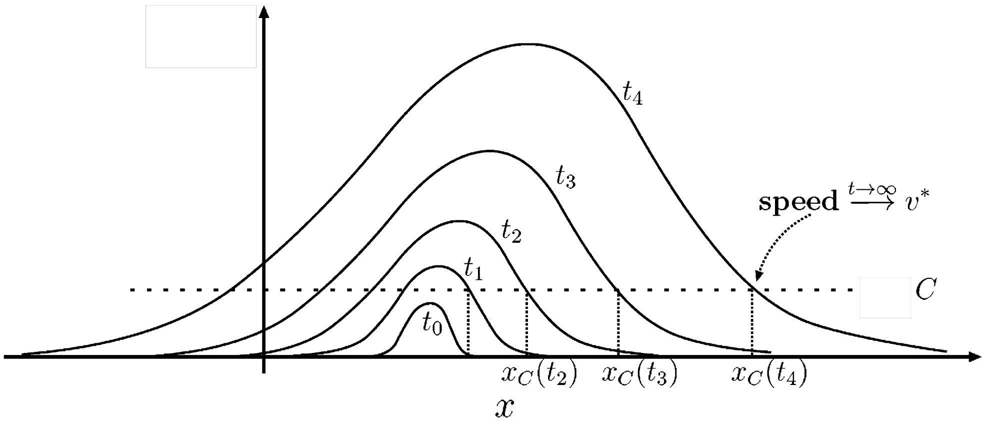

Figure 2.9: A plot of the solution $u(x,t)$ at a set of time snapshots t_k. The initial perturbation grows in time, and its right flank $x_C(t)$ moves asymptotically at speed v^*. This figure is taken from [133].

agating front) by the level set $x_C(t) = \text{argmax}_x \{u_1(x,t) = C\}$ where C is some fixed small height that has an intersection with u_1. Transitioning to a frame moving at the right flank speed $v^* = \frac{dx_C}{dt}$ via $z = x - v^*t$ we obtain $u_1(z,t) = \int_{\mathbb{R}} \hat{u}_1(k) e^{[\sigma(k)+ikv^*]t - ikz} dk$. In the frame moving with speed v^* we see the right flank neither grow nor decay as $t \to \infty$. In this limit the dominant contribution to the integral can be determined by a saddle point approximation applied to the coefficient of t which yields $\frac{d}{dk}\left[\sigma(k) + ikv^*\right] = 0$. Then the requirement that the right flank neither grow nor decay is enforced by requiring the coefficient of t to be imaginary, $\Re\left[\sigma(k) + ikv^*\right] = 0$. These requirements are summarized by the conditions [133]

$$\Re\left[\frac{d\sigma(k^*)}{dk}\right] = 0, \quad -\Im\left[\frac{d\sigma(k^*)}{dk}\right] = \frac{\Re[\sigma(k^*)]}{\Im[k^*]} = v^*, \quad \Im[k^*] > 0 \tag{2.17}$$

from which one may compute the *complex*-valued wave number k^* and the *linear spreading speed* $v^* = \frac{\Re[\sigma(k^*)]}{\Im[k^*]}$ that characterize the leading edge of the perturbation [135]. The imaginary part of the wave number represents the spatial decay rate, $\Im[k^*] \equiv \kappa^*$, of the leading edge. If there are no phase-slips at the front then the wave number that is deposited by the instability is $-\frac{\Im[\sigma(k^*)]}{v^*}$ because the deposited pattern moves with speed v^* in the moving frame [15].

The reader is referred to [133] for a comprehensive review of the derivation of this criterion and its applications. Although this criterion relies on linearity it provides accurate predictions for many nonlinear front propagation problems when the front propagates into an unstable state. This is summarized by the so-called *marginal stability conjecture* which posits that given a sufficiently localized initial perturbation of an unstable state the asymptotic speed at which the perturbation spreads is v^*. The conjecture is also known to apply to systems that do not admit uniformly traveling profiles, such as the supercritical SHE [136], but is also known to fail in other problems [133]. These ideas have been employed extensively in the context of fluids [28, 80, 81], plasmas [22, 104] and biological systems [140].

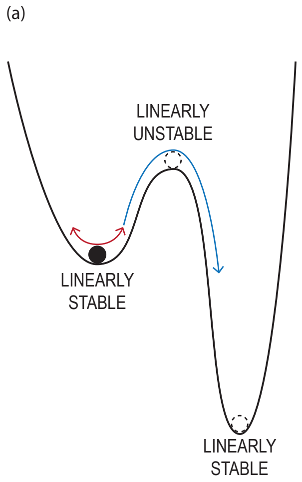

Figure 2.10: A classical dissipative particle sits in the upper well of a two well potential. The particle is stable to small perturbations (dynamics illustrated with red arrow) but unstable to sufficiently large perturbations that exceed the local potential barrier (blue arrow). In this case the particle may fall into a different stable state with lower potential energy. This figure was created by Sara Tepfer.

Nonlinear stability

While linear stability measures the effects of infinitesimal perturbations the evolution of finite amplitude perturbations to stationary solutions is significantly more complicated. The term *nonlinear stability* refers to such a scenario and has a precise mathematical definition [90] but for the purposes of this thesis we shall think of nonlinear stability through the analogy of a particle in a potential. Figure 2.10(a) shows a dissipative particle in a potential well that is linearly stable but nonlinearly unstable. If given a sufficiently large perturbation the particle may fall into the right well at a lower potential. Note that the right well is also nonlinearly unstable for a similar reason. An important concept in this context is that of a *global attractor*, which is a set in phase space that all initial conditions approach as $t \to \infty$. In the particle scenario here one might define the global attractor to be the union of the bottoms of both potential wells. It is important to note that the right well is not a global attractor by itself since there are initial conditions that do not approach it as $t \to \infty$. Although the particle in a potential picture is mathematically non-rigorous it is qualitatively representative of a large number of situations encountered in PDE stability.

Front propagation and instability in the Ginzburg-Landau equation

In the study of Eq. (1.1) as a model for the development of spatial patterns one central dynamical question is: "at what speed does a front between the patterned state and the trivial state propagate?" It turns out that in many cases physically relevant initial conditions evolve into a front whose profile and "spreading" speed as $t \to \infty$ depend only on the system parameters and not on the initial data. Indeed, in many systems these asymptotic front speeds are unique for a large class of sufficiently localized initial conditions [5, 6].

Front propagation into a trivial state may arise in one of two qualitatively different ways. When $\mu < 0$ and the primary pattern-forming instability is subcritical, as assumed here, the system exhibits bistability between a stable trivial state and a stable nontrivial state, implying that the front between them corresponds to a front propagating into a stable state. This type of front is known as a "pushed" front. In systems with gradient structure (here $a_2 = 0$) the speed of such fronts is determined by the energy difference between the two stable states connected by the front. Propagation favors the state with lowest energy and the front velocity vanishes when the energy difference vanishes, i.e., at the Maxwell point, $\mu = \mu_M$. More generally ($a_2 \neq 0$), if a stationary front between the two hyperbolic equilibria exists then it corresponds to a Maxwell-like point and the front speed v in the vicinity of this point satisfies $v \approx \frac{3(\mu-\mu_M)}{2(-\mu_M)^{\frac{3}{2}}} \left[4 - a_2(a_1 + a_2)\right]^{-1}$ [84]. In contrast to this picture, when $\mu > 0$ the trivial state is unstable and the speed of the resulting "pulled" front is frequently (but not always) determined by the properties of the linearization of Eq. (1.1) about $A = 0$ using the methods discussed previously. That is, the front propagates with the linear spreading speed v^* determined by Eqs. (2.17). This change in the speed selection mechanism is a consequence of the growth of infinitesimal perturbations of the $A = 0$ state ahead of the front [52].

Problems of front propagation into unstable states have been known in the plasma physics community since the 1950s [104] but the term "marginal stability" was not proposed until 1983 by Dee and Langer [52]. The marginal stability conjecture, which was formulated in the context of front propagation, is based on the idea that the front propagating into an unstable state that is selected at large times is marginally stable in the comoving frame. In practical terms this means that in the comoving frame of the selected front instabilities of the unstable state ahead of the front are neither advected to $-\infty$ behind the front nor grow into a faster front. This description is closely related to the notions of convective and absolute instability in systems with imposed flow. A system is said to be *convectively* unstable if sufficiently spatially localized perturbations grow but do not spread upstream rapidly enough to overcome the imposed flow. It is called *absolutely* unstable if the perturbation can spread upstream against the flow. In the former case the perturbation at any fixed position ultimately decays, while in the latter case instability is ultimately observed at all locations in the domain. The marginal stability condition corresponds to the transition between convective and absolute instabilities in the comoving frame.

In certain cases the selected asymptotic velocity for fronts propagating into unstable states cannot be predicted by the marginal stability criterion and a nonlinear mechanism produces velocities that differ from the linear prediction. This phenomenon, known as "nonlinear selection," was first pointed out in the work of [15]. Nonlinear selection is extensively reviewed in [134] where Eq. (1.1) is proposed as the most general model for the dynamics near a subcritical steady-state bifurcation. In [134] nonlinear selection is defined as follows: if there exists a front solution with velocity $v^\dagger$ and spatial decay rate $\kappa^\dagger$ that satisfy

$$v^\dagger > v^*, \quad \kappa^\dagger > \kappa^* \tag{2.18}$$

then this front is established as $t \to \infty$ from localized initial conditions. That is, only under these conditions is a "pulled front" moving at speed v^* not selected and a "pushed front" moving at speed $v^\dagger$ is selected instead. This conjecture also requires that the initial conditions have a spatial decay rate not less than $\max\left(\kappa^\dagger, \kappa^*\right)$. These criteria for nonlinear selection are lent mathematical credence by the work of [127]. Specific cases of nonlinear selection are studied rigorously in [6] and lower bounds on front speeds quantifying violations of linear speed selection are derived in [13, 14] among others. Although a general result characterizing the speed $v^\dagger$ is not known, the wide applicability of the linear criterion determining v^* makes it relatively easy to test the hypothesis in (2.18) numerically.

Front propagation, both pushed and pulled, is further complicated by the presence of secondary instabilities in the wavetrain left by the leading edge. While a propagating front solution to Eq. (1.1) is nonstationary and thus technically an unstable solution in the lab frame it is frequently stable in the frame that is comoving with the leading edge. In this frame the instabilities that remain are due either to the asymptotic states (the essential spectrum) or due to point eigenvalues. While no general statements can be made in the latter case, the former is known as a Benjamin-Feir (BF) instability. If the wavetrain behind the front is BF unstable then the marginal stability conjecture can be applied (in this case to the linear problem for disturbances to the wavetrain in the lab frame) generating an associated velocity, v_{BF}. This velocity is associated to the propagation of a front within the asymptotic wavetrain as it goes unstable and is distinct from the primary front. We refer to this as a secondary front. When v_{BF} exceeds the velocity of the primary front the instability manifests as an instability of the essential spectrum of the primary front in its comoving frame. A detailed analysis of pulled and pushed fronts along with the associated secondary instabilities in Eq. (1.1) is carried out in chapter 4.

Finally, though beyond the scope of this thesis, we remark that front instabilities are further complicated in higher dimensions. For example, the fronts of Eq. (1.1) can be thought of as 1D projections of a more general class of fronts with trivial transverse spatial dependence in a more general 2D amplitude equation [78]. In two dimensions these fronts not only carry all of the instabilities of the 1D system in the direction normal to the front but also a new set that occur in the transverse direction. These transverse instabilities can lead to new behavior including breaking up the front into fingers and altering the propagation speed of the interface.

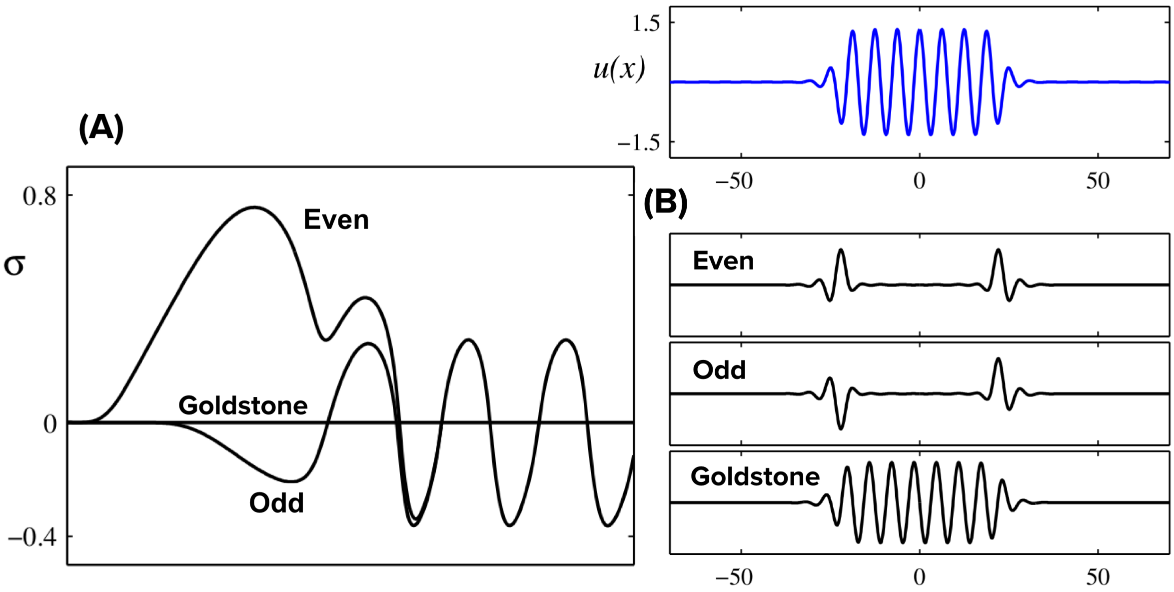

Figure 2.11: (a) The three largest eigenvalues as a function of arclength along the L_0 snaking branch. These eigenvalues correspond to the even, odd, and Goldstone eigenfunctions examples of which are shown in (b) at a particular parameter value. This figure was adapted from [30].

Dynamics of snaking solutions of the Swift-Hohenberg equation

Temporal stability properties of the snaking solutions to the SHE follow a systematic structure. The linear stability of the snaking solutions to Eq. (2.12) is indicated in Fig. 2.8 by the line type used in the plot: stable (unstable) solutions are plotted using a solid (dotted) line. The trivial solution is stable provided that $r < 0$ and out of the primary bifurcation the periodic branch P along with the localized branches emerge subcritically and are therefore all unstable. The branch P acquires stability at its saddle node and it remains stable into the $r > 0$ regime as the branch is followed. Beginning at low amplitude the localized branches remain unstable until they enter the pinning region. Once there a regular stability structure develops as the branches are continued, and the stability switches at every fold. The alternating stability profile of the snaking branches in the pinning region means that experimental observations of snaking, which only involves stable solutions, take the form of a disconnected set of nearly parallel solution branches positioned at increasing amplitudes withing the pinning region.

Although the PDE stability problem for snaking states is infinite-dimensional only three eigenmodes have nonnegative eigenvalues. These eigenmodes include the Goldstone mode with eigenvalue zero and two edge modes localized at the boundaries of the localized struc-

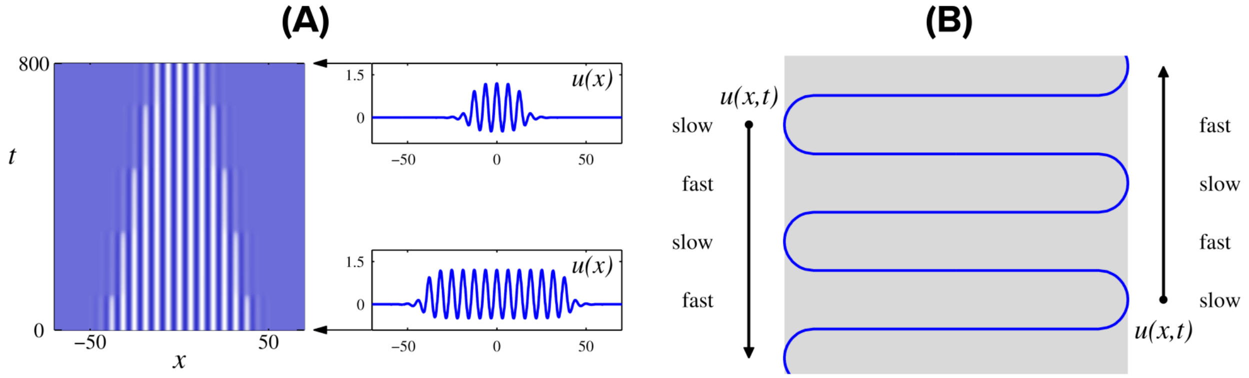

Figure 2.12: (a) A space time plot showing the dynamics of a localized state on the left side of the snaking branch outside of the pinning region. The central structure shrinks as time advances shedding wavelengths of the state P that makes up its center. Plots of the initial and final solution are also shown for clarity. (b) A schematic bifurcation diagram showing the dynamics of depinning. The dynamics of (a) are represented on the left side of the snaking branch where the solution shrinks in norm over time. This cartoon illustrates the two timescales that are present in the dynamics, where the solution norm changes more slowly when the solution is near a fold solution of the snaking branch. This figure was adapted from [30].

ture, at the positions of the fronts, that are of even and odd spatial symmetries, respectively. Examples of these modes and the base state from which they are computed are shown in Fig. 2.11(b). The three eigenvalues corresponding to these modes computed along the snaking branch as a function of arclength, s, are plotted in Fig. 2.11(a). At the base of the branch (small s) when the localized solutions have a large spatial extent the edge modes have significantly different eigenvalues. This difference shrinks as the branch is continued and for large s, high up the snaking structure, the eigenvalues are nearly indistinguishable. As such the snaking branch stability switching is wholly due to the bifurcation of these modes. The even parity eigenvalue crosses zero at the folds on branch of localized states while the odd parity one crosses zero nearby on the unstable parts of the snaking branches at the secondary symmetry breaking bifurcations generating the unstable asymmetric rung states.

When the parameter r is moved outside of the pinning region the time evolution of snaking states can be understood through the gradient structure of the system. Outside of the pinning region the free energies of the states $u = P$ and $u = 0$ differ to a sufficient degree that the fronts between them, in particular those bounding localized states, begin to propagate. This phenomenon is known as *depinning*. The fronts propagation occurs so as to enlarge the state with lower free energy and reduce the other. In each of the following cases we consider an initial condition consisting of a snaking solution that was computed inside the pinning region but time evolved in the SHE with the parameter r changed to a value outside the pinning region. Such dynamics are illustrated in Fig. 2.12. When r is set beyond the right boundary of the pinning region the lower energy state is P and the initial state begins to grow in extent as both bounding fronts advance outward. To the left of the snaking region $u \equiv 0$ is the lower energy state causing the fronts to instead propagate inward. This behavior persists at finite distance from the boundaries of the pinning region though when r is reduced past the fold on the branch of periodic states P the solution collapses to $u = 0$ through amplitude decay instead of front propagation since at this r-value the only solution is the trivial one. The projections on the bifurcation diagram of the depinning dynamics from both sides of the pinning region are shown schematically in Fig. 2.12(b). Part (a) of the figure shows the time evolution plot of the front behavior to the left of the pinning region.

As the parameter r is changed from the interior of the pinning region past a saddle node on the snaking branch, causing a snaking state to depin, a qualitative change in the dynamics of the SHE occurs. This bifurcation can be described by the SNIPER bifurcation normal form Eq. (2.8), where we think of the radial component as being fixed on the unit circle. In this formulation the variable θ in the normal form represents the position of one of the fronts bounding the snaking state. When r is inside the pinning region the front pins at a particular position corresponding to the case $|\mu| < 1$ when there is only a single stable fixed point. When r is outside of the pinning region the front advances and its motion is periodic in the frame moving with the front. This corresponds to the case when $|\mu| > 1$ so that θ executes a periodic orbit, i.e. the front advances by one half wave length and the state advances from one saddle-node to the next.

Nearby the depinning bifurcation when r is outside but close to the pinning region the dynamics can be described within a semi-analytical framework [30]. This analysis is formally carried out near one of the snaking folds where the dynamics of the system are governed by the null eigenmodes of the base state as shown in the calculation that follows. To be specific we focus on the right side of the pinning region and let $r = r_0 + \epsilon\rho$, where r_0 is the parameter value corresponding the right snaking folds high up the snaking structure, and assume that $u(x, T) = u_0(x) + \sqrt{\epsilon}u_1(x, T) + \epsilon u_2(x, T) + \mathcal{O}\left(\epsilon^{\frac{3}{2}}\right)$ where u_0 is the snaking solution at a right fold on a snaking branch. Because the dynamics occur nearby a stationary solution they occur on a slow time scale $T = \sqrt{\epsilon}\, t$. At lowest order one obtains the stationary SHE which u_0 solves and at order $\sqrt{\epsilon}$ one obtains the linear problem $\mathcal{L}(u_0)u_1 = 0$ where $\mathcal{L}(u_0)$ is the linear operator formed by the linearization of SHE around the base state u_0. This linear equation has a solution of the form $\sum_i \alpha_i(T)n_i(x)$ where n_i are functions that solve $\mathcal{L}(u_0)n_i = 0$ i.e. they are the null eigenfunctions at the saddle node on the snaking branch. As discussed there are three such modes, although in the space of reflection symmetric perturbations associated with the depinning dynamics only the even mode, n_e, has nonzero amplitude. From a physical point of view there is no symmetry breaking that allows the dynamics to have a nonzero projection onto modes that are antisymmetric in space. Proceeding to order ϵ one obtains the following linear problem

$$\mathcal{L}(u_0)u_2 = \partial_T u_1 - \rho u_0 - 3bu_1^2u_0 + 10u_1^2u_0^3,$$

which has a solution provided that the RHS is orthogonal to the nullspace of the adjoint linear operator $\mathcal{L}^\dagger(u_0)$. Since the linear operator is self-adjoint the null eigenfunctions n_i span the nullspace of $\mathcal{L}^\dagger(u_0)$. Both u_0 and u_1 are reflection symmetric in space therefore the RHS is symmetric overall and is automatically orthogonal to the the odd eigenfunctions. The only remaining overlap with the even eigenfunction produces the condition,

$$\frac{d\alpha_e}{dT} = I_1\rho + I_2\alpha_e^2, \tag{2.19}$$

where $I_1 = \int_{\mathbb{R}} u_0 n_e \, dx$, $I_2 = \int_{\mathbb{R}}(3b - 10u_0^2)u_0 n_e^3 \, dx$ and n_e is assumed to be normalized to unity under the inner product. The base state, eigenfunctions and inner products are computed numerically. Using Eq. (2.19) the time required in order for the solution to pass between successive saddle nodes on the snaking branch can be estimated as the time required for $\alpha_e(T)$ to pass from $-\infty$ to ∞. Although the equation was derived in the vicinity of the saddle node this estimate turns out to be a very accurate estimate of this depinning time. This time is $\frac{\pi}{\sqrt{I_1 I_2 \rho}}$ matching the scaling of the period of the periodic orbit in the SNIPER bifurcation. When compared with time evolution simulations this theory shows excellent agreement [30].

2.5 Periodically forced systems

As explained in chapter 1 this thesis is concerned with systems that are periodically forced in space, see in particular Eq. (1.1) with a coefficient that is periodic in x. Stationary solutions of Eq. (1.1) in this case satisfy a spatial dynamical system that is nonautonomous and periodic in x. The periodicity present in these problems alters the theory presented in section 2.1. Solutions to periodically forced linear problems are instead described by Floquet theory. In this section we first present Floquet theory for periodic linear ODEs and then briefly discuss some of the ramifications of spatial periodicity for nonlinear ODEs and PDEs.

Periodically forced linear ODEs

Mirroring section 2.1 we introduce Floquet theory in the time domain but it can be equivalently interpreted in the spatial dynamics picture. The general form for a linear system of periodically forced ODEs is

$$\dot{\boldsymbol{u}} = A(t)\boldsymbol{u}, \tag{2.20}$$

where $A \in \mathbb{R}^{n\times n}$ is a matrix with entries that are periodic in time with period T, $A(t+T) = A(t)$. Problems of this type arise not only in forced systems but also more generally as linearizations about periodic orbits. In direct analogy to the analysis carried out for constant coefficient linear systems the solutions to Eq. (2.20) take the form

$$\boldsymbol{u} = \sum_{i=1}^{n} a_i \boldsymbol{\eta}_i(t) e^{\lambda_i t} \tag{2.21}$$

where the functions $\boldsymbol{\eta}_i(t)$ are periodic with period T and the constants $\lambda_i \in \mathbb{C}$ are referred to as *characteristic exponents*. These exponents can be determined by Floquet's Theorem which guarantees that any fundamental matrix solution $U(t)$ to Eq. (2.20) can be written $U(t) = Z(t)e^{Rt}$ for matrices Z and R where $Z(t+T) = Z(t)$ and R is a constant matrix [74]. The eigenvalues of R are the $\{\lambda_i\}$ and are termed characteristic exponents. The characteristic exponents play a similar role as eigenvalues in the autonomous problem and the vector functions $\boldsymbol{\eta}_i$ are the analog of eigenvectors. When $\Re[\lambda_i] \neq 0$ the dynamics of the associated mode in Eq. (2.21) are either exponentially growing or decaying. If Eq. (2.20) arises from a linearization about a periodic orbit the orbit is said to be hyperbolic if this is true for all modes i. On the other hand when $\Re[\lambda_i] = 0$ the dynamics of the associated i^{th} mode are either periodic or quasiperiodic.

The prototypical Floquet system and also one of the simplest cases of periodically forced ODEs is the Mathieu equation,

$$0 = u_{tt} + \left[m_0 + m_1 \cos\left(2\pi t\right)\right] u. \tag{2.22}$$

Here m_0 and m_1 are parameters and we seek a solution for $u : \mathbb{R} \to \mathbb{R}$. The Mathieu equation can be formulated as a dynamical system as in Eq. (2.20) of dimension two and therefore has a pair of distinct characteristic exponents. Neither the exponents nor the modes $\eta_i(t)$ can be written in terms of elementary functions; however, given the ubiquity of the Mathieu equation its fundamental solutions are named special functions. Rather than provide any expressions for these here we instead discuss the structure of the solution space in terms of the parameters (m_0, m_1) as shown in Fig. 2.13. As mentioned previously the dynamics of a fundamental mode vary greatly depending on the real part of the characteristic exponent. It is possible to show as a consequence of reversibility that for the Mathieu equation either the two characteristic exponents have zero real part (grey region in Fig. 2.13) or equal magnitude nonzero real parts with opposite signs (white region in Fig. 2.13). In the language of physics such a structure is frequently referred to as band structure where the white regions are *band gaps*. The solutions inside each of these wedges represent solutions whose period is commensurate with the period of the forcing. The first gap represents the 1:1 resonance, the second the 2:1 resonance...ad infinitum. Therefore outside of the band gaps solutions oscillate and inside they either decay or grow depending on initial conditions. As m_1 shrinks to zero the band gaps become thinner forming wedges. An asymptotic analysis reveals that only the first gap has a finite opening angle and that all higher gaps close in a cusp [12, 83].

Periodically forced nonlinear ODEs

Naturally periodic forcing can appear in nonlinear ODEs as well as linear ones. In this setting fixed points no longer exist and are replaced instead by periodic orbits. In general the computation of such solutions must be carried out numerically and once one is obtained its stability is evaluated by its linearization which is a Floquet problem.

One important mechanism by which an ODE can be periodically forced is through one-way coupling to an external oscillating field. For concreteness consider the following dynam-

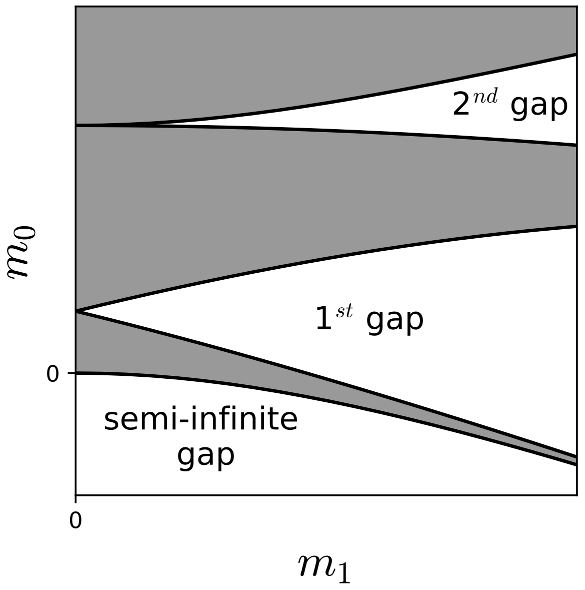

Figure 2.13: Band-gap structure in the (m_0, m_1) plane for the lowest three gaps of the linearization of Eq. (2.22). Outside of the bandgaps (grey regions) solutions oscillate and inside (white regions) they are either damped or divergent depending on initial conditions.

ical system

$$\begin{aligned} \frac{du}{dx} &= f(u) + v\,g(u) \\ \frac{dv}{dx} &= w \\ \frac{dw}{dx} &= -v. \end{aligned}$$

Here the field u represents the physical quantity of interest and the field v is an external oscillator to which it is coupled. It is critical here that the coupling is only in one direction: the evolution of the field v does not depend on u. In the present case the second two equations can be trivially integrated yielding $v(t) = a\cos(x+b)$ for $a, b \in \mathbb{R}$ but the system is illustrative of a more general concept. In general *any* periodic forcing v is the solution to *some* dynamical system which can be coupled to u. In particular one may view the nonautonomous problem for u as a higher-dimensional autonomous one where the forcing is represented by its governing equations. In fact, even in systems where the coupling is bidirectional, i.e. u appears in the equations for v and w, this coupling can be weak for certain solutions and be effectively unidirectional.

Although the external forcing may result from an arbitrary number of external fields in general, periodic forcing generically only requires a two-dimensional external system. Thus the dimension of the unforced problem $\dot{u} = f(u)$ is effectively raised by two when the periodic forcing term is added. In this thesis stationary solutions to Eq. (1.1) effectively solve a four-dimensional dynamical system when the μ is periodic rather than a two-dimensional one. This added dimensionality allows us to observe phenomena similar to the SHE that we would not expect in second order systems.

Spatially periodically forced PDEs

In a PDE spatial forcing is analogous to a potential. Periodic spatial forcing arises frequently in this context, for example, the Schrödinger equation describing electrons in a semiconductor. Here the periodicity of the atomic structure imposes a periodic potential on the electron wavefunction. The spatially extended eigenmodes of such a system solve a periodically forced ODE and are typically described in terms of Bloch theory, a particular case of the Floquet theory described previously. When the systems are nonlinear localized solutions may also be found. As these solutions require hyperbolicity of the background state they are typically found within band gaps where the characteristic exponents of the linear problem have nonzero real parts. This is the genesis of the name "gap soliton" to describe solitary waves found in nonlinear optical systems.

A related type of localized solution that can exist in spatially forced PDEs is a front between two periodic states. Such fronts, sometimes known as Pomeau fronts, can be understood as being locked to the underlying potential [125]. In systems where the amplitude of the potential can be continuously increased from zero this locking is best viewed in terms of an energy balance. In the absence of the potential front solutions propagate but as the potential is added the fronts require more energy in order to pass the potential maxima. At some point the energy balance changes so that the fronts become pinned and cease to propagate. This phenomenon is the central idea explored in this thesis in which we show that the addition of a periodic potential to Eq. (1.1) causes fronts to pin paving the way for the existence of localized snaking states. Snaking does not occur in two-dimensional systems in the absence of spatial forcing to increase the system dimension. The remainder of this thesis is devoted to an understanding of the front solutions to Eq. (1.1) in the absence of periodic forcing and the snaking solutions of the equation when periodic forcing is present.

Chapter 3

Numerical Methods

The bulk of the results in this thesis take the form of numerical solutions to differential equations. The two techniques central to this work are numerical continuation of solutions to ODEs and time integration of PDEs. The former is performed using the publicly available software AUTO [55, 56, 57, 58] which is both accessible and standard in this field of research. Time integration methods for PDEs are more sensitive to the details of each specific problem but for the most part standard techniques were sufficient for the work here. This chapter is devoted to an overview of both continuation and time integration techniques.

3.1 Numerical continuation of solutions to ODEs

In this section we outline the mathematical basis for numerical continuation of solutions to ODEs and explain some details associated with their implementation. We focus here on the methods that are used in AUTO. The central problem is twofold: first to compute a solution $\boldsymbol{u}(x,\mu_0)$ to the equation

$$\frac{d\boldsymbol{u}}{dx} = \boldsymbol{f}(\boldsymbol{u},\mu) \tag{3.1}$$

along with appropriate boundary conditions at a fixed parameter value μ_0 and second to "continue" the solution as a function of μ as the parameter is smoothly changed. This produces a curve of solutions. By uniqueness of solutions to ODEs such a solution curve is well defined and in the space of solutions, $\mathbb{R}^n$, it is convenient to parametrize the curve by its arc-length, s. As a result the family of solutions takes the form $(\boldsymbol{u}(x;\mu(s)),\mu(s)) \in \mathbb{R}^{n+m}$ and in this space the curve is a single valued function of the argument s.

The basic foundation for numerical continuation is guaranteed by the implicit function theorem [74]. Consider a function $F:\mathbb{R}^{n+m}\to\mathbb{R}^n$ that is continuously differentiable and has a root $F(\boldsymbol{x}_0,\boldsymbol{a}_0)=0$ for $\boldsymbol{x}_0\in\mathbb{R}^n$ and $\boldsymbol{a}_0\in\mathbb{R}^m$. If the Jacobian $\left.\frac{\partial F_i}{\partial a_j}\right|_{\boldsymbol{x}=\boldsymbol{x}_0,\boldsymbol{a}=\boldsymbol{a}_0}$ is invertible then there exists an invertible function $h:\mathbb{R}^m\to\mathbb{R}^n$ in an open neighborhood of $(\boldsymbol{x}_0,\boldsymbol{a}_0)$ such that $F(h(\boldsymbol{a}),\boldsymbol{a})=0$. The theorem can be applied directly in the case of a fixed point of Eq. (3.1). In this case when the Jacobian is invertible a fixed point $\boldsymbol{u}_0$ persists in some neighborhood of the parameter value at which it was computed and the curve $(\boldsymbol{u}(\mu), \mu)$ is unique. More generally, when we seek to continue solutions that are not fixed points the spatial derivatives must be taken into account. This is done by laying down a mesh and evaluating the derivatives on the mesh points effectively turning the ODE into a high dimensional algebraic system.

Collocation

In order to approximate Eq. (3.1) as an algebraic system AUTO uses the method of orthogonal collocation [24]. This method lays down a mesh on the domain and represents the solution as a sum of polynomials. Then the derivatives of the solution are evaluated by differentiating the approximating polynomials at collocation points.

The collocation method is implemented via multiple meshes. These include a mesh representing a basic division of the domain and a second that is a refinement designed to improve the convergence of the approximation. The construction of these proceeds as follows. The spatial domain is scaled to the unit interval $[0, 1]$ and a set of N meshpoints $\{x_i\}_{i=0}^{N}$ is constructed where $x_0 = 0$ and $x_N = 1$. In what follows the subscript i will always be an integer. The positions of the points are not necessarily equispaced and the code adapts the mesh in order to equally distribute the discretization error during continuation [55, 131]. Next, every interval $[x_i, x_{i+1}]$ is further sub-divided with $m \leq 7$ equispaced points $x_{i+1-\frac{k}{m}} \equiv x_{i+1} - \frac{k}{m}(x_{i+1} - x_i)$ for $k = 0, 1, \ldots, m-1$. We call the full set of meshpoints $\left\{ x_{i+1-\frac{k}{m}} \middle| i = 0, \ldots, N-1 \text{ and } k = 0, \ldots, m-1 \right\} \cup \{x_N\}$ the *extended mesh.* The true calculations proceed not on this mesh but on a set of *collocation* points $z_{i,k}$ that are positioned at the zeros of the m^{th} order Legendre polynomial P_m relative to the i^{th} component of the mesh x_i. Specifically, the collocation points satisfy $P_m\left(2\frac{z_{i,k}-x_i}{x_i-x_{i-1}} - 1\right) = 0$. These points are chosen to improve the accuracy of the approximation and can be viewed as adjustments of the extended meshpoints.

In order to transfer the solution from the collocation points to the mesh and vice versa Lagrange interpolating polynomials are constructed

$$l_{i,k}(x) = \prod_{\substack{j=0 \\ j\neq k}}^{m} \frac{x - x_{i-\frac{j}{m}}}{x_{i-\frac{j}{m}} - x_{i-\frac{k}{m}}}.$$

These polynomials have the property $l_{i,k}\left(x_{i-\frac{k}{m}}\right) = 1$ and $l_{i,k}\left(x_{i-\frac{j}{m}}\right) = 0$ for $j \neq k$. That is, for a given k and interval $[x_i, x_{i+1}]$ the Lagrange polynomial takes the value 1 on the meshpoint $x_{i-\frac{k}{m}}$ and zero on the others in the interval. Thus the solution is represented on $[x_i, x_{i+1}]$ by

$$\boldsymbol{p}_i(x) = \sum_{k=0}^{m} \tilde{\boldsymbol{u}}_{i-\frac{k}{m}} l_{i,k}(x) \tag{3.2}$$

where the coefficients $\tilde{\boldsymbol{u}}_\alpha$ approximate the solution amplitude at each meshpoint. The coefficients are unknown a priori and are determined in solving Eq. (3.1). The total number of undetermined coefficients is $mN + 1$.

Using the solution representation (3.2) Eq. (3.1) can be evaluated at the collocation points in each interval $[x_i, x_{i+1}]$ as follows

$$\boldsymbol{p}_i'(z_{i,k}) = \boldsymbol{f}(\boldsymbol{p}_i(z_{i,k}), \mu).$$

Here the derivative can be computed easily and analytically since $\boldsymbol{p}_i$ is a polynomial. Because $\tilde{\boldsymbol{u}}_\alpha$ is an n component vector the system has nmN algebraic equations for $n(mN+1)+1$ scalar coefficients plus the parameter μ. Typically the extra equations needed to determine the coefficients are provided by boundary conditions imposed on the solution. When continuing a branch of solutions, rather than solving for them for fixed μ, an additional equation is inherited from the continuation procedure thus determining μ at the next step as well.

Newton's method

Once a system of algebraic equations is obtained the solution is found by Newton's method. The method is designed to find roots of equations of the form $\boldsymbol{F}(\boldsymbol{x}) = 0$ where $\boldsymbol{F}$ has continuous first derivatives. Beginning with an initial guess of the root, $\boldsymbol{x}_0$, we may expand $\boldsymbol{F}$ in a Taylor series

$$\boldsymbol{F}(\boldsymbol{x}) = \boldsymbol{F}(\boldsymbol{x}_0) + \nabla \boldsymbol{F}|_{\boldsymbol{x}=\boldsymbol{x}_0} \cdot (\boldsymbol{x} - \boldsymbol{x}_0) + \mathcal{O}\left[(\boldsymbol{x} - \boldsymbol{x}_0)^2\right].$$

Then in order to determine the next guess for the root, $\boldsymbol{x}_1$, we assume that $-\boldsymbol{F}(\boldsymbol{x}_0) = \nabla \boldsymbol{F}|_{\boldsymbol{x}=\boldsymbol{x}_0} \cdot (\boldsymbol{x}_1 - \boldsymbol{x}_0)$ so that $\boldsymbol{F}(\boldsymbol{x}_1) = \mathcal{O}\left(\|\boldsymbol{x}_1 - \boldsymbol{x}_0\|^2\right)$, i.e. that $\boldsymbol{x}_1$ is the root up to quadratic corrections. This procedure is then iterated in order to generate a sequence $\boldsymbol{x}_i$ that converges to the true root. The geometric interpretation of this is that $\boldsymbol{x}_1$ represents a step from $\boldsymbol{x}_0$ in the tangent hyperplane to $\boldsymbol{F}$ at $\boldsymbol{x}_0$ in the direction of steepest descent. If $\nabla \boldsymbol{F}$ is not invertible then the update equation can be solved with the added constraint that $\boldsymbol{x}_1$ have minimal norm which produces a unique solution. Generically $\nabla \boldsymbol{F}$ is full rank near simple roots though roots of higher degeneracy may require more care. In practice if the initial guess is close enough to the root that the linear approximation of the Taylor series expansion is valid at the root then the method converges, although precise mathematical conditions for convergence are well established. If the function is continuously differentiable then the iterates satisfy $\boldsymbol{x}_{i+1} - \boldsymbol{x}_{root} = o\left(\|\boldsymbol{x}_i - \boldsymbol{x}_{root}\|\right)$ and if $\boldsymbol{F}$ is Lipschitz this bound is quadratic $\mathcal{O}\left(\|\boldsymbol{x}_i - \boldsymbol{x}_{root}\|^2\right)$ [53, 115]. Convergence is typically checked by evaluating $\|\boldsymbol{F}(\boldsymbol{x}_i)\|$ as i increases and the method is terminated when either the norm is sufficiently small, the relative change in norm $\frac{\|\boldsymbol{F}(\boldsymbol{x}_{i+1})\|}{\|\boldsymbol{F}(\boldsymbol{x}_i)\|}$ is small or after finite number of iterations.

For the continuation problem the Jacobian of the algebraic equations can be evaluated analytically. By the chain rule the derivative of the equations with respect to a particular $\tilde{\boldsymbol{u}}_\alpha$ is

$$\nabla_{\tilde{\boldsymbol{u}}_\alpha}\left(\boldsymbol{p}_i'(z_{i,k}) - \boldsymbol{f}(\boldsymbol{p}_i(z_{i,k}), \mu)\right) = \partial_{\tilde{\boldsymbol{u}}_\alpha}\boldsymbol{p}_i'(z_{i,k}) - \nabla_{\boldsymbol{u}}\boldsymbol{f} \cdot \partial_{\tilde{\boldsymbol{u}}_\alpha}\boldsymbol{p}_i(z_{i,k})$$

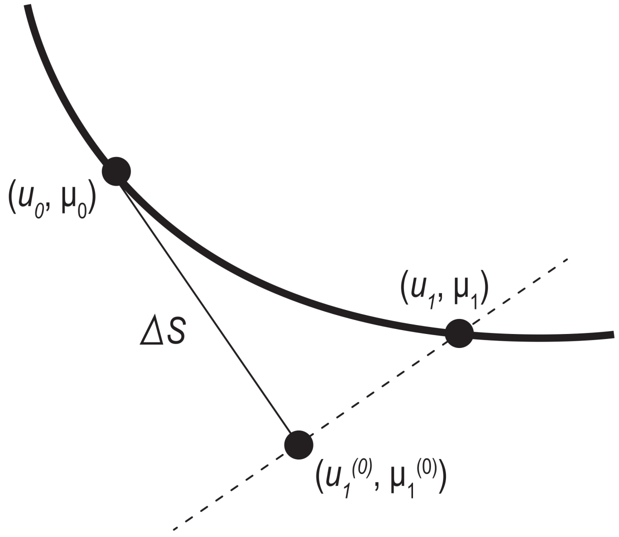

Figure 3.1: Schematic drawing of pseudo-arclength continuation. The solution branch is depicted with a thick line and the starting point is (u_0, μ_0). A step of size Δs is taken along the tangent direction to a point $\left(u_1^{(0)}, \mu_1^{(0)}\right)$ and then Newton iterations are conducted along the hyperplane normal to the tangent vector. These iterations finally terminate on the next solution branch point (u_1, μ_1). This figure was created by Sara Tepfer.

where the derivatives of the polynomials can be evaluated analytically and so can $\nabla_{\boldsymbol{u}} \boldsymbol{f}$ since the functional form of $\boldsymbol{f}$ is known. A similar derivative by the parameter μ can also be computed analytically. This allows us to avoid numerical approximations of the Jacobian and greatly improves the performance of the Newton updates.

Pseudo-arclength continuation

Once an algebraic system has been obtained and a solution computed then continuation of the solution involves changing the parameter μ and tracking the changes in the solution branch. For concreteness consider the problem $\boldsymbol{F}(\boldsymbol{u}, \mu) = 0$ where we know a particular solution $(\boldsymbol{u}_0, \mu_0)$. AUTO uses a method known as pseudo-arclength continuation to step along the solution branch. While multiple methods for continuation exist pseudo-arclength avoids issues at folds in the solution branch where naive methods typically fail. The geometric picture of the continuation process is shown in Fig. 3.1. Here the step is taken first by moving along the tangent vector to the solution curve and then correcting the step in an orthogonal direction by a series of Newton iterations.

The basic concepts behind continuation are well represented by standard arclength continuation in which a step of fixed distance is taken in $(\boldsymbol{u}, \mu)$ space. Concretely this means that the update step must satisfy

$$\boldsymbol{F}(\boldsymbol{u}(x;s),\mu(s)) = 0, \qquad \left\|\frac{d\boldsymbol{u}}{ds}\right\|^2 + \left(\frac{d\mu}{ds}\right)^2 = \Delta s^2,$$

where Δs is the length of the step. The Newton iterations use an initial guess along the tangent direction and then refine the solution by varying the step direction for fixed Δs. Although promising in theory the imposition of the fixed Δs constraint is nontrivial.

Pseudo-arclength continuation represents a slight modification of standard arclength continuation that employs a more numerically tractable constraint for the continuation step size. In this method rather than fixing the Newton iterations to lie on a hypersphere they are constrained to be in a hyperplane orthogonal to the tangent vector, see Fig. 3.1. In this way the iterations are still able to correct the initial step and the constraint can be implemented as an inner product. Mathematically this is formulated by the conditions

$$\boldsymbol{F}(\boldsymbol{u}_1,\mu_1) = 0, \qquad \left\langle \boldsymbol{u}_1 - \boldsymbol{u}_0, \frac{d\boldsymbol{u}_0}{ds} \right\rangle + (\mu_1 - \mu_0)\frac{d\mu_0}{ds} = \Delta s, \tag{3.3}$$

where $(\boldsymbol{u}_1,\mu_1)$ is the new guess after the step. Here since $\boldsymbol{u}$ is intended to approximate a continuous function the inner product is taken to be $\langle u, v\rangle = \int u\,v\,dx$ which AUTO computes by quadrature,

$$\langle \boldsymbol{u}, \boldsymbol{v}\rangle = \sum_{j,k}\left(\int_{x_j}^{x_{j+1}} l_{j,k}(x)\,dx\right)\tilde{\boldsymbol{u}}_{j-\frac{k}{m}}\cdot\tilde{\boldsymbol{v}}_{j-\frac{k}{m}}.$$

Here the integrals over $l_{j,k}$ are independent of j up to a scaling and $\tilde{\boldsymbol{u}}_\alpha, \tilde{\boldsymbol{v}}_\alpha$ represent the function values at the meshpoints. The initial guess along the tangent vector takes the form

$$\boldsymbol{u}_1^{(0)} = \boldsymbol{u}_0 + \Delta s\frac{d\boldsymbol{u}_0}{ds}, \qquad \mu_1^{(0)} = \mu_0 + \Delta s\frac{d\mu_0}{ds},$$

where the superscript (0) refers to the number of Newton iterations and the subscript to the step number along the solution branch. The tangent vector is initially computed using the known Jacobian but subsequently carried over from the previous step.

After the initial step along the tangent vector Newton iterations are used to refine the guess. The Newton method involves the following update equation

$$\begin{pmatrix} \partial_{\boldsymbol{u}}\boldsymbol{F}\left(\boldsymbol{u}_1^{(\nu)},\mu_1^{(\nu)}\right) & \partial_\mu\boldsymbol{F}\left(\boldsymbol{u}_1^{(\nu)},\mu_1^{(\nu)}\right) \\ \frac{d\boldsymbol{u}_0}{ds} & \frac{d\mu_0}{ds} \end{pmatrix}\begin{pmatrix} \Delta\boldsymbol{u}_1^{(\nu)} \\ \Delta\mu_1^{(\nu)} \end{pmatrix} = -\begin{pmatrix} \boldsymbol{F}\left(\boldsymbol{u}_1^{(\nu)},\mu_1^{(\nu)}\right) \\ \left\langle \boldsymbol{u}_1^{(\nu)} - \boldsymbol{u}_0, \frac{d\boldsymbol{u}_0}{ds}\right\rangle + \left(\mu_1^{(\nu)} - \mu_0\right)\frac{d\mu_0}{ds} - \Delta s \end{pmatrix},$$

where each row corresponds to a Taylor expansion of each condition in Eqs. (3.3). Because solving this large linear system is expensive AUTO only updates the matrix on the LHS for a fixed number (user specified) of Newton iterations. After that chord iterations are used instead where the matrix is frozen. The next tangent vector is defined by the conditions

$$\partial_{\boldsymbol{u}}\boldsymbol{F}(\boldsymbol{u}_0,\mu_0)\frac{d\boldsymbol{u}_1}{ds}+\partial_{\mu}\boldsymbol{F}(\boldsymbol{u}_0,\mu_0)\frac{d\mu_1}{ds}=0, \qquad \frac{d\boldsymbol{u}_0}{ds}\frac{d\boldsymbol{u}_1}{ds}+\frac{d\mu_0}{ds}\frac{d\mu_1}{ds}=1,$$

where the second is a normalization condition. These equations may be derived by differentiation of Eq. (3.3). The orientation of the tangent vector is preserved provided that Δs is sufficiently small.

The above procedure is iterated in order to map out the curve of solutions to Eq. (3.1). The step size Δs is automatically adapted depending on how fast the Newton iterations converge to a user specified tolerance. If convergence does not occur within a specified finite number of iterations or the adapted step size falls below a specified minimum the procedure terminates and reports an error.

Bifurcation detection, branch switching and multiple parameters

In addition to following solution curves one of the goals of continuation is to detect bifurcations. Bifurcations occur when the conditions in the inverse function theorem fail, namely the Jacobian is not invertible. Away from bifurcation points the solution is referred to as *regular* and the Jacobian $\partial_{\boldsymbol{u}}\boldsymbol{F}$ is full rank ensuring that a unique solution branch passes through. This also occurs at points where $\partial_{\boldsymbol{u}}\boldsymbol{F}$ is not full rank but the extended system $[\partial_{\boldsymbol{u}}\boldsymbol{F}|\partial_{\mu}\boldsymbol{F}]$ (an extended matrix) is. These points are called *simple folds*.

When the rank of the extended system is not full the point is said to be *singular*. At such points there is not a unique curve of solutions and at least one other branch bifurcates out of the point. Simple singular points are those for which the rank of the extended system is one less than the maximum. Here one additional solution branch emerges. In order to detect these points AUTO monitors the determinant $\det([\partial_{\boldsymbol{u}}\boldsymbol{F}|\partial_{\mu}\boldsymbol{F}])$ as a function of arclength. When the determinant changes sign AUTO looks for the root with secant iteration. Simple folds, where the determinant does not change sign but $\frac{d\mu}{ds}$ does, are detected in a similar manner. Since AUTO tracks the tangent vector anyway the same root finding procedure is applied to locate these fold points. Bifurcations of codimension two and higher cannot be reliably found in this manner since the determinant may pass through zero without changing sign. Bifurcations to other branches may also occur at Hopf points where an eigenvalue of $\partial_{\boldsymbol{u}}\boldsymbol{F}$ has a real part passing through zero but a nonzero imaginary part. In this case $\partial_{\boldsymbol{u}}\boldsymbol{F}$ is still of full rank and more care must be taken in order to detect these points and follow the emergent branches. This will not be discussed here.

At a simple singular point the continuation can proceed along either the current branch or switch to the new one. At such a point the nullspace of $[\partial_{\boldsymbol{u}}\boldsymbol{F}|\partial_{\mu}\boldsymbol{F}]$ is two-dimensional. It contains the tangent vector of the original branch, $\left(\frac{d\boldsymbol{u}}{ds},\frac{d\mu}{ds}\right)$, and also the tangent vector in the direction of the new branch. Though the new branch need not emerge orthogonal to the original one AUTO uses a direction in the nullspace and also orthogonal to the original tangent vector as a guess. This is typically successful in practice when the step size is small enough.

Finally a natural extension of the continuation procedure described above is to perform continuation in multiple parameters. Such a task can easily be implemented in the existing framework because little distinction is made between the solution components and the parameters. All that is required is an additional constraint so that the system has enough equations in order to determine a unique solution. These constraints can take the form of boundary conditions, integral conditions or the requirement to stay at a bifurcation point. For example, AUTO includes a feature to continue fold points in a secondary parameter. This is accomplished by including a constraint that $\partial_{\boldsymbol{u}}\boldsymbol{F}$ have a nullspace that is at least one-dimensional. This is enforced by extending the system to

$$F(\boldsymbol{u},\mu)=0, \qquad [\partial_{\boldsymbol{u}}\boldsymbol{F}]\phi=0, \qquad |\phi|^2=1.$$

Here ϕ is the nullvector of $\partial_{\boldsymbol{u}}\boldsymbol{F}$ that is characteristic of a fold. Continuation is then performed on these equations instead.

Convergence and stability

Rigorous conditions for convergence and stability of the methods used in AUTO are well established [55, 57, 58]. In carrying out this work the validity of solutions obtained from AUTO are checked first by refining the mesh used by AUTO and then by consistency. Specifically we check using an independent implementation of Newton's method that the obtained solutions do solve the governing equations and secondarily that stable solutions are indeed stable when time evolved.

3.2 Solving linear eigenvalue problems

In the study of temporal stability of a stationary PDE solution a differential linear eigenvalue problem is obtained. These take the form of a differential equation $\mathcal{L}u=\sigma u$ plus boundary conditions where $\mathcal{L}$ is a differential operator and (u,σ) is an eigenfunction-eigenvalue pair. These problems typically fail to have analytical solutions and must be treated numerically. This is accomplished by laying down a mesh or choosing a complete set of basis functions with which to approximate $\mathcal{L}$. After this is done the problem becomes a matrix eigenvalue problem that can be solved with standard numerical linear algebra libraries. In this section we discuss two main techniques for the discretization of $\mathcal{L}$.

The first and most obvious method is to lay down an equispaced spatial mesh and write differential operators in terms of finite differences. Suppose that the meshpoints are separated by a distance Δx, then by use of Taylor series at a point x_i the first and second derivatives may be written,

$$\begin{aligned}\partial_x u &= \frac{u(x_i) - u(x_{i-1})}{\Delta x} + \mathcal{O}(\Delta x) \\ \partial_{xx} u &= \frac{u(x_{i+1}) - 2u(x_i) + u(x_{i-1})}{(\Delta x)^2} + \mathcal{O}\left[(\Delta x)^2\right]\end{aligned}$$

where the associated truncation error is included. This error affects the accuracy of both the eigenvectors and eigenvalues. Given the finite accuracy of numerical approximations it is natural to search for higher order methods. Higher order approximations to derivatives can be derived by expanding the function in higher order Taylor series on the meshpoints. As the method becomes higher order the stencil involves function values at an increasing number of meshpoints.

An alternative approach to approximating derivatives is through spectral methods. These methods are characterized by "spectral" accuracy that is far greater than finite differences and are the primary methods used here. The basic idea behind spectral methods is to represent the solution with a Fourier series so that instead of searching for values of the functions at the meshpoints the eigenvalue problem is posed in terms of the amplitudes of the Fourier modes. These methods are supported mathematically by the following theorem [147]

Theorem. *Let $u \in L^2(\mathbb{R})$ and let v be the grid function on $\Delta x\mathbb{Z}$ defined by $v_j = u(x_j)$. If u has $p-1$ continuous derivatives in $L^2(\mathbb{R})$ for some $p \geq 1$ and a p^{th} derivative of bounded variation then*

$$|\hat{v}(k) - \hat{u}(k)| = \mathcal{O}\left[(\Delta x)^{p+1}\right] \ \text{as } \Delta x \to 0$$

which holds uniformly for all $k \in \left[-\frac{\pi}{\Delta x}, \frac{\pi}{\Delta x}\right]$.

Here the accuracy of the discrete Fourier transform improves with the regularity of the function to be approximated! Using Parseval's Theorem it is also possible to show that u and v themselves are spectrally close [147]. In practice this fact results in a very accurate method well beyond the capability of finite differences.

For problems in which the linear operator does not depend explicitly on x the entire linear problem can be Fourier transformed and the eigenvalue calculation can be performed in Fourier space where the discrete approximation to the spatial derivatives are diagonal matrices. This is not the case when $\mathcal{L}$ depends explicitly on x which arises frequently in studying the stability of spatially varying solutions. When such a scenario arises on a periodic domain a finite difference-type differentiation matrix can be derived by re-summing the Fourier basis functions. Specifically, suppose that the number of modes N is even and the corresponding spatial meshpoints have separation Δx. Then the discrete Fourier transform of the delta function $\delta_j = \begin{cases} 1 & j = 0 \mod N \\ 0 & j \neq 0 \mod N \end{cases}$ is $\hat{\delta}_k = \Delta x$ for all Fourier modes k. Using this the band limited interpolant of the delta function is,

$$I(x) = \frac{1}{2\pi}\sum_{k=-\frac{N}{2}}^{\frac{N}{2}} \Delta x\, e^{ikx} = \frac{\Delta x}{2\pi}\frac{\sin\left(\frac{Nx}{2}\right)}{\sin\left(\frac{x}{2}\right)}.$$

Any periodic function u on the grid can then be interpolated by $\sum_{j=1}^{N} u(x_j)I(x-x_j)$. Thus the derivative of the interpolating function on the mesh can be written in terms of the derivatives of $I(x)$. Evaluated on the meshpoints the first derivative becomes [147],

$$I'(x_j) = \begin{cases} 0 & j = 0 \mod N \\ \frac{(-1)^j}{2}\cot\left(\frac{j\Delta x}{2}\right) & j \neq 0 \mod N \end{cases}. \tag{3.4}$$

Since the grid function is interpolated with shifted copies of $I(x)$ this gives rise to a *spectral differentiation matrix* created by stacking N shifted copies of Eq. (3.4) to form a banded matrix. When this matrix acts on the vector $[u(x_j)]$ it produces the derivative vector $[u'(x_j)]$ on the mesh, i.e. it acts like a finite differences scheme but uses values at all N points. In addition, because the interpolation is done by Fourier modes this differentiation inherits all of the spectral accuracy properties of spectral methods. Higher order derivatives can easily be derived by further differentiating $I(x)$. These techniques are in widespread use and many properties of these differentiation matrices have been studied [35, 147].

Finally a key component to any numerical scheme is a method to evaluate its accuracy. In practice this is carried out by refining the mesh and tracking the convergence of the eigenspectra. Enough meshpoints have been used when the eigenvalues stop changing. As a rule of thumb when the spectrum is bounded, as in Sturm-Liouville problems, the error in the eigenvalues and eigenfunctions is smaller near the bounded side of the spectrum and gets worse for larger eigenvalues at the unbounded end [26]. Hence we typically only take at most the lowest half of the modes from a numerical calculation.

3.3 Timestepping methods for PDEs

Solving PDEs numerically involves two distinct discretizations for space and time. If the spatial discretization is performed first then a set of ODEs in time are obtained for the discretized function values at spatial meshpoints. Both the spatial and temporal derivatives may be approximated though basic finite differences but spectral methods improve accuracy significantly and are therefore used whenever possible. In this section we describe the three schemes that are used in this thesis. Although the governing equation changes very little three distinct methods are needed since the physics of the equation changes significantly in the various parameter regimes. The schemes are crafted to maximize accuracy with fidelity to this physical behavior in mind.

Finite difference method

For front propagation into an unstable state studied in chapter 4 a simple finite difference method is used. In such a problem the solution $u = 0$ ahead of the front interface is unstable and the goal of the simulation is to capture the speed with which it destabilizes. This speed drives pulled front motion. The scheme solves Eq. (1.1) with $\mu > 0$ constant and takes the form

$$\frac{u_i^{j+1} - u_i^j}{\Delta t} = \mathcal{L}\left(u_{i-1}^{j+1}, u_i^{j+1}, u_{i+1}^{j+1}\right) + \mathcal{N}\left(u_{i-1}^{j}, u_i^{j}, u_{i+1}^{j}\right), \tag{3.5}$$

where u_i^j is the solution value at spatial point i and time step j and centered differences are used for all of the spatial derivatives. The operators $\mathcal{L}$ and $\mathcal{N}$ indicate the linear and nonlinear terms in the evolution equation, respectively. The linear part of the method is first order accurate in time and second order in space but for the simulations we always choose $\Delta t = (\Delta x)^2$. The method handles the linear terms implicitly and the nonlinear ones explicitly. This is common in problems with nonlinear terms in order to avoid solving a nonlinear equation at each timestep. As such the method need not be unconditionally stable but numerical experiments reveal that the method is stable for even moderate ratios $\frac{\Delta t}{\Delta x}$. All the work here is done at values well below the Courant–Friedrichs–Lewy bound for the linear problem [102].

Finally, we mention that front propagation in Eq. (1.1) is naturally diffusive and does not have a sharp front interface unlike front propagation in a Hamilton-Jacobi equation. This physical difference permits a simple scheme like Eq. (3.5) to reliably capture the correct behavior. In fact significant work has been done to understand the accuracy of schemes like this for front propagation in dissipative diffusive systems [63]. Moreover spectral methods do not work here. Specifically, since each Fourier mode affects every spatial point in the system small errors in a Fourier mode destabilize the state ahead of the front. In chapter 4 we detail some techniques to mitigate this but for simulations where μ is large finite differences perform much better.

Spectral method

For time evolution of Eq. (1.1) when $\mu < 0$ and when $\mu = \mu_0 + \mu_1(x)$ with μ_1 periodic we use a method that is spectral in space. This method is carried out in Fourier space, i.e. the method evolves the Fourier transform of the solution [147]. The scheme takes the form

$$\frac{\hat{u}_i^{j+1} - \hat{u}_i^j}{\Delta t} = \left(\mu_0 - k_i^2\right)\hat{u}_i^{j+1} + \mathcal{F}\left[\mathcal{N}\left(x, \mathcal{F}^{-1}\left[\hat{u}_i^j\right]\right)\right] \tag{3.6}$$

where $\hat{u}$ and $\mathcal{F}[u]$ both denote the Fourier transform of u, k_i is the Fourier wavenumber of the i^{th} mode, $\mu_0 < 0$ is the homogeneous part of the forcing and the periodic part $\mu_1(x)$ is lumped with the nonlinear terms $\mathcal{N}$. At each timestep the solution is inverse Fourier transformed to real space so that the nonlinear terms can be evaluated and then Fourier transformed back. In real space the equation is solved with periodic boundary conditions on a grid of

N equispaced points through a domain $[-L, L]$ while in Fourier space this corresponds to a grid of wavenumbers $k_j = \frac{j\pi}{2L}$ for $-\frac{N}{2} \leq j \leq \frac{N}{2}$.

This method is spectrally accurate in space and first order in time. This was sufficient for all of the applications here. Like the previous method, here the linear terms are treated implicitly and the nonlinear ones explicitly. However, because the spatial resolution is spectral we observed stability even for generous timesteps.

In using Fourier methods with nonlinear equations one issue that may arise is aliasing of modes due to the nonlinear terms. Specifically a term of the form u^p can project a mode e^{ikx} of wavenumber k onto modes with wavenumbers as large as pk. When the spatial resolution does not distinguish these high spatial frequency terms from the low frequency ones aliasing occurs. The high frequency mode is incorrectly attributed to the amplitude of a low frequency one. Another view of this is that Fourier modes are defined modulo $\frac{N\pi}{4L}$ in k-space so modes that are beyond $|k| = \frac{N\pi}{4L}$ are aliased. One can prevent this by proactively zeroing the amplitudes of the highest $\frac{p-1}{p+1}N$ modes at each timestep. This need only be done for the nonlinearity with the largest p in the governing equation [26].

Split step method

In chapter 7 we consider an application to nonlinear optics and consequently solutions to a Gross-Pitaevskii equation that has the same stationary solutions as Eq. (1.1) but different dynamics. This equation takes the form $-iA_t = A_{xx} + \mu(x)A + |A|^2 A - |A|^4 A$ and is not dissipative but rather energy conserving. Although the equation can be solved with a numerical scheme similar to Eq. (3.6) the scheme fails to reliably conserve the physical quantities of interest. This new physics calls for a different scheme.

We employ one of the standard schemes that is in use in nonlinear optics research. The scheme is referred to as a split-step method and is described in [160]. The method involves splitting the differential equation into two:

$$\begin{aligned} U_t &= iU_{xx} \\ V_t &= i\left(\mu(x) + |V|^2 - |V|^4\right) V \end{aligned}$$

and solving each exactly,

$$\begin{aligned} U(x,t) &= \mathcal{F}^{-1}\left[e^{-ik^2 t}\mathcal{F}\left[U(x,0)\right]\right] \\ V(x,t) &= V(x,0)e^{i\left(\mu(x)+|V(x,0)|^2-|V(x,0)|^4\right)t}. \end{aligned} \tag{3.7}$$

The time-stepping proceeds by alternate steps in time using either solution and carefully selected weighting factors. These are chosen so that the resulting method is spectrally accurate in space and fourth order accurate in time. Details can be found in [160]. Because (3.7) corresponds to rotations in either real or Fourier space it preserves the L^2 norm and energy of the solution up to numerical errors. We observe good energy preservation for long simulation times.

Convergence and accuracy

We validate the numerical methods used here through a number of techniques. In every case we verify that the qualitative and quantitative dynamics are invariant upon refinement of the spatial mesh and timestep once they are sufficiently small. Another step that we have taken is to compare the methods detailed here to methods with higher order time integration. If the methods agree then the lower order method is sufficiently accurate to capture the dynamics. In the case of conservative schemes like (3.7) we monitor the conservation of energy during the time evolution and its improvement as the spatial and dynamical meshes are refined. Finally, in certain specific cases (see chapter 4) we are able to compare the numerical methods to an exact PDE solution. This is rarely possible in the study of nonlinear PDEs but provides a good validation of the numerical scheme when available.

Chapter 4

Fronts in Subcritical Systems

4.1 Introduction

In this chapter we are interested in the speed with which a nontrivial pattern invades either a stable homogeneous state or an unstable one. These types of problems arise frequently in applications [3, 50, 72, 133, 146] but the speed selection process remains imperfectly understood despite much effort. This is because in the former case the speed is inevitably selected by nonlinear processes (the pushed front case) while in the latter case selection may be via linear processes (the pulled front case) although nonlinear selection may survive well into the supercritical regime. Moreover, the selected speed depends in general on the initial condition, and in particular on the steepness of the front connecting the pattern to the homogeneous state at the initial instant.

In order to present a unified discussion of both processes we focus here on the bistable Ginzburg-Landau equation Eq. (1.1) [59, 61, 64, 84, 86, 87, 88, 139]. Equation (1.1) has the symmetries

$$A(x,t) \to \bar{A}(-x,t), \quad A(x,t) \to A(x,t)\, e^{i\phi},$$

inherited from the assumed invariance of the original system for $u(x,t)$ under spatial reflections and translations with respect to the fast spatial scale. In the absence of spatial forcing on scales of order $O(\epsilon^{-2})$ the equation is also invariant under spatial translations with respect to the slow spatial scale x. Furthermore, the equation possesses a Maxwell-like point $\mu = \mu_M$ at which a multitude of stationary spatially localized structures of varying widths is present [86]. This point exists even when $a_2 \neq 0$, i.e., when the equation lacks gradient structure. In the latter case μ_M corresponds to the presence of a heteroclinic cycle connecting the trivial state $A = 0$ to a stationary nontrivial state $R_M e^{iq_M x}$ given by

$$R_M = \frac{12}{16 - (3a_1 - 5a_2)(a_1 + a_2)},$$

$$q_M = \frac{3(a_1 + a_2)}{(3a_1 - 5a_2)(a_1 + a_2) - 16}$$

and back again.

In the present work we are interested in the properties of traveling fronts that are present when $\mu \neq \mu_M$. Since the system is bistable two types of fronts are possible: pushed fronts describing the elimination of the nontrivial state by an invading trivial state ($\mu < \mu_M$) or vice versa ($\mu_M < \mu < 0$), and pulled fronts describing the invasion of a linearly unstable trivial state by a stable nontrivial state ($\mu > 0$). In fact, as first pointed out by van Saarloos [134] the transition between these two types of fronts does not take place exactly at $\mu = 0$, even when $a_1 = a_2 = 0$, and this transition is of particular interest in the present work as well.

The chapter is organized as follows. In Sec. 4.2 we obtain a three-parameter family of exact traveling front solutions of Eq. (1.1) and study the stability of these solutions in the relevant parameter region. This solution set is a special case of that derived in [145]. The dynamic nature of these fronts is closely related to the stability of the asymptotic states at either end. In Sec. 4.3 we briefly review our methodology for carrying out an analysis of front propagation from localized initial conditions. Sections 4.4 and 4.5 describe case studies of these two front propagation regimes, focusing in Sec. 4.4 on the case in which $A = 0$ is stable and in Sec. 4.5 on the case in which it is unstable. In the latter case the "marginal stability criterion" of Dee and Langer [52] can be applied to characterize the motion of the front, subject to certain restrictions on the initial conditions [135]. Section 4.5 also investigates the stability of the state deposited by the moving front with respect to spatial modulation. Brief conclusions follow in Sec. 4.6 and numerical methods are described in section 4.7.

4.2 Nonlinear Front

A procedure for finding exact coherent traveling structures of the Ginzburg-Landau equation has been outlined by van Saarloos and Hohenberg [132, 136]. Such traveling solutions inform bifurcation structure as well as dynamics and are thus of significant value. One of the most famous such examples is the one-parameter family of Nozaki-Bekki hole solutions for the complex Ginzburg-Landau equation which have been shown to play an important role in its dynamics [116]. In this section we derive an exact traveling front solution to Eq. (1.1) with fully general parameter dependence and study the region of existence and stability of the solution. These put restrictions on the parameter values for which the exact front is valid and dynamically relevant.

Spatial dynamics

If we restrict attention to traveling solutions, Eq. (1.1) can be rewritten in the form of three real first order ODEs [132] in a traveling frame with coordinate $\xi \equiv x - vt$. To do this we write

$$A(x,t) = W(\xi)e^{-i\omega t},$$

where ω is a constant, and $W(\xi) \equiv a(\xi)e^{i\phi(\xi)}$. In addition, we introduce the quantities $q \equiv \phi'$ and $\kappa \equiv \frac{a'}{a}$, where the prime denotes differentiation with respect to ξ. This procedure yields the real-valued equations

$$a' = a\kappa, \tag{4.1}$$

$$q' = -\left(a_1 + a_2\right) a^2\kappa - q(v + 2\kappa) - \omega, \tag{4.2}$$

$$\kappa' = a^2\left[\left(a_1 - a_2\right) q - 1\right] + a^4 - \mu + q^2 - v\kappa - \kappa^2. \tag{4.3}$$

The traveling front solutions that we seek correspond to heteroclinic orbits between fixed points $(a, q, \kappa) = (a_N, q_N, 0)$ (the nontrivial state) and $(0, q_L, \kappa_L)$ (the trivial state). Given arbitrary values of the parameters μ, a_1, a_2, these heteroclinics may exist only for certain values of v, ω. If a heteroclinic orbit exists only for discrete values of v and ω (for each set of μ, a_1, a_2) it will be known as a "discrete front;" otherwise it is a "k-parameter front" where k indicates the number of free parameters.

We suppose, without loss of generality, that the front solution approaches $(a_N, q_N, 0)$ as $\xi \to -\infty$ (the source or upstream state) and $(0, q_L, \kappa_L)$ as $\xi \to \infty$ (the sink or downstream state). It follows that the former must be unstable in the space variable ξ while the latter must have at least one stable eigendirection. An upper bound on the number of free parameters within a family of such heteroclinic solutions is therefore determined by the dimensions of the unstable manifold of the source fixed point and the stable manifold of the sink [136]. If the source has n unstable eigendirections then the solution curve must lie in the corresponding n-dimensional unstable manifold. This condition restricts the number of degrees of freedom of the solution curve by 1 leaving $n-1$ degrees of freedom. Adding the two free parameters v, ω the total number of degrees of freedom becomes $n+1$. A necessary condition for the existence of a heteroclinic between the source and sink is that the solution curve also lies in the stable manifold of the sink. If the sink has l unstable eigendirections this requirement generically requires that l variables are fixed thereby leaving $k \equiv n - l + 1$ variables free. If $k > 0$ the solution curve corresponds to a k-parameter front, if $k = 0$ it is a discrete front, and if $k < 0$ no heteroclinic orbit exists between the two fixed points. A complete analysis of the fixed points of Eqs. (4.1)–(4.3) and the dimensions of the associated stable and unstable manifolds is carried out in [61].

We follow [132] in using the Ansatz

$$q = q_N + e_0\left(a^2 - a_N^2\right), \quad \kappa = e_1\left(a^2 - a_N^2\right), \tag{4.4}$$

and suppose that the resulting front travels with speed $v = v_N$. This front is a discrete front, i.e., $k = 0$, and both ω and v are determined by the system parameters. Differentiating the Ansatz and using Eq. (4.1) we find that $q' = 2e_0a^2\kappa$ and $\kappa' = 2e_1a^2\kappa$. Next, we eliminate q and κ from Eqs. (4.2) and (4.3), obtaining a pair of polynomial identities in a. In order for these to be satisfied identically each coefficient of the polynomials must vanish. These conditions produce a set of algebraic equations sufficient to determine the constants $a_N, q_N, e_0, e_1, v_N, \omega_N$. There are generically two sets of values of the constants that solve

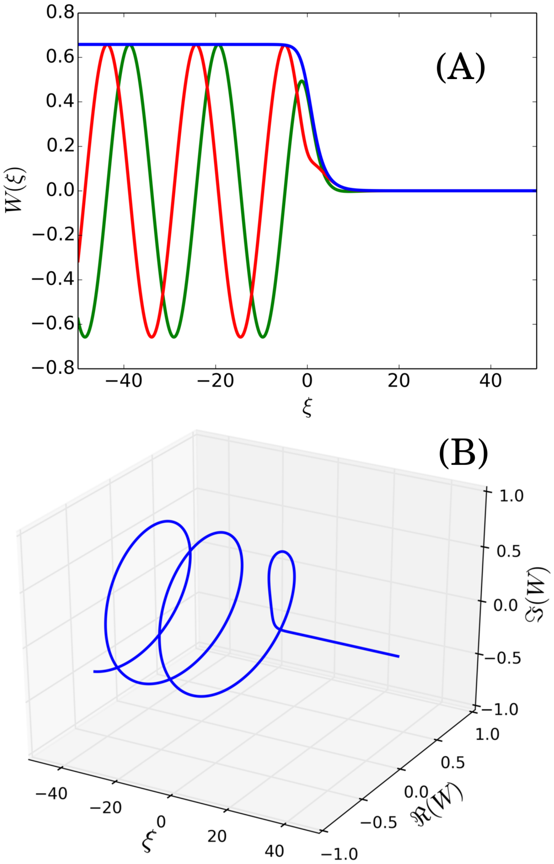

Figure 4.1: The nonlinear front with parameters $(a_1, a_2) = (2, 3)$ and $\mu = 0$ shown at a fixed time. (a) The real (green) and imaginary (red) parts of the solution $A(\xi, \cdot)$ along with its amplitude $|A|$ in blue. (b) A 3D representation of the solution in (a).

these equations due to a fold bifurcation in the $\mu < 0$ region. The explicit form of the front can be found by recalling the definition of κ and solving the second relation in Eq. (4.4) as a first order differential equation for a:

$$W(\xi) \equiv a_N e^{iq_N\xi} \left(1 + e^{2a_N^2 e_1 \xi}\right)^{-\frac{1}{2} - i\frac{e_0}{2e_1}} . \tag{4.5}$$

Here $e_1 > 0$ since we choose fronts that decay to zero as $\xi \to \infty$. Figure 4.1 shows a sample plot of the solution (4.5) with $(a_1, a_2) = (2, 3)$ and $\mu = 0$. The front solution connects the rotating wave state $A = a_N e^{i(q_N\xi - \omega_N t)}$ as $\xi \to -\infty$ to the trivial state $A = 0$ as $\xi \to \infty$.

We now exhibit the explicit Ansatz parameters for $(a_1, a_2) \neq (0, 0)$. For simplicity of presentation we first introduce the auxiliary parameters

$$\begin{aligned}\Gamma &= 16 - (3a_1 - 5a_2)(a_1 + a_2),\\ \Delta &= 16 - (a_1 + a_2)\left[4a_1 - 3a_2^3 - a_1a_2^2 + 2\left(a_1^2 - 10\right)a_2\right],\\ \Upsilon &= 8 - (3a_1 - 7a_2)(a_1 + a_2),\\ \Lambda &= 2 + a_2(a_1 + a_2),\end{aligned}$$

yielding $e_0 = -\frac{1}{4}(a_1 + a_2)$, $e_1 = \frac{1}{4}\sqrt{\frac{\Gamma}{3}}$, $\omega_N = -q_N v_N$, together with

$$\begin{aligned}a_{N\pm}^2 &= \frac{2(5\Lambda - 6) \pm 2\Upsilon\sqrt{(2\Lambda + \mu\Delta)/\Gamma}}{\Delta},\\ q_{N\pm} &= \frac{a_1 + a_2}{\Delta}\left[-2\Lambda \pm (6 - \Lambda)\sqrt{(2\Lambda + \mu\Delta)/\Gamma}\right],\\ v_{N\pm} &= \sqrt{\frac{\Gamma}{3}}\frac{\Lambda - 6 \pm \sqrt{(2\Lambda + \mu\Delta)\Gamma}}{\Delta}.\end{aligned} \tag{4.6}$$

One of these solutions (±) is stationary at the Maxwell-like point $\mu = \mu_M(a_1, a_2) \equiv -\frac{3}{\Gamma}$ [86]. Depending on the sign of the quantity $\Lambda - 6$ the stationary front may be located on either the a_{N+} or the a_{N-} branch. These branches meet at a fold at $2\Lambda + \mu\Delta = 0$. In addition, since $\omega_N + q_N v_N = 0$, the source state is always stationary in the original frame. The coefficients for the Ansatz shown here may be obtained from the more general solution derived in [145] that uses this Ansatz in a quintic Ginzburg-Landau equation with complex coefficients.

The Ansatz yields well-defined solutions even when $\Delta = 0$, despite the vanishing denominators in Eqs. (4.6), although there is now only one solution rather than two (up to an overall sign):

$$\begin{aligned}a_N^2 &= \frac{\mu\Upsilon^2 - 9(a_1 + a_2)^2}{(6 - 5\Lambda)\Gamma},\\ q_N &= \frac{a_1 + a_2}{4\Lambda\Gamma}\left[\mu(6 - \Lambda)^2 - 6\Lambda\right],\\ v_N &= \sqrt{\frac{\Gamma}{3}}\frac{(\mu\Gamma + 3)}{2(6 - \Lambda)}.\end{aligned}$$

Here e_0 and e_1 are as above but all the auxiliary variables are understood to be restricted to the curve $\Delta = 0$. There is now only one branch of fronts with positive a_N and no fold in the branch. The Maxwell point is still given by $-\frac{3}{\Gamma}$. This case is not discussed in [145].

In the special case $a_1 = a_2 = 0$ we recover the result of [49, 134]. The front solution (4.5) then takes the form

$$W(\xi) \equiv \frac{a_N}{\sqrt{1 + e^{2a_N^2\xi/\sqrt{3}}}}$$

with

$$a_N^4 - a_N^2 - \mu = 0, \qquad v_N = \frac{4a_N^2 - 3}{\sqrt{3}}, \tag{4.7}$$

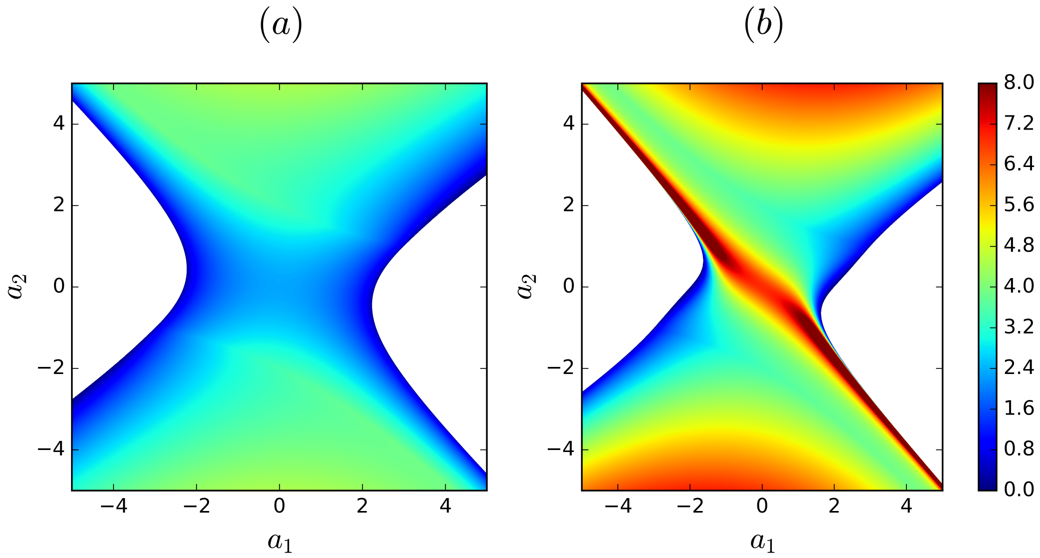

Figure 4.2: The length scale $\lambda \equiv (e_1 a_N^2)^{-1}$ at the Maxwell point $\mu = \mu_M(a_1, a_2)$ for fronts on (a) the a_{N+} branch and (b) the a_{N-} branch. Regions colored dark red represent values ≥ 8. The solution that lies below the fold on the branch of front solutions has a smaller amplitude and decay rate as compared to that above the fold.

provided $\mu > -\frac{1}{4}$. The polynomial equation for a_N^2 in Eq. (4.7) has two real roots. A front with $a_N^2 = \frac{1+\sqrt{1+4\mu}}{2}$ connects a stable constant amplitude state to the stable trivial state and travels with speed $v_N = \frac{2\sqrt{1+4\mu}-1}{\sqrt{3}}$. Such a front moves in the positive ξ direction when $\mu > -\frac{3}{16}$ and in the negative ξ direction when $-\frac{1}{4} < \mu < -\frac{3}{16}$. The Maxwell point is at $\mu_M = -\frac{3}{16}$. The other solution, which only exists when $-\frac{1}{4} < \mu < 0$, always travels in the negative ξ direction as it connects an unstable constant amplitude state to the stable trivial state.

In fact, the general case (4.6) reduces to Eq. (4.7) along the whole line $a_1 = -a_2$, along which all of the constants Γ, Δ, Υ, Λ become independent of *both* a_1 and a_2. This reduction results because, in this case, the quantity $ia_1(\bar{A}A_x - A\bar{A}_x)$ is real. As a result the ansatz (4.4) becomes independent of a_1.

For strongly nonlinear front propagation problems it is useful to develop a characterization of the intrinsic length scale in the model. In view of the exact front solution (4.5), it is natural to define this length scale, hereafter λ, as the inverse spatial decay rate of the front envelope, i.e., $\lambda \equiv \frac{1}{e_1 a_N^2}$. We show this length scale, evaluated at the Maxwell point $\mu = \mu_M(a_1, a_2)$, in Fig. 4.2. The figure shows that in the case of a_{N+}, increasing $|a_1|$ leads to front steepening while increasing $|a_2|$ leads to broadening. Unsurprisingly, the a_{N-} solution has both a smaller amplitude and a smaller spatial decay rate than its sibling above the fold. Specifically, when $a_2 > 0$ the a_{N-} front steepens for decreasing a_1 and broadens for

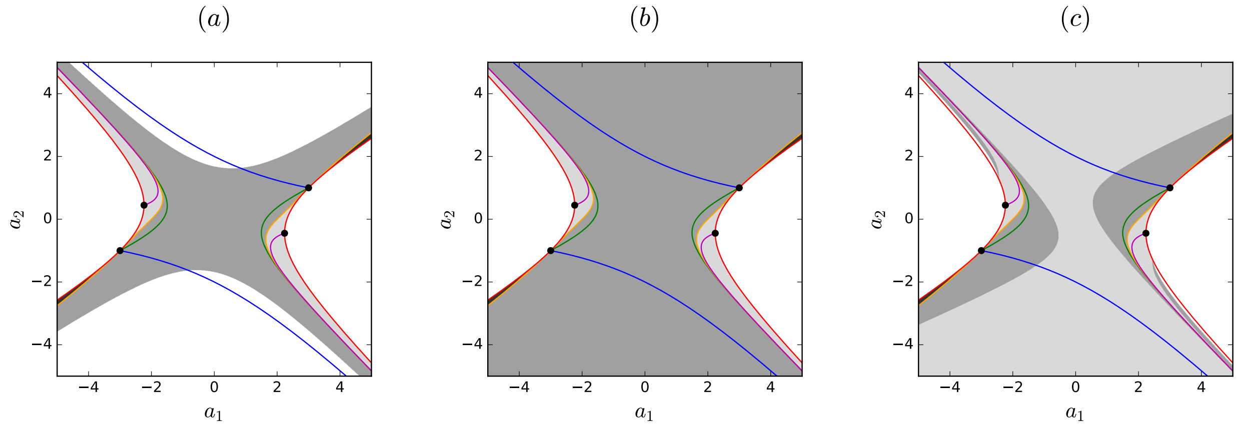

Figure 4.3: The existence regions for $a_{N\pm}$ when (a) $\mu = -0.1$, (b) $\mu = 0$, (c) $\mu = 0.1$. The dark grey indicates existence of both solutions, light grey indicates existence of only a_{N+}, black indicates existence of only a_{N-}, while white implies nonexistence of both solutions. The lines $\Gamma = 0$ (red), $\Lambda = 6$ (blue), $5\Lambda = 6$ (magenta), $\Upsilon = 0$ (green) and $\Delta = 0$ (orange) are shown restricted to the region $\Gamma > 0$, required for the validity of the Ansatz (4.4). The dots indicate the locations $(a_1, a_2) = (\pm 3, \pm 1)$, $\left(\pm\sqrt{5}, \mp\frac{1}{\sqrt{5}}\right)$ on the curve $\Gamma = 0$.

increasing a_2 throughout the bulk of the parameter regime.

Existence conditions for the nonlinear front

The Ansatz (4.4) does not always generate a front solution. For this to be the case the coefficients in Eqs. (4.6) must be real and the amplitude of the nontrivial asymptotic state must be positive, i.e.,

$$\Gamma > 0, \qquad a_N^2 > 0, \qquad 2\Lambda + \mu\Delta > 0. \tag{4.8}$$

These conditions place restrictions on the allowed values of a_1, a_2 and μ. We remark that $\Gamma > 0$ implies $\Lambda > 0$, a result that follows from the identity $\Gamma = 8\Lambda - 3(a_1 + a_2)^2$. Verifying these conditions requires an understanding of the allowed values of μ which we examine next.

The front solutions typically bifurcate from the trivial state in a subcritical pitchfork bifurcation, leading to the coexistence of the trivial state with the two front solutions, $a = a_{N\pm}$. This bifurcation is located at $\mu = \mu_P \equiv \frac{9(a_1+a_2)^2}{\Upsilon^2} \geq 0$ and the initial front amplitude scales as $a_N \propto |\mu - \mu_P|^{\frac{1}{2}}$ unless $5\Lambda = 6$ in which case $a_N \propto |\mu - \mu_P|^{\frac{1}{4}}$ and the pitchfork is degenerate. As a consequence, when $\Delta(5\Lambda - 6) > 0$ a fold bifurcation is present at $\mu = \mu_F \equiv -\frac{2\Lambda}{\Delta}$. This fold lies to the left (right) of the pitchfork bifurcation when the pitchfork is subcritical (supercritical) and no fronts of the assumed form is present $\mu < \mu_F$ ($\mu > \mu_F$), with only one front present for $\mu > \mu_P$ ($\mu < \mu_P$). Note that $\mu_P = 0$ along the line $a_1 = -a_2$.

The imposition of the requirements (4.8) leaves distinct generic parameter regimes within which the nonlinear front (4.5) exists. These depend on the values of Δ, Υ, and Λ. The first of these that we shall consider depends on the signs of Δ and $5\Lambda - 6$. Most of the parameter space is covered by $\Delta > 0$ but there is a sliver near the boundary of the existence region where $\Delta < 0$ (Fig. 4.3). While the former case displays expected behavior, the latter complicates the validity of the Ansatz and in many cases only one of the solutions in Eqs. (4.6) remains valid. In the following analysis we shall consider the effects of passing through the sign change in the auxiliary variables by increasing a_1. Since $5\Lambda > 6$ whenever $\Delta > 0$ there are three possible regimes encountered as a_1 increases from 0: (1) $\Delta > 0$ and $5\Lambda > 6$, (2) $\Delta < 0$ and $5\Lambda > 6$, and (3) $\Delta < 0$ and $5\Lambda < 6$. As a_1 increases from 0, Δ decreases towards zero and $\mu_F \to -\infty$. When $\Delta = 0$ there is no fold bifurcation on the front branch: the branch of exact fronts bifurcates from the trivial state at $\mu = \mu_P$ and extends to $\mu = -\infty$. This behavior persists into the region $\Delta < 0$ and $5\Lambda > 6$ in which only the a_{N+} solution is valid. Finally, if $|a_2| > \frac{1}{\sqrt{5}}$ then a third regime becomes accessible in which $\Delta < 0$ and $5\Lambda < 6$. At $5\Lambda = 6$ the pitchfork switches from subcritical to supercritical and in so doing regenerates a fold at μ_F, now to the right of the pitchfork. For $\mu_P \leq \mu \leq \mu_F$ both solutions of Eqs. (4.6) are valid.

The remaining degenerate parameter regimes involve Υ and Λ (Fig. 4.3), and have direct physical interpretation as a result of their effect on the μ dependence of the solutions. First, as $\Upsilon \to 0$ from both above and below $\mu_P \to \infty$. When $\Upsilon = 0$, Δ is always positive and $5\Lambda > 6$ so both solutions in Eqs. (4.6) are valid but have the same μ-independent amplitude, $a_N^2 = \frac{2(5\Lambda-6)}{\Delta}$. A similar phenomenon occurs in the case $\Lambda = 6$ when the deposited wave number, q_N, becomes independent of μ and takes the same value for both solutions in Eqs. (4.6). That is, the nonlinear front leaves the same patterned state in its wake regardless of the forcing μ. Because μ represents the bifurcation parameter that pushes the system into the pattern-forming regime, a dependence of a_N and q_N on μ is to be expected. The fact that this expectation fails in these subcases is indicative of a nontrivial front selection mechanism and a nongeneric balance among the cubic nonlinear terms of Eq. (1.1). These effects are new and cannot be seen in the well-studied case $a_1 = a_2 = 0$.

Bifurcation diagrams for the amplitude of the front solutions for sample parameters are shown in Figs. 4.4 and 4.5 in which we plot $\|W\|_\infty = a_N$ versus the parameter μ. First, Fig. 4.4(a) demonstrates the generic behavior of the nonlinear fronts for $a_2 = 0$, while Figs. 4.4(b) and (c) show nongeneric behavior that arises when the remaining key coefficients Υ and Δ pass through zero. Since $\Upsilon = 0$ at $a_1 = \sqrt{\frac{8}{3}}$ while $\Delta = 0$ at $a_1 = 2$ we separate Fig. 4.4 into three diagrams around $a_1 = 0$, $\sqrt{\frac{8}{3}}$, and 2. In the bulk of the parameter space the generic case with $a_1, a_2 \neq 0$ shares the same qualitative characteristics as the cases in Fig. 4.4 with the corresponding signs of Δ, Υ and Λ. Second, Fig. 4.5 focuses on the regime $5\Lambda - 6 \approx 0$, only realizable for $|a_2| > \frac{1}{\sqrt{5}}$. Here the pitchfork bifurcation responsible for the branch of fronts switches from subcritical to supercritical (at $5\Lambda = 6$). The resulting solution branch moves towards the left with decreasing a_1 until the Ansatz fails at $a_1 = -\frac{7}{3} \approx -2.33$

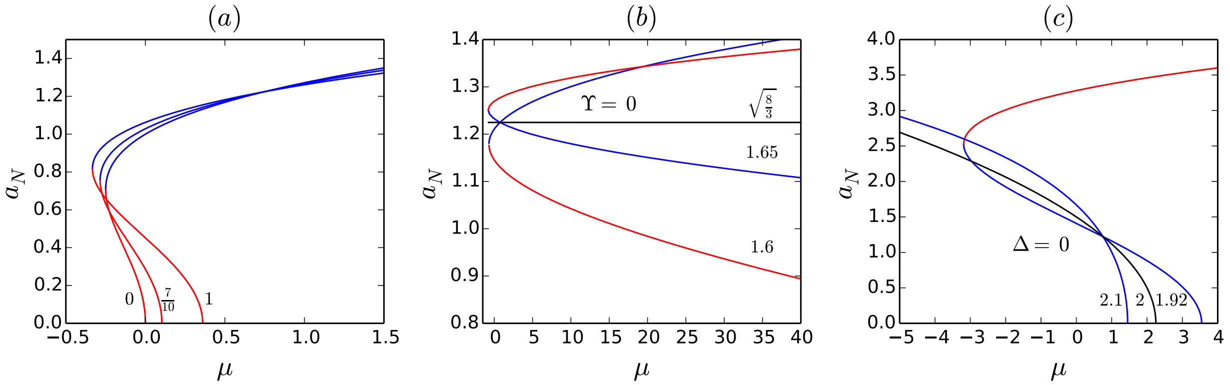

Figure 4.4: The front amplitudes a_{N+} (blue) and a_{N-} (red) for (a) $\Upsilon > 0$, $\Delta > 0$, (b) several values of $\Upsilon \approx 0$ while $\Delta > 0$, and (c) for several values of $\Delta \approx 0$ while $\Upsilon < 0$. The parameter values in each of these plots are $a_2 = 0$ and (a) $a_1 = (0, 0.7, 1)$, (b) $a_1 = \left(1.6, \sqrt{\frac{8}{3}}, 1.65\right)$, and (c) $a_1 = (1.92, 2, 2.1)$ as indicated in the panels. The special cases $\Upsilon = 0$ and $\Delta = 0$ are shown in black.

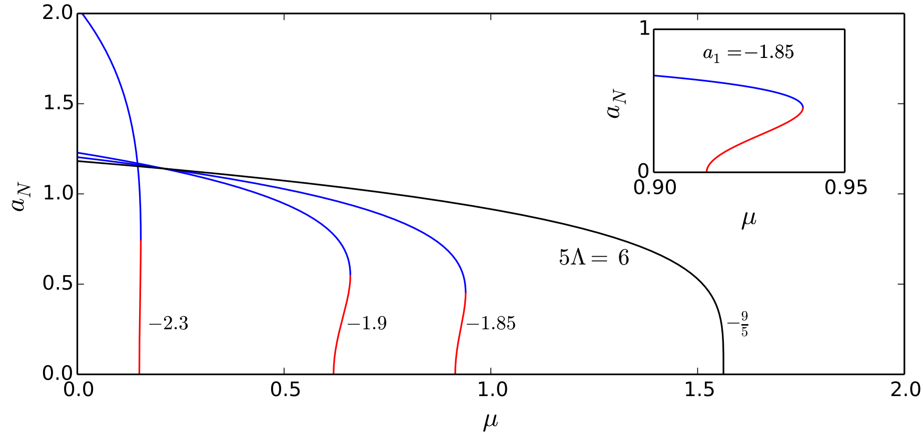

Figure 4.5: The front amplitudes a_{N+} (blue) and a_{N-} (red) as functions of μ for $a_2 = 1$ and $a_1 = -2.3, -1.9, -1.85, -\frac{9}{5}$; the latter branch, corresponding to $5\Lambda = 6$, is shown in black.

where $\Gamma = 0$.

Stability of exact front solutions

We analyze the linear stability of a front by linearizing Eq. (1.1) about such a front, i.e., writing $A = W(\xi)e^{-i\omega t}(1 + \delta(\xi, t))$, $|\delta| \ll 1$. This yields

$$\delta_t = \delta_{\xi\xi} + U\delta_\xi + ia_2|W|^2\bar{\delta}_\xi + V(\delta + \bar{\delta}),$$

where

$$\begin{aligned} U(\xi) &\equiv v + 2W^{-1}W_\xi + ia_1|W|^2, \\ V(\xi) &\equiv |W|^2 - 2|W|^4 + i\left(a_1\bar{W}W_\xi + a_2W\bar{W}_\xi\right). \end{aligned}$$

The quantities $U(\xi) \equiv U_r + iU_i$ and $V(\xi) \equiv V_r + iV_i$ may be computed from the identities

$$\begin{aligned} |W|^2 &= \frac{a_N^2}{1 + e^{2a_N^2 e_1 \xi}}, \\ W^{-1}W_\xi &= iq_N + (e_1 + ie_0)\left(|W|^2 - a_N^2\right). \end{aligned}$$

We search for temporal eigensolutions of the form $\delta(\xi, t) = e^{\sigma t}(\delta_1 + \delta_2) + e^{\bar{\sigma} t}(\bar{\delta}_1 - \bar{\delta}_2)$, where δ_1 and δ_2 are functions of ξ alone, leading to the eigenvalue problem

$$\sigma \begin{pmatrix} \delta_1 \\ \delta_2 \end{pmatrix} = \begin{pmatrix} \partial_{\xi\xi} + U_r\partial_\xi + 2V_r & i\left(U_i - a_2|W|^2\right)\partial_\xi \\ i\left(U_i + a_2|W|^2\right)\partial_\xi + 2V_i & \partial_{\xi\xi} + U_r\partial_\xi \end{pmatrix} \begin{pmatrix} \delta_1 \\ \delta_2 \end{pmatrix} \equiv \mathcal{L} \begin{pmatrix} \delta_1 \\ \delta_2 \end{pmatrix}.$$

The spectrum of the operator $\mathcal{L}$ consists of a point spectrum σ_p and the essential spectrum σ_c. However, this operator is non-normal: it does not commute with its adjoint. Non-normal operators do not obey the spectral theorem, may not have orthogonal eigenfunctions and can have a point spectrum with high sensitivity to perturbations [43, 148]. Such operators arise, for example, in the study of spatially varying fluid flows [43, 138]. Conclusions about stability from point spectra of non-normal operators are complicated by the possibility of transient growth and we opt in this work to treat only the essential spectrum of $\mathcal{L}$, which can be computed analytically.

The essential spectrum for a front solution consists of the union of the essential spectra of the $\xi \to \pm\infty$ states. The trivial state (at $\xi \to \infty$) is only stable when μ is negative. In the notation of [84] infinitesimal perturbations of the periodic state present at $\xi \to -\infty$ have the growth rate

$$\sigma(q) = ivq - (g + q^2) \pm \sqrt{g^2 + q^2\left(2g - f\right)}, \tag{4.9}$$

where q is the perturbation wave number and

$$\begin{aligned} g &\equiv 2(\mu - q_N^2) + \left[1 + q_N(a_2 - a_1)\right]a_N^2, \\ f &\equiv (4 + a_2^2 - a_1^2)a_N^4 - 2\left[1 + q_N(a_2 + a_1)\right]a_N^2 - 4q_N^2. \end{aligned}$$

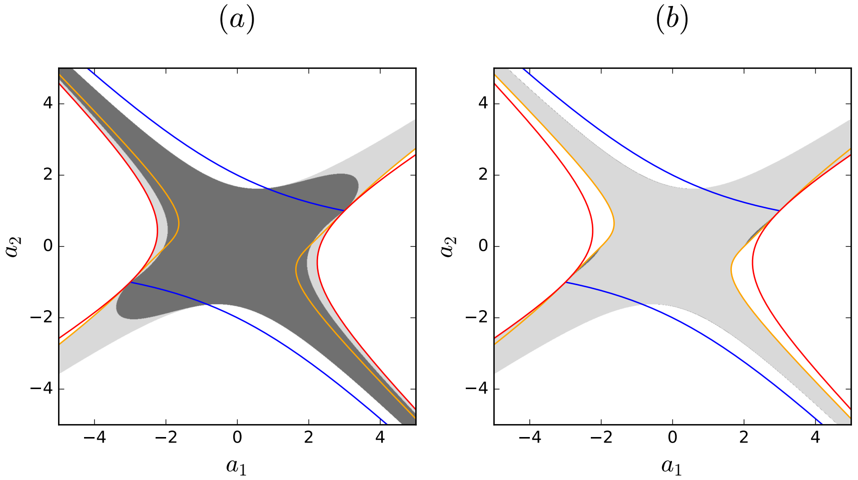

Figure 4.6: Stability of the rotating wave selected in the wake of an a_{N+} front (a) and an a_{N-} front (b) in the (a_1, a_2) plane at $\mu = -0.1$. Stable regimes are indicated in dark grey, unstable regimes in light grey, and regions with no front solutions in white. The lines $\Gamma = 0$ (red) and the lines $\Lambda = 6$ (blue) and $\Delta = 0$ (orange) in the region $\Gamma \geq 0$ are also shown.

We call a solution linearly stable if its spectrum is contained in the left half of the complex plane. In [84] it was shown that this rotating wave state is stable if and only if f and g are both nonnegative. Thus the essential spectrum of the front is stable provided $f, g \geq 0$ and $\mu < 0$. It was further shown in [84] that there are two distinct regimes by which the rotating wave can go unstable: (I) $f < 0$ and $f \leq g$ or (II) $g < 0$ and $f > g$. The first is characterized by a marginal wave vector with nonzero real part and the latter by one with zero real part. Though a complete analysis of the point spectrum is not included here we can calculate the eigenfunctions of the zero eigenvalue analytically. This eigenvalue has double multiplicity: translation symmetry gives rise to a zero eigenvalue "Goldstone mode" [54] $\delta(\xi, t) = W^{-1}W_\xi$ while rotation symmetry generates the zero eigenvalue phase mode $\delta(\xi, t) = i$.

Although the rotating wave states of Eq. (1.1) form a one parameter family of states (for fixed system parameters) [84, 86], the front solution computed here selects one particular rotating wave in the asymptotic limit $\xi \to -\infty$. This reduction enables us to plot the stability in the (a_1, a_2) plane for fixed μ. In Figs. 4.6 and 4.7 we exclude the spectrum of $A = 0$ and plot the stability of the rotating wave selected by the nonlinear front Ansatz in the two qualitatively distinct regimes $\mu \lessgtr 0$. For $\mu < 0$ the a_{N+} branch is stable in a region of parameter space surrounding the line $a_1 = -a_2$, while the a_{N-} branch is rarely stable. For $\mu > 0$ the a_{N+} branch is stable in a significantly larger parameter region while the a_{N-} branch remains mostly unstable. Despite the large regions of instability revealed in the figure, the dynamical significance of an unstable rotating wave in the wake the front solution is more subtle. Because we are concerned with the asymptotic dynamics of the front as $t \to \infty$, instabilities behind it are only relevant provided that they propagate to the right

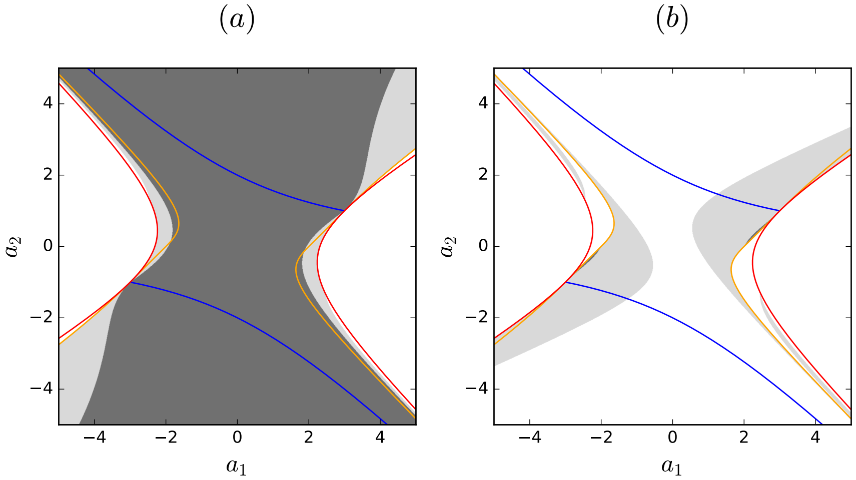

Figure 4.7: Stability of the rotating wave selected in the wake of an a_{N+} front (a) and an a_{N-} front (b) in the (a_1, a_2) plane at $\mu = 0.1$. Stable regimes are indicated in dark grey, unstable regimes in light grey, and regions with no front solutions in white. The lines $\Gamma = 0$ (red), $\Lambda = 6$ (blue) and $\Delta = 0$ (orange) in the region $\Gamma \geq 0$ are also shown.

with a speed not less than that of the front, i.e., to have an effect the instability must be absolute in the frame of the leading edge. The propagation speeds of these instabilities and their effect on the front are computed and analyzed in Sec. 4.5 below.

The stability of the deposited rotating wave is particularly relevant at the Maxwell point $\mu = -\frac{3}{\Gamma}$ at which the front is stationary. This front is associated with the branch a_{N+} when $\Lambda - 6 < 0$ and a_{N-} when $\Lambda - 6 > 0$. We show the stability of the rotating wave selected by the stationary front in Fig. 4.8. It is easy to see from the figure that the region of stability is contained in the intersection of $\Gamma(a_1, a_2) > 0$ and $\Lambda(a_1, a_2) < 6$, so the rotating wave selected at the Maxwell point is only stable for fronts on the a_{N+} branch. The instability of the a_{N-} fronts is always of type II and has been confirmed using direct numerical simulation. The stability at $\mu = \mu_M$ of other branch of the Ansatz for which $v_N \neq 0$ can also be studied. The rotating wave selected by this branch is always unstable. When $\Lambda - 6 < 0$ the instability can be either of type I or II depending on parameters but for $\Lambda - 6 > 0$ it is always of type II.

4.3 Front dynamics methodology

In the next two sections we apply the ideas of front propagation into stable and unstable states as discussed in chapter 2 to front propagation in Eq. (1.1). To validate theoretical predictions we study the evolution of either a localized pulse in the stationary frame or a half-pulse in the moving frame. Specifically, we take two types of initial half-pulses (reflecting in x to get a localized pulse): $A(\xi) = \Theta(-\xi - \ell)$ (Heaviside), where $\Theta(\xi)$ is the Heaviside function and ℓ is a constant, and $A(\xi) = \gamma_1(\xi)e^{i\gamma_2(\xi)}\Theta(-\xi - \ell)$ (random-Heaviside), where

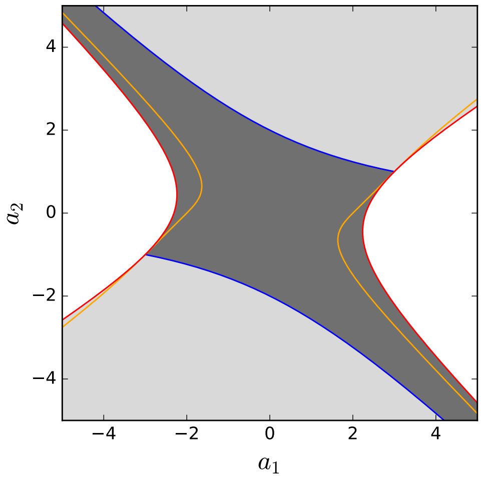

Figure 4.8: Stability of the rotating wave selected in the wake of the stationary front at the Maxwell point $\mu = -\frac{3}{\Gamma}$ in the (a_1, a_2) plane. The relevant solution branch is determined by the sign of the quantity $\Lambda - 6$. Stable regimes are indicated in dark grey, unstable regimes in light grey, and regions with no front solutions in white. The lines $\Gamma = 0$ (red), $\Lambda = 6$ (blue) and $\Delta = 0$ (orange) in the region $\Gamma \geq 0$ are also shown.

γ_1, γ_2 are chosen randomly from uniform distributions on $(0.7, 2)$ and $(0, 2\pi)$, respectively. The latter initial condition is constructed so that it does not select any wave number or amplitude preferentially but still has sufficient amplitude not to decay. The time integration is carried out using a finite differences (FD) method and a spectral method that are outlined in chapter 2. Further details about the numerical techniques that are used can be found in section 4.7.

4.4 Front propagation into a stable state

We turn first to the regime in which the asymptotic state $A = 0$ ahead of the front is stable ($\mu < 0$). We are concerned with the time evolution of localized initial conditions. Since the state $A = 0$ is stable in this regime, the initial condition must be of sufficient amplitude so as to avoid immediate decay back to $A = 0$. When the pitchfork bifurcation to the branch of front states is subcritical and $\mu < \mu_F$ all initial conditions collapse towards $A = 0$. When $\mu_F < \mu < 0$, initial conditions of sufficiently large amplitude typically evolve in their bulk towards one of the stable rotating wave states of Eq. (1.1) generating a pair of fronts connecting the interior rotating wave at either end to $A = 0$. After an initial transient the fronts travel at a constant speed and in opposite directions. When the pitchfork bifurcation is supercritical the fold always occurs at $\mu > 0$ and the dynamical picture depends more strongly on the parameters. We address specific cases capturing the distinct behaviors that result next.

We find empirically that the selected speed from Heaviside but not random Heaviside initial conditions is correctly predicted by Eqs. (4.6) in many cases, provided that the corresponding solution is stable and the system is known to be well-posed. In Fig. 4.9 we plot the speed of the two possible fronts, $v_{N\pm}$, as a function of the parameter μ in the subcritical regime for a series of values of the coefficients (a_1, a_2). Figure 4.9(a) shows the classical case $a_1 = a_2 = 0$ and similar behavior is obtained when one of a_1 or a_2 is increased to 1. For these parameters Heaviside initial conditions evolve on a fast time scale towards the rotating wave corresponding to the stable branch indicated in a continuous blue line and then a pair of fronts propagate outwards at speed $v_{N+} > 0$ expanding the structure, or inwards if $v_{N+} < 0$ contracting the structure. Random Heaviside initial conditions in contrast typically do not approach a fully developed front and instead decay. The red (dashed) part of the velocity curves below the fold corresponds to v_{N-} and these fronts are unstable since they connect to an unstable rotating wave. These findings extend previous results for $(a_1, a_2) = (0, 0)$.

In panel (b) of Fig. 4.9 we show that the rotating wave selected by Eqs. (4.6) need not be stable. For $\mu < 0$ the curve with parameter values $(a_1, a_2) = (\frac{9}{2}, 4)$ is always unstable while the $(a_1, a_2) = (0, 4)$ solution restabilizes at a finite negative value of μ. In the former case the initial value problem is well-posed and initial conditions appear to decay to $A = 0$. For the $(0, 4)$ solution it is not known whether the initial value problem is well-posed, but when the wave selected by Eqs. (4.6) is stable we observe that Heaviside initial conditions converge to a steady front solution with velocity v_{N+} and random Heaviside initial conditions do not. Also shown in this plot is the case $(a_1, a_2) = (0, 2)$ in which the Maxwell point is located at the fold on the branch of fronts of Eqs. (4.6). Time stepping simulations suggest that solutions initiated at the Maxwell point on this branch are not stable and decay to $A = 0$. Moreover, since the Maxwell point coincides with the fold there is no parameter region in which fronts can contract; amplitude decay occurs when $\mu < \mu_F$ and expansion when $\mu > \mu_F$.

We next turn to some of the cases in which $\Delta < 0$ and only one branch of the front solution exists, persisting for all $\mu < 0$. This branch may be either stable or unstable. In panel (c) of Fig. 4.9 this is the + branch of the Ansatz and it is stable below some finite $\mu < 0$. For $(a_1, a_2) = (-2, 1)$ and when the predicted velocity $v_{N+} > 0$, we find convergence to the Ansatz solution from both Heaviside and random Heaviside initial conditions. When $(a_1, a_2) = (2.2, 0)$ and the solution is unstable, both types of initial conditions converged to a solution with wave number and speed near but not equal to the Ansatz prediction. In contrast, when the front is predicted to be stable and $v_{N+} > 0$, we do not observe convergence to this solution unless initial conditions of the form $A(\xi) = e^{iq_N\xi}\Theta(-\xi - \ell)$ are adopted. In both cases when $v_{N+} < 0$ neither Heaviside nor random Heaviside initial conditions evolve towards a steady front. We are able to realize a front moving at speed $v_{N+} < 0$ only with the initial condition $A(\xi) = e^{iq_N\xi}\Theta(-\xi - \ell)$. In panel (d) of the figure a similar bifurcation structure is present but all initial conditions adopted immediately collapsed to $A = 0$. This behavior supports the conjecture of [136] that whenever $v_N < 0$, the selection process is more complex and depends strongly on initial conditions. Furthermore the behavior in the $(a_1, a_2) = (2.2, 0)$ case for which a stable front with a positive velocity is predicted suggests that the system may select a different front solution even when the predicted front is stable.

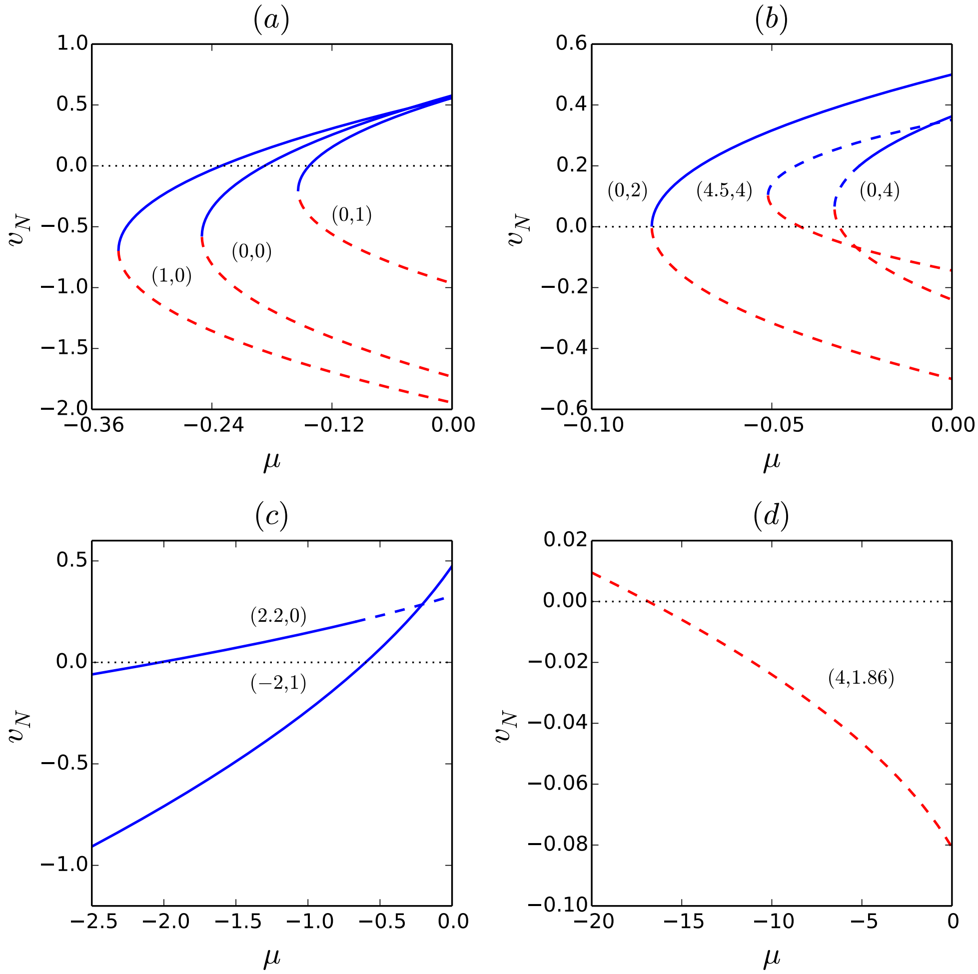

Figure 4.9: The velocity $v_{N\pm}$ of the exact front solution is shown in blue and red, respectively. The parameters (a_1, a_2) are indicated next to each curve and dashed lines represent instability of the essential spectrum. The line $v = 0$, shown as a black dotted line, is included for reference.

Moreover, the fronts in Figs. 4.9(c,d) persist as $\mu \to -\infty$, while the fronts computed in [86] do not. This is because each is computed for a fixed wave number whereas the exact front computed here has a wave number that is μ-dependent. In this case all sufficiently large amplitude initial data with wave number near q_N result in dynamics associated with the + branch of the exact front solution.

4.5 Front propagation into an unstable state: spreading and marginal stability

When $\mu > 0$ the state $A = 0$ ahead of the front is unstable. In the case of Eq. (1.1) the spreading speed is easy to calculate but its interpretation is complicated by the nonlinear terms. An application of Eq. (2.17) to Eq. (1.1) linearized about the state $A = 0$ leads to the prediction

$$v^* = 2\sqrt{\mu}, \quad q^* = i\sqrt{\mu}, \quad \sigma^* = 2\mu.$$

This result implies that the leading edge of a pulled front takes the form $e^{2\mu t - \sqrt{\mu}x}$ but does not predict the nonlinear state that is left in its wake. The simplest possibility is that the front moves at a constant speed in which case $A \equiv A(x - v^*t)$. A necessary condition for this to be the case is that the traveling wave $A = R\, e^{iq(x-v^*t)+i\Im(\sigma^*)t}$ solves the full nonlinear problem for some amplitude R but trails the leading edge of the front [136]. This is distinct from the "node-counting" argument of [52], which is automatically satisfied for fronts that are uniformly propagating. In the present case $\Re[q] = 0$ and $R^2 = \frac{1}{2}\left(1 + \sqrt{4\mu + 1}\right)$, so this front moving with speed v^* would deposit a zero wave number. This front is excluded, however, whenever $a_1, a_2 \neq 0$: at the location of the front interface $ia_1|A|^2 A_x, ia_2 A^2 \bar{A}_x \neq 0$ and Eq. (1.1) cannot have a purely real solution. In the following we show that dynamics at the leading edge of the front nonetheless result in the deposition of a state with zero wave number in the wake of a pulled front.

Pulled versus pushed: nonlinear selection

In this section we investigate the validity of the nonlinear marginal stability hypothesis (see, Eq. (2.18)) for the case of front propagation into an unstable state in Eq. (1.1). This is carried out through a series of numerical studies. Moreover, since v_N and κ_N have been computed exactly and we analyze all possible selection regimes predicted by Eq. (2.18) analytically in Appendix B.

Figure 4.10 shows standard behavior of the front speeds predicted from Eq. (2.18). The case $(a_1, a_2) = (0, 0)$ is well-studied [49, 135] and is shown in Fig. 4.10(a). Here the transition from pushed to pulled as determined by (2.18) occurs at $\mu = \frac{3}{4}$. Although $v_N \geq v^*$ for all $\mu > 0$, the linear decay rate surpasses κ_N at $\mu = \frac{3}{4}$ and remains above it as $\mu \to \infty$. This behavior is typical and validates the intuitive prediction that at high enough forcing all fronts will be pulled. The data points shown in the figure are computed with a finite difference (FD) code and are plotted with an error bar indicating an associated deterministic correction to the speed. Details of this correction and its interpretation can be found in Appendix 4.7. As shown in Fig. 4.10(b) and (c), v_N and κ_N depend strongly on a_1, a_2 and v_N need not supersede v^* at large μ. We mention that despite the continuity in the speed at the pushed-pulled transition the selected wave number of the deposited state in the wake of the front is generally discontinuous. This "structural instability" has been observed previously in the

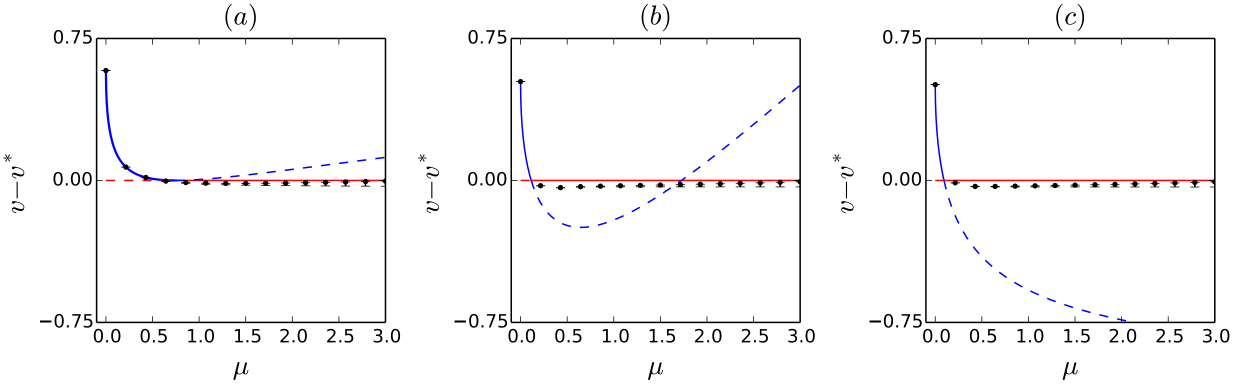

Figure 4.10: Front speed v_N (blue) relative to the linear spreading speed v^* (red) for parameters (a_1, a_2): (a) $(0, 0)$, (b) $\left(-\frac{8}{5}, \frac{1}{2}\right)$, (c) $\left(\sqrt{\frac{8}{3}}, 0\right)$. The selected (not selected) speed is indicated by a solid (dashed) line according to Eq. (2.18). The black dots represent speeds calculated by time-stepping Heaviside initial conditions with FD in the stationary frame and tracking the motion of the front. The space and time discretizations are $\Delta x = 0.05$ and $\Delta t = (\Delta x)^2$; further details are contained in Appendix 4.7. The deterministic corrections as a result of the FD approximation (computed in Appendix 4.7) are shown using error bars on the data points.

cubic-quintic complex Ginzburg-Landau equation [136] and appears here generically with the inclusion of either a_1 or a_2.

Fig. 4.11 shows some nonstandard predictions of Eq. (2.18) when $a_2 \neq 0$. In Fig. 4.11(a) the nonlinear front possesses a speed and decay rate that always exceed the linear one. This serves as a counter-example to the suggestion [136] that the linear front will always be selected at sufficiently large μ. In this particular case the decay rate of the selected front is quite small when $\mu \approx 0$. Consequently a very large domain is needed to measure the front speed accurately, significantly larger than our standard domain length $L = 300$. The best results were obtained for Gaussian initial conditions and a spectral method with a domain size $L(\mu)$ determined by the decay rate $\lambda(\mu)$, here $L = 400\lambda(\mu)$ so that $L(0) \approx 1100$. In Fig. 4.11(b) the nonlinear front has a negative velocity for all $\mu > 0$ where it exists. In this case Eq. (2.18) does not apply and the asymptotically selected front depends more strongly on initial conditions. We have found that initial conditions in the form of a sharply peaked Gaussian pulse undergo blow-up in finite time, while Heaviside initial conditions decay immediately to $A = 0$. We conjecture that in this parameter regime the Cauchy problem is not well posed. In Fig. 4.11(c) the nonlinear front Ansatz fails at some finite $\mu > 0$. When μ is larger than this value it is not clear whether the nonlinear terms in the equation saturate for all initial conditions or not. Whereas the case in (b) suffers from blowup we have found that fronts initiated beyond the μ value where the Ansatz fails are well behaved. After an initial transient, Heaviside initial conditions evolve with a leading

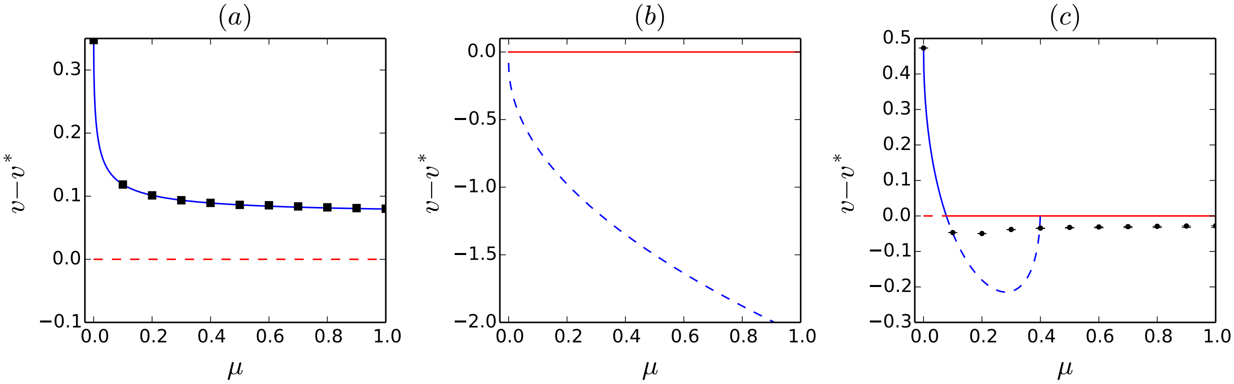

Figure 4.11: Front speed v_N (blue) relative to the linear spreading speed v^* (red) for parameters $(a_1, a_2, \pm)$, where the symbol $\pm$ specifies the front: (a) $(-15, 16, +)$, (b) $(4, 1.86, -)$, (c) $(-2, 1, +)$. The selected (not selected) speed is indicated by a solid (dashed) line according to Eq. (2.18). The black squares represent speeds calculated in a domain of length $L = 400\lambda$ by time-stepping Gaussian initial conditions in the stationary frame using a spectral method with parameters $\Delta t = 0.01$, $N_x = 4096$ and $\epsilon = 10^{-8}$ (Appendix 4.7). The black dots represent speeds calculated by time-stepping Heaviside initial conditions in the stationary frame using a finite difference code with space and time discretizations $\Delta x = 0.05$, $\Delta t = (\Delta x)^2$, and tracking the motion of the front (Appendix 4.7). The deterministic corrections as a result of the FD approximation (computed in Appendix 4.7) are shown using error bars on the data points.

edge moving at the pulled front speed and deposit a rotating wave with a finite wave number in their wake.

The Benjamin-Feir instability and secondary fronts

Further complicating the selection problem is the fact that the dynamically realized front may suffer from secondary instabilities. The deposited rotating wave in the wake of the front can undergo two types of instabilities [84] that may interfere with the propagation of the front. One such possibility is a Benjamin-Feir (BF) instability that generates a state of nonzero wave number. If this instability propagates with a large enough velocity that it overtakes the leading edge of the front, phase slips and spatio-temporal chaos can occur [52, 117, 136, 146].

If the deposited state is unstable to the BF instability then a secondary front inside the deposited state can result. This front is a pulled Kuramoto-Shivashinsky front [133]. In this case there are two regimes corresponding to whether or not the secondary front speed, v_{BF}, is less or greater than the primary one, v. If $v_{BF} < v$ then the deposited pattern behind the primary front grows in size at a rate $v - v_{BF}$ and the instability is advected away from the leading edge. This leads to a double-front structure in the profile of the solution in which the distance between the primary and secondary fronts grows with time [72]. In the second case, $v_{BF} > v$, the instability catches up with the leading edge producing a front whose asymptotic character depends on the existence of stable rotating waves. If the primary front is pushed and the secondary instability deposits a stable rotating wave then a different pushed front results. If the primary front is pulled and the secondary instability deposits a stable rotating wave then phase slips at the leading edge must take place in order that the rotating wave be deposited in the wake of the front. If no stable rotating waves exist then the pulled front may become incoherent [136]. We have searched a variety of regimes in which all rotating waves are unstable but have not observed incoherent pulled fronts. On the other hand incoherent front dynamics can occur for pushed fronts provided the deposited state with wave number q_N is unstable. In the following we elaborate on these notions for both pulled and pushed fronts.

Pulled fronts suffer from secondary instability to phase-winding states with nonzero wave number. The dispersion relation for disturbances to a generic rotating wave state in the stationary frame is provided by Eq. (4.9) with $v = 0$ and the instabilities only occur when one or both of f, g is non-positive [84, 86]. As shown at the beginning of Sec. 4.5 the leading edge of pulled fronts coincides with that of the front that deposits a state of constant amplitude R and zero wave number. Although these fronts cannot be the true pulled fronts for generic values of a_1 and a_2, our observation is that pulled fronts nonetheless deposit a rotating wave with approximately zero wave number in their wake and the necessary phase gradient θ_x (where $A = Re^{i\theta}$) takes the form of a strongly localized pulse at the leading edge. Consequently the prediction of v_{BF} for the zero wave number rotating wave is a good estimate for the speed of pulled fronts undergoing this secondary instability.

The zero wave number rotating wave has $f = (4 + a_2^2 - a_1^2)\, R^4 - 2R^2$, $g = 2\mu + R^2$, where $R^2 = \frac{1}{2}\left(1 + \sqrt{4\mu + 1}\right)$. When $\mu > 0$ one can show that $g > 0$ always but $f > 0$ only if $a_1^2 - a_2^2 < 2$. The state suffers from instability when $a_1^2 - a_2^2 \geq 4$ for any positive μ, and when $4 > a_1^2 - a_2^2 > 2$ for $0 \leq \mu < \frac{2(a_1^2 - a_2^2 - 2)}{(4 - a_1^2 + a_2^2)^2}$. Applying the marginal stability criterion to the dispersion relation for the secondary instabilities produces a prediction for the front speed, wave number, and frequency of the secondary front. This calculation is shown explicitly at the end of Appendix A. We discuss an application next.

As an example we consider the case $(a_1, a_2) = \left(\frac{5}{2}, 1\right)$ and plot the speeds v^*, v_N, and v_{BF} in Fig. 4.12. In this figure we plot speeds as a function of a variable h which is an order-preserving one to one reparametrization of μ and depends on a_1 and a_2. The choice of $h(\mu)$ arises naturally in the calculation of v_{BF} and is defined in Appendix A. In this plot the BF velocity corresponds to instabilities of the zero wave number rotating wave and not the rotating wave left in the wake of the nonlinear front. The rotating wave for the nonlinear front Ansatz is stable for $\mu \lesssim 5$, throughout the pulled-pushed crossover. After the transition occurs from pushed to pulled at $\mu \approx 0.072$ (left black dot), $v_{BF} > v^*$ and the pulled front is unstable. This is shown in Fig. 4.13 for $\mu = 0.4$ (for clarity, larger than the threshold) and the prediction of the leading edge motion based on the speed v^* is shown in red. After a transient, the front propagates at the linear spreading speed but deposits a nonzero wave

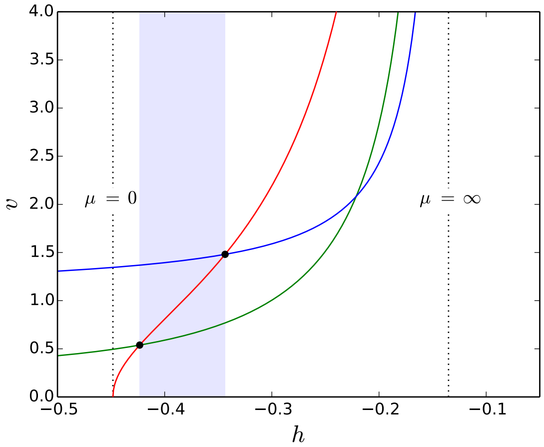

Figure 4.12: Speeds v^* (red), v_N (green), and v_{BF} (blue) for pulled fronts as a function of the variable h defined in Appendix A.4 for $(a_1, a_2) = \left(\frac{5}{2}, 1\right)$. Increasing h corresponds to increasing μ. The parameters corresponding to $\mu = 0, \infty$ are indicated with dotted lines and the region in which pulled fronts are selected **and** $v_{BF} > v^*$ is delimited by blue shading. The transition from pushed to BF-unstable pulled fronts, and subsequently from BF-unstable to BF-stable pulled fronts is marked by black dots.

number approximately equal to q_N. This is enabled by phase slips at the leading edge. By $\mu \approx 0.55$ (right black dot) the pulled front restabilizes as its speed exceeds that of the BF instability for the zero wave number rotating wave. This phenomenon is pictured in Fig. 4.14 ($\mu = 1$) in which the speeds v^* and v_{BF} are shown in red and blue, respectively. The primary front deposits a state with near-zero wave number followed by a secondary front that generates a larger amplitude asymptotic state with a different wave number in its wake, but still close to q_N. The separation of the primary and secondary fronts hearkens to the double front structure observed in [72].

Figures 4.13 and 4.14 also reveal two features at the leading edge that we cannot predict theoretically. First is the periodic nucleation of amplitude holes or "grooves" whose profile is shown in Fig. 4.15. These holes increase and then decrease in depth as time passes eventually merging with the otherwise homogeneous amplitude state left in the wake of the front. In the case of Fig. 4.13 the time scale on which the holes anneal is much longer than the time scale for the front propagation and the holes therefore grow in number as the front propagates. In the case of 4.14 the holes vanish on a comparable time scale to the primary front and thus only one is present at any given time. This phenomenon can also be seen in Figs. 4.16 and 4.17 at the secondary front interface and has been verified using both FD and Fourier discretizations. This feature has also been observed in [72] in a nonvariational case, although there the holes, once nucleated, do not disappear. The second feature visible in both figures is the presence of phase slips. These occur at the leading edge of the front in Fig. 4.13 and at the edge of the secondary front (which we suspect is also pulled) in Fig. 4.14. These phase

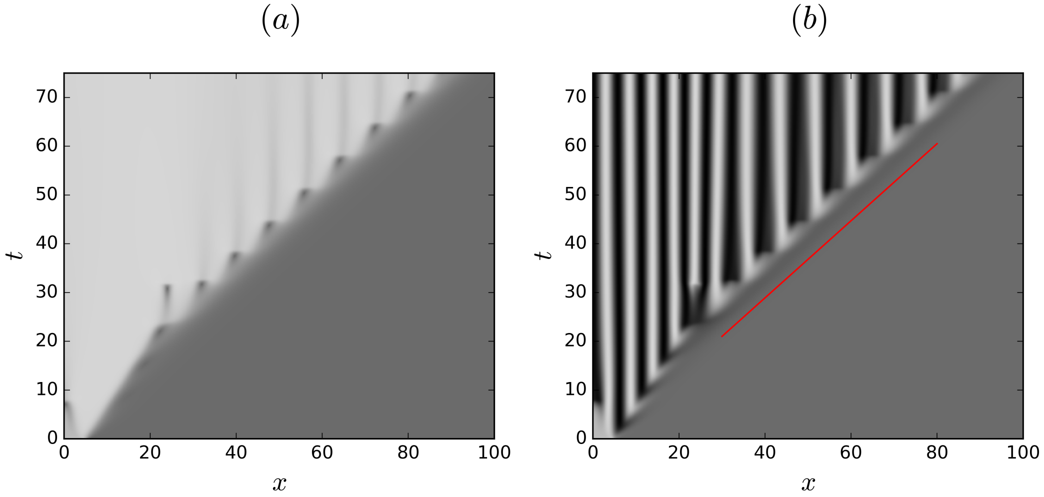

Figure 4.13: Space-time plot of the evolution of (a) $|A(x,t)|$ and (b) $\Re[A(x,t)]$ from Heaviside initial conditions in the stationary frame for $(a_1, a_2) = \left(\frac{5}{2}, 1\right)$ and $\mu = 0.4$ computed using FD. The calculation is done on a domain $[-100, 100]$ with Dirichlet boundary conditions on both $\Re[A]$ and $\Im[A]$ and only half of the simulation window is shown. The space and time discretizations are $\Delta x = 0.2$ and $\Delta t = 0.0025$. In this regime after an initial transient the front is pulled, traveling at speed v^* to a good approximation. An offset line representing propagation at speed v^* is shown in red.

slips occur at the spatial location of the holes and at the time when the holes reach their greatest depth. These locations correspond to the darkest points along the hole trajectory in a space-time plot of $|A(x,t)|$. The phase slips are not a surprise, since the leading edge dynamics for pulled fronts are set by the linearization about the unstable state and these may not generate in their wake a stable solution to the nonlinear problem. The eventual wave number that is deposited by the passage of the front is near q_N throughout the domain but modulated on a much larger length scale.

Turning now to pushed fronts, we compute the velocity of propagation for the BF instability around an arbitrary phase-winding state deposited in the wake of the front in Eq. (4.4). Although this analysis was carried out in [84], we generalize it and show that there are additional solutions to the marginal stability equations for type I instabilities that have not been previously reported. The details of this calculation are included in Appendix A. There are two broad instability regimes for pushed fronts depending on whether the far-field marginal wave number has a nonzero (type I) or zero (type II) real part.

We first discuss the case of instability to perturbations with a wave number of finite real-part at onset, type I. This case includes the parameter values $(a_1, a_2) = \left(\frac{5}{2}, 1\right)$ of the previous discussion but not near $\mu = 0$ where a pushed front is predicted. In order to find finite wave number instability near $\mu = 0$ we must choose parameters in the region $\Delta < 0$ and so select $(a_1, a_2) = \left(-2, \frac{1}{2}\right)$. The corresponding far-field rotating wave is unstable for

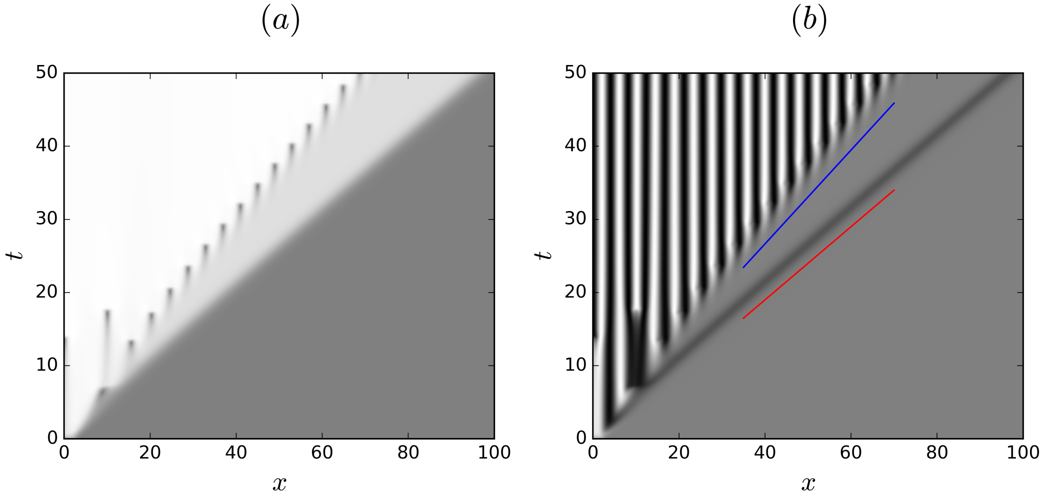

Figure 4.14: Space-time plot of the evolution of (a) $|A(x,t)|$ and (b) $\Re[A(x,t)]$ from Heaviside initial conditions in the stationary frame for $(a_1,a_2)=\left(\frac{5}{2},1\right)$ and $\mu=1$ computed using FD. The calculation is done on a domain $[-100,100]$ with Dirichlet boundary conditions on both $\Re[A]$ and $\Im[A]$ and only half of the simulation window is shown. The space and time discretizations are $\Delta x=0.1$ and $\Delta t=0.005$. In this regime after an initial transient the front is pulled, traveling at speed v^* and a secondary front separates from the leading edge traveling at a speed v_{BF}. Offset lines representing propagation at speeds v^* (red) and v_{BF} (blue) are also pictured.

$\mu\in(-0.1888,0.5184]$. An evolution plot for Heaviside initial data at $\mu=0$ is shown in Fig. 4.16 in a frame moving at speed v_N. The initial data are immediately unstable to a traveling wave which is advected leftwards relative to the primary front moving at speed v_N to the right. Simultaneously the leading edge of the front generates a distinct rotating wave with a wave number *exactly* equal to q_N as can be seen from Fig. 4.17 in which we plot the amplitude $\tilde{A}(\xi,t)$ that omits the wave number of the primary rotating wave (Appendix 4.7). The resulting secondary front between these two rotating waves is slower than the primary one indicating that the secondary front instability is convective in the frame moving at speed v_N and so separates from the leading edge. Our prediction for the secondary front speed, v_{BF}, can be checked by transitioning to a frame moving at that speed as shown in Fig. 4.17. Because the rotating wave in the wake of the primary front has not been restored in this plot the secondary front can be clearly distinguished. After a transient the secondary front is stationary in this frame and generates a rotating wave behind the primary one with a different wave number.

The case of instability with respect to perturbations with asymptotically zero wave number (type II) is realized when $(a_1,a_2)=(\frac{9}{2},5)$. The corresponding far-field rotating wave exhibits instability for $\mu\in[-0.0283,0.1087)$. When $\mu<0$ Heaviside initial data decay to $A=0$ but for $\mu>0$ a front subsists. A space-time plot is shown in Fig. 4.18. Initially

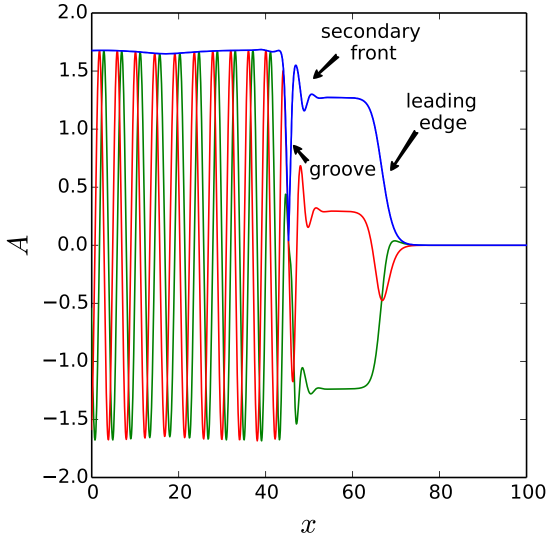

Figure 4.15: Solution $A(x, t = 35)$ computed from Heaviside initial conditions in the stationary frame using FD for $(a_1, a_2) = \left(\frac{5}{2}, 1\right)$ and $\mu = 1$, showing $\Re[A]$ (green), $\Im[A]$ (red) and $|A|$ (blue) on half of the computation domain. The discretization parameters are $\Delta x = 0.1$ and $\Delta t = 0.005$.

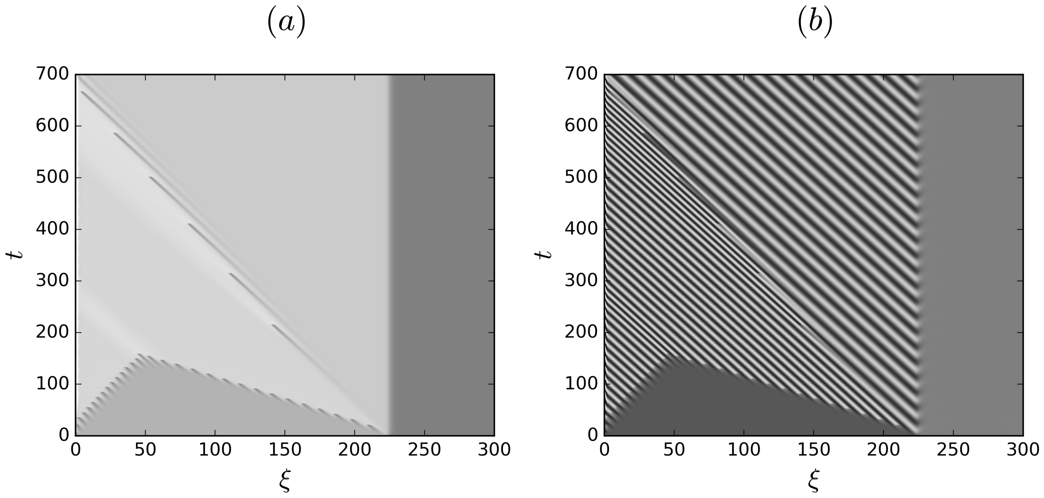

Figure 4.16: Space-time plot of the evolution of (a) $|A(\xi, t)|$ and (b) $\Re[A(\xi, t)]$ from Heaviside initial conditions in the moving frame for $(a_1, a_2) = \left(-2, \frac{5}{2}\right)$ and $\mu = 0$. The speed of the moving frame is v_N and the front is pushed. In this simulation we use time step $\Delta t = 0.01$, number of Fourier modes $N_x = 6144$, and cutoff $\epsilon = 10^{-10}$.

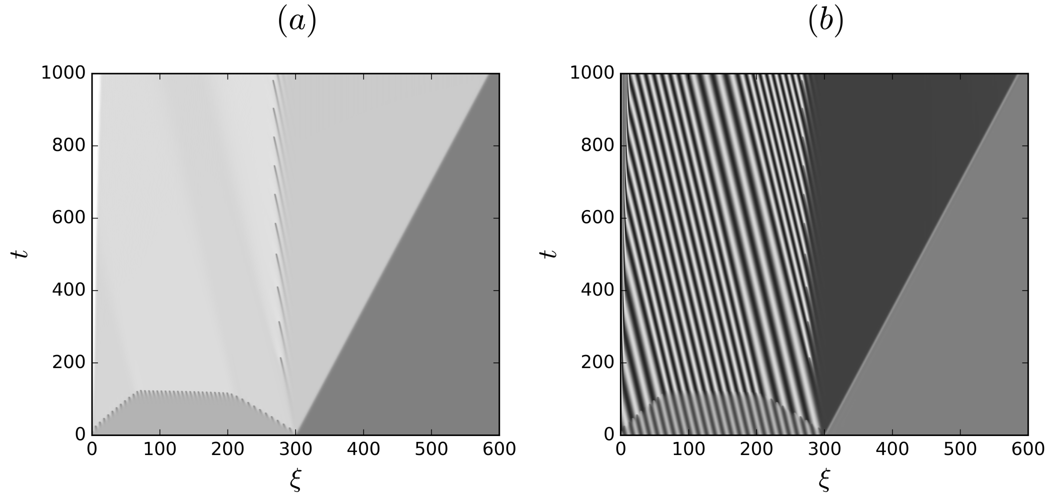

Figure 4.17: Space-time plot of the evolution of (a) $|\tilde{A}(\xi,t)|$ and (b) $\Re[\tilde{A}(\xi,t)]$ from Heaviside initial conditions in a frame moving at speed v_{BF} for $(a_1,a_2)=\left(-2,\frac{5}{2}\right)$ and $\mu=0$. In this simulation we use time step $\Delta t=0.005$, number of Fourier modes $N_x=6144$, and cutoff $\epsilon=10^{-10}$.

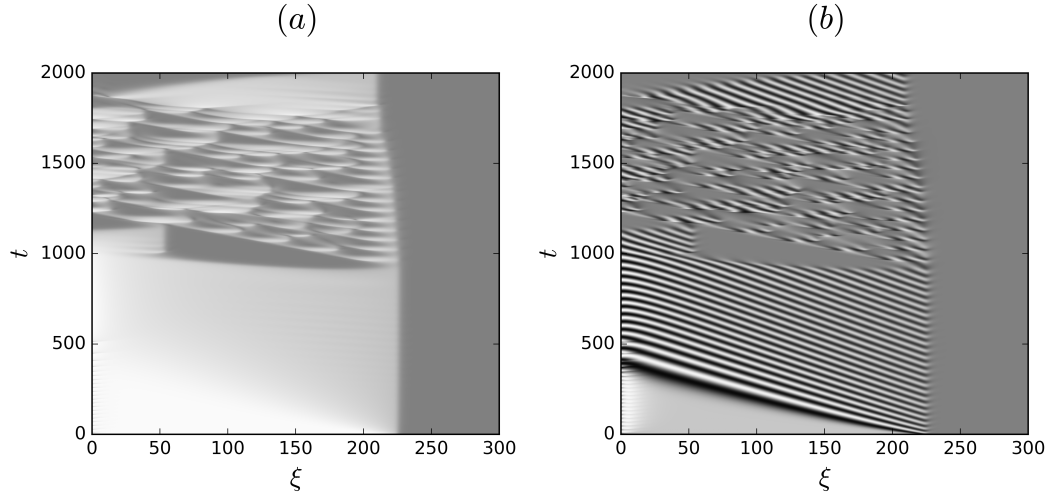

Figure 4.18: Space-time plot of the evolution of $A(\xi,t)$ from Heaviside initial conditions in the moving frame for $(a_1,a_2)=(\frac{9}{2},5)$ and $\mu=0.025$. The speed of the moving frame is v_N and the front is pushed. In this simulation we use time step $\Delta t=0.01$, number of Fourier modes $N_x=3072$, and cutoff $\epsilon=10^{-5}$.

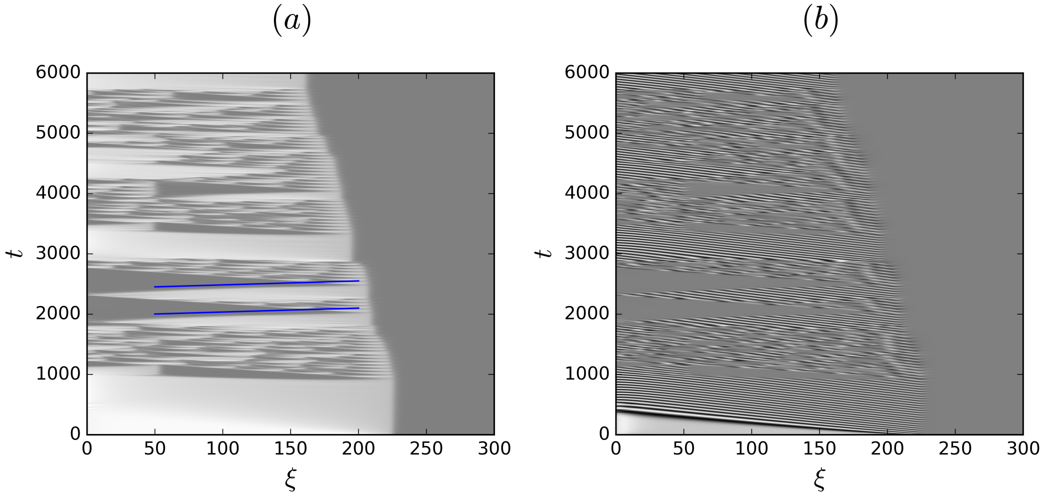

Figure 4.19: Continuation of the space-time plot in Fig. 4.18 over a longer time interval with an initial condition of different amplitude. Offset lines representing propagation at speed v_{BF} (blue) are also pictured.

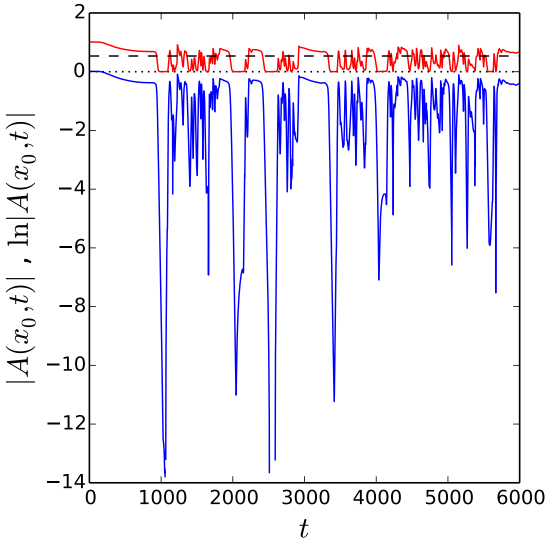

Figure 4.20: Time-series of $|A(\xi_0, t)|$ (red) and $\ln |A(\xi_0, t)|$ (blue) representing a vertical slice of the evolution shown in Fig. 4.19 at $\xi_0 = 100$. The amplitude $A = a_N$ is plotted with a thick dashed line (black) and $A = 0$ is also shown for reference.

a rotating wave born at the front interface invades the initial condition to the left, leaving an amplitude gradient across the structure. The invasion is largely complete by $t \approx 500$ and the resulting state persists over a long time scale, until $t \approx 1000$. At this point an amplitude perturbation grows to such an extent that it triggers an abrupt collapse of the structure. Since $\mu > 0$ the $A = 0$ solution is unstable, and the remnant of the front near the leading edge generates a sequence of traveling pulses that break-up into an interval of spatio-temporal chaos ($1000 \lesssim t \lesssim 1800$). Near $t \approx 1800$ the chaos abruptly subsides and most of the original front is restored. This state persists for a few hundred timesteps or so before it collapses again. The longer time series shown in Fig. 4.19 shows that this is part of a recurrent process with alternating coherent and incoherent episodes. The space-time plots demonstrate that the primary front travels at the predicted speed v_N when the deposited state is coherent but that the front is slightly delayed when the deposited state is incoherent. We cannot predict the front speed in these chaotic intervals. Figure 4.20 provides another perspective on the chaotic behavior shown in Fig. 4.19. The figure shows the time series $|A(\xi = 100, t)|$ and highlights the abrupt collapse episodes towards $|A| \approx 0$ that trigger the intervals of spatio-temporal chaos, before the system returns to coherence. It is noteworthy that even in the coherent phase the amplitude $|A|$ always initially overshoots the target amplitude a_N and thereafter decreases, ultimately triggering a collapse episode.

Since the secondary instability is of type II we can easily compute $v_{BF} \approx 1.878$ using the methods in [84]. This speed is much greater than both the frame speed $v_N \approx 0.3623$ and the linear spreading speed $v^* \approx 0.3162$ and so the secondary instability quickly catches up with the front. The speed v_{BF} is indicated in Fig. 4.19 as an offset blue line and shows good agreement with the observed speed at which large amplitude perturbations impact the front triggering the onset of incoherent front propagation. In contrast, the speed between the $A \approx 0$ amplitude holes behind the leading edge and the spatio-temporally chaotic state is also well defined but cannot be predicted with our methods. It is also worth noting that in the intervals of incoherent motion the leading edge of the front propagates neither at v_N nor v^*. If the episodic breakdown of the front exhibited in Fig. 4.19 persists for all time it would generate a counterexample to the nonlinear marginal stability conjecture of van Saarloos and Hohenberg that the front must in the long time limit propagate at the predicted speed, v_N [136].

We were unable to find parameter regimes for which $v_{BF} > v_N$ in the pushed front regime and the secondary instability was of type I. This would be an interesting case since it is not clear what would happen to the speed of the primary front. In the pushed case the front speed depends on a nonlinear mechanism and is affected by the rotating wave in the wake of the front. If an instability overtakes the front thereby changing it to one outside of the family described by the Ansatz would the speed change? The search for this situation is nontrivial because for every different choice of (a_1, a_2) one must recompute and invert the function $h(\mu)$ whose branches must in general be chosen by hand (Appendix A), evaluate v_{BF} on the appropriate elliptic curve and write v_N in terms of h on each branch. As a result it is not straightforward to scan parameter space.

4.6 Discussion

In this chapter we analyze in some considerable detail the properties of fronts connecting a stripe pattern to a spatially homogeneous state. For this purpose we use the generic amplitude equation describing a weakly subcritical bifurcation to the pattern state. For $\mu < 0$ (the subcritical regime) this equation exhibits bistability between the pattern and the homogeneous state implying that the speed of the front is determined by nonlinear processes. Fronts of this type are called *pushed* fronts. In contrast, in the supercritical regime ($\mu > 0$) the homogeneous state is unstable and the marginal stability criterion of Dee and Langer [52] then suggests that sufficiently localized initial conditions evolve into an invasion front whose speed is selected by linear processes. Such fronts are *pulled*.

To examine these predictions and the transition between them as the bifurcation parameter μ varies we construct a class of exact nonlinear front solutions with an explicit expression for the front speed. In the subcritical regime this speed vanishes at an analogue of a Maxwell point, corresponding to the presence of a heteroclinic connection between the stripe state and the homogeneous state. These exact solutions extend into the supercritical regime and the question arises therefore as to when the marginal stability criterion prevails. This question is addressed already in the work of van Saarloos [134] (see also [49]) but only for the special case when the coefficients (a_1, a_2) both vanish, and the system exhibits gradient dynamics. This early work highlighted the fact that pushed fronts, propagating at v_N, do indeed persist well into the supercritical regime and are dynamically selected by localized initial conditions. Our work extends this result to cases where (a_1, a_2) are nonzero and shows that (i) the linear stability mechanism does indeed prevail for sufficiently large μ and most values of (a_1, a_2), i.e., that for $0 < \mu \leq \mu^\ddagger(a_1, a_2)$ nonlinear speed selection does indeed take place while the speed is selected by linear processes only for $\mu > \mu^\ddagger(a_1, a_2)$, and that (ii) there exist parameters (a_1, a_2) for which $\mu^\ddagger(a_1, a_2) = 0$ and others for which $\mu^\ddagger(a_1, a_2) = \infty$. Examples of these degenerate cases are shown in Fig. 4.11(a),(b). In Appendix B we show that options (i) and (ii) are the only ones that can occur and obtain the conditions on (a_1, a_2) for the presence of the degeneracies mentioned above. These conditions are complicated, but can in principle be replotted in the (a_1, a_2) plane. In particular, we show that the speed selection inequalities do not allow the selection of a nonlinear front after the first transition from pushed to pulled ($\mu > \mu^\ddagger(a_1, a_2)$).

In fact, the details of the transition from pushed to pulled fronts are complex since the selection process depends on the steepness of the initial solution profile, and the stripe state deposited in the wake of the moving front may or may not be stable. We emphasize that the wave number of this state is selected dynamically and is not in general the equilibrium wave number k_c of the underlying pattern. As a result the deposited state is susceptible to secondary instabilities. These are of Benjamin-Feir type and may be convective or absolute in the frame of the front [146]. The former do not disrupt the stripe state since the growing perturbations are advected away from the front, but in the latter case the instability manifests itself in the vicinity of the front and may lead to its disruption. We have exhibited several examples where the front undergoes episodic complex time-dependence that we attribute to this process. Specifically, we have identified four distinct processes that bear on the wave number of the invading stripe state:

- The wave number becomes $k_c + \epsilon q_N$ if the front is pushed and the rotating wave with this wave number is stable,
- The wave number remains k_c when the front is pulled and $v_{BF} < v^*$, where v_{BF} corresponds to the secondary instability of the invading k_c state,
- We do not have an analytical prediction of the wave number if the front is pulled and $v_{BF} > v^*$ and the secondary instability interacts with the original k_c front, although it appears to remain near $k_c + \epsilon q_N$ despite the presence of phase slips,
- We do not have an analytical prediction of the wave number if the front is pushed and $v_{BF} > v_N$, where v_{BF} is now the speed of the secondary front generated by instability of the $k_c + \epsilon q_N$ front; in the example shown in Fig. 4.19 the intermittent dynamics of the front preclude the selection of an asymptotic wave number.

Our work provides a detailed discussion of the different regimes that may be encountered as one traverses the (a_1, a_2) parameter space. We believe that some of the conditions required for the applicability of the Ansatz are likely related to the conditions for well-posedness of the non-gradient system $a_2 \neq 0$. We have not, however, studied instabilities associated with unstable point eigenvalues in the spectrum of the front but note that these, if present, may lead to rich dynamics localized at the front. Evidently much remains to be learned about problems involving the invasion of one state by another, even in situations as simple as that studied here.

4.7 Numerical methods

Time-stepping simulations were carried out using two numerical approximation schemes as outlined in chapter 3. Depending on the initial data and the possible types of front propagation behavior the simulations are either performed in a frame at rest or in one moving at constant speed. In the moving frame the spatially extended front solutions typically have a nontrivial wave number $q_N \neq 0$ in the limit $\xi \to -\infty$. To overcome the difficulty of approximating the boundary condition for this state, we write $A(x,t) = \tilde{A}(\xi,t)e^{i(q_N\xi-\omega t)} = \tilde{A}(\xi,t)e^{iq_N x}$ and solve the following equation instead:

$$\tilde{A}_t = (\mu - q_N^2)\tilde{A} + (v + 2iq_N)\tilde{A}_\xi + \tilde{A}_{\xi\xi} + i\left(a_1|\tilde{A}|^2\tilde{A}_\xi + a_2\tilde{A}^2\bar{\tilde{A}}_\xi\right) + \left(1 + q_N(a_2 - a_1) - |\tilde{A}|^2\right)|\tilde{A}|^2\tilde{A}$$

subject to Neumann (Dirichlet) conditions on the real (imaginary) part of the solution at both boundaries. After an initial de-aliasing Heaviside initial conditions generate continuous initial data.

We also employ the finite difference (FD) method Eq. (3.5) using implicit Euler for the time discretization. The FD simulation is carried out in the stationary frame with Dirichlet boundary conditions imposed on both real and imaginary parts of the solution. We study the evolution of localized Heaviside initial data originating in the center of the domain.

When $\mu > 0$ the $A = 0$ state is unstable resulting in the amplification of any numerical instabilities that occur ahead of the front. Growth of such instabilities interferes with the propagation of the leading edge and renders a velocity measurement of the initial leading edge impossible. For the FD code this is not a problem since solution values initialized at 0 remain 0 until the leading edge reaches them. However, the Fourier scheme propagates small errors in each mode throughout the spatial domain and can nucleate instabilities ahead of the front. To prevent this we set $A(x) = 0$ for any x such that $|A(x)| < \epsilon$ at every time step. If ϵ is small enough this has the effect of quenching instabilities ahead of the front before they can grow but leaves the front at amplitude above ϵ intact. The required magnitude of ϵ depends on both the time-step and the value of μ and is chosen to be as large as feasible. Values of ϵ used here vary from 10^{-12} to $10^{-4.5}$. The smaller ϵ is, the smaller is its effect on the speed of the front. Because it quenches the instability of the leading state the speed of pulled fronts is reduced. This makes the computation of the front velocity difficult and typically produces a speed less than the analytical prediction. Consequently we use almost exclusively the FD method to measure front speeds.

In order to measure the speed of fronts numerically we select a fixed height h and calculate the trajectory, x_f, of the level set $|A(x_f)| = h$. After an initial transient the front reaches a constant velocity and we measure its speed $\dot{x}_f$ by a linear fit to $x_f(t)$. We keep h as small as possible to avoid behavior that occurs behind the leading edge. The prescription for computing the data in Figs. 4.10 and 4.11 is:

- Initialize Heaviside initial data of extent 50 at the center of the domain of length 300. Run a simulation with $\Delta x = 0.05$ and $\Delta t = (\Delta x)^2$.
- The simulation is run for time $T = \frac{100}{2\sqrt{v^*}\Delta t}$ and the location of the front is measured by the level set with $h = 0.01$. This allows the front to remain a distance > 50 away from the boundary throughout the experiment. For simulations near $\mu = 0$, where $v^* = 0$, the simulation time is taken to be in the range $[30000, 50000]$ such that a stable velocity is achieved and $h = 0.0001$.
- A line is fitted to the second half of the data $x_f(t)$ (i.e. $t > \frac{T}{2}$) to measure the front speed. This ensures that we discard the transient associated with the initial condition and measure the front speed only for a well-developed front.

It is pointed out in [63] that for an FD scheme an exact prediction of the errors in the linear spreading speed in terms of the FD discretization can be derived. Letting $A_m^n = \epsilon e^{\sigma_{FD}(n\Delta t) - iq_{FD}(m\Delta x)}$ in (3.5) and keeping lowest order terms in ϵ yields the FD dispersion relation $\sigma_{FD}(q_{FD})$ which solves the transcendental equation

$$\frac{1 - e^{-\sigma_{FD}\Delta t}}{\Delta t} = \mu - \left(\frac{2}{\Delta x}\sin\left(\frac{\Delta x q_{FD}}{2}\right)\right)^2 .$$

In the limit $\Delta x, \Delta t \ll 1$ we can apply the marginal stability criterion and determine that

$$\begin{aligned}
v^*_{FD} &= 2\sqrt{\mu} + 2\mu^{\frac{3}{2}}(\Delta t) + \frac{5\mu^{\frac{5}{2}}}{3}(\Delta t)^2 + \frac{\mu^{\frac{3}{2}}}{12}(\Delta x)^2 + \mathcal{O}(\Delta t, \Delta x)^3 , \\
q^*_{FD} &= i\left[\sqrt{\mu} - \mu^{\frac{3}{2}}(\Delta t) + \frac{5\mu^{5/2}}{6}(\Delta t)^2 - \frac{\mu^{3/2}}{8}(\Delta x)^2\right] + \mathcal{O}(\Delta t, \Delta x)^3 , \\
\sigma^*_{FD} &= 2\mu + \frac{4\mu^3}{3}(\Delta t)^2 - \frac{\mu^2}{6}(\Delta x)^2 + \mathcal{O}(\Delta t, \Delta x)^3 \qquad (4.10)
\end{aligned}$$

by solving linear algebraic problems order by order. Since Δx, Δt are assumed to be positive, the signs of the resulting corrections are determined. Here we assume that the errors do not cause the spreading wave number to become complex. We have not seen any evidence in our numerics that this should be the case and it greatly simplifies the calculation. Because the time integration uses a first order method the resulting velocity has an error of first order in Δt. However, since we impose the constraint that $\Delta t = (\Delta x)^2$ in every simulation the error is $\mathcal{O}((\Delta x)^2)$.

Assuming that the method for measuring the velocity from simulations is accurate and a pulled front occurs, then the measured front velocity is biased deterministically by the corrections in Eq. (4.10). We can interpret the analytically predicted corrections in two ways. We can either compare simulation results directly to v^*_{FD} and not v^* or we can subtract the deterministic correction $v^*_{FD} - v^*$ from the data and compare it to v^*. In this work we have chosen to plot the simulation data with an error bar showing the unbiased quantity because we do not have any result concerning the corrections to v_N due to FD (Figs. 4.10 and 4.11). The corrected value effectively *eliminates the discretization error* caused by the finite differences approximation but does not mitigate any other errors that could be introduced by the simulation parameters or implementation. A comparison of these corrections for simulations with varying discretizations Δx is shown in Fig. 4.21. Here the measured data are shown as circles and the corrected data as squares. The collapse of the data after corrections have been subtracted supports the robustness of the corrections in Eq. (4.10) and suggests that there is an additional slowing of the velocity below the expected v^* value. This slowing is almost certainly due to the imposed Dirichlet boundary conditions in the simulation which artificially pin the leading edge of the front. The effect of boundary conditions and finite domain size is studied in [63] and is known to lead to this type of slowing down.

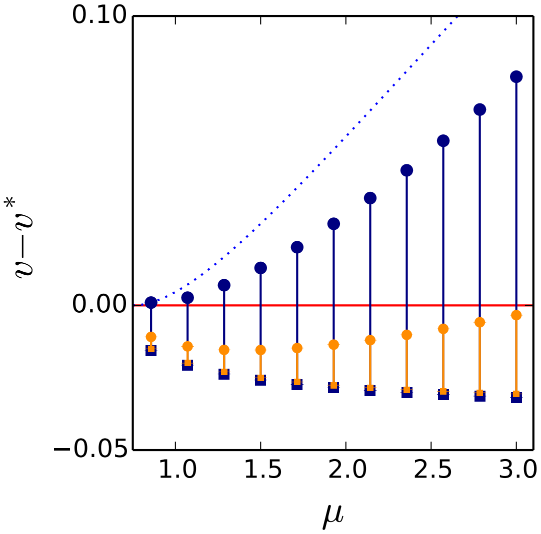

Figure 4.21: Front speed v_N (blue) relative to the linear spreading speed v^* (red) for parameters $(a_1, a_2) = (0, 0)$. The selected (not selected) speed is indicated by a solid (dashed) line according to Eq. (2.18). The navy ($\Delta x = 0.1$) and orange ($\Delta x = 0.05$) circles represent speeds calculated by time-stepping Heaviside initial conditions using FD in the stationary frame and tracking the motion of the front with $\Delta t = (\Delta x)^2$. The squares represent the values of the speeds after subtracting the corrections identified in Eq. (4.10).

Chapter 5

Forced Snaking

5.1 Introduction

Many natural systems form spatial patterns under stimulation by an external potential, or forcing, that is heterogeneous in space. One of the most successful approaches for studying such pattern formation has been by the use of model equations, most prominently the Swift-Hohenberg equation. In this work we shall concern ourselves with models such as SHE that are under the influence of weak, large scale, parametric periodic forcing. The evolution of a weakly subcritical pattern $A(x,t) = \epsilon A(X,T)e^{ikx} + c.c. + \ldots$ is then described by the envelope function $\epsilon A(X,T)$, where $X = \epsilon^2 x$ and $T = \epsilon^4 t$ and the small parameter ϵ is simultaneously a measure of the distance from the onset of pattern formation and of the subcriticality of the pattern. If the spatial forcing is on an ϵ^{-2} lengthscale then $A(X,T)$ satisfies Eq. (1.1) with $\mu = \mu(x)$ [86] where we use (x,t) in place of (X,T). The present chapter is concerned primarily with Eq. (1.1) in the simplest case, $a_1 = a_2 = 0$. We mention that the cubic GLE with $\mu = \mu(x)$ was derived and studied in [99].

When the pattern-forming instability is subcritical the SHE exhibits stationary localized states (LS) organized in a "snakes-and-ladders structure" within a snaking or pinning region [7, 10, 32, 34, 98]. The reduction of this equation to GLE, valid for $\epsilon \ll 1$, compresses this region into an exponentially thin interval in the vicinity of a codimension two point [32]. In a truncated system such as Eq. (1.1) with μ constant, stationary LS are found at a single value of the bifurcation parameter μ, corresponding to the formation of a heteroclinic cycle between the trivial state $A = 0$ and a nontrivial homogeneous state $A = A_0 \neq 0$. When $a_2 = 0$ this parameter value corresponds to the well-known Maxwell point at which the energies of $A = 0$ and $A = A_0$ coincide [84, 86]. We show here that the presence of spatial forcing, $\mu = \mu(x)$, restores classical homoclinic snaking, and discuss its similarities to and differences from the homoclinic snaking observed in SHE with homogeneous forcing. We do not study SHE with spatial forcing (but see [85, 149]).

Steady states of Eq. (1.1), $A(x,t) = u(x)$, satisfy a nonautonomous second-order complex-valued ODE,

$$0 = \mu(x)u + u_{xx} + ia_1|u|^2u_x + ia_2u^2\bar{u}_x + |u|^2u - |u|^4u$$

in contrast to SHE with homogeneous forcing, which is an autonomous fourth-order real-valued ODE. The LS in the latter are the result of pinning of fronts between a spatially homogeneous state and a spatially periodic state [98, 125]. This effect is absent from Eq. (1.1) when μ is constant. However, spatially periodic forcing turns $A_0 = u_0$ into a periodic state, thereby producing the conditions favoring pinning and hence the presence of LS. Experiments by Haudin et al. [75, 76] confirm this basic idea even though they employ both additive and multiplicative spatial forcing. We call the snaking that results *forced snaking.*

5.2 Localized states with homogeneous and inhomogeneous forcing

The bifurcation diagram for homogeneous forcing $\mu = m_0$ is shown in Fig. 5.1. The figure shows that the localized states (LS) bifurcate subcritically from the primary branch of constant amplitude states, u_0, and exhibit an abrupt increase in L^2 norm near the Maxwell point μ_M corresponding to monotonic growth in length. This growth ends when the structure comes close to filling the available domain and the LS branch terminates on the primary branch near its fold. In this region the LS resemble holes in an otherwise homogeneous state $u_0 \neq 0$. We examine here the effect on this structure of spatially periodic forcing of the form

$$\mu(x) = m_0 + m_1 \cos\left(\frac{2\pi x}{\ell}\right)$$

and consider two cases, $\ell = 10$ and $\ell = 50$. As shown below these two cases exhibit qualitatively different behavior. We do not discuss here the details of the transition between them.

All steady state solutions of Eq. (1.1) were computed using the numerical continuation software AUTO [56] with either Neumann or periodic boundary conditions. The localized states we compute are independent of the boundary conditions provided they remain well localized.

Periodic forcing with $\ell = 10$

When $m_1 \neq 0$, i.e., $\mu = \mu(x)$, the nontrivial homogeneous state u_0 becomes a periodic state with spatial period 10. Figure 5.2 shows the branch of periodic states for $m_1 = 0.1$. The associated LS bifurcate from this branch at small amplitude, undergo snaking in a well-defined interval of m_0 centered on μ_M, before terminating on the branch of periodic states near its fold. Since this process is absent when μ is constant we refer to the resulting behavior as *forced snaking.*

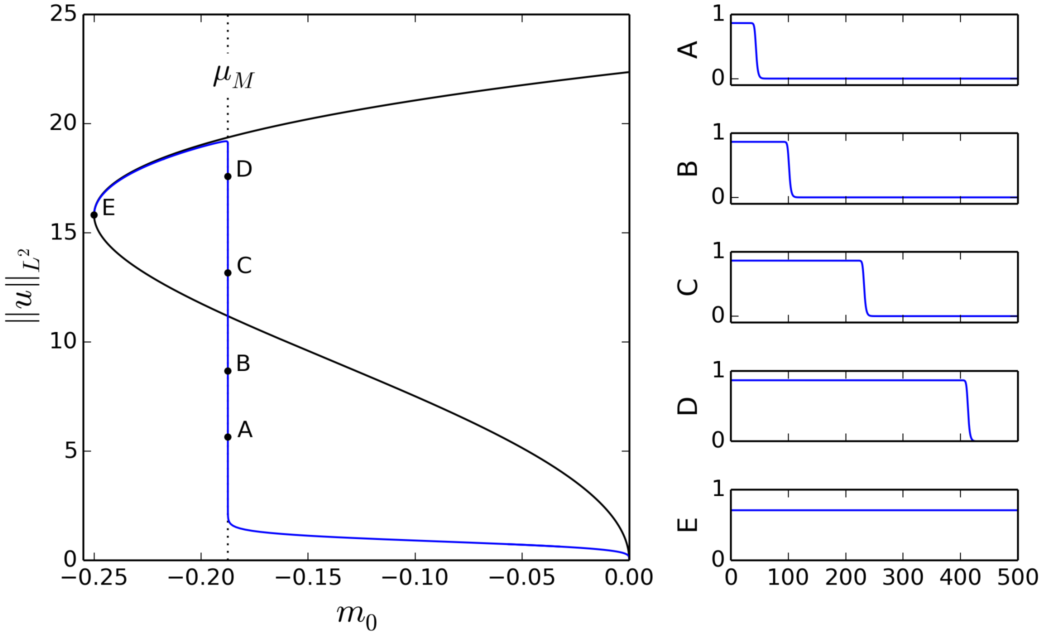

Figure 5.1: Bifurcation diagram showing homogeneous and localized states when $\mu = m_0$ is constant. Plots to the right show solutions $u(x)$ at the labeled points, computed on a half-domain with Neumann boundary conditions.

The LS shown in Fig. 5.2 consist of an odd number of peaks. The figure shows that each back and forth excursion across the snaking or pinning region results in the addition of one wavelength of the forcing on either side of the localized structure, thereby maintaining parity. Figure 5.3 shows that the snaking branch of Fig. 5.2 is one of a pair of intertwined LS branches shown in blue (even number of peaks) and red (odd number of peaks) and accompanied by a set of asymmetric “rung” states (green) that connect opposite folds on the two snaking branches. These exist between every pair of folds. Thus the resulting structure echoes the properties of standard homoclinic snaking such as that observed in SHE with homogeneous forcing [34, 98].

To explore the similarities to standard homoclinic snaking in greater detail we perform a linear stability analysis of the LS states on the branch of even LS between successive saddle nodes on the left as pictured in the schematic bifurcation diagram in Fig. 5.4 (top left). For this purpose we compute stationary solutions $u(x)$ homoclinic to $u = 0$ at evenly spaced points in arclength s and solve the nonautonomous linear problem. We make the Ansatz for perturbations around the base state $A(x,t) = u(x) + (a(x) + b(x))e^{\sigma t} + \left(\overline{a}(x) - \overline{b}(x)\right) e^{\bar{\sigma} t}$ which yields the linear problem,

$$\sigma \begin{pmatrix} a \\ b \end{pmatrix} = \begin{pmatrix} L_{11} & L_{12} \\ L_{21} & L_{22} \end{pmatrix} \begin{pmatrix} a \\ b \end{pmatrix} \equiv \mathcal{L}(u) \begin{pmatrix} a \\ b \end{pmatrix} \tag{5.1}$$

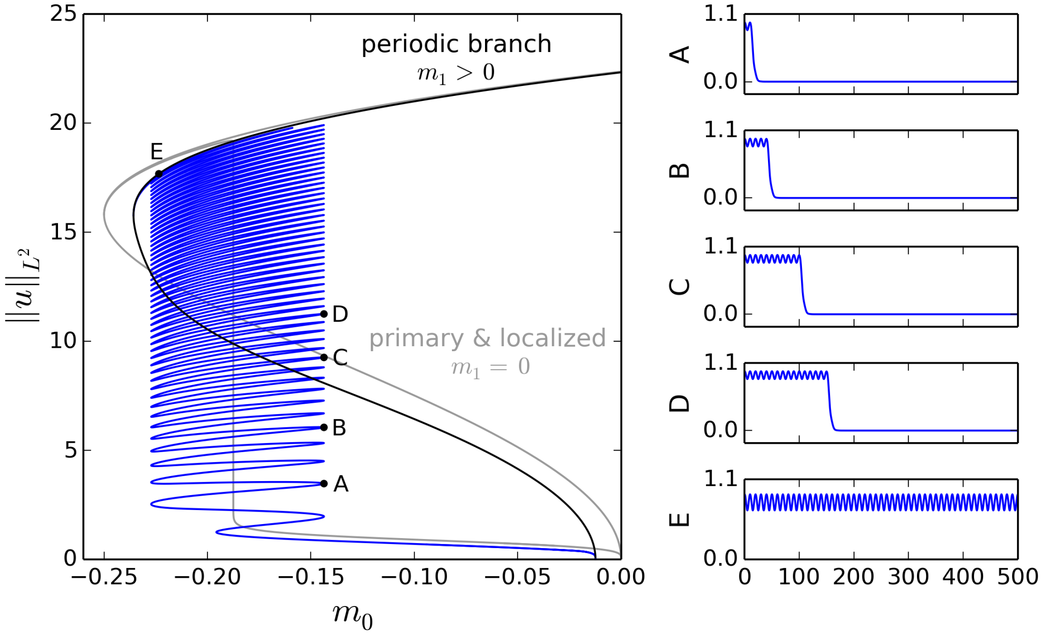

Figure 5.2: Bifurcation diagram showing periodic and localized states when $m_1 = 0.1$, $\ell = 10$ on a domain of size $L = 500$ with Neumann boundary conditions. The homogeneous and localized states for $m_1 = 0$ are shown in grey for comparison. Plots on the right show solutions $u(x)$ at the labeled points.

where

$$\begin{aligned}
L_{11} &= \partial_{xx} + \mu(x) - 3|u|^4 + |u|^2\left(2 - \bar{u}^2 - u^2\right) + \frac{\bar{u}^2 + u^2}{2} \\
&\quad + ia_2\left(u\bar{u}_x - \bar{u}u_x\right) + i\frac{a_1}{2}\left(\bar{u} + u\right)\left(u_x - \bar{u}_x\right) + i\frac{a_2}{2}\left(u^2 - \bar{u}^2\right)\partial_x \\
L_{12} &= \frac{1}{2}\left(u - \bar{u}\right)\left(\bar{u} + u\right)\left(2u\bar{u} - 1\right) + ia_2\left(\bar{u}u_x + u\bar{u}_x\right) - i\frac{a_1}{2}\left(u - \bar{u}\right)\left(u_x - \bar{u}_x\right) \\
&\quad + i\left[a_1|u|^2 - \frac{a_2}{2}\left(\bar{u}^2 + u^2\right)\right]\partial_x \\
L_{21} &= -\frac{1}{2}\left(u - \bar{u}\right)\left(\bar{u} + u\right)\left(2u\bar{u} - 1\right) + ia_2\left(\bar{u}u_x + u\bar{u}_x\right) + i\frac{a_1}{2}\left(\bar{u} + u\right)\left(\bar{u}_x + u_x\right) \\
&\quad + i\left[a_1|u|^2 + \frac{a_2}{2}\left(\bar{u}^2 + u^2\right)\right]\partial_x \\
L_{22} &= \partial_{xx} + \mu(x) - 3|u|^4 + |u|^2\left(2 + u^2 + \bar{u}^2\right) + \frac{\bar{u}^2 - u^2}{2} \\
&\quad + ia_2\left(u\bar{u}_x - \bar{u}u_x\right) - i\frac{a_1}{2}\left(u - \bar{u}\right)\left(\bar{u}_x + u_x\right) + i\frac{a_2}{2}\left(\bar{u}^2 - u^2\right)\partial_x.
\end{aligned}$$

When $a_2 = 0$ then $\mathcal{L}(u)$ is self-adjoint and therefore has a real spectrum. In this case solutions take the form $f(x)e^{\sigma t}$ in which f may be complex-valued but $\sigma \in \mathbb{R}$. Figure 5.4

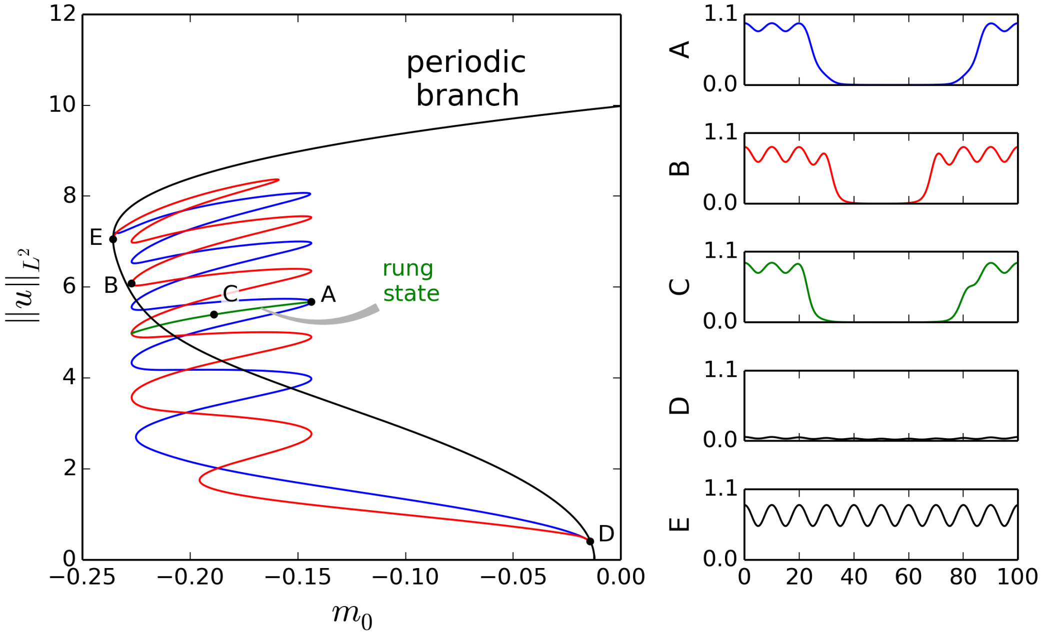

Figure 5.3: Bifurcation diagram showing periodic and localized states when $m_1 = 0.1$, $\ell = 10$ on a periodic domain of size $L = 100$. The two snaking branches shown are characterized by the number of peaks: even (blue) and odd (red). Connecting each pair of folds is a branch of asymmetric rung states (green) only one of which is shown. The snaking branches bifurcate together from (and reconnect together to) a domain-filling periodic state. Plots on the right show solutions $u(x)$ at the labeled points, shown over the full domain $0 \leq x \leq 100$.

shows the six most positive eigenvalues σ of $u(x)$ as a function of s; the vertical dashed lines indicate the locations of the saddle nodes. The eigenfunctions corresponding to the five largest eigenvalues at the locations indicated in solid grey lines are shown in the top right panels in order of decreasing eigenvalue.

The results show that branch segments slanting up from left to right are stable while those slanting up from right to left are unstable as in standard homoclinic snaking. Moreover at each saddle node the number of unstable eigenvalues changes by two, one with an even eigenfunction and one with an odd eigenfunction; latter is responsible for the presence of the asymmetric rung states that bifurcate from the branch of LS. We note that this is unlike the behavior in the SHE where the odd eigenvalue bifurcates on the unstable branch away from the fold and thus only a single mode bifurcates through the fold. In this case both modes are localized at the fronts bounding the LS. In addition, there is (an extended) neutrally stable phase mode iu along the entire snaking branch, corresponding to invariance with respect to the symmetry $\{u \to e^{i\alpha}u \,|\, \alpha \in \mathbb{R}\}$. This mode corresponds, respectively, to the first and third eigenfunctions at locations A and B. This symmetry is inherited from invariance of SHE with respect to small scale translations; translation invariance on large scales is broken

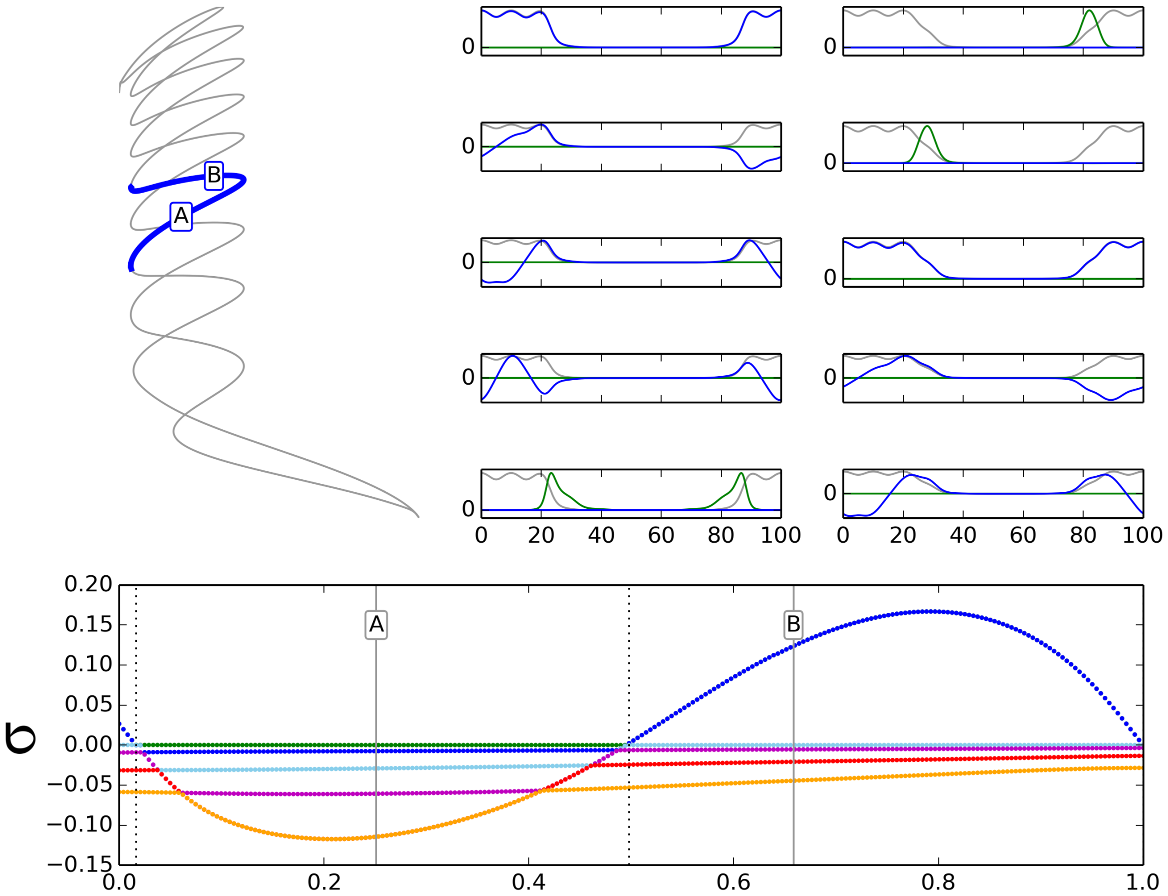

Figure 5.4: The real (green) and imaginary (blue) parts of the eigenfunctions $f(x)$ corresponding in order to the five largest eigenvalues σ (largest first) at locations marked by the letters A (top center) and B (top right) along with $u(x)$ shown in grey. The bottom plot shows the six largest eigenvalues σ for LS between successive left saddle nodes indicated by the thick blue trace in the schematic snaking diagram (top left); the nonmonotonic eigenvalue has multiplicity two. The two top eigenfunctions at B can be combined into even and odd eigenfunctions. Parameters are $m_1 = 0.1$, $\ell = 10$.

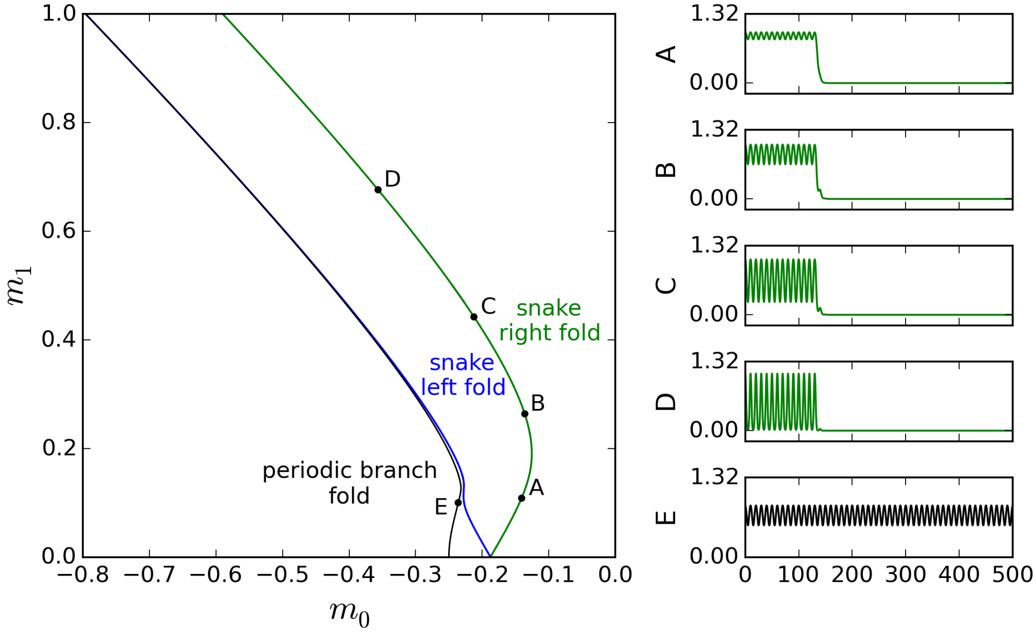

Figure 5.5: The width of the region of forced snaking when $\ell = 10$. The blue and green traces show the continuation of the left and right folds on the snaking branch, respectively. The black trace is the continuation of the fold on the primary branch. Plots on the right show solutions $u(x)$ at the labeled points.

by the forcing. Consequently the usual Goldstone mode is absent.

Despite the commonalities between forced and standard snaking there are significant differences. In forced snaking the width of the snaking region grows linearly with the amplitude of the forcing, in contrast to classical snaking in which the snaking region is initially exponentially thin. This behavior hearkens to the linear theory of Arnold tongues, here corresponding to the 1:1 spatial resonance. Figure 5.5 shows the corresponding behavior in the present case. The figure shows the left (blue curve) and right (green curve) folds high up the snaking branch in the (m_0, m_1) plane; forced snaking occurs in between. The figure shows that the left folds asymptotically approach (but do not reach) the fold on the branch of periodic states (black curve) and that the behavior of the loci of the folds near $m_1 = 0$ is linear, $m_0 \propto m_1$.

Inclusion of a_1 and a_2

When (a_1, a_2) are nonzero the snaking structure of localized states is preserved though the pinning region changes. We first consider the effects of including a_1 alone which does not break the gradient structure of the equation. As a_1 is increased from zero the snaking solutions of Eq. (1.1) are no longer real-valued. In particular, the solutions acquire an

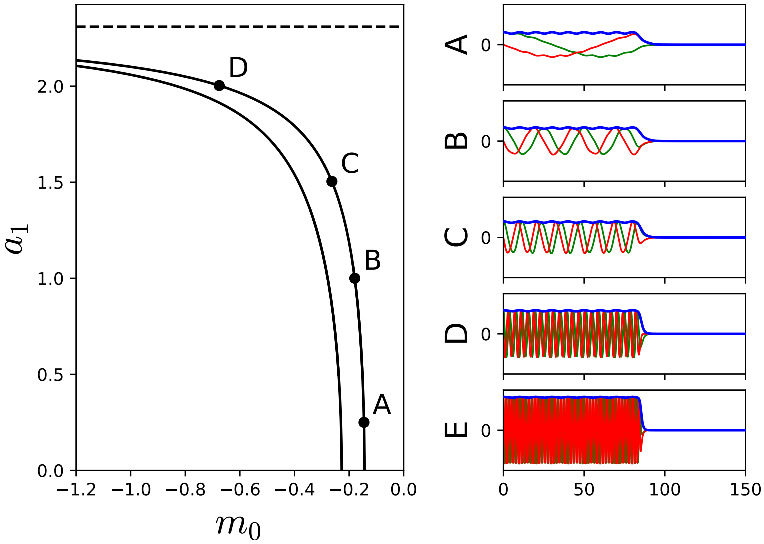

Figure 5.6: The width of the region of forced snaking for $\ell = 10$ and $m_1 = 0.1$ is delimited with solid black lines. The dashed line $a_1 = \frac{4}{\sqrt{3}}$ beyond which the homogeneous problem is not well-posed is shown for reference. Plots on the right show solutions $u(x)$ at the labeled points. As a_1 increases the phase wave number of the solutions increases as it does in the fronts of chapter 4.

approximately uniform phase gradient which we refer to as a phase wave number. An example of such solutions is shown in Fig. 5.6. This figure depicts the boundaries of the pinning region as a_1 is increased from zero and shows that the snaking is preserved but the pinning region occurs at different m_0 values. In addition the wave number of the snaking states grows larger with a_1 which is consistent with the behavior of the exact front solutions to Eq. (1.1) derived in chapter 4. As a_1 grows large the size of the pinning region expands and the folds on the snaking branch appear to approach the bound $a_1 = \frac{4}{\sqrt{3}}$ for well-posedness of the homogeneous problem. This prevents the computation of any snaking solutions beyond this bound via parameter continuation.

This type of analysis can also be carried out with the parameter a_2. Snaking solutions for increasing a_2 are depicted in Fig. 5.7. In each subplot we depict the boundaries of the pinning region in the (m_0, a_2) plane and fix either a_1 (a) or m_1 (b). In subplot (a) we set $a_1 = 0$ and only focus on a_2. As expected the pinning region widens as m_1 is increased and the curve $m_1 = 0$ corresponds to the generalized Maxwell point given by $v_N(m_0) = 0$ of the branch of exact front solutions derived in chapter 4. This behavior also occurs for $a_2 = 0$ and $a_1 < \frac{4}{\sqrt{3}}$ when m_1 increases from zero (not shown). On the other hand unlike the previous case, $a_2 = 0$ and $a_1 > 0$, the pinning region here shrinks as a_2 is increased and moves asymptotically close to $m_0 = 0$. In Fig. 5.7(b) the parameter $m_1 = 0.1$ is fixed and the pinning region boundaries are drawn for $a_1 = 0, 1$ and 5. When a_1 is included the

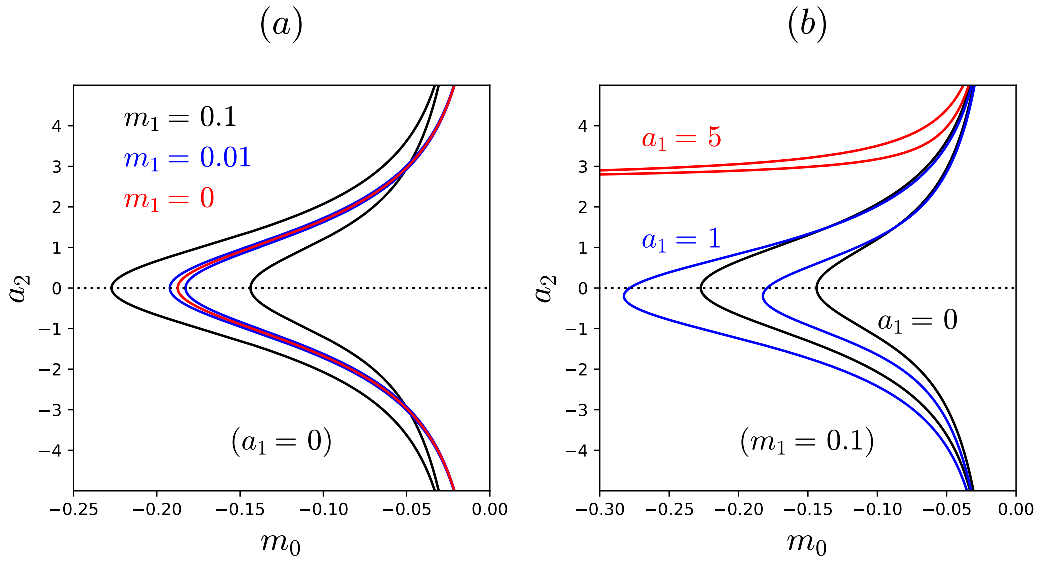

Figure 5.7: The width of the region in the (m_0, a_2) plane of forced snaking for $\ell = 10$. (a) Here $a_1 = 0$ and the region width is plotted for $m_1 = 0$ (red), 0.01 (blue), 0.1 (black). (b) Here $m_1 = 0.1$ and the region width is plotted for $a_1 = 0$ (black), 1 (blue), 5 (red).

main effect is to shift the pinning region in the (m_0, a_2) plane so that it is not symmetric under $a_2 \to -a_2$. In addition, with $a_2 \neq 0$ it is possible to access parameter regimes in which $a_1 > \frac{4}{\sqrt{3}}$ through continuation, the case $a_1 = 5$ is shown here. Interestingly these solutions appear to be trapped away from $a_2 = 0$. For the homogeneous problem the known sufficient condition for well-posedness of Eq. (1.1) when $a_1 = 5$ is $3 < a_2 < 7$. As shown the continuation is carried out past this point and it is not known whether the initial value problem is well-posed in this regime despite the existence of these ODE solutions. As shown in chapter 4 this need not be the case and there are likely many families of stationary solutions in poorly posed parameter regimes. Although there are no known conditions for well-posedness of Eq. (1.1) when μ is spatially periodic the conditions for the homogeneous problem are a are reference point.

We next turn to the linear stability of snaking solutions when a_1 and a_2 are nonzero. When $a_1 > 0$ and $a_2 = 0$ the linear stability properties of the snaking states are largely unchanged. The linear operator in Eq. (5.1) remains self-adjoint and has a real spectrum. The snaking branches destabilize and restabilize in the same fashion as in the $a_1 = 0$ case where a pair of eigenvalues oscillates through $\sigma = 0$ changing stability at folds. The associated eigenfunctions are localized at the fronts bounding the localized state. This similarity to the $a_1 = 0$ case is expected since the new term in Eq. (1.1) does not break any symmetries of the problem.

In contrast to the previous behavior inclusion of $a_2 \neq 0$ breaks the gradient structure of the system and renders the linear stability operator non self-adjoint. Breaking the gradient structure of the system opens a pathway for oscillations and Hopf bifurcations to occur and has been studied in the case of homoclinic snaking in the SHE [31]. For concreteness we study one specific case here, $a_1 = 0$ and $a_2 = 1$. In this case we find that the stability structure is similar to previous cases at the right folds of the snaking branches but not at those on the left. Specifically, at the right fold on a branch of snaking states two real eigenvalues cross the imaginary axis simultaneously destabilizing the branch. These eigenfunctions are localized at the two fronts bounding the localized state as in previous cases. In contrast, near the left fold an additional pair of real eigenvalues cross the imaginary axis. This is portrayed in Fig. 5.8 where the arclength value associated to the fold is marked with a vertical dashed line. The eigenfunctions associated to this crossing are shown in Fig. 5.9 where the third eigenmode is the neural phase rotation, iu. For a short distance beyond the fold the branch remains unstable with four unstable modes. Then the modes combine in pairs to form doublets with $\sigma = \sigma_r \pm i\sigma_i$ and eventually re-stabilize generating a pair of Hopf bifurcations. These bifurcation points give rise to branches of time-dependent localized states which we do not attempt to compute here. We remark further that in the SHE with nongradient terms [31] only one pair of complex eigenvalues is present and thus only one Hopf bifurcation is expected. Here the case is different because every eigenmode destabilization caused by the bifurcation of a symmetric eigenmode is accompanied by the asymmetric one. Then unstable modes with the same parities are combined into pairs of complex eigenvalues. Thus there are four unstable modes (two Hopf bifurcations) rather than two (one Hopf bifurcation).

Periodic forcing with $\ell = 50$

We now repeat the previous analysis with $\ell = 50$, i.e., with forcing on a substantially larger scale. In this regime we also observe forced snaking but the snaking structure is destroyed for large enough m_1. This destruction occurs via the interaction of the snaking states with nearby periodic states consisting of an array of strongly localized pulses centered in regions where the cosine forcing is positive, $\{x \mid \cos\left(\frac{2\pi x}{\ell}\right) > 0\}$. Much like particle wavefunctions in quantum mechanics, these states either have or do not have a pulse at each "location." This behavior becomes possible when the characteristic lengthscale of the front is smaller than the forcing lengthscale so that a complete localized pulse can fit on each positive lobe of the forcing. As a result these states interact only weakly and no longer snake.

Snaking and breakup for small m_1

For small m_1 the forced snaking observed with $\ell = 50$ shares many characteristics with that observed for $\ell = 10$. In particular, as m_1 increases a snaking branch opens with finite angle around the Maxwell point of the homogeneously forced system (Fig. 5.10(a)). Figure 5.10(b) shows that for small m_1 these snaking branches bifurcate from and reconnect to a periodic state that fills the domain. This state (not shown) is readily obtained by continuing the extended states in the parameter m_1; during this process the wavelength of this state remains equal to the forcing wavelength but the state develops hysteresis. As a result the

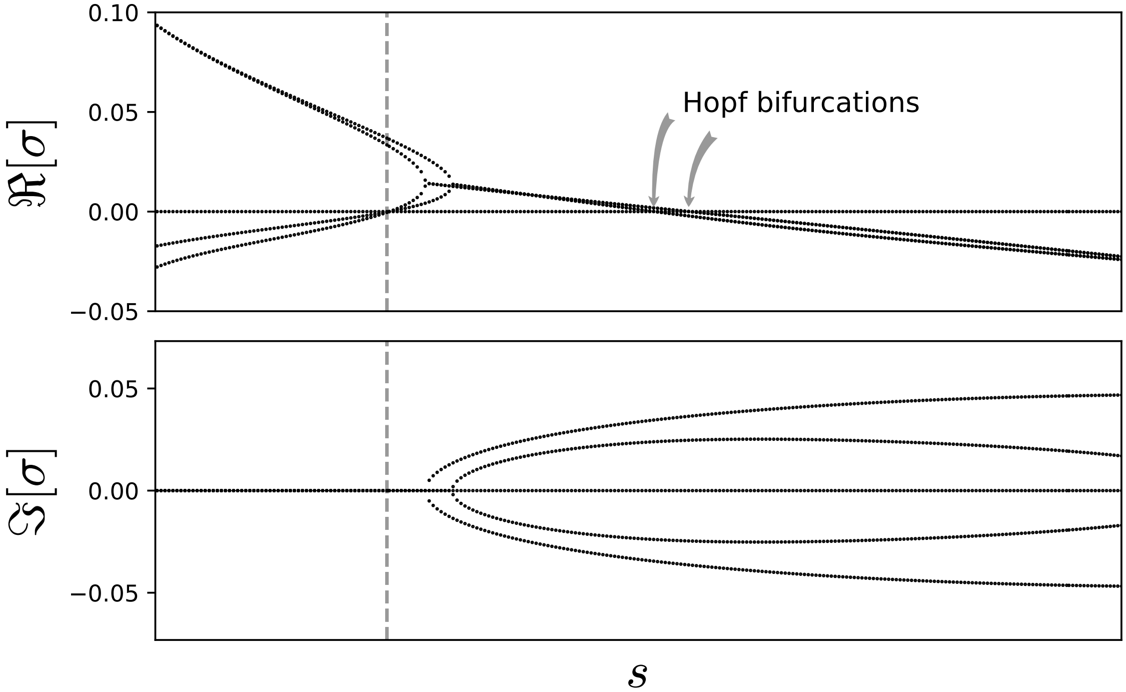

Figure 5.8: The top five stability eigenvalues σ are plotted as a function of arclength, s, near the left fold of the snaking branch when $m_1 = 0.1$, $\ell = 10$ and $(a_1, a_2) = (0, 1)$. The arclength value associated with the fold in the branch is marked by a vertical grey dashed line and correspond to a pair of additional eigenvalues becoming unstable. The eigenfunctions at this fold are plotted in Fig. 5.9. Beyond the fold four unstable eigenvalues recombine into pairs of doublets ($\sigma = \sigma_r \pm i\sigma_i$) and then stabilize in a pair of consecutive Hopf bifurcations (pictured).

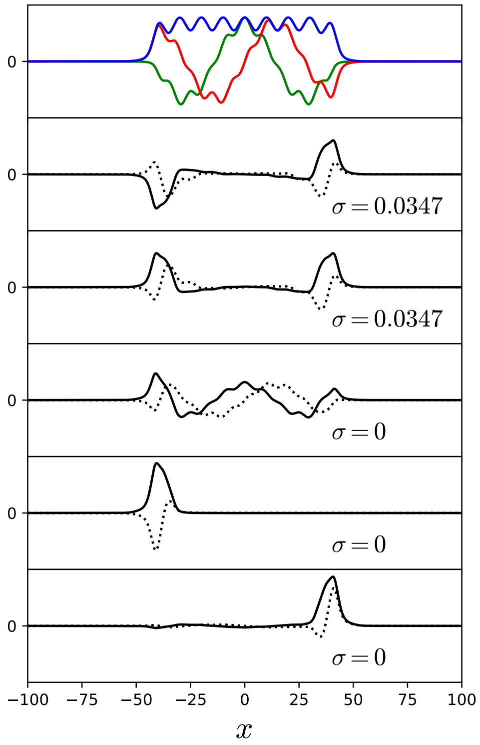

Figure 5.9: Eigenfunctions at a left fold on the snaking branch when $m_1 = 0.1$, $\ell = 10$ and $(a_1, a_2) = (0, 1)$. The top plot shows the base state at the fold where $|u|$ (blue), $\Re[u]$ (green), $\Im[u]$ (red) and the plots below show eigenfunctions in order of decreasing $\Re[\sigma]$. At this fold the five largest eigenvalues are real and thus the eigenfunctions take the form $u_1 = u_{1r} + iu_{1i}$. We plot u_{1r} with a solid line and u_{1i} with a dotted one.

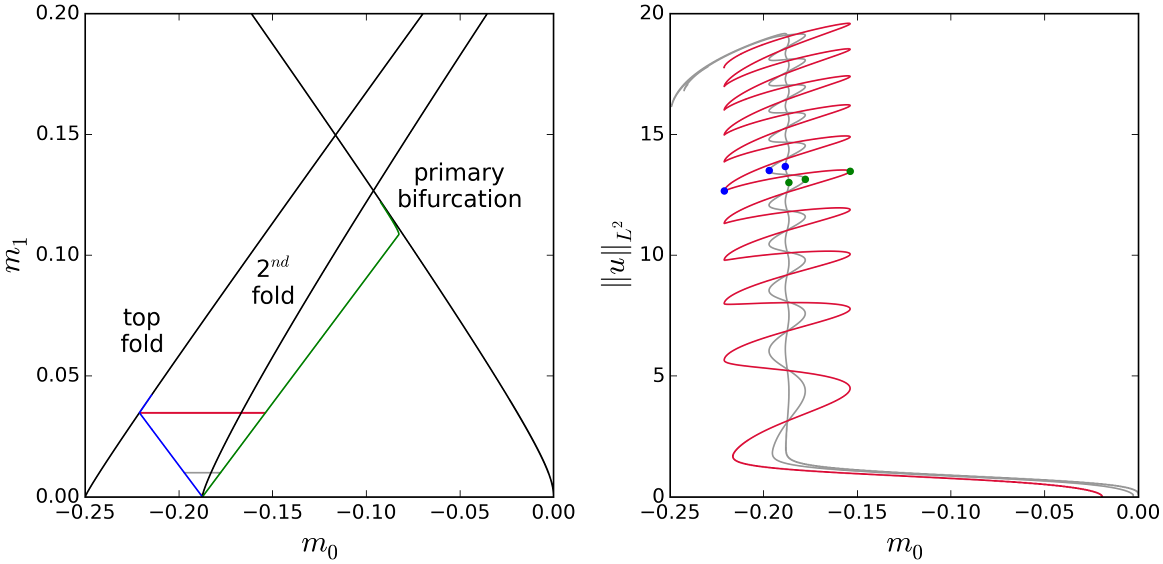

Figure 5.10: (a) The boundaries of the snaking region (blue & green lines) when $\ell = 50$. The loci of the primary bifurcation from $u = 0$ and of the top left and right folds of the primary periodic state are shown in black. In this region the primary periodic states exhibit tristability (not shown). (b) Bifurcation diagram for $m_1 = 0.001, 0.01, 0.035$ showing LS branches on a domain of size $L = 500$ with Neumann boundary conditions. The snaking branches were continued from the saddle nodes marked with dots and their widths are indicated in (a) using horizontal lines and corresponding colors.

snaking region overlaps the region of tristability of the periodic state (Fig. 5.10(a)) and as the snaking interval broadens with increasing m_1 the left folds of the snake collide with the top left fold of the periodic state (this occurs at $m_1 \approx 0.035$, Fig. 5.10(a)) leading to the destruction of the snake as shown in Fig. 5.11.

Foliated snaking in the tristable regime

As m_1 increases beyond breakup and m_0 is appropriately reduced the holes between adjacent peaks deepen towards the trivial state $u = 0$ and the periodic states begin to resemble an array of isolated pulses. We refer to such solutions as *pulse trains* (PT). Figure 5.12 shows that for $m_1 = 0.1$ the pulse trains below the bottom left fold take the form of a periodic array of *spikes* while those above the fold resemble a periodic array of *lumps*. This dichotomy is reflected in the spatially mixed pulse trains that bifurcate from this fold as indicated in the solution profiles at the right of Fig. 5.12. The pulse trains emerging from the fold possess either a lump or spike at each location of a maximum in the cosine forcing. As a result there are 2^N distinct domain-filling states of this type where N is the number of such maxima in the domain. Since the norm of a state with n lumps and $N - n$ spikes does not change when

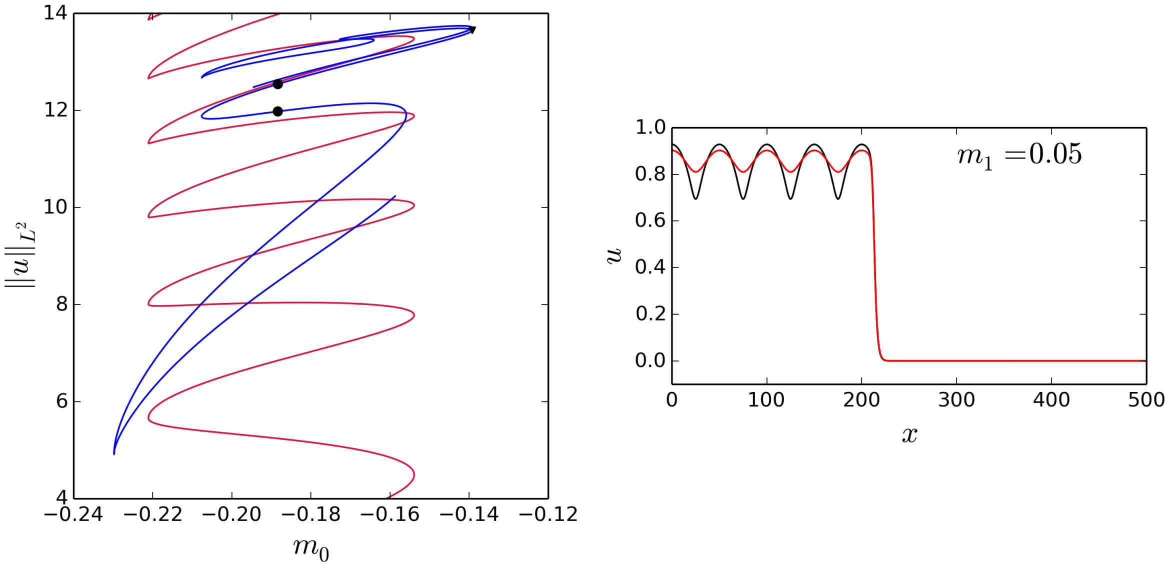

Figure 5.11: (a) Bifurcation diagrams for $m_1 = 0.035$ (red) and $m_1 = 0.05$ (blue) when $\ell = 50$. (b) Solution profiles for $m_0 \approx -0.188$ and $m_1 = 0.05$ with the red (black) profiles corresponding to the upper (lower) black dots in (a). Owing to its complexity the blue curve in (a) was terminated after a finite arclength.

these are reordered we only show one example for each pair $(n, N-n)$ (blue curves).

Far from the fold, the mixed PT enter the tristability region and interact with other periodic states. The alignment of the corresponding folds suggests that these correspond to tangencies between appropriate stable and unstable manifolds. Those on the left involve the upper periodic state whose peaks are no longer isolated, those in the center appear to involve periodic states with a smaller wavelength likely originating in a different spatial resonance, while those on the right correspond to the right boundary of the snaking structure before the collision with the fold. To avoid clutter these branches have been terminated after a finite arclength (blue curves).

Figures 5.13 and 5.14 provide a more detailed look at the structure in this region, and reveal the presence of a series of branches of *finite pulse trains* (FPT). These are connected via pulse-adding bifurcations in which solutions consisting of n pulses add two additional pulses in the tristability region, one on either side, that enable the solution to connect to a branch of $n+2$ pulses. Since this process preserves the parity of the pulse train there is a separate series of such states for odd and even numbers of pulses. Of course, when the domain size prevents further pulse-adding bifurcations this process stops and the FPT branches with $n = 8$ and $n = 9$ both terminate close to the fold of the domain-filling state with 10 pulses in the domain.

We understand this behavior as follows. The pulses in an n-pulse state at the left are essentially noninteracting (they are trapped by the forcing potential); as a result a finite pulse

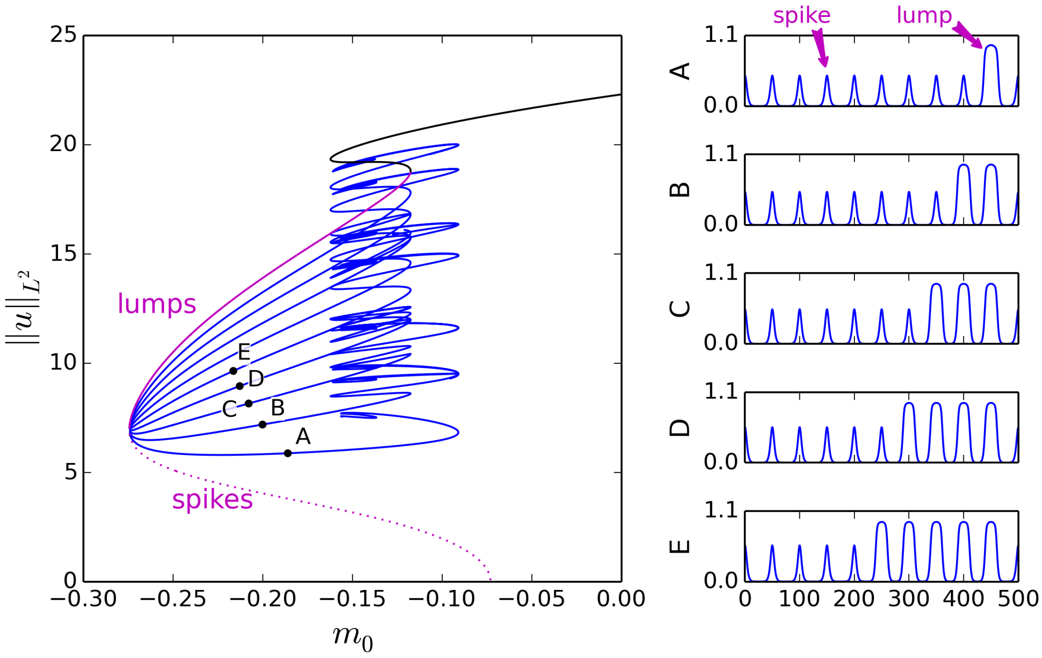

Figure 5.12: Bifurcation diagram for $m_1 = 0.1$ when $\ell = 50$ showing periodic PT (in magenta and black) consisting of lumps (stable, above lower left fold) and spikes (unstable, below lower left fold), as well as 9 branches of spatially mixed PT (blue) that bifurcate from this fold. These consist of n lumps and $10 - n$ spikes, where $n = 1, 2, \ldots 9$. Solution profiles, $u(x)$, corresponding to the labeled points are shown on the right.

train cannot grow via snaking. Instead, the pulse train enters an interval in m_0 where the pulses interact more strongly and the state takes the form of a LS with n peaks. In this region the pulse train is able to snake, and thereby grow in length. Once a pair of pulses is added, one on either side, the solution moves out of the region of strong interaction, generating a state with $n + 2$ noninteracting pulses. Figure 5.15 shows details of this mechanism for $n = 2$. Based on the connectivity of the corresponding FPT branches we call this bifurcation structure *foliated snaking*.

For larger m_1, e.g., $m_1 = 1$, the two upper folds on the branch of periodic states move to the right of the primary bifurcation thereby destroying the region of tristability and subsequently annihilate. In this case the mixed PT emerging from the spike-lump fold continue all the way to the right edge of the bistability region (blue curves in Fig. 5.16(a)). As in the $m_1 = 0.1$ case these states have either a spike or lump at each forcing maximum and we only compute states with adjacent lumps. As these mixed PT are continued to the right the amplitude of the lumps (spikes) grows (decreases); at the right boundary of the bistability region the spikes vanish and the mixed PT states merge with the FPT emerging from the primary bifurcation to periodic states (red curves in Fig. 5.16(a)). The fact that

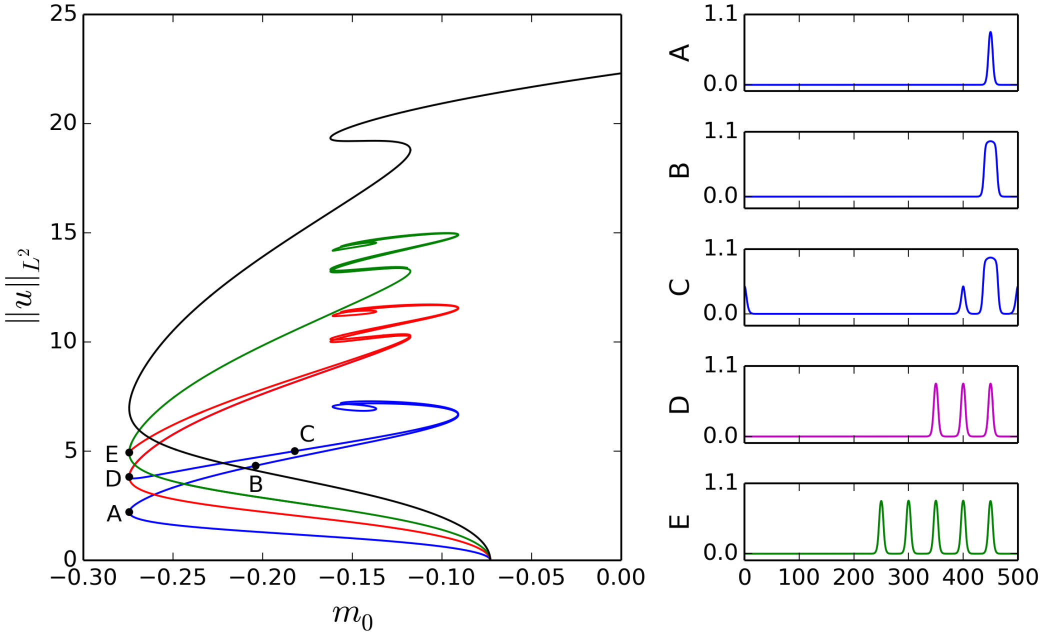

Figure 5.13: Bifurcation diagram for $m_1 = 0.1$ when $\ell = 50$ showing branches of FPT based on one spike (blue), three spikes (red) and five spikes (green). The periodic branch is shown in black. Sample solutions at locations indicated by corresponding letters are shown on the right. The solution corresponding to the connection between the blue and red LS branches is colored magenta. The branches interconnect at the left folds. Mixed PT branches are omitted.

these mergers occur in cusps provides evidence that each state is made up of independent "particles." To see this, suppose that a single lump state at $x = X$ can be written $u_l\chi(x-X)$, in which χ vanishes whenever $|x - X| > C$, and a spike state at $x = Y$ can be written $u_s\chi(x - Y)$. Then we can write the state representing a 1 lump, 2 spike FPT (blue curve in Fig. 5.16(b)) as $u_l\chi(x-X)+u_s\sum_m \chi(x-Y_m)$ and the state representing a single lump (red curve in Fig. 5.16(b)) $u_l\chi(x - X)$. If the "particles" do not interact, i.e., $|X - Y_m| \geq 2C$ (which appears to be true in the numerics), then these states have norms proportional to $\sqrt{u_l^2 + 2u_s^2}$ and $\sqrt{u_l^2}$, respectively. As m_0 increases towards the primary bifurcation, m_c, these converge to the same norm; moreover, since $u_s \to 0$ linearly in $m_c - m_0$ the branches meet at an angle. Figure 5.16(b) shows that for these values of m_1 these cusps are also the termination points of the mixed FPT originating at the left folds of the FPT branches, i.e., the foliated snaking structure now collides with the primary bifurcation at $m_0 \approx -0.913$.

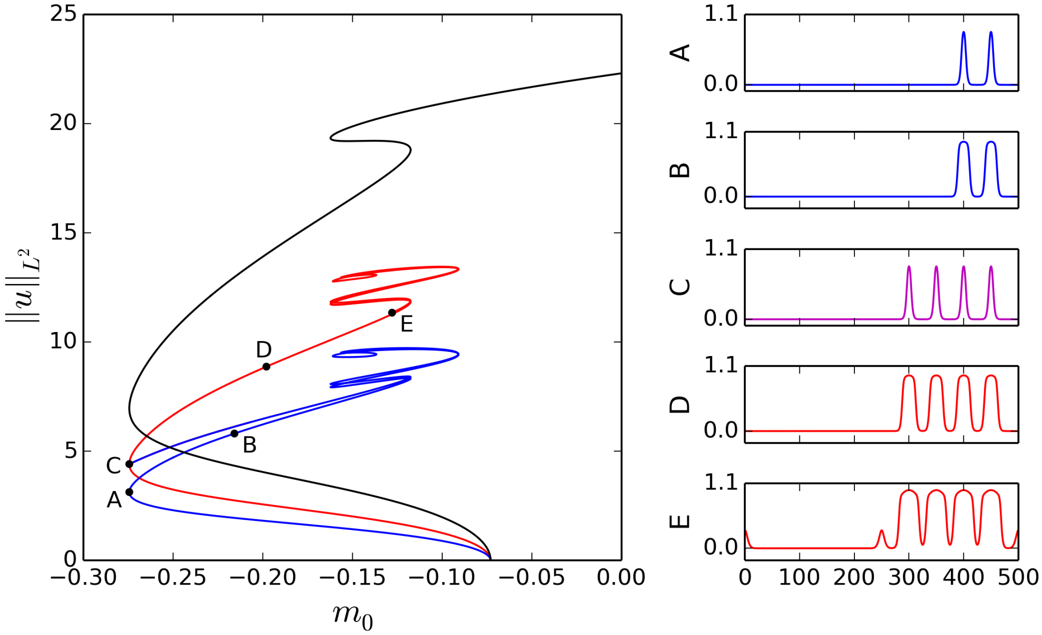

Figure 5.14: Bifurcation diagram for $m_1 = 0.1$ when $\ell = 50$ showing branches of FPT based on two spikes (blue) and four spikes (red). The periodic branch is shown in black. Sample solutions at locations indicated by corresponding letters are shown on the right. The solution corresponding to the connection between the blue and red LS branches is colored magenta. The branches interconnect at the left folds. Mixed PT branches are omitted.

5.3 Discussion

We have discussed in some detail the effects of spatial forcing with different wavelengths on the existence and properties of spatially localized states in the subcritical Ginzburg-Landau equation describing the primary bifurcation to a stationary roll or stripe pattern. We have found that when the amplitude of the forcing is sufficiently small its presence generates the familiar snakes-and-ladders structure of localized states in the vicinity of the Maxwell point. We have called the resulting behavior *forced snaking*. We have also shown that larger scale forcing degrades the interaction between adjacent peaks leading to the appearance of finite pulse trains. In these trains the pulses interact indirectly via the imposed forcing. Such trains cannot grow in length via snaking and so extend into a parameter regime where direct interaction between adjacent pulses dominates and snaking can take place. Once the train has added peaks on either side the solution branch returns to the noninteracting regime as a longer pulse train. This sequence of transitions proceeds apparently indefinitely leading to *foliated snaking*. We present cartoons of these two scenarios in Fig. 5.17.

Our results bear considerable similarity to recent work on forced snaking in other systems [7, 25, 38]. In each of these cases the forcing opens a wedge of finite opening angle containing

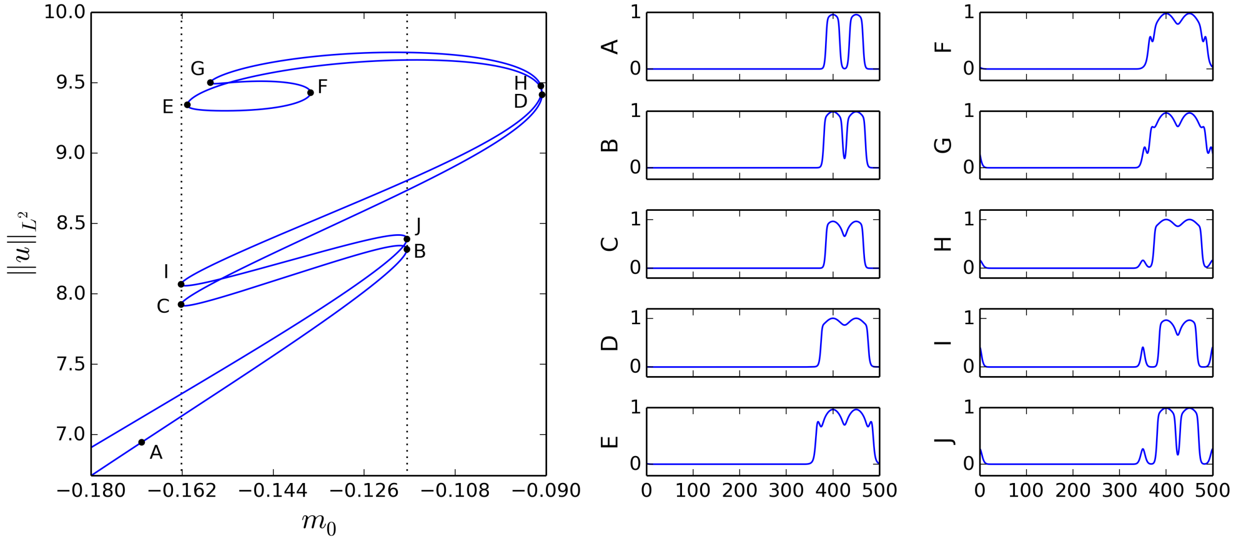

Figure 5.15: Bifurcation diagram for $m_1 = 0.1$ when $\ell = 50$ showing details of the FPT branch with two spikes (blue curve in Fig. 5.14). The folds on the periodic branch are denoted by dotted lines. Sample solutions corresponding to the labeled points are shown on the right.

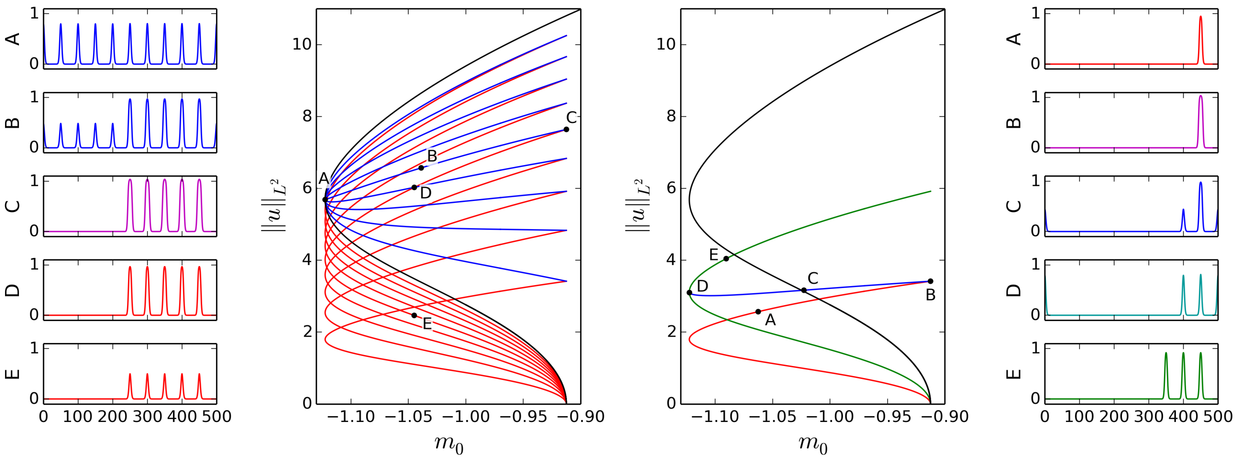

Figure 5.16: Bifurcation diagram for $m_1 = 1$ when $\ell = 50$. (a) The first two panels show FPT branches emanating from the primary bifurcation (red) and mixed PT branches (blue) emanating from the fold on the periodic branch (black). Sample solutions profiles are shown on the left. (b) The second two panels show the one and three lump FPT branches (red, green) connected by a mixed FPT branch composed of one lump and two spikes (blue). Solution profiles are shown on the right.

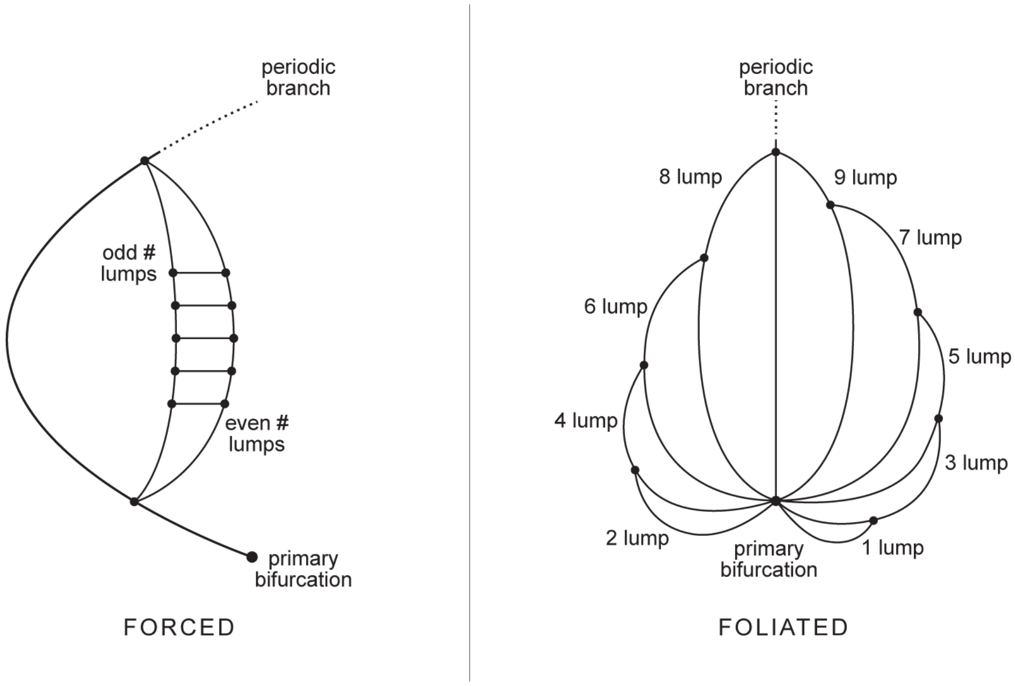

Figure 5.17: Schematic bifurcation diagram illustrating the topologial differences between forced snaking and foliated snaking in spatially parametrically forced systems.

localized states that snake for small forcing amplitude, but the snaking breaks down with increasing forcing amplitude. This breakdown is associated with the interaction between the LS and the fold of the periodic state generated by the forcing. This interaction can lead to the formation of a stack of isolas as in [161]–[25] or, as in the present case, foliated snaking. In the former case the LS interact with right folds on periodic states, while here and in [7] the interaction is with a left fold. These situations profoundly differ since in the former case the manifolds of the periodic states that are involved extend beyond the fold while this is not the case in the latter. Thus an interaction with a right fold leads to the breakup of the snake into a stack of isolas connecting n pulse states with $n+2$ pulse states [38, 161] while an interaction with a left fold leads to the pulse-adding bifurcations organized within the foliated snaking structure identified here. The interaction with the right fold is here played by the interaction of the snaking structure with the primary instability to the periodic state. No isolas appear in this case and the FPT branches remain interconnected [29].

The results of this work extend to two dimensions: all the states discussed here may be extended in the y direction by writing $U(x, y) = u(x)$ although these may suffer y-dependent instabilities [32], thereby further complicating the snaking structure [8]. In addition, there are patterned structures that are fully localized in two dimensions such as those observed in the experiments of Ref. [75]. The study of these states is beyond the scope of this work.

Chapter 6

Depinning: Spatially Periodic Forcing and Subcritical Fronts

This chapter focuses on the dynamics of localized structures in Eq. (1.1) and links the front dynamics studied in chapter 4 with the stationary snaking solutions of chapter 5. The dynamical regimes nearby the snaking branch for Eq. (1.1) are summarized in Fig. 6.1. In this chapter we discuss dynamics in regions I–IV focusing mainly on the dynamics in the shaded regions (II and IV) where depinning occurs. Studies of dynamics in region V are left to future work.

6.1 Dynamics of forced snaking

To begin a discussion of the dynamics of snaking structures we first set $a_1 = a_2 = 0$. Because in this case Eq. (1.1) is a gradient system its dynamics in a given parameter regime approach stable stationary states. The most basic dynamical regime occurs in region I. There the only stationary solution is $A = 0$ and it is the global attractor of the dynamics. As a result when any snaking solution is taken as an initial condition with parameters set in region I the entire solution collapses to $A = 0$ in amplitude as shown in Fig. 6.2(a).

The next straightforward regime is in region III, the pinning region. Here the periodic branch is stable as are snaking states of all integer numbers of cosine wavelengths. Given a small perturbation an unstable snaking state solution evolves into a stable one either below it or above it on the bifurcation diagram. This is illustrated in Fig. 6.2(b). This occurs by the translation of the fronts bounding the localized state by a single cosine period. If a finite amplitude perturbation is given then the solution may evolve into any of the stable solutions.

A more complicated picture emerges in regions II ans IV where there are no snaking solutions but the periodic branch remains stable. The result of this is that the snaking solutions evolve by the motion of their fronts, like in region III, but these do not halt after a single cosine period. In light of this the fronts bounding the snaking solution are said to

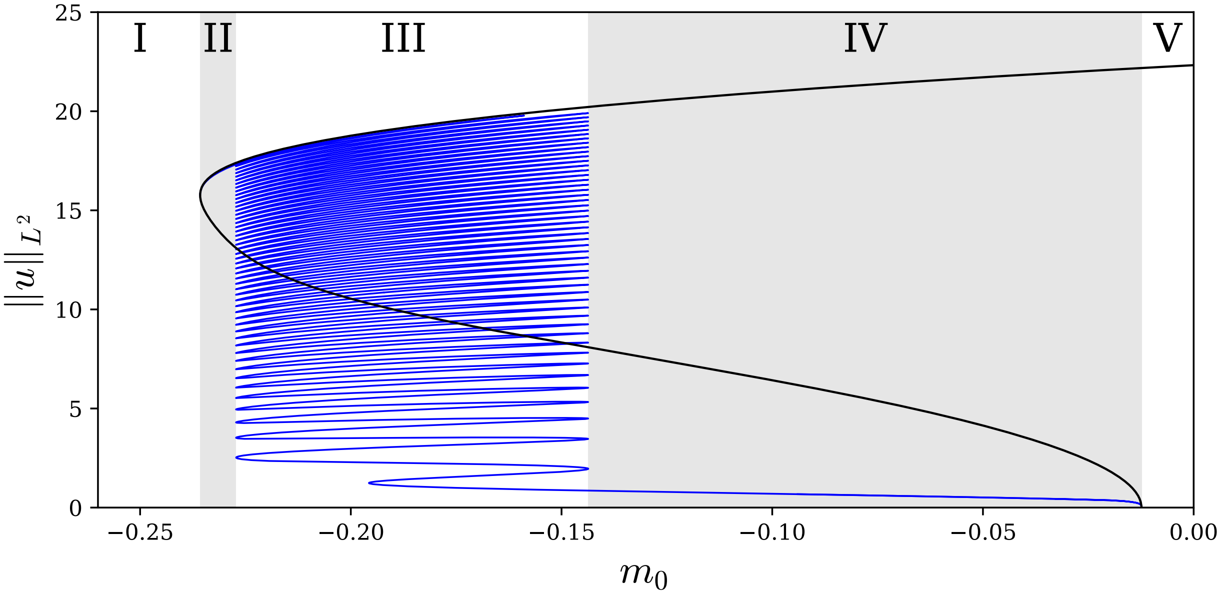

Figure 6.1: Bifurcation diagram for snaking solutions (blue) and the periodic branch, P (black) when $m_1 = 0.1$, $\ell = 10$ and $a_1 = a_2 = 0$. Regions I–V demarcate distinct dynamical regimes: (I) all solutions collapse to $u = 0$, (II) and (IV) depinning occurs as snaking solutions destabilize but P remains stable, (III) snaking solutions are stable, (V) $u = 0$ destabilizes and pulled front propagation may occur.

be "depinned." This depinning process is illustrated for region II in Fig. 6.3 and for region IV in Fig. 6.4. The space-time plot shows that the fronts move in increments, slowing as the stationary state with $n \pm 2$ bumps is neared. In the bifurcation diagram this can be understood as evolution just outside the pinning region towards increasing or decreasing norm. As this occurs fold solutions higher or lower on the the branch of localized states are inevitably approached. The slow dynamics near these folds suggests that an asymptotic procedure might be carried out to capture the dynamics nearby.

We seek to compute the branch of traveling waves that bifurcates out from a snaking branch fold just outside of the pinning region. This calculation is analogous to the one carried out in chapter 2 for the SHE [30] and here we perform it in full generality including the terms $a_1, a_2 \neq 0$. We focus on the right side of the pinning region, though an analogous procedure can be carried out on the left, and set $m_0 = m_+ + \epsilon\rho$ where m_+ is the m_0 value corresponding to the right boundary of the pinning region. This value is asymptotically approached exponentially from the right by the folds high up on the snaking branch. We next assume that $A(x,\tau) = A_0(x) + \sqrt{\epsilon}\, A_1(x,\tau) + \epsilon\, A_2(x,\tau) + \mathcal{O}\left(\epsilon^{\frac{3}{2}}\right)$ where A_0 is the solution at a right fold high up on the snaking branch. The dynamics occur on a slow time scale $\tau = \sqrt{\epsilon}\, t$. At lowest order we obtain the stationary GLE which A_0 solves and at order $\sqrt{\epsilon}$ we obtain

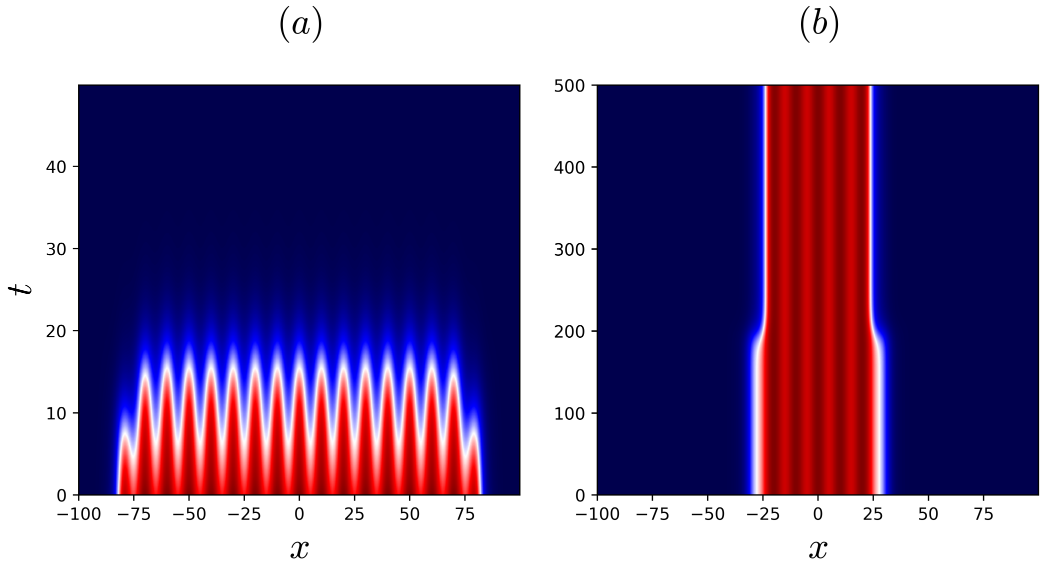

Figure 6.2: Space-time plots showing the dynamics of snaking solutions in region I (a) and region III (b) where $\ell = 10$, $m_1 = 0.1$, $a_1 = a_2 = 0$. The amplitude $|A(x,t)|$ is plotted. The solution in region I exhibiting amplitude decay to $A = 0$. The initial solution in (b) is from an unstable snaking branch and quickly evolves into a stable snaking solution.

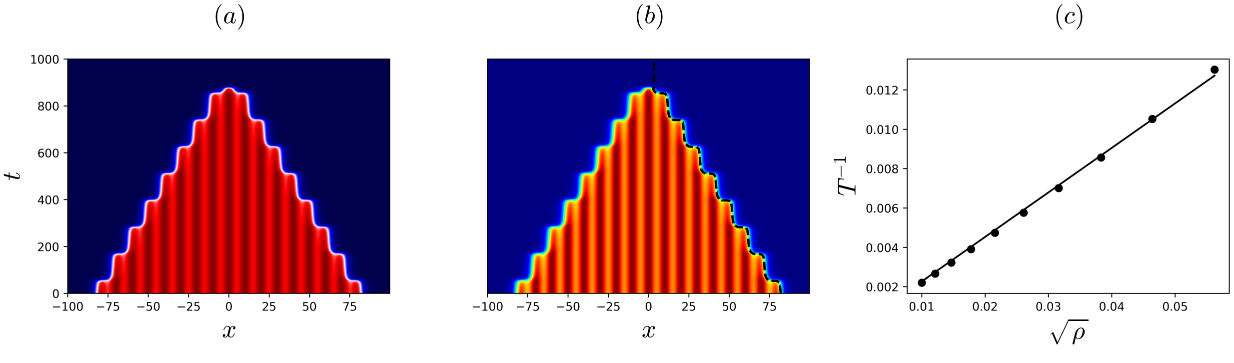

Figure 6.3: Space-time plots showing depinning dynamics in region II where $\ell = 10$, $m_1 = 0.1$, $a_1 = a_2 = 0$: (a) the amplitude $|A|$, (b) $\Re[A]$, (c) the measured depinning time versus the distance from the pinning region ρ. The tracked front position is shown in (b) with a dashed line.

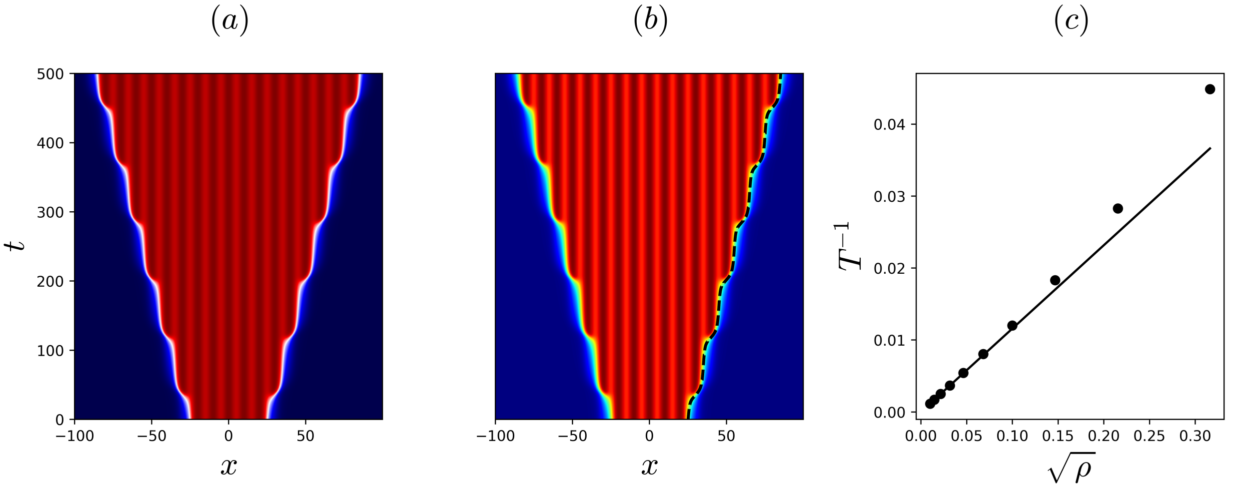

Figure 6.4: Space-time plots showing depinning dynamics in region IV where $\ell = 10$, $m_1 = 0.1$, $a_1 = a_2 = 0$: (a) the amplitude $|A|$, (b) $\Re[A]$, (c) the measured depinning time versus the distance from the pinning region ρ. The tracked front position is shown in (b) with a dashed line.

the linear problem $\mathcal{L}(A_0)A_1 = 0$ where $\mathcal{L}(A_0)$ is the linear operator formed by linearization of Eq. (1.1) around A_0. This linear equation is solved by $A_1 = \sum_i \alpha_i(\tau)n_i(x)$ where n_i are the null eigenfunctions of the linear operator. There are three such modes at a fold: the phase mode iA_0 and two edge modes, one spatially symmetric and one antisymmetric as discussed in chapter 5. Since there is nothing breaking spatial reflection symmetry or the phase symmetry in the initial value problem only the even mode, n_e, has a nonzero coefficient. At order ϵ one obtains the linear problem

$$\begin{aligned}-\mathcal{L}(A_0)A_2 = &-\frac{d\alpha_e}{d\tau}A_1 + \rho A_0 + \left(\bar{A}_0 A_1^2 + 2A_0|A_1|^2\right)\left(1 - 3|A_0|^2\right) - 3A_0^3\bar{A}_1^2 \\ &+ ia_1\left(|A_1|^2 A_{0x} + \bar{A}_0 A_1 A_{1x} + A_0\bar{A}_1 A_{1x}\right) + ia_2\left(A_1^2\bar{A}_{0x} + 2A_0 A_1\bar{A}_{1x}\right)\end{aligned}$$

which has a solution if the RHS is orthogonal to the nullspace of $\mathcal{L}^\dagger(A_0)$. This operator is not self-adjoint when $a_2 \neq 0$ in which case the null eigenfunctions are computed numerically.

After imposing the orthogonality conditions an ODE in $\alpha_e(\tau)$ is obtained. When $a_2 = 0$ and the linear operator is self-adjoint the only nonzero overlap results from the inner product with the adjoint null eigenfunction n_e. When $a_2 \neq 0$ we have found in practice that there is only one reflection symmetric adjoint null eigenfunction and thus also only one nonzero overlap. The resulting ODE is of the same form as that obtained for the SHE,

$$\frac{d\alpha_e}{d\tau} = I_1\rho + I_2\alpha_e^2,$$

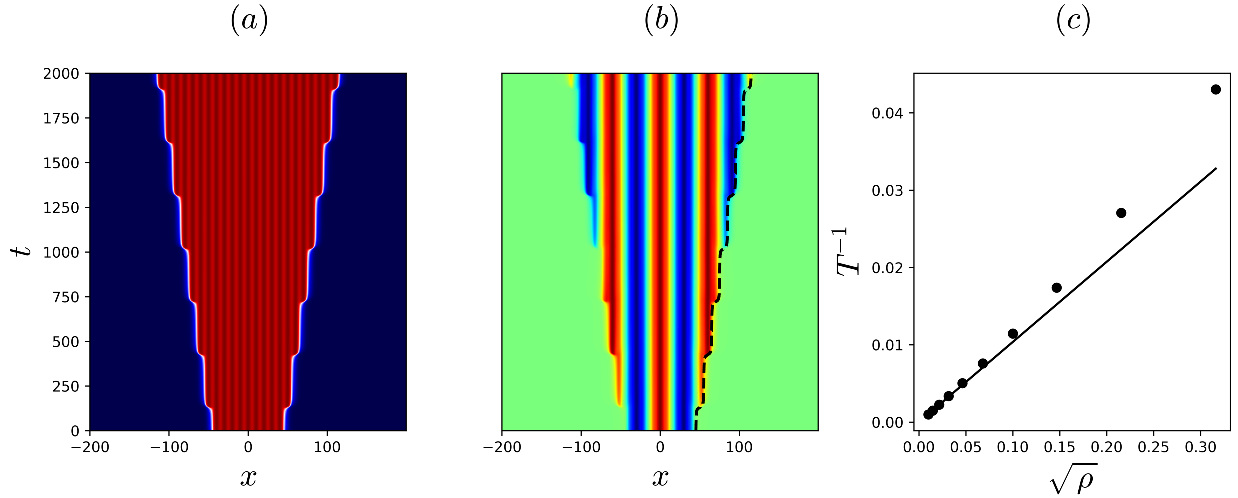

Figure 6.5: Space-time plots showing depinning dynamics in region IV where $\ell = 10$, $m_1 = 0.1$, $a_1 = \frac{1}{2}$ and $a_2 = 0$: (a) the amplitude $|A|$, (b) $\Re[A]$, (c) the measured depinning time versus the distance from the pinning region ρ. The tracked front position is shown in (b) with a dashed line.

where we assume that n_e is normalized by $\langle n_e^\dagger, n_e \rangle = 1$ and

$$\begin{aligned} I_1 &= \langle n_e^\dagger\,,\ A_0 \rangle \\ I_2 &= \langle n_e^\dagger\,,\ \left(\bar{A}_0 A_1^2 + 2A_0|A_1|^2\right)\left(1 - 3|A_0|^2\right) - 3A_0^3\bar{A}_1^2 + ia_1\left(|A_1|^2 A_{0x} + \bar{A}_0 A_1 A_{1x} + A_0 \bar{A}_1 A_{1x}\right) \\ &\qquad + ia_2\left(A_1^2 \bar{A}_{0x} + 2A_0 A_1 \bar{A}_{1x}\right) \rangle\,. \end{aligned}$$

As in the case of the SHE this ODE can be integrated from $\tau = -\infty$ to $\tau = \infty$ as a proxy for the complete depinning process from one saddle-node to the next. This produces the time estimate $T = \frac{\pi}{\sqrt{I_1 I_2 \rho}}$ to travel between saddle-nodes. This estimate is compared with the observed depinning in time evolution simulations and is shown in Figs. 6.3(c) and 6.4(c) as a straight line.

As in the case of linear stability inclusion of $a_1 \neq 0$ does not change the qualitative behavior of the system. A case of depinning to the right of the pinning region is shown in Fig. 6.5. Here the solution can be seen to have a wave number but otherwise acts like the $a_1 = 0$ case. The asymptotic depinning calculation also shows excellent agreement.

When $a_2 \neq 0$ the dynmaics change and the asymptotic calculation fails to capture the observed behavior. Figure 6.6 shows the measured depinning speed at the right side of the pinning region. The measured speeds do not collapse to the theoretical prediction and instead approach a finite value at $\rho = 0$. Moreover as shown in Fig. 6.7 for $\rho \lesssim 10^{-4}$ the solution exhibits a long transient before approaching the traveling wave branch. One possible reason for this is that the branch of traveling waves that emerges from the fold does not do

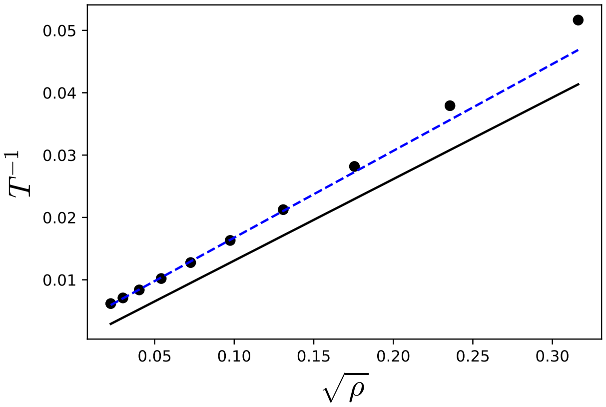

Figure 6.6: A plot of depinning speeds versus the distance from the pinning region for $\ell = 10$, $m_1 = 0.1$, $a_1 = 0$ and $a_2 = 1$. A linear fit to all but the last two points is also shown (blue dashed). This linear fit $a\sqrt{\rho} + b$ has slope $a = 0.13923$ and $b = 0.0028350$ whereas the predicted depinning speed has a slope 0.130753.

so to the right, i.e. $\rho > 0$. In this case the transient could be due to the slow dynamics governed by the null eigenmodes at the fold.

The finite velocity at $\rho = 0$ also suggests that the stable branch of traveling fronts may persist to the left of the fold in the interior of the snaking region. In order to check this we perform time evolution simulations in which we first set $\rho = 10^{-4}$ and wait for the system to reach the traveling front branch and then reduce the parameter into the pinning region ($\rho < 0$). Figure 6.8 shows the measured speeds as a function of ρ. As expected these speeds suggest the existence of the traveling front branch in the interior of the pinning region, a phenomenon that does not occur in the gradient system. Unfortunately we were only able to perform these calculations up until $\rho \approx -0.003$. Since we do not initialize the time simulations exactly on the traveling front branch after ρ is reduced the mismatch becomes larger with $|\rho|$. Eventually the simulations only follow the traveling wave for a short time before converging to a stable snaking state as shown in Fig. 6.9.

6.2 A strongly nonlinear asymptotic approximation of depinning

We are interested in capturing dynamics of depinning fronts that occur outside of the pinning region. The analysis here uses the exact nonlinear front solution derived in chapter 4 as a base state for the asymptotics. In principle we wish to do this analysis for arbitrary values of a_1 and a_2 although the presence of a_2 at lowest order causes all higher orders to involve a non self-adjoint linear operator. This makes imposing solvability conditions difficult since there is no general method to determine the null eigenfunctions of the adjoint operator analytically.

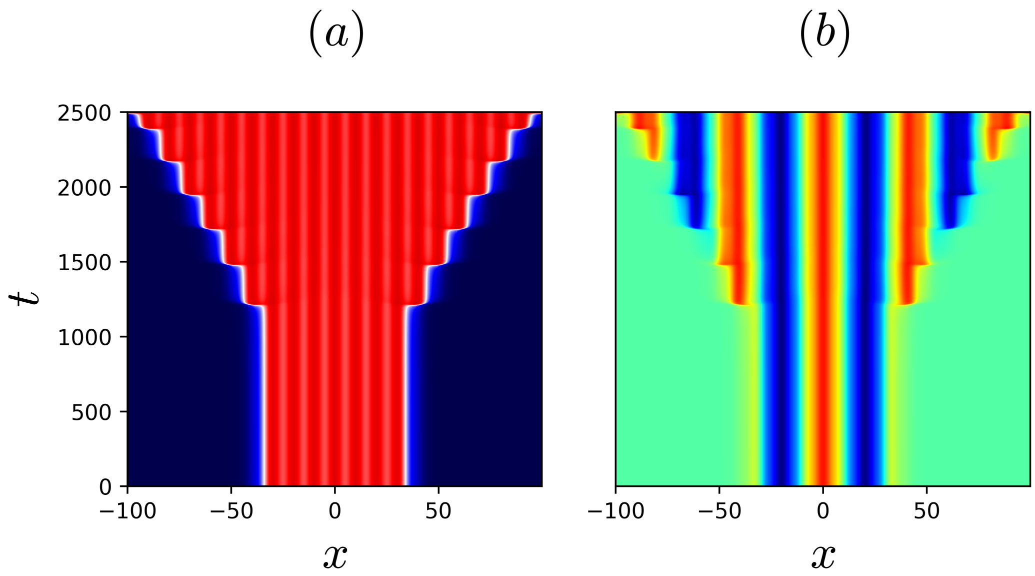

Figure 6.7: Space-time plots showing long transient dynamics in depinning from the right side of the pinning region when $\ell = 10$, $m_1 = 0.1$, $a_1 = 0$ and $a_2 = 1$: (a) the amplitude $|A|$, (b) $\Re[A]$. Here $\rho = 0.0001$ and the initial state undergoes a long transient before escaping to a traveling front branch.

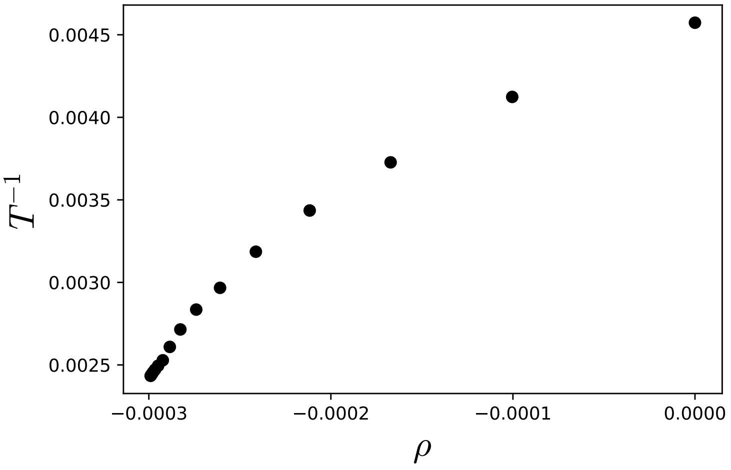

Figure 6.8: A plot of depinning speeds *inside* the pinning region for $\ell = 10$, $m_1 = 0.1$, $a_1 = 0$ and $a_2 = 1$. These calculations are initiated by initially time stepping a depinning solution for $\rho = 0.0001$ and then reducing the parameter ρ and measuring the average speed.

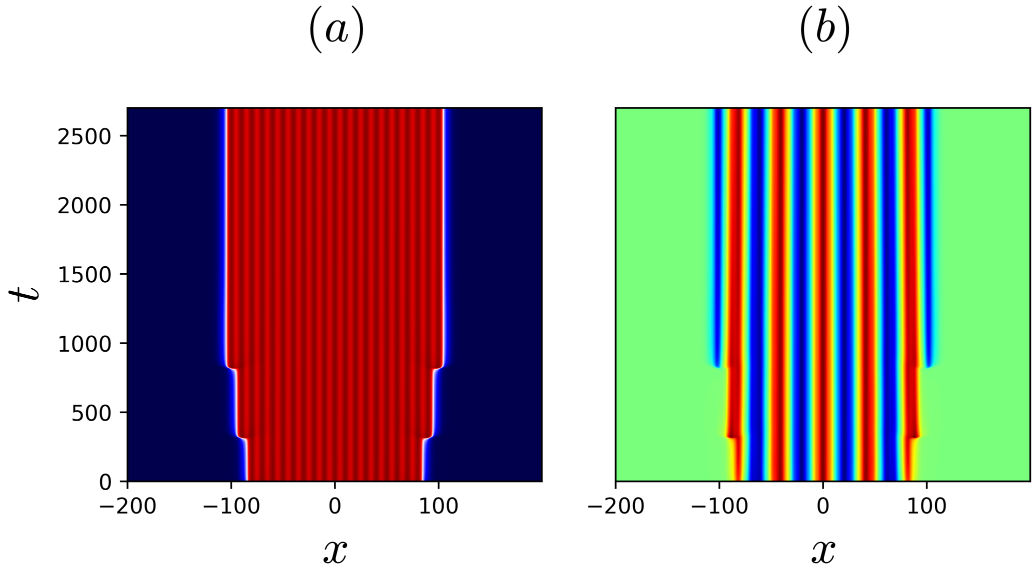

Figure 6.9: Space-time plots showing repinning dynamics in the interior of the pinning region when $\ell = 10$, $m_1 = 0.1$, $a_1 = 0$ and $a_2 = 1$: (a) the amplitude $|A|$ (b) $\Re[A]$. Here $\rho = -0.00035$ and the initial state propagates a short while along a traveling front branch before repinning on a stable snaking solution.

To mitigate this we consider small $a_2 = \epsilon\,\tilde{a}_2$.

The basic strategy for the asymptotics is to approximate a pulse solution by a pair of displaced fronts. Equation (1.1) has an exact front solution when $m_1 = 0$, as computed in chapter 4, and a pair of these are glued together to form a pulse. Equations of motion for the positions of both fronts are then derived through an asymptotic expansion by imposing solvability conditions order by order.

Setup of the asymptotic procedure

This calculation is performed near the Maxwell point of the unforced system $m_0 = -\frac{3}{\Gamma}$ where the dynamics are slow. We first move to a center of mass frame, $z = x - \phi(t)$, and introduce a time dependent phase $\omega(t)$: $A(x,t) = e^{-i\int \omega(t)\,d\tau} u(z,t)$. We also choose a width for the pulse $L(t)$ that is a function of time. Next we make the central assumptions of this procedure, (1) that $m_1 = \epsilon\,\tilde{m}_1$, $a_2 = \epsilon\,\tilde{a}_2$, $m_0 = -\frac{3}{\Gamma} + \epsilon\,\tilde{m}_0$ and (2) that all of the time dependence of the solution associated to corrections of the exact front solution (including ϕ, ω and L) occur on a slow time $\tau = \epsilon t$. Making these assumptions and substituting into Eq. (1.1) yields

$$\begin{aligned}\epsilon\, u_\tau =& -\frac{3}{\Gamma}u + u_{zz} + |u|^2 u + i a_1 |u|^2 u_z - |u|^4 u\\ &+ \epsilon\left[\tilde{m}_0 u + i\omega u + \dot{\phi}\, u_z - \dot{L}\,\frac{\partial u}{\partial L} + m_1 \cos\left(\frac{2\pi(z+\phi)}{\ell}\right) u + i\tilde{a}_2 u^2 \bar{u}_z\right].\end{aligned}$$

We then expand the solution as $u = u_0(z,\tau) + \epsilon\, u_1(z,\tau) + \ldots$ and impose solvability conditions order by order to extract the dynamics.

The lowest order problem is the nonlinear ODE

$$0 = -\frac{3}{\Gamma}u_0 + u_{0zz} + |u_0|^2 u_0 - |u_0|^4 u_0 + i a_1 |u_0|^2 u_{0z}. \tag{6.1}$$

When the fronts bounding the pulse u_0 are far apart then the derivative $\frac{\partial u_0}{\partial L}$ is equal to $\frac{1}{2}u_{0z}$ in the vicinity of each front and vanishes elsewhere up to exponentially small terms. Thus at least locally this equation reduces to the one considered in chapter 4 at the Maxwell point and a pulse can be constructed using the exact front solution. This front deposits a homogeneous solution with wave number q_N and takes the form,

$$a_N e^{i q_N z}\left(1 + e^{2 a_N^2 e_1 z}\right)^{-\frac{1}{2} - i\frac{e_0}{2e_1}} \equiv a_N e^{i q_N z} F(z).$$

By reflection symmetry $a_N e^{i q_N z}\bar{F}(-z)$ is also a solution. This allows us to construct the pulse,

$$\begin{aligned}u_0 &= a_N e^{i q_N z} F\left(z - \frac{L(\tau)}{2}\right)\bar{F}\left(-\left[z + \frac{L(\tau)}{2}\right]\right)\\ &= a_N e^{i q_N z} F_1(\xi_+)\, F_2(\xi_-)\end{aligned} \tag{6.2}$$

where $\xi_\pm = z \mp \frac{L(\tau)}{2}$. This pulse has a width $L(\tau)$ and is an approximate solution to Eq. (6.1). Specifically, for large L (6.2) solves Eq. (6.1) up to exponentially small terms in L.

The linear operator

The lowest order problem gives rise to a linear operator, $\mathcal{L}$, that is based on (6.2) and appears at all higher orders. The linear operator may be written,

$$\begin{aligned}\mathcal{L}(W) \equiv& -\frac{3}{\Gamma}W + W_{zz} + i a_1\left(\bar{u}_0 u_{0z} W + u_0 u_{0z}\bar{W} + |u_0|^2 W_z\right)\\ &+ |u_0|^2\left(2 + 3|u_0|^2\right) W + u_0^2\left(1 + 2|u_0|^2\right)\bar{W}.\end{aligned}$$

This operator is self-adjoint despite the presence of skew-Hermitian terms such as $\bar{W}$. Because of these terms and the complex coefficients one must be careful in computing the adjoint operator in the basis $(W, \bar{W})$ and it is more straightforward to do so in the basis (R, I) where $R(z)$ and $I(z)$ are the real and imaginary parts of W. We ommit such a calculation here.

The operator $\mathcal{L}$ has 3 approximate null eigenfunctions all inherited from symmetries. This is normal for linearizations about pulse states. The eigenfunctions consist of a phase rotation mode, $n_0 = iu_0$, plus two Goldstone-type modes $n_1 = u_{0z} = a_N e^{iq_N z}\left(F_1' F_2 + F_1 F_2'\right) + ia_N q_N e^{iq_N z} F_1 F_2$ and $n_2 = \partial_L u_0 = \frac{a_N}{2}\left(-F_1' F_2 + F_1 F_2'\right)$. The first of these, n_1, is the *true* Goldstone mode for the pulse and is antisymmetric with respect to its center $z = 0$. This mode is inherited from global translation symmetry. Also related to translation symmetry, the mode n_2 is symmetric about the pulse center reflecting the fact that for $L \gg 1$ the two fronts are independent and can translate freely in opposite directions. This mode arises only in the limit of large L i.e. as a result of our lowest order approximation.

At each order in the asymptotics a linear problem of the form $0 = \mathcal{L}(f) + g$ is obtained. This problem is solved by first imposing solvability conditions on g and then inverting $\mathcal{L}$. The imposition of solvability conditions is somewhat subtle and we review it here. Suppose that $n(x)$ is a null eigenfunction of $\mathcal{L}$ and therefore in the self-adjoint case also its adjoint, $\mathcal{L}^\dagger$. In order for the linear problem to be solvable we must require that $\langle n, g\rangle = 0$ where $\langle \cdot, \cdot \rangle$ is the inner product defined on the space of functions in which we seek a solution to the linear problem. If we write g and n in terms of their real and imaginary parts then this can be posed on $L^2 : \mathbb{R} \to \mathbb{R}^2$ so the inner product is written

$$\langle n, g\rangle_{\mathbb{R}^2} = \int_{-\infty}^{\infty} (n_r, n_i) \cdot \begin{pmatrix} g_r \\ g_i \end{pmatrix} dx = \int_{-\infty}^{\infty} n_r g_r + n_i g_i \, dx.$$

Thus there is one real-valued condition for each null eigenfunction of $\mathcal{L}^\dagger$. Though this basis makes the condition clear it is typically simpler to write down these inner products in the space of complex valued functions i.e. $L^2 : \mathbb{R} \to \mathbb{C}$ where,

$$\langle n, g\rangle_{\mathbb{C}} = \int_{-\infty}^{\infty} \bar{n} g \, dx.$$

In this form note that $\langle n, g\rangle_{\mathbb{R}^2} = \Re[\langle n, g\rangle_{\mathbb{C}}]$ so only the real part of the inner product corresponds to the true solvability condition and not the imaginary part. In many problems imposing this constraint causes the entire inner product to vanish but it is not strictly necessary and does not happen for the calculations in this chapter. We thus adopt the convention $\langle n, g\rangle = \Re[\langle n, g\rangle_{\mathbb{C}}]$ to impose solvability conditions.

A few identities

Before initiating the asymptotics it is useful to review a few identities that elucidate the structure of the null eigenfunctions and are helpful in simplifying solvability conditions. The identities are

$$\begin{aligned}
u_{0z} &= a_N^2 \lambda \, u_0 \, (e_1 S_1 - i e_0 S_2) + i q_N A_0 \\
n_2 &= \frac{a_N^2}{2} \lambda \, u_0 \, (e_1 S_2 - i e_0 S_1) \\
S_1(\varphi) &\equiv \frac{1-\varphi^2}{(\varphi+\lambda)(1+\varphi\lambda)} \\
S_2(\varphi) &\equiv \frac{\varphi^2 + 2\varphi\lambda + 1}{(\varphi+\lambda)(1+\varphi\lambda)} \\
\varphi &\equiv e^{2 a_N^2 e_1 z} \\
\lambda &\equiv e^{-a_N^2 e_1 L}.
\end{aligned}$$

These identities are written so that symmetries in z become apparent. Specifically when $z \to -z$ then $\varphi \to \frac{1}{\varphi}$. The identity $S_1(\varphi) = -S_1\left(\frac{1}{\varphi}\right)$ shows that S_1 is antisymmetric and $S_2(\varphi) = S_2\left(\frac{1}{\varphi}\right)$ shows that S_2 is symmetric.

Asymptotics beyond lowest order

The $\mathcal{O}(\epsilon)$ problem is

$$0 = \mathcal{L}(u_1) + (\tilde{m}_0 + i\omega)u_0 + i\tilde{a}_2 u_0^2 \bar{u}_{0z} + \dot{\phi}\, u_{0z} - \dot{L}\, \frac{\partial u_0}{\partial L} + m_1 \cos\left(\frac{2\pi(z+\phi)}{\ell}\right) u_0$$

and each null eigenfunction gives rise to a solvability condition:

$$\begin{aligned}
0 &= \left[q_N I_0 - e_0 a_N^2 \lambda I_1\right] \dot{\phi} + \omega I_0 \\
0 &= \left[\lambda a_N^2 \left(e_0^2 I_3 + e_1^2 I_2\right) - e_0 q_N I_1\right] \dot{\phi} - e_0 \omega I_1 - e_1 m_1 \sin\left(\frac{2\pi\phi}{\ell}\right) I_4 \\
0 &= \tilde{m}_0 I_1 - \frac{\lambda a_N^2 \dot{L}}{2 e_1} \left(e_0^2 I_2 + e_1^2 I_3\right) - \tilde{a}_2 e_0 \lambda a_N^2 I_7 + m_1 \cos\left(\frac{2\pi\phi}{\ell}\right) I_5 + \tilde{a}_2 q_N I_6
\end{aligned}$$

where I_k are the integrals

$$
\begin{aligned}
I_0 &= \int_{-\infty}^{\infty} |u_0|^2 \, dz = \frac{\log(\lambda)}{e_1\left(\lambda^2-1\right)} \\
I_1 &= \int_{-\infty}^{\infty} S_2 |u_0|^2 \, dz = \frac{-\lambda^2 + 2\lambda^2 \log(\lambda) + 1}{e_1 \lambda \left(\lambda^2-1\right)^2} \\
I_2 &= \int_{-\infty}^{\infty} S_2^2 |u_0|^2 \, dz = \frac{-7\lambda^4 + 8\lambda^2 + 4\left(2\lambda^4+\lambda^2\right)\log(\lambda) - 1}{2e_1\lambda^2\left(\lambda^2-1\right)^3} \\
I_3 &= \int_{-\infty}^{\infty} S_1^2 |u_0|^2 \, dz = \frac{\lambda^4 - 4\lambda^2\log(\lambda) - 1}{2e_1\lambda^2\left(\lambda^2-1\right)^3} \\
I_4 &= \int_{-\infty}^{\infty} S_1 |u_0|^2 \sin\left(\frac{2\pi z}{\ell}\right) dz = \frac{\pi^2 \sin\left(\frac{\pi L}{\ell}\right) \operatorname{csch}\left(\frac{\pi^2}{a_N^2 e_1 \ell}\right)}{a_N^2 e_1^2 \left(\lambda^3-\lambda\right)\ell} \\
I_5 &= \int_{-\infty}^{\infty} S_2 |u_0|^2 \cos\left(\frac{2\pi z}{\ell}\right) dz = -\frac{\pi^2 \cos\left(\frac{\pi L}{\ell}\right) \operatorname{csch}\left(\frac{\pi^2}{a_N^2 e_1 \ell}\right)}{a_N^2 e_1^2 \left(\lambda^3-\lambda\right)\ell} - \frac{2\pi\lambda \sin\left(\frac{\pi L}{\ell}\right) \operatorname{csch}\left(\frac{\pi^2}{a_N^2 e_1 \ell}\right)}{e_1\left(\lambda^2-1\right)^2} \\
I_6 &= \int_{-\infty}^{\infty} S_2 |u_0|^4 \, dz = a_N^2 \log(\lambda) \frac{-5\lambda^4 + 4\lambda^2 + 4\left(\lambda^2+2\right)\lambda^2 + 1}{2e_1\lambda\left(\lambda^2-1\right)^4} \\
I_7 &= \int_{-\infty}^{\infty} \left(S_1^2 + S_2^2\right) |u_0|^4 \, dz \\
&= \frac{4a_N^6 \lambda^2 \left(\lambda^6 + 15\lambda^4 + 30\lambda^2 + 10\right)}{e_1\left(\lambda^2-1\right)^9} \log(\lambda) - \frac{a_N^6\left(247\lambda^8 + 1672\lambda^6 + 1372\lambda^4 + 72\lambda^2 - 3\right)}{30 e_1 \lambda^2 \left(\lambda^2-1\right)^8}.
\end{aligned}
$$

These can be performed using contour integration after the substitution $z = \frac{\log\varphi}{2a_N^2 e_1}$. We assume in the asymptotics that $L \gg 1$. This implies that $\lambda \ll 1$ since the existence of the front requires $|a_1| < \frac{4}{\sqrt{3}}$ and thus $\frac{\sqrt{3}}{4} \leq a_N^2 e_1$. To keep the asymptotics consistent we only keep the leading order terms in λ in the solvability conditions.

Finally the solvability conditions may be rearranged to give the following ODEs:

$$
\begin{aligned}
\omega &= \dot{\phi} \frac{\sqrt{1-\alpha^2}}{\alpha} \left(\frac{\sqrt{3}}{4\alpha} - \frac{1}{L}\right) \\
\dot{\phi} &= -\frac{\alpha^4 \gamma}{1 + \frac{8\sqrt{3}}{3L}\alpha\left(\alpha^2-1\right)} \sin\left(\frac{\pi L}{\ell}\right) \sin\left(\frac{2\pi\phi}{\ell}\right) \\
\dot{L} &= \tilde{m}_0 \frac{16\alpha^3}{\sqrt{3}} - \tilde{a}_2 \frac{3\left(80\alpha^4 - 9\right)\sqrt{1-\alpha^2}}{160\alpha^5} + 2\alpha^4\gamma \cos\left(\frac{\pi L}{\ell}\right) \cos\left(\frac{2\pi\phi}{\ell}\right)
\end{aligned}
$$

where we have reparametrized a_1 by inverting the relation $\alpha = \frac{\sqrt{3}}{4a_N^2 e_1} = \sqrt{1 - \frac{3a_1^2}{16}}$ and set $\gamma = \frac{32\pi^2 m_1}{3\ell} \operatorname{csch}\left(\frac{4\pi^2\alpha}{\sqrt{3}\ell}\right)$. The phase ω is slaved to the dynamics of ϕ and can thus be ignored.

a_1	m_+	$\lvert A\rvert = \lvert B\rvert$	depinning time scaling	v_{adler} scaling
0	-0.14377	-0.14034	0.116	0.142
$\frac{1}{2}$	-0.15108	-0.14807	0.104	0.134

Table 6.1: This table compares the asymptotic calculation modeling depinning using the exact front solution to the behavior measured in time simulations. The comparison includes: the parameter value delimiting the right boundary of the pinning region m_+ along with the predicted value from the condition $|A| = |B|$ in the asymptotics, and semi-analytical scaling of the depinning time with the distance from the pinning region (the slope α of the line $T^{-1} = \alpha\sqrt{\rho}$) with the corresponding scaling from the asymptotic calculation of the depinning speed v_{adler}.

In the context of a reflection-symmetric initial value problem as we have here the appropriate initial conditions for these ODEs are $\phi(0) = 0$ and $L(0) = L_0$. In this case $\dot{\phi} = 0$ for all time and therefore both the center of mass and phase have no dynamics. In general this need not be the case and the phase responds to the width mode if the initial conditions are asymmetric. Thus in the symmetric case the relevant ODE is

$$\dot{L} = A(\tilde{m}_0) + B(\tilde{m}_1)\cos\left(\frac{\pi L}{\ell}\right), \tag{6.3}$$

an Adler equation for L. Note also that this is exactly the normal form for a SNIPER bifurcation which is responsible for depinning.

Dynamics of the Adler equation

The Adler equation, Eq. (6.3), has two dynamical regimes. If $|A| < |B|$ then Eq. (6.3) has two fixed points. One of the fixed points is unstable and the other is stable. These two fixed point persist until $|A| = |B|$ where they coincide. In this context this condition provides an estimate of the size of the pinning region. When $|A| > |B|$ there are no fixed points and L increases with time. This corresponds to the depinned case where the fronts propagate outwards. In this regime one can compute the average speed of propagation by the time required for the pulse to expand by 2ℓ (or each front to propagate distance ℓ),

$$v_{adler} = 2\ell\left(\int_0^{2\ell}\frac{dL}{\dot{L}}\right)^{-1} = \sqrt{A^2 - B^2}.$$

This velocity can be compared to the time estimate for depinning while the m_0-value associated to the condition $|A| = |B|$ can be compared to the parameter value delimiting the right boundary of the pinning region $m_0 = m_+$. These comparisons for a few of the cases considered here are shown in Table 6.1. While the estimate of the boundary of the pinning region is very good the estimated depinning speed is only accurate in order of magnitude. This could likely be improved by generalizing the asymptotic calculation away from the Maxwell point by using the full velocity dependence of the traveling front solution at arbitrary parameter values. Unfortunately this generates a non self-adjoint linear operator in the first order problem and prevents a fully analytical calculation.

The ability of this method to capture depinning is remarkable mainly because it is entirely analytical and does not require any numerically computed solutions. This suggests that the traveling front branch that depinned solutions approach is a perturbed version of the heteroclinic front solution derived in chapter 4, giving the latter further significance. Moreover this also suggests that the non-depinning behavior of snaking states with $a_2 \neq 0$ might be understood by computing the branch of depinned traveling fronts in a similar manner. This analysis can be performed analytically up to the computation of the adjoint eigenfunctions at which point some numerical solutions will be necessary. One possible approach would be to keep all of the possible terms in the solvability conditions, derive the ODES, compute the conditions on their coefficients delimiting each dynamical regime and only afterwards compute the solvability integrals. This would allow one to study the dynamical regimes as a function of $\tilde{m}_0$ rather than deriving a single set of ODEs for each $\tilde{m}_0$ value.

Chapter 7

Application: Gap Solitons

7.1 Introduction

Discrete solitons have been the subject of intense study in nonlinear optics since their prediction in 1988 [42, 45]. A particular type of soliton known as the “gap soliton,” first proposed in 1994 [95], arises amidst a competition between nonlinear self-focusing effects and anomalous diffraction in periodic waveguides. These structures are typically modeled using a nonlinear Schrödinger equation (NLSE) in the presence of an external periodic potential, i.e., the Gross-Pitaevskii equation (GPE). An enormous amount of theoretical work has been done on the structure and stability of solutions to this model for a variety of nonlinearities, e.g. [2, 114, 123]. More recently an effort has been made to understand solutions referred to as multipole solitons or soliton complexes that involve arrays of nearly identical solitons pinned to the periodic potential [1, 94, 157, 163, 164]. Related work has investigated multipulse solutions in a cubic-quintic medium in which the solution possesses a finite set of identical maxima but is not composed of isolated solitons [23, 44, 114, 151]. Our work connects these two distinct types of structures providing a unified picture of how they relate to one another in the cubic-quintic case and elucidates their stability properties.

The simplest models for optical solitons describe a Kerr medium resulting in a NLSE with a cubic nonlinearity. More complex nonlinearities arise in other systems, however, and cubic-quintic nonlinearities in particular have been observed in a plethora of experiments [101, 118, 142, 155, 162]. These are the subject of the present chapter. In the presence of an externally imposed spatially periodic potential $V(x)$ the resulting cubic-quintic GPE takes the form

$$-iA_t = A_{xx} - V(x)A + |A|^2A - |A|^4A. \tag{7.1}$$

This is an equation for a complex-valued order parameter $A(x,t)$. In the following we focus on the case of sinusoidal potentials and seek oscillatory solutions of the form $A(x,t) = e^{-im_0t}u(x)$ describing a rotating wave with fixed albeit nonuniform spatial profile. Such states are solutions of the nonlinear ordinary differential equation (ODE)

$$\begin{aligned} 0 &= u_{xx} + \left[m_0 + m_1 \cos\left(\frac{2\pi x}{\ell}\right)\right] u + |u|^2 u - |u|^4 u \\ &\equiv u_{xx} + \mathcal{N}(u, x). \end{aligned} \tag{7.2}$$

This equation takes the form of Eq. (1.1) for stationary solutions with $a_1 = a_2 = 0$ and a periodically oscillating bifurcation parameter. Therefore it shares the forced snaking solutions that were discussed in chapter 5 [126]. Here we are interested in particular in spatially localized solutions of this equation, i.e., in solitary wave solutions of the GPE. Such solutions are frequently called solitons (a custom we follow below) although they are not true solitons, i.e., solutions of a completely integrable partial differential equation (PDE).

To determine solitary wave solutions of Eq. (7.1) one must understand the (spatial) linear dispersion relation around the trivial solution $u = 0$ of Eq. (7.2). Because the linear problem is periodically forced it is described by Floquet theory and possesses a characteristic band-gap structure. Specifically, the Floquet exponents for the linear problem only have a nonzero real part in certain regions of the (m_0, m_1) parameter plane and are otherwise purely imaginary. These regions in the (m_0, m_1) plane are referred to as band-gaps and are shown in white in Fig. 7.1. For parameters in these regions $u \equiv 0$ is a hyperbolic fixed point of Eq. (7.2) and the ODE can therefore support solutions that are homoclinic to $u = 0$. These solitary wave solutions are colloquially referred to as gap solitons.

For fixed m_1 the band structure (white regions in Fig. 7.1) takes the form of a countable set of intervals in m_0. The first of these intervals, $-\infty < m_0 < m^*(m_1)$, is of infinite extent and is called the semi-infinite gap. All higher gaps are finite open intervals. In the following we study gap solitons restricted to the semi-infinite gap in which the ODE (7.2) has two simultaneously hyperbolic fixed points. These two solutions are $u(x) = 0$ and a periodic solution with period ℓ, the period of the externally imposed potential. Here we interpret the forced snaking solutions of chapter 5 in terms of gap solitons of the GPE. Some of the solutions appear in earlier work [114, 151] but are not discussed at the level of detail included here.

Homoclinic snaking [32, 33] is present in both discrete [37, 44, 144, 161] and continuous [41, 67, 109, 150, 151] models of optical systems. This term describes the origin and properties of a large or infinite multiplicity of spatially localized structures present within an interval of parameter values such as those present in the Lugiato-Lefever equation [41], a complex-valued equation for the amplitude of the (transverse) electric field in a continuously pumped optical cavity. This equation is of second order in space and consequently its stationary states solve a 4th order ODE which supports standard homoclinic snaking, eg., [67, 120, 150]. In contrast, the focus of this paper is on snaking that results from imposed periodic spatial modulation, i.e., on *forced* snaking. It is generally assumed that the effects of discreteness in a discrete system are analogous to the imposition of a periodic potential, the Peierls-Nabarro potential. However, in such systems the spatial period is the discretization length, in contrast to the system we study in which the period ℓ of the imposed potential is much larger than the discretization length which is taken to vanish (the continuum

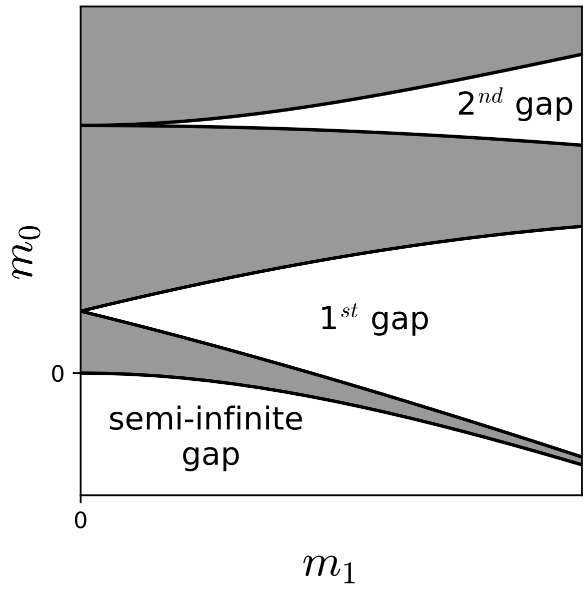

Figure 7.1: Band-gap structure in the (m_0, m_1) plane for the lowest three gaps of the linearization of Eq. (7.2). Solutions that are homoclinic to $u \equiv 0$ (equivalently $A \equiv 0$) represent solitons and exist only within the band gaps (white regions in the diagram).

limit). Since ℓ may be smaller than, comparable to, or larger than the intrinsic (nonlinear) lengthscale of the fronts present in the continuum regime, several distinct cases arise. In other words, the continuum problem contains a nontrivial extra parameter, the length ℓ of the imposed potential, and its dynamics are therefore necessarily richer than those of the discrete models studied, for example, in [37, 107].

This chapter is organized as follows. In section 7.2 we summarize the bifurcation structure of the solutions in chapter 5 highlighting the aspects that are relevant in the gap soliton context. We show that the spatial scale of the potential, ℓ, has a major impact on the bifurcation structure of these solutions. In section 7.3 we compute the linear stability of the snaking solutions in the context of Eq. (7.1) and discuss the dynamics of perturbed solutions in section 7.4. The chapter concludes with a discussion in section 7.5 and in section 7.6 we detail our numerical methods. In Appendix C we report on a strongly nonlinear theory that captures the behavior of oscillating localized states.

7.2 Forced snaking

For fixed parameters Eq. (7.2) possesses multiple multipulse solutions. As a function of the parameter m_0 these solutions lie on a countable set of distinct bifurcation curves. In chapter 5 we term this behavior *forced snaking.* These localized solutions are real-valued despite

Eq. (7.2) admitting complex solutions. To see this we write $u(x) = r(x)e^{i\phi(x)}$ yielding

$$\begin{aligned} r_{xx} - r\phi_x^2 - V(x)r + r^3 - r^5 &= 0 \\ \frac{d}{dx}\log\left(r^2\phi_x\right) &= 0. \end{aligned} \tag{7.3}$$

Integrating Eq. (7.3) once leads to $\phi_x = Kr^{-2}$, implying that $r_{xx} - K^2r^{-3} - Vr + r^3 - r^5 = 0$. When $K \neq 0$ this equation does not admit solutions that are homoclinic to $r = 0$, i.e. to $u = 0$, implying that such states are only possible when $K = 0$ and that ϕ is therefore constant. Without loss of generality we take $\phi = 0$.

The details of this bifurcation structure depend significantly the three parameters m_0, m_1 and ℓ characterizing the equation. In the following we summarize the main results concerning localized states in Eq. (7.2). These fall into two distinct regimes depending on the lengthscale of the forcing, ℓ, and in each case are analyzed in stages as we increase the potential depth, m_1, from zero.

Short-scale forcing, $\ell = 10$

For small values of ℓ the addition of periodic parametric forcing to the GLE model produces localized states that exhibit classic snaking. The addition of parametric forcing on a short lengthscale (here $\ell = 10$) causes the constant amplitude solutions on the primary branch of the GLE to become periodic with the same period as the forcing. Figure 7.2 shows a pair of intertwined branches of localized states that bifurcate from the newly periodic primary branch at low amplitude (location D) and enter a pinning region as they are continued in the parameter m_0, exhibiting snaking, before terminating on a branch of domain-filling periodic states (location E). The solutions on these branches are characterized by the number N of bumps of the periodic state contained within them. This number can be either odd or even. Each back and forth excursion of the solution branch across the pinning region results in the addition of one new bump on either side the solution thereby maintaining the parity of N. In addition, a set of spatially asymmetric "rung" states connects opposite folds on the snaking branches. Only one rung is shown in the figure. This structure does not change qualitatively when m_1 is increased.

Each N-bump solution occupies two consecutive sections of the snaking branch separated by a fold on the right, a lower section with a larger slope and an upper one with a smaller slope (Fig. 7.2). Figure 7.3 shows a pair of solutions, the dashed line from an upper section and the solid line from the previous lower section, both at the same parameter value, showing the process whereby the folds on the right are responsible for the appearance of an extra pair of pre-bumps on either side. The center parts of the solutions are the same. As m_0 decreases the pre-bumps grow into full bumps turning the state into a $N + 2$-bump solution.

The asymmetric rung branches can be understood in terms of this dichotomy. Rung states, like the one shown in Fig. 7.2, are made up one half of the dashed solution and one half the solid solution shown in Fig. 7.3. As they are continued in m_0 the structure gains

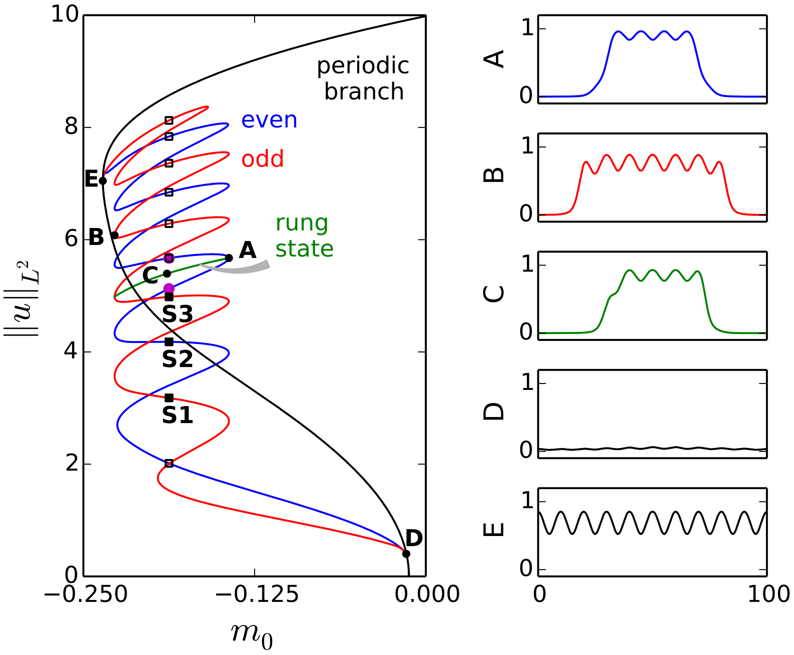

Figure 7.2: Bifurcation diagram showing periodic and localized states when $m_1 = 0.1$, $\ell = 10$ on a periodic domain. The two snaking branches shown are characterized by the number N of bumps: even (blue) and odd (red). Connecting each pair of folds is a branch of asymmetric rung states (green) only one of which is shown. The snaking branches bifurcate together from (and reconnect together to) a domain-filling periodic state. Plots on the right show solutions $u(x)$ at points marked with (●), shown over the full domain $0 \leq x \leq 100$. Solutions labeled with (□, ■) have $m_0 = -\frac{3}{16}$ and are relevant to the stability calculations (Fig. 7.6) and time simulations shown below. Solutions marked with magenta circles are shown explicitly in Fig. 7.3.

a single full bump on one side and thus changes parity (N bumps to $N + 1$). Thus rung branches connect opposite folds on the odd and even branches. Previous work on "symmetry breaking" in gap-soliton systems [103] has found similar asymmetric solutions.

Long-scale forcing, $\ell = 50$

For larger values of the forcing wavelength, ℓ, localized states persist but are not arranged in the traditional "snakes and ladders" structure. As documented in chapter 5, the bifurcation structure of the localized states now depends more strongly on m_1. For small m_1 classical snaking is observed but at a moderate value, here $m_1 \approx 0.035$ with $\ell = 50$, the snaking structure breaks down entering a regime that we have termed "foliated snaking." An example of this scenario is pictured in Fig. 7.4 in which we plot soliton states taking the form of finite pulse trains (FPT), with an odd number of peaks. Similar states consisting of a finite even

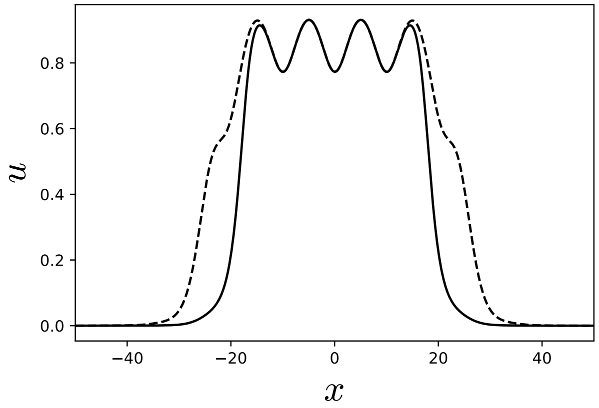

Figure 7.3: Two successive 4-bump snaking solutions at $m_0 = -\frac{3}{16}$, $m_1 = 0.1$, $\ell = 10$. The stable solution is drawn with a solid line and the unstable one with a dashed line (see section 7.2). These solutions correspond to the magenta points in Fig. 7.2.

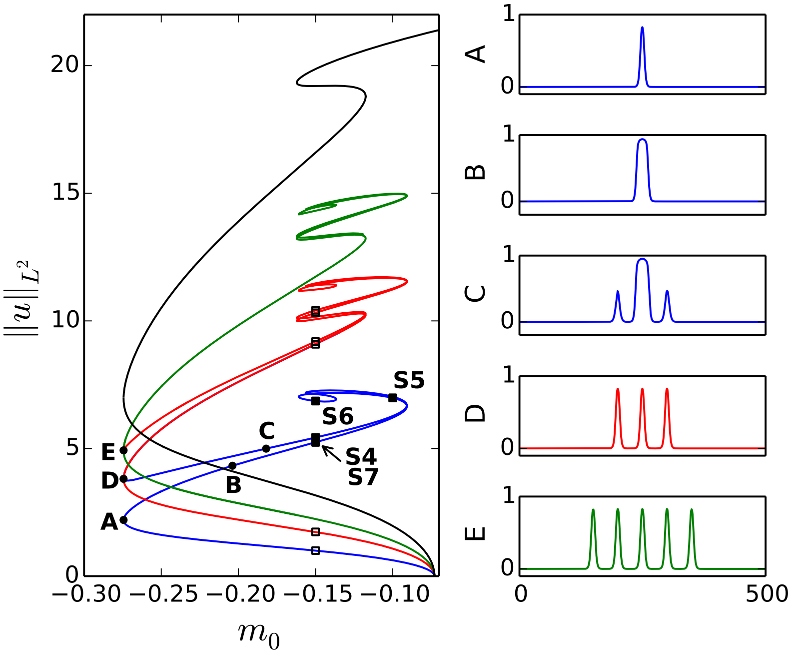

Figure 7.4: Bifurcation diagram for $m_1 = 0.1$ when $\ell = 50$ showing FPT branches based on one spike (blue), three spikes (red) and five spikes (green). The periodic branch is shown in black. The branches interconnect at the left folds. Panels on the right show solutions $u(x)$ at points marked with (•), shown over the full domain $0 \le x \le 500$. Solutions labeled with (□, ■) have $m_0 = -0.15$ or $m_0 = -0.1$ and are relevant to the stability calculations (Fig. 7.7) and time simulations shown below.

number of solitons are also present. In the foliated snaking regime soliton branches with odd/even number of peaks maintain parity-preserving interconnectivity, but the bifurcation diagram is significantly different. This is because the FPT states may sample solitons from either the upper (lump) or the lower (spike) branch of periodic states (black curve in the figure) resulting in FPT with all possible combinations of lumps and spikes, with gaps ($u = 0$) permitted. The lumps and spikes are located at the cosine maxima (i.e., minima of $V(x)$, as expected). Because of the up-down symmetry, $u \to -u$, states with negative (i.e., dark) lumps are also present. Thus FPT consisting of a mix of bright and dark solitons are possible, although these are not considered here.

All branches of localized states with spikes bifurcate from the primary bifurcation point at $m_0 = m_c$ and initially take the form of a pulse train with N spikes. As they are continued in m_0 the branch passes the leftmost fold thereby turning the spikes into lumps. Upon further continuation the lump state undergoes a complicated set of bifurcations that ultimately add a pair of spikes, one at either edge of the structure, and allow the branch of N lumps to connect to that with $N + 2$. In principle arbitrary combinations of spikes and lumps can be combined to form localized states indicating that the complete bifurcation diagram is in fact much more complicated. Here we only consider states formed by either N spikes or N lumps that are adjacent to each other.

The above scenario becomes yet clearer at larger m_1 when the rightmost folds collide with $m_0 = m_c$. Figure 7.5 shows the results for $m_1 = 1$. Like the lower m_1 value, pulse trains can be constructed with either a lump, spike or $u = 0$ at each cosine maximum and thus one can construct families of soliton states. A FPT with N lumps and M spikes when continued in m_0 below m_c turns around at the left fold on the branch of periodic states. At this fold the lumps and spikes coincide but as m_0 increases back towards m_c any spikes in the structure shrink to $u \equiv 0$. Thus a 1-lump, 2-spike solution coincides with a 1-lump solution when $m_0 = m_c$ and the two branches meet in what is effectively a cusp.

The presence of the cusp is indicative of the separation of scales in Eq. (7.2). Between the bumps the ODE solution is exponentially small (a property that is exacerbated as ℓ increases) and the nonlinear terms in Eq. (7.2) are therefore even smaller while the potential is $\mathcal{O}(1)$. Thus to high accuracy the solution between the bumps may be taken to be $u = 0$. This means that the localized soliton states behave as independent concatenations of lumps and spikes rather than a single family: the nonlinear terms do couple the bumps, but do so exponentially weakly. The cusps that are observed in the bifurcation diagram are thus expected to be blunt upon close inspection, but with curvature inversely related to the exponentially small coupling between the pulses.

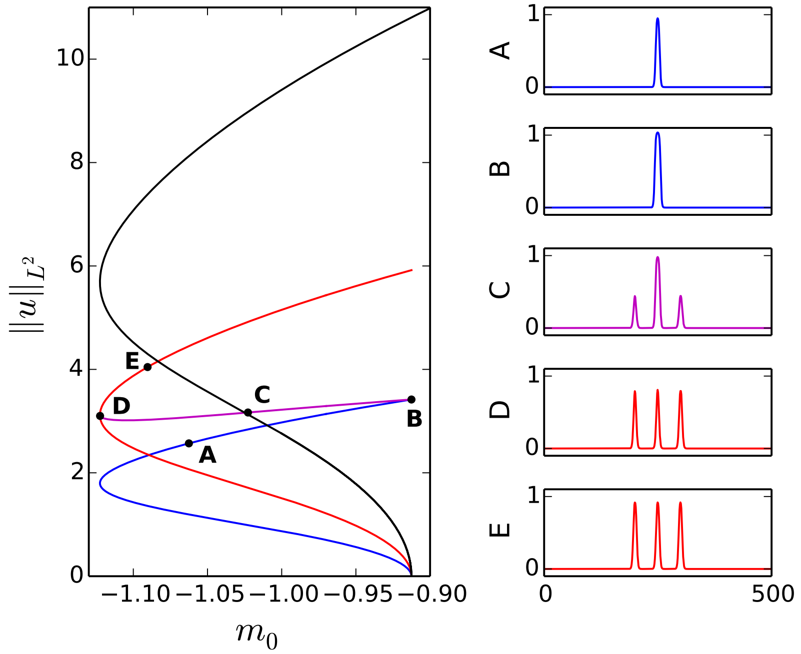

Figure 7.5: Bifurcation diagram for $m_1 = 1$ when $\ell = 50$ showing FPT branches based on one spike (blue) and three spikes (red) emanating from the primary bifurcation and a mixed PT branch consisting of one lump and two spikes (magenta) connecting the two. The periodic branch in shown in black. Sample solution profiles are shown on the right.

7.3 Stability

The linear stability of the solution $A(x,t) = e^{-im_0 t}u(x)$ of Eq. (7.1) may be studied using the Ansatz

$$A(x,t) = e^{-im_0 t}\left(u(x) + [a(x) + b(x)]e^{\sigma t} + [\bar{a}(x) - \bar{b}(x)]e^{\bar{\sigma} t}\right)$$

followed by linearization in the complex amplitudes a and b. This procedure leads to a linear eigenvalue problem for the growth rate σ:

$$-i\sigma \begin{pmatrix} a \\ b \end{pmatrix} = \begin{pmatrix} 0 & \partial_{xx} + \tilde{\mathcal{N}}(u,x) \\ \partial_{xx} + \mathcal{N}_u(u,x) & 0 \end{pmatrix} \begin{pmatrix} a \\ b \end{pmatrix} \equiv \mathcal{L} \begin{pmatrix} a \\ b \end{pmatrix}. \tag{7.4}$$

In writing this equation we have assumed that $u(x)$ is real-valued, with $\tilde{\mathcal{N}}(u,x) \equiv \mathcal{N}(u,x)/u$, $\mathcal{N}_u(u,x) \equiv \partial_v \mathcal{N}(v,x)|_{v=u}$ and $\mathcal{N}$ defined as in Eq. (7.2). We solve this eigenvalue problem using a Fourier pseudo-spectral method details of which are discussed in Appendix 7.6. This eigenvalue problem has the null eigenfunction $(a,b) = (0,u)$ with algebraic multiplicity 2. The multiplicity of the eigenvalue can be seen by differentiating $u_{xx} + \mathcal{N}(u,x) = 0$ with respect to m_0 yielding the identity

$$-\left[\partial_{xx} + \mathcal{N}_u(u,x)\right]\frac{\partial u}{\partial m_0} = u \tag{7.5}$$

from which it follows that $\partial_{m_0} u$ is a generalized eigenfunction with eigenvalue 0. The presence of the potential breaks translation invariance which would otherwise generate an additional null eigenfunction.

When $\sigma \neq 0$ this eigenvalue problem can be diagonalized, viz.

$$\sigma^2 a = -\left[\partial_{xx} + \tilde{\mathcal{N}}(u,x)\right]\left[\partial_{xx} + \mathcal{N}_u(u,x)\right] a.$$

From reflection symmetry it is clear that if σ is an eigenvalue of this equation, then $-\sigma$ and $\pm\sigma^*$ are eigenvalues also. Thus stable solutions have a spectrum entirely confined to the imaginary axis. Instabilities occur when eigenvalues exit the imaginary axis into the right half-plane. If these eigenvalues have zero imaginary part the instability is known as an exponential instability; otherwise it is an oscillatory instability (OI). In this work we have only found exponential instabilities; however, the occurrence of OI can be subtle [96] and eigenvalues may have very small real parts. We leave a careful study of OI to future work. In the diagonalization performed here $\sigma^2 > 0$ corresponds to a pair of eigenvalues on the real axis, symmetric about $\sigma = 0$, whereas $\sigma^2 < 0$ corresponds to a pair of symmetrically disposed eigenvalues on the imaginary axis. Since the diagonalized eigenvalue problem may not capture all of the zero eigenvalues that are present we check the results by computing the nullspace of the operators $\partial_{xx} + \tilde{\mathcal{N}}(u,x)$ and $\partial_{xx} + \mathcal{N}_u(u,x)$ as well.

Short-scale forcing, $\ell = 10$

Stability results for forced snaking solutions replicate known results at low amplitude and exhibit stability switching at folds higher up on the snaking branch. In Fig. 7.6 we plot curves of the squares of the three largest eigenvalues, σ^2, as a function of the arclength s along the two branches of snaking solutions measured from the bottom. These are computed by calculating the entire eigenspectrum for a series of solutions along the bifurcation curve. Folds on the solution branches are denoted by grey vertical dotted lines at the associated location s. The continuation is initiated at low amplitude (point D in Fig. 7.2) where the branch with an odd (even) number of bumps is stable (unstable). In the even case the branch restabilizes before the first fold is reached but no stability change occurs in passing the first fold on the odd branch. Despite this behavior at the lowest folds subsequent folds do coincide with stability switching for the snaking solutions. Most of the unstable segments of each branch are in fact unstable with respect to an additional unstable eigenvalue as well that leaves the imaginary axis and returns to it between the folds. However, the real part of this second eigenvalue is strictly smaller than that of the primary one and is thus of little dynamical importance. As can be seen by the ordering of eigenvalues in the figure no other eigenvalues go unstable in traversing either branch.

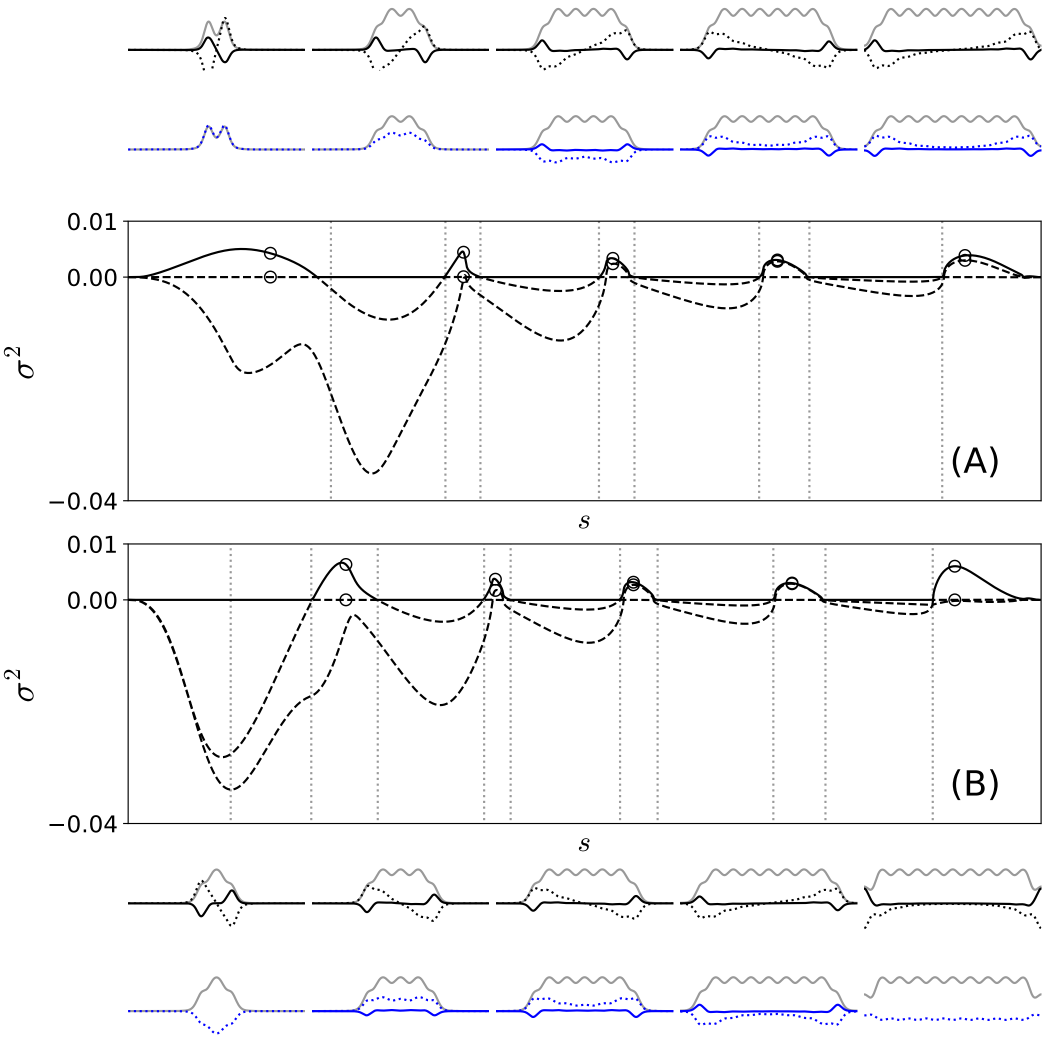

Figure 7.6: The three largest linear stability eigenvalues σ^2 for the solutions in Fig. 7.4 computed as a function of the arclength s. The largest eigenvalue σ^2 is plotted using a solid black line while all smaller eigenvalues are shown using a dashed line. Inset (A) represents a branch of solutions with an even number of bumps while inset (B) represents a branch with an odd number. Specific base states at $m_0 = -\frac{3}{16}$ (grey) and the corresponding eigenfunctions (largest eigenvalue in black, second largest eigenvalue in blue) of the even-bump branch are plotted above (A) with the corresponding results for the odd-bump branch shown below (B). In each case the real part $\Re[a(x)]$ of the eigenfunction is shown using a solid line while the imaginary part $\Im[b(x)]$ is plotted using a dotted line. In some cases $a(x) \equiv 0$ and we omit it from the eigenfunction plot. In each case the open circles (which may overlap) indicate the location of the base states used to compute the eigenfunctions shown.

The decorrelation between stability switching and the location of the folds is a consequence of the structure of the temporal stability eigenvalue problem for solutions of the GPE as explained in [159]. In this paper the author shows that for a large class of NLS-type equations the algebraic multiplicity of the 0 eigenvalue does not change at fold bifurcations in the ODE (7.2). Thus, no eigenvalues can escape into the right half-plane. Instead, the effect of the 0 eigenvalue of the operator $\partial_{xx} + \mathcal{N}_u(u, x)$ is to change the geometric multiplicity of the 0 eigenvalue of $\mathcal{L}$. Specifically, at the fold bifurcation the identity (7.5) is invalid and the eigenvalue 0 does not have any generalized eigenfunctions [159]. However, the algebraic multiplicity of the zero eigenvalue of $\mathcal{L}$ is preserved by the presence of a "fold eigenfunction" of the operator $\partial_{xx} + \mathcal{N}_u(u, x)$. The effect on the 0 eigenspace of $\mathcal{L}$ can be thought of as a change between the following Jordan blocks:

$$\begin{pmatrix} 0 & 1 \\ 0 & 0 \end{pmatrix} \rightarrow \begin{pmatrix} 0 & 0 \\ 0 & 0 \end{pmatrix}.$$

The "fold eigenfunction" is intimately related to the divergence of the function $\partial_{m_0} u$ as the fold $m_0 = m_F$ is approached, $\partial_{m_0} u \approx (m - m_F)^{-\frac{1}{2}}$. Multiplying the identity (7.5) by $\sqrt{m - m_F}$ before taking the limit shows that $\partial_{m_0} u$ passes smoothly into an eigenfunction of the operator $\partial_{xx} + \mathcal{N}_u(u, x)$ at m_F. Of course this mechanism does not preclude additional eigenvalues passing through 0 at folds in the ODE but it does not mandate it. For a rigorous treatment of this argument we direct the reader to Ref. [159].

The character of the instabilities and the failure to switch stability at the first folds can be gleaned from the structure of the associated stationary state and its eigenfunctions. Figure 7.6 shows the two eigenfunctions corresponding to the most unstable eigenvalues (black and blue) at arclength locations marked by open circles. These points were chosen all to be at the parameter value $m_0 = -\frac{3}{16}$ so that the periodic state is the same in all cases. Because the eigenvalues observed here are all real the Ansatz (7.4) for the perturbations is too general and we find that $a(x)$ is purely real while $b(x)$ is purely imaginary. We thus plot $\Re[a]$ with a solid line and $\Im[b]$ with a dashed line in each subplot. In a few cases $\Re[a] \equiv 0$ and is omitted. In each case the corresponding base state is shown in grey. All of the subplots in each row have a consistent vertical scaling so the amplitudes of the nonlinear states can be compared. The largest eigenvalue for the unstable states corresponds to an eigenmode (black) that is antisymmetric across the structure with $a(x)$ localized at the structure boundaries. This type of edge-localized mode is observed in classical snaking systems. However, because the corresponding $b(x) \not\equiv 0$ this mode also rotates the real-valued stationary state $u(x)$ into a fully complex and hence dynamic state.

When there is a second unstable eigenvalue, the associated eigenmode is symmetric across the structure. This mode thus corresponds either to growing or shrinking of the structure depending on the sign of $a(x)$. As in classical snaking, this mode takes the solution to the branch segment above or below in the snaking structure by growing or shedding the bumps at both boundaries of the structure simultaneously. However, because the associated $b(x)$ is again nonzero the resulting solution becomes fully complex and hence also time-dependent.

Which mode is selected depends of course on the nature of perturbation around the stationary state.

The symmetric mode is not always unstable, however, and remains stable along the first instability intervals on both branches. We believe that this nonuniversal behavior, just like the decorrelation between the first folds and stability switching, is a consequence of the small spatial extent (and hence small norm) of the soliton states in this regime. Similar pre-localized behavior near the base of the snaking branches is present in classical snaking as well and causes the small-norm solutions to have different properties from their more spatially extended brethren higher up on the branch.

Long-scale forcing, $\ell = 50$

In the foliated snaking regime the stability results are considerably different. Figure 7.7 shows the squares of the largest eigenvalues, σ^2, for the 1-lump and 3-lump foliated snaking branches (blue and red branches from Fig. 7.4). The 1-lump branch is stable except during pulse addition, i.e. between its second and last fold, where it is unstable. This instability is the result not only of eigenvalue crossings at the folds but of additional crossings inside the instability interval as well. The 3-lump branch has a similar structure with all the instability intervals associated with the pulse addition process. The most remarkable feature of these results is that stability switching does not occur at the spike-lump fold and pulse trains with both spikes and lumps are stable. This is in significant contrast to the dissipative case studied in chapter 5 where spikes are always unstable.

Solutions with N lumps and M spikes have a multiplicity $N + M$ zero eigenvalue. The intuition for this is as follows. The null eigenfunction $(a, b) = (0, u)$ is localized at the position of the solution. In a finite pulse train the solution nearly vanishes between the lumps or spikes and therefore the nullspace can be parametrized by linear combinations of the eigenfunctions $(0, u_k)$, where u_k is the null eigenfunction corresponding to a solitary lump or spike positioned at the kth cosine maximum.

7.4 Dynamics

In order to validate our stability calculations and determine the effects of perturbations to the stationary snaking states we turn to time evolution of Eq. (7.1). These simulations are executed in a rotating frame, that is, we set $A(x,t) = e^{-im_0 t}u(x,t)$ and study the evolution of $u(x,t)$. Details of the numerical implementation are documented in section 7.6. Equation (7.1) has a number of conserved quantities including an "energy"

$$\mathcal{E} \equiv \int_\Omega |u_x|^2 - \left[m_0 + m_1 \cos\left(\frac{2\pi x}{\ell}\right)\right] |u|^2 - \frac{1}{2}|u|^4 + \frac{1}{3}|u|^6 \, dx, \tag{7.6}$$

where Ω is the system domain, as well as the L^2 norm or "power" of the solution. We refer to the integrand of Eq. (7.6) as the *energy density* $E(u)$ of the solution. Because of these

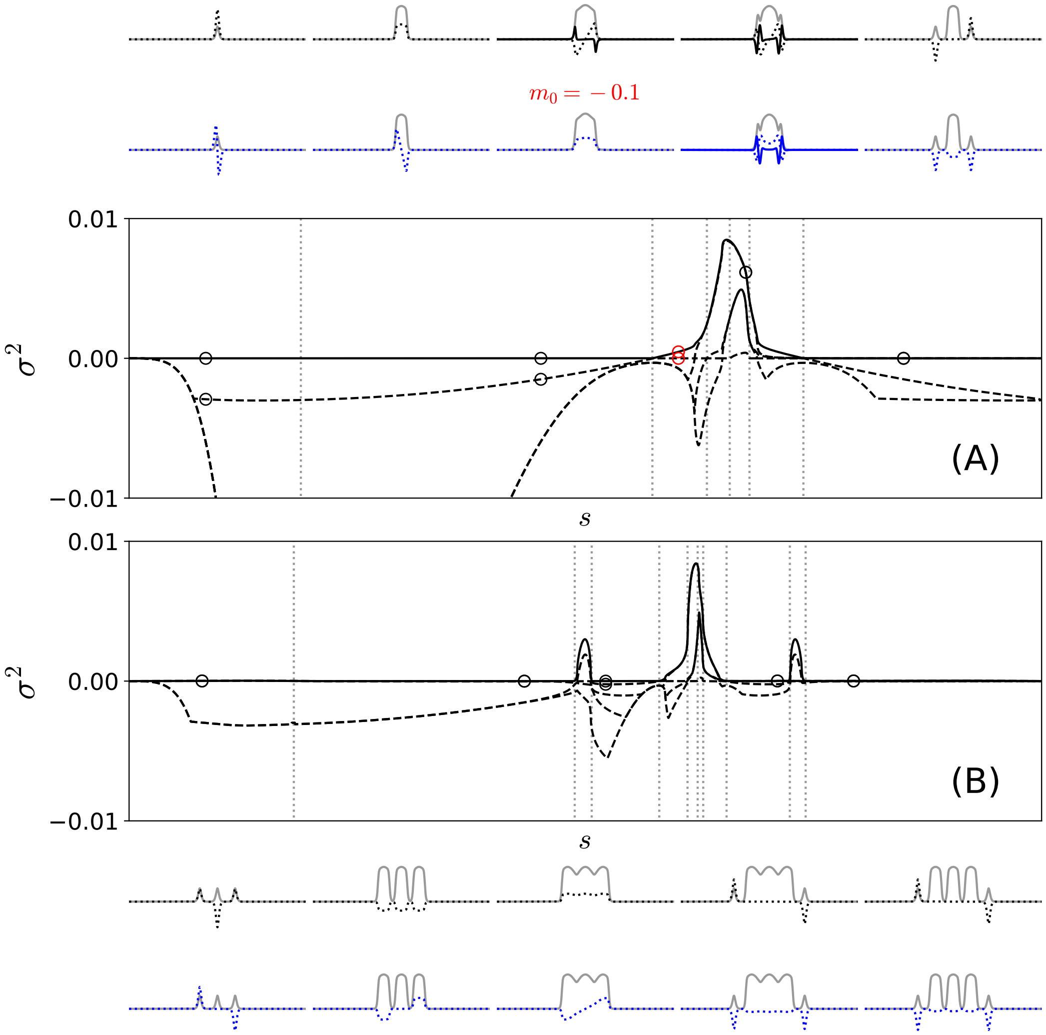

Figure 7.7: The five largest linear stability eigenvalues σ^2 for the solutions in Fig. 7.5 computed as a function of the arclength s. The largest eigenvalue σ^2 is plotted using a solid black line while all smaller eigenvalues are shown using a dashed line. Inset (A) represents the single pulse FPT branch while inset (B) represents the three-pulse FPT branch. Typical base states (grey) and eigenfunctions (largest eigenvalue in black, second largest eigenvalue in blue) on the branch with with an even number of bumps are plotted above (A) with the corresponding results for the branch with an odd number of bumps shown below (B). In each case the real part $\Re[a(x)]$ of the eigenfunction is shown using a solid line while the imaginary part $\Im[b(x)]$ is plotted using a dotted line. In some cases $a(x) \equiv 0$ and we omit it from the eigenfunction plot. The states are mostly computed at $m_0 = -0.15$ (except for the one marked in red); their location is indicated using open circles (which overlap when an eigenvalue is degenerate).

conserved quantities it is often difficult to simulate dynamics on the real line if the solution radiates energy. When the domain is unbounded radiation may escape to infinity and though energy is conserved globally local dynamics appear to be dissipative [121, 122]. In simulations of this type it is popular to replace the real line by a finite interval with artificial damping imposed at the boundaries. We elected not to do this since there is no well-established method for imposing the damping and incorrect methods will result in unphysical reflected waves that interfere with the solution. For the simulations performed here we chose periodic boundary conditions without any artificial damping. This choice allows us to make precise statements about the time evolution of structures on a periodic domain.

This section is divided into three parts. We first focus on the linear dynamics associated to gap soliton solutions, i.e., the time evolution of gap solitons subjected to *small* perturbations. We observe that a perturbed unstable gap soliton typically evolves into a coherent state that oscillates around a distinct stable stationary gap soliton. This observation leads to the second part of the section in which we describe a set of strongly nonlinear dynamics of perturbed stable gap solitons. We report a pair of *unbinding* phase transitions (or *depinning* bifurcations) in which perturbed stable gap solitons transition from being bound (pinned) by the periodic potential and confined in space, to having sufficient energy to propagate in space. These transitions are strongly nonlinear because they require $\mathcal{O}(1)$ perturbations. Aspects of these results are also supported by an asymptotic theory described in Appendix C in which we show that the dynamics are well described by two degrees of freedom. The third section ties these two parts together. We first show that the bound coherent states arising from perturbed linearly stable and unstable gap solitons can be mapped onto the theory we develop in Appendix C. We also show that the theory accurately describes one of the unbinding transitions.

All of the time simulations performed here are done using the same basic set of parameters. The time integration is performed with a split-step method (see Appendix 7.6) with $n = 1000$ spatial grid points and a time step $dt = 0.001$. The method is pseudo-spectral and periodic boundary conditions are adopted. The energy $\mathcal{E}$ of the solution is well conserved during all of the time simulations, varying at most on the order 10^{-9}. To present the time evolution results we have elected to show three solution measures: the amplitude $|u|$ of the solution, its real part $\Re[u]$ and its energy density $E(u)$. Since each of these solution measures has very different scales we plot them with three distinct color maps that are kept consistent throughout the chapter. This is reflected in Figs. 7.8 through 7.12.

Linear dynamics of gap solitons

Time simulation of snaking solutions for $\ell = 10$ replicate known results for low amplitude gap solitons in the semi-infinite gap. We confirmed through the linear stability calculation in Fig. 7.6 and by time-stepping snaking solutions of Eq. (7.1) the well-known result that the 1-bump branch is stable and the 2-bump branch is unstable near the primary bifurcation [160]. Owing in part to energy conservation, asymmetric perturbations such as multiplication by a phase gradient, $e^{i\eta x}$ with $\eta \ll 1$, cause both 1-bump and 2-bump solutions to oscillate in space around the stationary solution. This is similar to known behavior for 1- and 2-bump gap solitons both in the continuum regime [160] and in discrete models [107] although in the present case the oscillations are more visible. We suspect that these oscillations are largely suppressed by the damping boundary conditions and large value of $m_1 \sim 6$ for the confining potential that are typically used in the literature [151, 160] in contrast to the case of periodic boundary conditions with a modest value $m_1 = 0.1$ used here. Stable solutions higher up on the snaking branches have dynamics similar to those near the primary bifurcation. Because solutions retain any energy associated with the initial perturbation these stable solitons all execute qualitatively similar dynamics.

Linearly unstable solutions higher up on the snaking branches also all behave in a systematic fashion. Every N-bump solution exists on a stable and unstable branch segment separated by a right fold (Fig. 7.2). The main difference in the profiles of the solutions on these two segments is the presence of defects on either side as shown in Fig. 7.3. As can be seen from Fig. 7.6 an odd parity eigenfunction is always associated to the most unstable eigenvalue. This eigenfunction acts to grow one of the defects and eliminate the other. This causes an N-bump unstable solution to evolve into an oscillatory solution that cycles around another stable snaking state with $N + 1$ bumps. This evolution can be seen in Fig. 7.8. The solution oscillates in space as can clearly be seen by comparing panels (a) and (b). We emphasize here that although the simulation is conducted in a particular rotating frame (fixed m_0) *all* the snaking solutions with different m_0 remain valid solutions in *this* frame although they now rotate in time. Thus, if the solution migrates towards another snaking solution then generically it is expected to rotate as we observe. As alluded to above we conjecture that the spatial oscillations would be suppressed or at least damped if the radiation given off were allowed to escape. In this case the stable snaking solution to which the dynamics appear to migrate may become an attractor in time.

When appropriate perturbations are selected the unstable symmetric eigenmode can also be observed. In Fig. 7.9 the time evolution of a 3-bump snaking solution (point S3 in Fig. 7.2) is perturbed by the symmetric eigenfunction. The growth of this mode causes the solution to evolve into a breather whose width fluctuates sinusoidally in time. When the solution width expands laterally ($t \sim 200, 500, 700$) the inter-bump height decreases, preserving the L^2 norm. This is best seen in Fig. 7.9(a) or (c). At $t \sim 800$ this process ends when the more unstable asymmetric mode becomes visible. Because the equation is reflection-symmetric this is likely due to the growth of numerical errors in either the initial condition or the subsequent timesteps. Further time evolution (not pictured) confirms that beyond $t = 800$ both asymmetric and symmetric oscillations occur but the solution still remains localized near a 3-bump snaking state.

Like stable forced snaking solutions, stable solutions in the foliated regime also have simple dynamics. We focus on stable solutions with a phase gradient perturbation. Although there are many qualitatively different types of stable solutions in the foliated regime they all have oscillatory dynamics similar to the forced snaking case. To look at one specific case we consider a 1-lump 2-spike solution from the 1-lump branch with a larger phase gradient perturbation, $\eta = 0.1$. The initial solution, point S4 in Fig. 7.4, is the last base state pictured

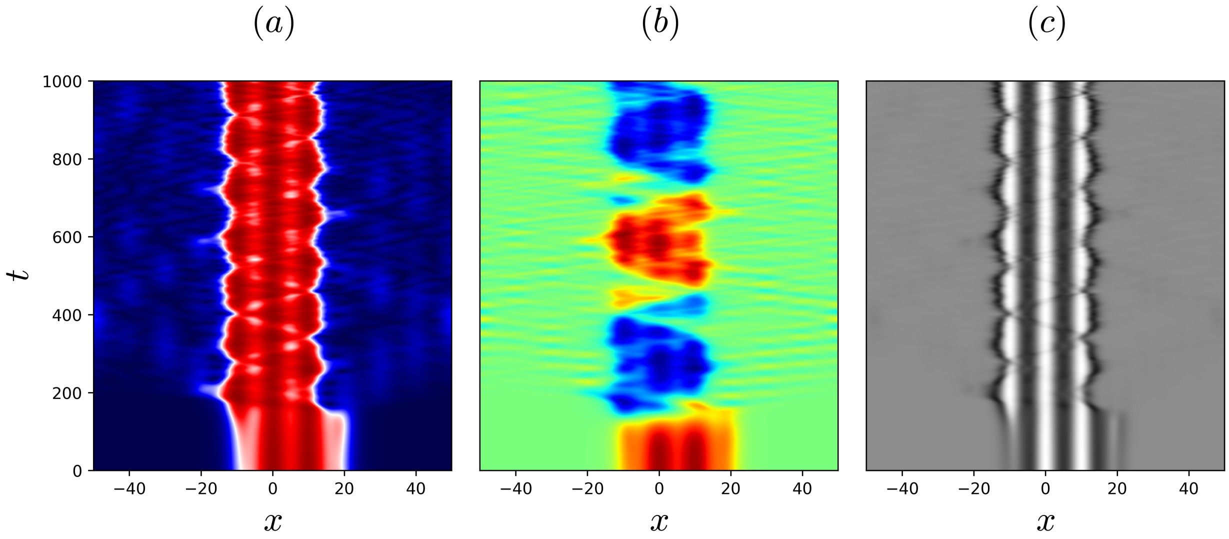

Figure 7.8: Time evolution of an unstable 2-bump snaking solution (point S2 in Fig. 7.2) perturbed by the unstable antisymmetric eigenfunction. The initial condition is the second base state pictured in Fig. 7.6 on the even branch. The simulation is performed with $m_0 = -\frac{3}{16}$, $\ell = 10$. Plot (a) shows $|u|$, (b) $\Re[u]$ and (c) $E(u)$. The solution decays after $t \approx 180$ into an asymmetric oscillatory state that appears to cycle around a stable three-bump snaking solution. Wave radiation is visible in panel (b).

in Fig. 7.7. When the phase gradient is this large the spatial and temporal oscillations are clearly distinguishable (Fig. 7.10). Furthermore the lumps and spikes appear to oscillate independently with oscillation frequencies that depend on the amplitude and spatial extent of $u(x)$. The lump oscillates in space and rotates in time while the spikes maintain their phase and only oscillate in space. The spatial oscillation frequencies of the two spikes are identical but smaller than that of the central lump.

The dynamics arising from the unstable branches of the foliated snaking states are complicated. We only treat two examples here. Although the FPT made up of clearly separated lumps and spikes are stable, the regime near $m_0 \approx -0.15$ includes a variety of unstable solutions as well. As shown in Fig. 7.7 unstable solutions may possess a variety of unstable modes but we only focus here on two examples, and only on the most unstable eigenmodes. The first of these, S5 in Fig. 7.4, is the third base state on the 1-lump branch as pictured in Fig. 7.7. This state has only one unstable eigenfunction and this eigenfunction is odd. The time simulation in Fig. 7.11 shows that the solution decays after $t \approx 500$ in a spectacular fashion into three oscillatory pulses and a single traveling pulse. The spatial extent of the oscillatory pulses varies and hearkens to the fact that lumps and spikes vary in amplitude and width with m_0. The oscillatory pulses are deposited in adjacent wells of the potential and oscillate as trapped states.

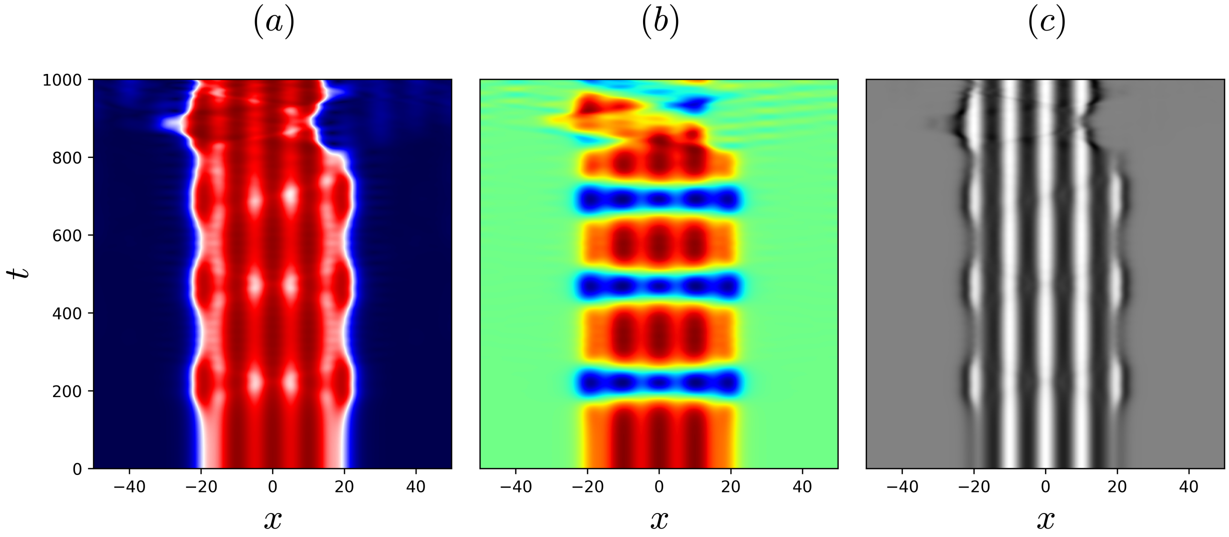

Figure 7.9: Time evolution of an unstable 3-bump solution on the odd snaking branch snaking branch (point S3 in Fig. 7.2) perturbed by the symmetric unstable eigenfunction. The initial condition is the second base state pictured in Fig. 7.6 on the odd branch. The simulation is performed with $m_0 = -\frac{3}{16}$, $\ell = 10$. Plot (a) shows $|u|$, (b) $\Re[u]$ and (c) $E(u)$. As a consequence of the initial perturbation the solution oscillates symmetrically in space while rotating; at $t \approx 800$ the (more unstable) asymmetric mode becomes apparent. Though not shown here, evolution beyond this point is oscillatory and both symmetric and antisymmetric dynamics occur.

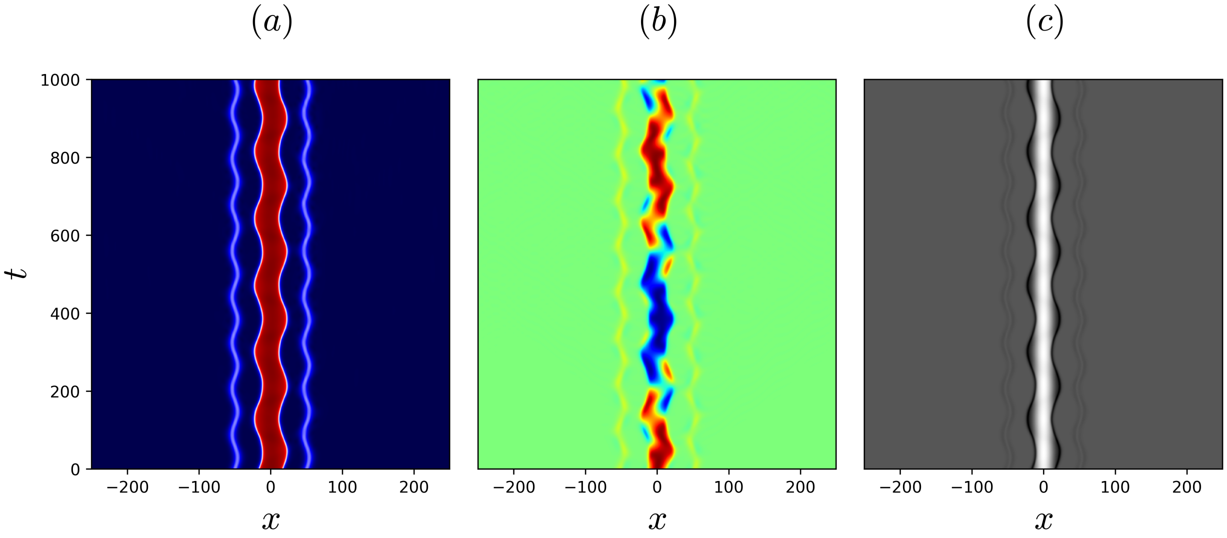

Figure 7.10: Time evolution of a stable 1-lump 2-spike solution on the first foliated snaking branch (point S4 in Fig. 7.4) perturbed by a phase gradient $\eta = 0.1$. The initial condition is the fourth base state pictured in Fig. 7.7 for the 1-lump foliated branch. The simulation is performed with $m_0 = -0.15$, $\ell = 50$. Plot (a) shows $|u|$, (b) $\Re[u]$ and (c) $E(u)$. As a consequence of the initial phase gradient perturbation the central lump oscillates in space and rotates while the spikes at the sides only oscillate. The frequencies of the oscillations depend on the spatial extent of the lumps/spikes.

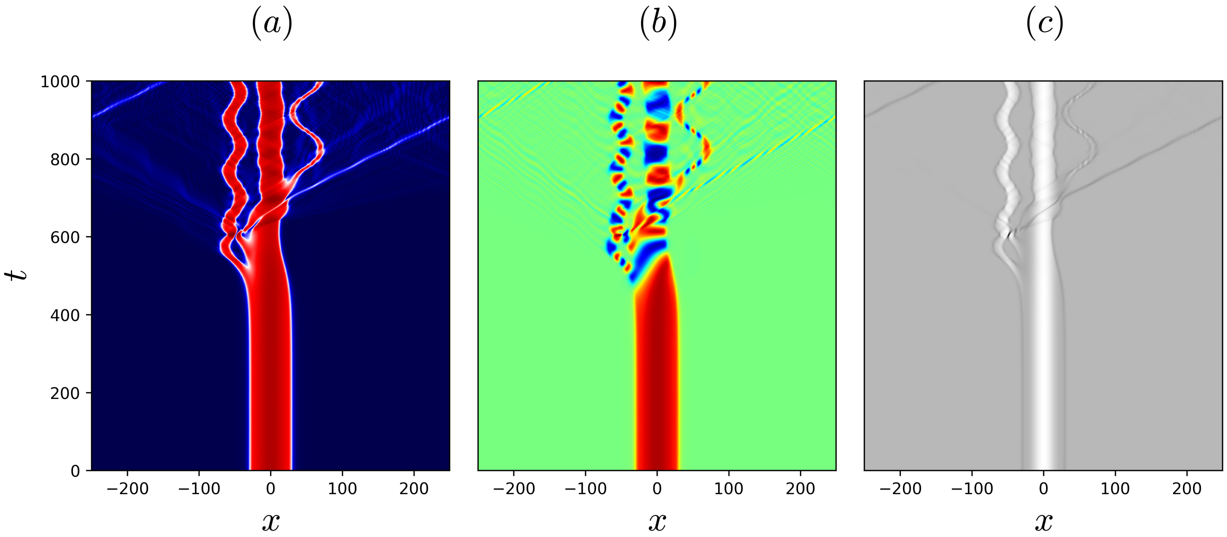

Figure 7.11: Time evolution of a 1-lump unstable solution on the first foliated snaking branch (point S5 in Fig. 7.4) perturbed by an unstable antisymmetric eigenfunction. The initial condition is the third base state pictured in Fig. 7.7 on the 1-lump foliated branch. The simulation is performed with $m_0 = -0.1$, $\ell = 50$. Plot (a) shows $|u|$, (b) $\Re[u]$ and (c) $E(u)$. The solution decays after $t \approx 500$ into four distinct states. Three of these oscillate in space and phase and appear to cycle around a variety of 1-pulse solutions. The oscillation frequencies depend on the height and spatial extent of the pulses. A remaining pulse is shed with a definite average speed to the right and in an infinite domain we expect this "radiation" to continue propagating to infinity.

The last case of instability we consider is one in which one of the most unstable eigenfunctions is of even parity. The base state, S6 in Fig. 7.4, is the fourth on the 1-lump branch as pictured in Fig. 7.7 and the time simulation is shown in Fig. 7.12. The evolution shows that the state quickly evolves into a breather whose width oscillates regularly in time. We have not investigated even parity instabilities systematically but conjecture that many of them manifest themselves in a similar fashion.

Unbinding transitions

The study of traveling solitons in optical latices has a rich history. The specific phenomenon of soliton unbinding and propagation takes the name "mobility" in much of the gap soliton literature. A great deal of work has examined the mobility of solitons in discrete lattices where uniformly traveling solutions do exist; we direct the reader to the review [91] for a comprehensive history. This work includes proofs of existence of traveling solutions [112] and examinations of the effects of phase gradient perturbations on stationary solitons [107]. For example, in [111] the speeds of solitons subject to such a perturbation are computed.

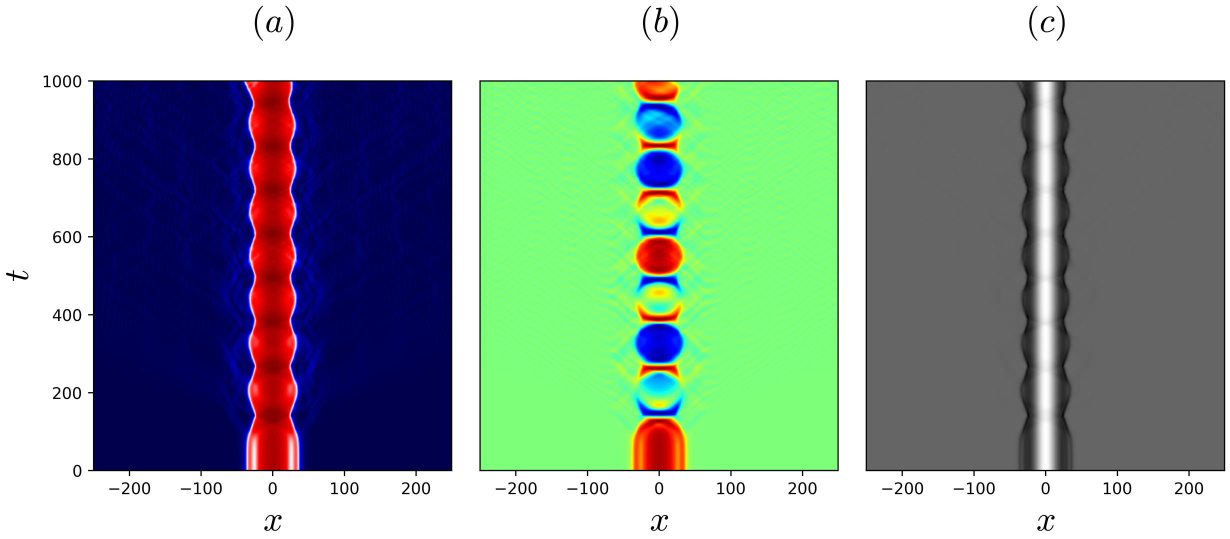

Figure 7.12: Time evolution of a 1-lump unstable solution on the first foliated snaking branch (point S6 in Fig. 7.4) perturbed by the symmetric unstable eigenfunction. The initial condition is the fourth base state pictured in Fig. 7.7 on the 1-lump foliated branch. The simulation is performed with $m_0 = -0.15$, $\ell = 50$. Plot (a) shows $|u|$, (b) $\Re[u]$ and (c) $E(u)$. After $t \approx 100$ the solution decays into a breather that maintains its parity in space but oscillates in space, phase and amplitude.

To our knowledge less analytical work has been done in the continuum context [93, 165]. A notable exception is Ref. [92] that focuses on a PT-symmetric cubic NLSE with spatially periodic modulation in both linear and nonlinear terms and employs an adaptation of the inverse scattering transform to compute soliton speeds analytically in the shallow potential limit. We are unaware of any similar work on gap solitons in the cubic-quintic NLSE studied in this chapter and now turn to examine, both numerically and analytically, the mobility of gap solitons in this context.

Stable stationary gap soliton solutions have a temporal spectrum entirely contained on the imaginary axis and thus oscillate when a small perturbation is added. Since Eq. (7.1) conserves energy it is natural to parametrize perturbed stationary solitons by their extra energy. When this energy is small the dynamics are determined by the linear spectrum of the stationary solution and are thus oscillatory. For larger energies the dynamics are fully nonlinear. When the energy of the perturbed soliton is sufficiently high it unbinds from the potential allowing the fronts flanking the localized state to propagate. Some of this dynamical behavior is captured by the strongly nonlinear asymptotic analysis contained in Appendix C.

We first turn to asymmetric perturbations. In line with the theory (Appendix C) we consider perturbations with a uniform phase gradient so that the initial condition is $u(x, 0) = e^{i\eta x}u_0(x)$ where $u_0(x)$ is a stationary gap soliton solution. As shown in Appendix C the

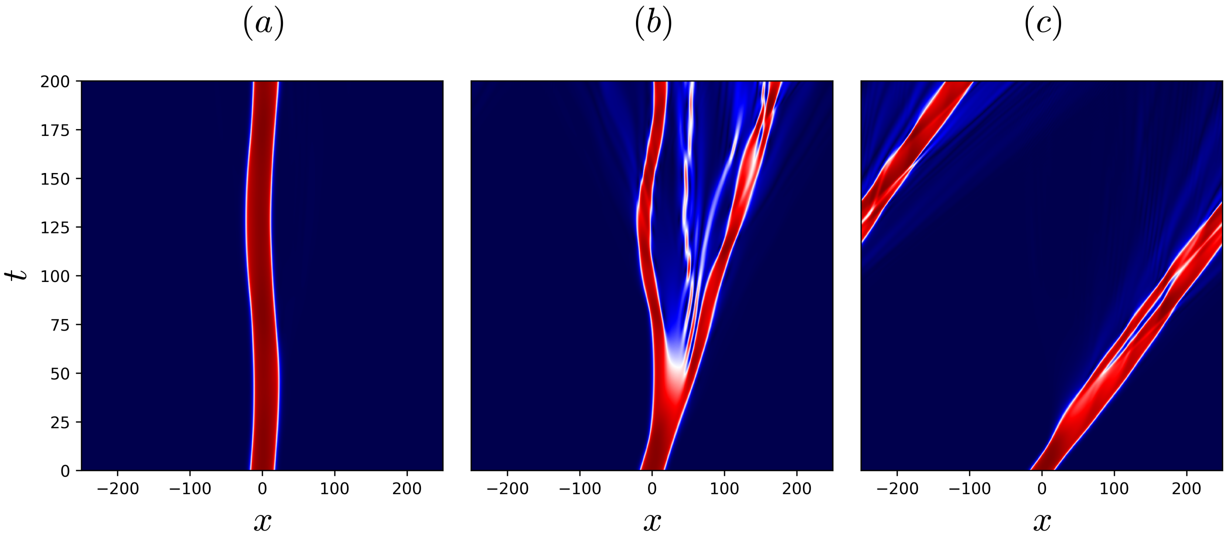

Figure 7.13: Time evolution of a stable 1-lump solution on the first foliated snaking branch (point S7 in Fig. 7.4) with a phase gradient perturbation of magnitude (a) $\eta = 0.1$, (b) $\eta = 0.4$ and (c) $\eta = 1$ shown in terms of a space-time plot of $|u(x,t)|$. The simulation is performed with $m_0 = -0.15$, $\ell = 50$. For small η (a) libration occurs. As η is increased the solution begins to unbind (b) and when η is sufficiently large the solution travels with nonzero average speed (c).

dynamics of the center of mass of such an initial condition follow that of a mathematical pendulum. Specifically, as η is increased from zero the motion transitions from the "libration" regime, in which the soliton's center of mass oscillates with zero average speed, to the "rotation" regime, where the center of mass moves with nonzero average speed. Three snapshots of this transition are shown in Fig. 7.13. In panel (a) of the figure a 1-lump gap soliton (solution S7 from Fig. 7.4) with an added initial phase gradient $\eta = 0.1$ executes libration motion. As the initial phase gradient is increased the soliton begins to depin and splits into pulses some of which move with a nonzero average speed (rotation regime) while others remain pinned executing libration. This is shown in panel (b) of Fig. 7.13 where $\eta = 0.4$. As the leading pulse propagates it deposits "mass" into successive wells of the potential. Because the equation is mass-preserving the leading pulse is drained of mass as this occurs and may itself become trapped (Fig. 7.14). Further increase in η shifts the motion more solidly into the rotation regime. For large enough η the bulk of the pulse does not split but moves with a single nonzero average speed, Fig. 7.13(c). Although a small amount of mass appears to escape from the moving pulse the fraction of mass lost is trivial compared to the total. On a periodic domain integration for longer times reveals a stationary state in which the pulse travels at a same constant average speed. The average speeds of the center of mass of these pulses are well predicted by our asymptotics (see below).

The crossover from the libration to the rotation regime is associated with complex behavior, particularly in the long time limit. In the early stages of unbinding solution S7 propagates with a nonzero average speed but still loses mass in the potential. A long time simulation is shown in Fig. 7.14. The solution propagates while shedding pulses which are trapped by the potential much like occurs for an unstable solution in Fig. 7.11. Because the domain is periodic the leading pulse eventually collides with the remains of the original state near $t = 700$, giving up most of its mass but allowing a small and faster untrapped pulse to propagate away on the far side. This reconnection is facilitated by the potential and is unlike the true soliton behavior of the unforced NLSE since mass is exchanged between the colliding pulses. A later stage of this dissolution process for a larger perturbation gradient, $\eta = 0.8$, is shown in Fig. 7.15. Here the bulk of the mass travels with a nonzero average speed. Fracturing of the leading pulse leads to smaller pulses that are slower but still untrapped Only a small amount of mass is trapped in the wells of the potential. As time progresses splitting of the pulses continues until masses traveling at a range of average speeds are present. Of particular interest are the small amplitude quasistationary structures deposited by the drifting pulse; these represent lost mass trapped in different wells of the potential. We have not investigated this behavior for arbitrarily large domains but here, in a finite domain, the solution appears to reach a pseudo-steady state. We conjecture that on an infinite domain the initial pulse or soliton disintegrates in a similar fashion, and eventually ceases to exist as an identifiable structure. As η increases further the pulses travel at larger and larger average speeds and appear to execute fewer oscillations. These oscillations are never eliminated, however, since states traveling at constant speed cannot exist in equations like Eq. (7.1) when m_1 is nonzero, cf. [124].

We next examine the effect of a symmetric perturbation on the unbinding transition. In order to study symmetric modes we consider a phase perturbation of a stationary gap soliton that is symmetric with respect to the soliton's center of mass. Specifically, we take initial conditions of the form $u(x, 0) = e^{i\rho(x-\alpha)^2}u_0(x)$, where $x = \alpha$ represents the location of the soliton's center of mass.

Because of the mass-conserving property of Eq. (7.1) symmetric perturbations of sufficient amplitude cause a qualitatively different transition from antisymmetric ones. As in the antisymmetric case the local phase gradient at the position of the fronts flanking the localized state determines the direction of the front motion. In the antisymmetric case the phase gradient at both fronts is identical and both fronts move in the same direction with the same speed, regardless of whether the motion is a libration or a rotation. The main qualitative difference in the symmetric case is that the sign of the phase gradient is now opposite at the two fronts. As a result for small ρ each front moves with the same speed but in *opposite* directions generating a state that is a symmetric analog of libration, i.e., a breathing state, as shown in Fig. 7.16(a) where $\rho = 0.01$. As can be discerned from the coloring of the plot the amplitude of the pulse grows when its width decreases and vice versa. Thus the dynamics conserve the soliton mass. When ρ is increased to a sufficient extent the fronts acquire a nonzero mean speed and propagate outward away from the center of the structure, Fig. 7.16(b). This causes a competition between the growth in width of the pulse and decrease

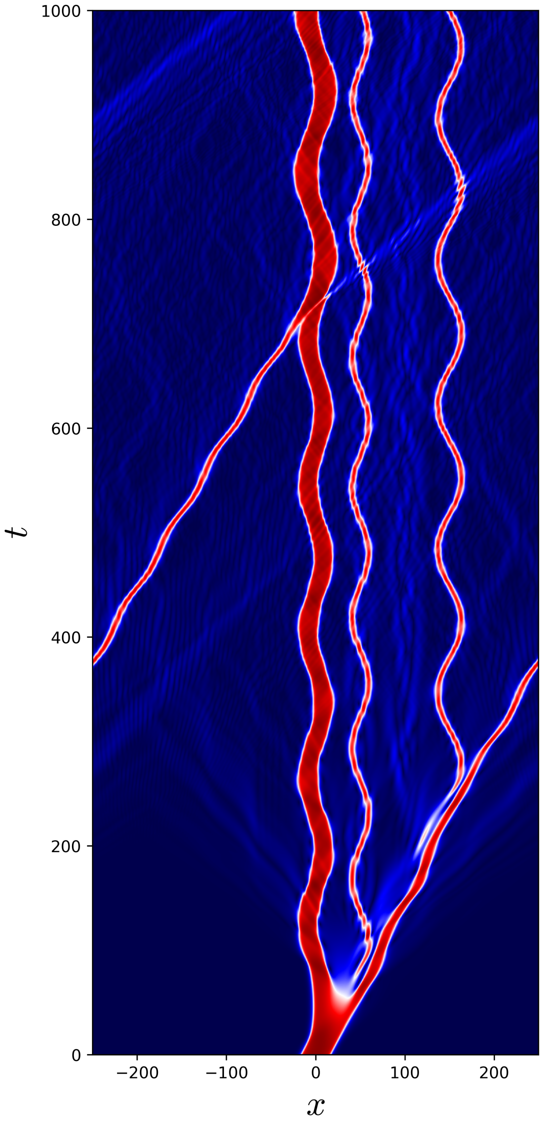

Figure 7.14: Long time evolution of a stable 1-lump solution on the first foliated snaking branch (point S7 in Fig. 7.4) with a phase gradient perturbation of magnitude $\eta = 0.3$ shown in terms of a space-time plot of $|u(x,t)|$. The simulation is performed with $m_0 = -0.15$, $\ell = 50$. The simulation shows that initially the pulse propagates with the theoretically predicted velocity but soon breaks up at $t \approx 50$ into an oscillating structure and a propagating pulse which subsequently sheds mass into the wells of the potential depositing a sequence of trapped pulses. Because the domain is periodic a collision between the remaining traveling pulse and the original pulse occurs near $t \approx 700$ resulting in the reabsorption of most of its mass by the original pulse and diffraction of the traveling pulse that remains.

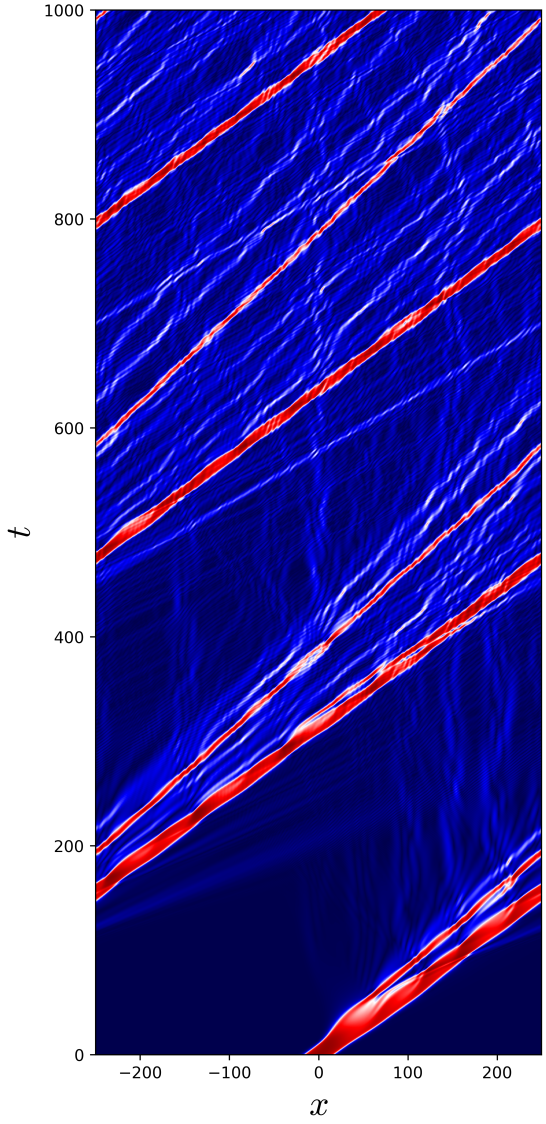

Figure 7.15: Long time evolution of a stable 1-lump solution on the first foliated snaking branch (point S7 in Fig. 7.4) with a phase gradient perturbation of magnitude $\eta = 0.8$ shown in terms of a space-time plot of $|u(x, t)|$. The simulation is performed with $m_0 = -0.15$, $\ell = 50$. The simulation shows that even at late times the solution continues to propagate and shed mass into the wells of the potential. Because the domain is periodic a type of pseudo-steady state is achieved at very long times in which the solution mass disperses into components propagating at a range of speeds.

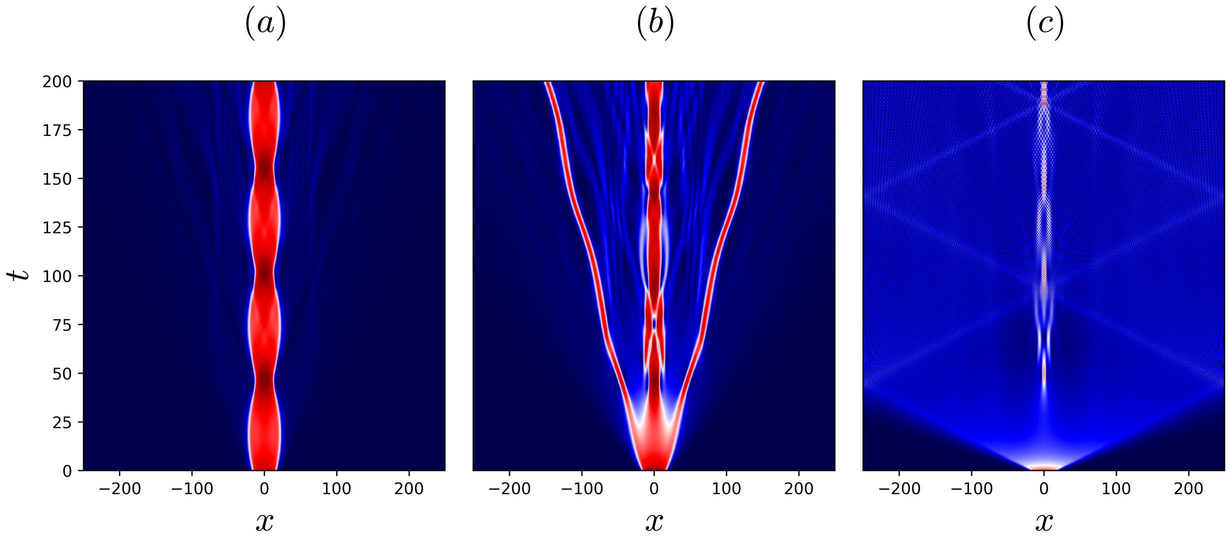

Figure 7.16: Time evolution of a stable 1-lump solution on the first foliated snaking branch (point S7 in Fig. 7.4) with a symmetric phase gradient perturbation of magnitude (a) $\rho = 0.01$, (b) $\rho = 0.02$, (c) $\rho = 0.1$ shown in terms of a space-time plot of $|u(x,t)|$. The simulation is performed with $m_0 = -0.15$, $\ell = 50$. For small ρ (panel (a)) breathing motion occurs. As ρ is increased the solution begins to unbind symmetrically and the fronts bounding the pulse propagate in opposite directions with identical speeds (panels (b) and (c)).

in its amplitude. For $\rho = 0.02$, panel (b), the fronts detach from the central structure in the form of two traveling pulses, and leave a librating or breathing mode at the center. For even larger gradients, $\rho = 0.1$ in panel (c), the soliton expands yet more rapidly although a breathing structure in the center remains. We have found a qualitatively similar sequence of transitions for other symmetric perturbations, such as $e^{i\rho|x-\alpha|}u_0(x)$, and conjecture it to be generic.

Perturbations that involve a combination of symmetric and asymmetric parts exhibit similar “two regime” dynamics. We do not perform a complete analysis of the general case, $e^{i\eta(x-\alpha)+i\rho(x-\alpha)^2}u_0(x)$, but provide two examples in Figs. 7.17 and 7.18. In Fig. 7.17 we set $\eta = 0.1$, $\rho = 0.01$ and show that the gap soliton falls into a libration regime in which both symmetric and antisymmetric oscillations of different periods occur. When η and ρ are increased sufficiently the soliton undergoes an unbinding transition similar to those described above albeit asymmetrically. That is, the fronts on either side propagate outward at different speeds. This is shown in Fig. 7.18 where $\eta = 0.2$ and $\rho = 0.02$. Initially the two fronts propagate in opposite directions with different speeds. In a short time the structure is shorn apart when a series of pulses escape to the right leaving a librating mode at the origin. The process of unbinding is evidently complex and we do not attempt to analyze it further. In principle one could predict thresholds in the (ρ, η) parameter space for the

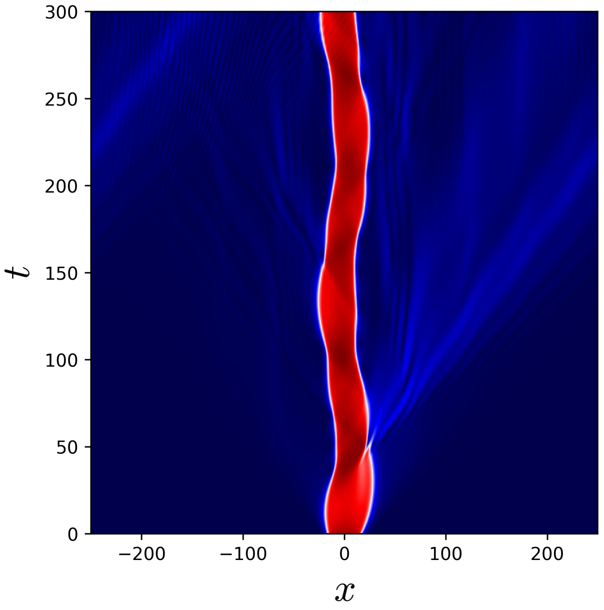

Figure 7.17: Time evolution of a stable 1-lump solution on the first foliated snaking branch (point S7 in Fig. 7.4) with a phase perturbation with $\eta = 0.1$ and $\rho = 0.01$ shown in terms of a space-time plot of $|u(x,t)|$. The simulation is performed with $m_0 = -0.15$, $\ell = 50$.

unbinding transition but we leave this type of analysis to future work.

Analysis of coherent states

In this section we project the time evolution dynamics of the previous sections onto the two degrees of freedom described by the theory in Appendix C. This theory is designed to capture the dynamics of the center of mass of a pulse-like solution, for which we derive an ODE, and is therefore applicable to dynamics governed by spatially asymmetric modes. Concretely, the theory applies to scenarios such as those portrayed in Figs. 7.8, and 7.10 but not those in Figs. 7.9 or 7.12. The theory also applies in situations where the center of mass has a nonzero average speed as in the case of the first unbinding transition (Fig. 7.13).

We divide this section as follows. We first discuss the application of our theory in the libration regime for a pulse with a phase gradient perturbation. In this case the PDE initial condition can be mapped directly to an initial condition for the ODE. Next we describe the evolution shown in Fig. 7.8 in which an unstable solution evolves into an oscillatory coherent state. In this case we do not know the initial conditions for the ODE. Finally, we discuss the application of the theory in the rotation regime and compute the average speed of a traveling pulse.

As a first application of the theory in Appendix C we turn to the evolution of the single pulse solution S7 with a phase gradient perturbation $\eta = 0.1$. This is the same simulation

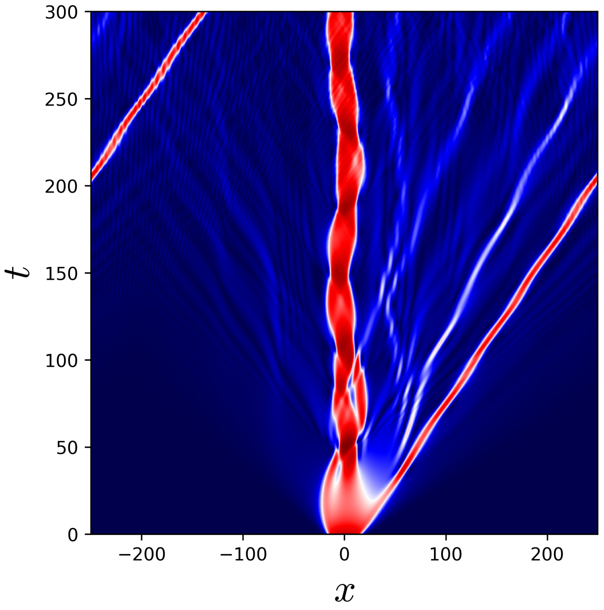

Figure 7.18: Time evolution of a stable 1-lump solution on the first foliated snaking branch (point S7 in Fig. 7.4) with a phase perturbation with $\eta = 0.2$ and $\rho = 0.02$ shown in terms of a space-time plot of $|u(x,t)|$. The simulation is performed with $m_0 = -0.15$, $\ell = 50$.

as that shown in Fig. 7.13(a) but we integrate the solution until $t = 3000$. Although the full time evolution plot is omitted here the dynamics are nearly identical to those of the central pulse in Fig. 7.10. The Ansatz for the solution that is used in our theory is

$$A(x,t) = e^{i\int \omega(t)dt + i\frac{\dot{\alpha}(t)}{2}(x-\alpha)} v(x,t)$$

where v is a near-stationary pulse and α is its time-dependent center of mass (see Appendix C for more details). At every time step we compute the center of mass, $x = \alpha(t)$, of the solution using Eq. (7.8) and extract the phase $\int \omega \, dt$ from the nearest point on the mesh to $x = \alpha$. We fit a linear regression to $\int \omega \, dt$ and subtract the trend, producing $\Omega(t)$. The time series for α and Ω are easiest to understand in Fourier space and are shown in Fig. 7.19(a) and (b). These signals can be messy and difficult to differentiate with respect to time which is required to compare the numerical results with the ODE description. To regularize them we set to zero all Fourier amplitudes corresponding modes with wave number outside the boundary of the figure. After regularization the phase ω is reconstructed by differentiating Ω in Fourier space and adding back the slope of the trend in real space. Finally, a snapshot of the solution amplitude is shown at a fixed time in Fig. 7.19(c) in order to map the pulse width onto the theory. Here we show the theoretically predicted pulse width L (dashed black line) according Appendix C along with an empirically determined width (grey line). These lines indicate the locations of the fronts bounding the structure at each instant in time.

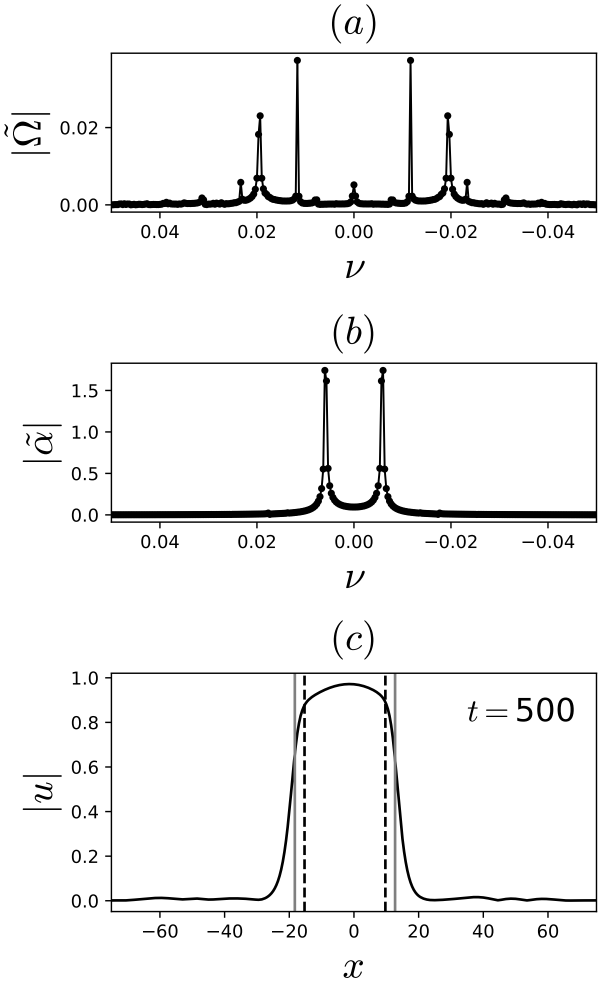

Figure 7.19: Amplitude of a discrete Fourier transform of the time series for (a) $\Omega(t)$ and (b) $\alpha(t)$ as a function of the Fourier space wave number ν for the time evolution of solution S7 with $\eta = 0.1$. All Fourier amplitudes corresponding to frequencies beyond the domain size are set to 0. (c) $|u(x, 500)|$ on the interval $[-100, 100]$ along with lines denoting the positions of the fronts. Each pair of lines is placed symmetrically with respect to $\alpha(500)$: width $L = 25$ (black dashed) and width $L = 31$ (grey).

We evaluate the accuracy of the ODE description of the PDE dynamics (Eqs. (C.3)-(C.4)) using three distinct projections as depicted in Fig. 7.20. The first of these, (a) in the figure, uses the energy of the solution (Eq. (7.6)). We plot the PDE energy, $\mathcal{E}$, using a dashed black line which is conserved along with the energy in the Ansatz used in the theory, Eq. (C.1). After performing the energy integral with Eq. (C.1), the *Ansatz energy* becomes a function of α and $\dot{\alpha}$ ($\mathcal{E} = f(\alpha, \dot{\alpha})$) which we evaluate using the measured signal. Because of inaccuracies arising from the numerical differentiation of the signal near the boundary of the time domain we suppress the plotted signal near the boundary both here and in subsequent plots in this section. A red line denotes the average of the Ansatz energy. Though the Ansatz energy fluctuates in time its average represents approximately $\sim 84\%$ of the total energy. This mismatch is likely a consequence of the fact that the Ansatz is a low order approximation allowing energy loss in the form of radiation (which is not in our Ansatz), and that the sampling of $\alpha(t)$ is insufficiently precise. This is potentially the cause of the very slight drift in Ansatz energy (Fig. 7.20(a)) seen over the sampling interval.

The second projection, Fig. 7.20(b), is onto the phase space of Eq. (C.4). We plot the trajectory in the space $(\beta, \dot{\alpha})$ where $\beta = \sqrt{\frac{2\lambda\ell}{\pi}\sin\left(\frac{\pi L}{\ell}\right)}\sin\left(\frac{\pi\alpha}{\ell}\right)$. In these variables true trajectories of the ODE are circles. By inspecting Eq. (C.1) it is evident that an initial phase gradient perturbation η corresponds to an initial value $\dot{\alpha}(0) = 2\eta$ for the ODE. The ODE trajectory corresponding to this initial condition is shown as a red circle. In order to plot the sampled dynamics the pulse width, L, must be specified. The theory predicts that $L = 25$ (shown in black) but we also plot an empirically chosen width $L = 31$ in grey (see Fig. 7.19(c)). Although the theoretical prediction is not far off, the grey curve is in near perfect alignment while the black curve is not. We suspect that this has to do with the extent to which the Ansatz can model lump states at *lowest* order and conjecture that a higher order asymptotic calculation would lead to an improved prediction of the location of the two fronts.

The last projection onto the ODE, Fig. 7.20(c), examines the prediction for the phase variable ω. The theory predicts a phase $\omega = \frac{3}{16} + \epsilon\,\omega_2(t) \equiv \omega_T$ which we plot for $L = 25$ (black) and $L = 31$ (grey) along with the sampled signal $\omega \equiv \omega_S$ (blue). The averages of the signals are plotted with dashed lines. The figure shows that despite the fact that the signals are not perfectly periodic the dominant period is the same for all three and ω_S is exactly out of phase with the other two. When we use the theoretically predicted width $L = 25$, we find that the signal amplitudes of ω_T and ω_S appear to be in good agreement although their means differ. However, with the empirically determined width $L = 31$ the means are in good agreement. It is worth noting here that because the evolution of the PDE solution behaves as $e^{i\int\omega\,dt}$ the mean of ω provides the dominant contribution to the oscillations observed in the $\Re[u]$ plots earlier in this section.

Next we turn to the evolution in Fig. 7.8. Because there is an initial transient during which the initial condition destabilizes before entering a coherent state we measure the signals α and ω only after $t \sim 300$. The signals are much noisier in this case although the same double peak signal is present for α (not pictured). In this case we have chosen not to set an

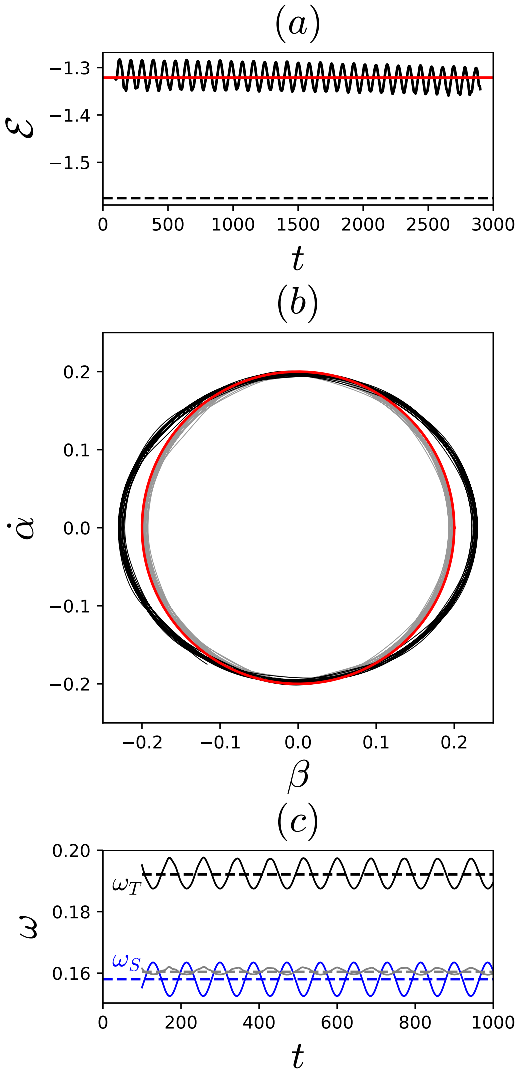

Figure 7.20: ODE projections for dynamics of solution S7 with $\eta = 0.1$. (a) The PDE energy $\mathcal{E}$ (Eq. (7.6)) as a function of time (black dashed) along with the instantaneous energy $\mathcal{E}(t)$ from the Ansatz (C.1) (black solid) and its mean (red). (b) $\alpha(t)$ in the phase space of Eq. (C.4) where $\beta = \sqrt{\frac{2\lambda\ell}{\pi}\sin\left(\frac{\pi L}{\ell}\right)}\sin\left(\frac{\pi\alpha}{\ell}\right)$. Trajectories of the sampled signal are plotted for the cases $L = 25$ (black) and $L = 31$ (grey) along with the analytical trajectory for the initial condition $\dot{\alpha}(0) = 0.2$ (red). (c) The sampled signal ω_S as a function of time (blue) along with ω_T for the cases $L = 25$ (black) and $L = 31$ (grey). The means of the signals are shown with a dashed line. To make the periods distinguishable the signals are plotted up to $t = 1000$ though the time evolution is carried out to $t = 3000$.

empirical pulse width and use the analytical prediction $L = 25$. The ODE projections are shown in Fig. 7.21. Here the Ansatz energy, panel (a), appears to be much noisier than in the previous case. This is likely due both to the relative increase in radiation which is visible in Fig. 7.8 and also to the fact that the PDE solution does not map directly to a single ODE trajectory. This is because the projection of the PDE dynamics provides a 1D picture of the dynamics in the ODE phase space. Unlike the case of a phase gradient perturbation, which maps to a unique ODE trajectory, arbitrary perturbations of the PDE solutions can lead to energy transfer between different PDE modes potentially resulting in the evolution of the ODE energy when projected down to the ODE phase space even though the ODE conserves energy.

Despite the noise, the average energy is again close to the total PDE energy and we therefore argue that the model captures a significant portion of the dynamics. Using the mean Ansatz energy an initial value for $\dot{\alpha}$ can be constructed by setting $\alpha = 0$. The ODE trajectory corresponding to this energy level is plotted in Fig. 7.21(b) in red along with the sampled trajectory for α in black. The solution can be seen to oscillate near the red line although occasionally it makes deviations. Since the PDE dynamics occur in a nominally infinite-dimensional phase space we cannot hope to capture all the details using a 1D model. However, the agreement that we see in panel (b) of the figure suggests that despite this fact our 1D theory does indeed capture a large portion of the dynamics even though energy contained in other PDE modes does cause deviations from the ODE phase space trajectory.

Panel (c) of Fig. 7.21 shows the behavior and prediction of the phase. As is obvious from Fig. 7.8(b) the phase behavior in this simulation is complicated and sampling ω is somewhat messy. Despite regularizing the signal the sampled phase (blue curve) likely has an exaggerated amplitude although the mean should be accurate. We find that the theoretical prediction with $L = 25$ agrees well with this mean (black line) and this is so for the oscillation period as well. The oscillations do not, however, agree in amplitude.

To close this section we look at the theoretical predictions in Appendix C for the rotation regime. Specifically we return to the evolution of solution S7 with a large phase gradient perturbation (Fig. 7.13(b) and (c)). Our theory predicts that for sufficiently large phase gradients the center of mass of the solution will begin to propagate with nonzero mean speed. This speed can be computed analytically as done in Appendix C. In Fig. 7.22 we show this analytical prediction (black) along with the numerically measured speeds for increasing initial phase gradient η (blue points). The simulations are carried out by timestepping the solution to $t = 100$ and tracking the center of mass $x = \alpha(t)$. A linear regression is fit to the trajectory in order to measure the speed. For lower values of η, nearer the transition from the libration regime, the speed measurement is less accurate. By $\eta = 0.8$ the measured and predicted speeds are in near perfect agreement. Although not shown here we have verified that Eq. (C.3) also becomes increasingly accurate as η moves farther into the rotation regime.

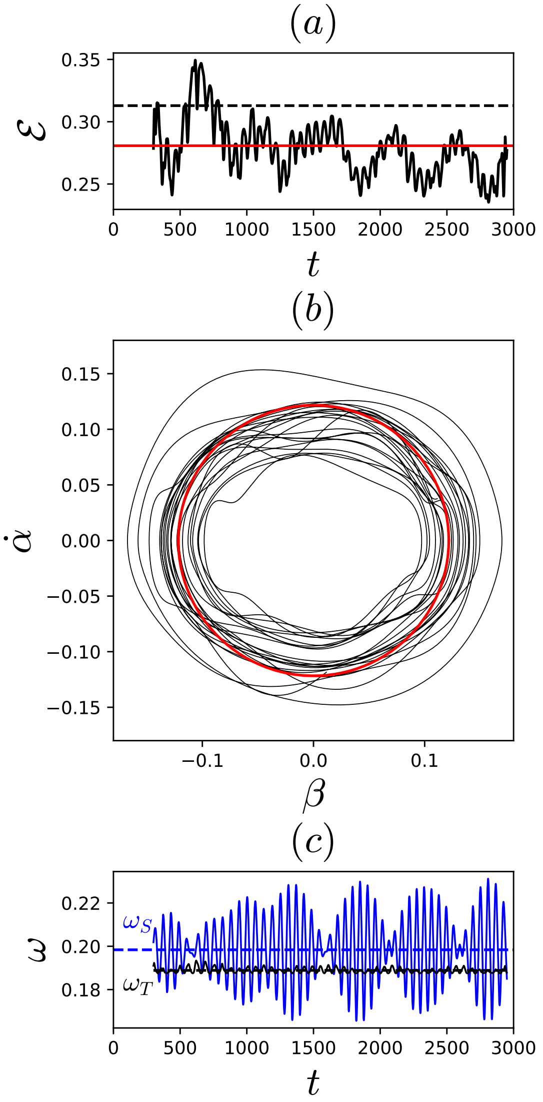

Figure 7.21: ODE projections for dynamics of Fig. 7.8. (a) The PDE energy $\mathcal{E}$ (Eq. (7.6)) as a function of time (black dashed) along with the instantaneous energy $\mathcal{E}(t)$ from the Ansatz (C.1) (black solid) and its mean (red). (b) $\alpha(t)$ in the phase space of Eq. (C.4) where $\beta = \sqrt{\frac{2\lambda\ell}{\pi}\sin\left(\frac{\pi L}{\ell}\right)}\sin\left(\frac{\pi\alpha}{\ell}\right)$, with the black line showing the PDE trajectory for the sampled signal with $L = 25$ and the red line the trajectory from Eq. (C.4) with initial condition determined by the mean Ansatz energy. (c) The sampled signal ω_S as a function of time (blue) along with ω_T for the case $L = 25$ (black). The means of the signals are shown with a dashed line.

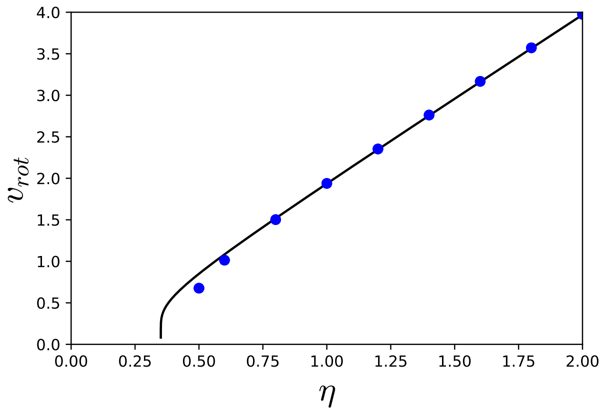

Figure 7.22: Average speed v_{rot} of the center of mass of solution S7 as a function of η, the phase gradient of the applied perturbation. The theoretical prediction given by Eq. (C.6) is shown in black while the empirical speed obtained from the simulation results is shown in blue.

7.5 Discussion

Owing to the enormous body of work on gap solitons we begin the discussion by emphasizing the key new results in this work.

- We show that the lengthscale of the periodic potential, ℓ, can greatly affect the bifurcation structure of the solutions that are present in the semi-infinite gap. We report *new* gap solitons exhibiting foliated snaking along with their bifurcation structure and stability. Specifically we show that solutions are either "multipulse solitons" exhibiting classical snaking or "soliton complexes" exhibiting foliated snaking, depending on ℓ and m_1.
- We demonstrate that gap solitons depin in a systematic fashion when perturbed by asymmetric and symmetric phase gradients.
- We provide a strongly nonlinear theory to describe the dynamics of gap solitons subject to a phase gradient perturbation. This theory accurately predicts the speeds of rapidly propagating solitons.

The impact of the lengthscale of the potential, ℓ, is derived from its relation to the spatial decay rate of fronts in the unforced equation. When $m_1 = 0$ Eq. (7.2) has a unique lengthscale, λ, determined by the decay rate of fronts that connect $u = 0$ to $u = \frac{\sqrt{3}}{2}$. These fronts have a spatial decay rate equal to the spatial eigenvalue of the linearization around $u = 0$. These fronts are used in our asymptotic analysis in Appendix C. This lengthscale persists when $m_1 > 0$ and its value relative to the imposed lengthscale of the potential determines the bifurcation structure of localized solutions. In the limit $\ell \ll \lambda$ the fronts span multiple periods of the potential and classical snaking results. In the gap soliton literature these states are frequently referred to as multipulse solitons. In the opposite limit, $\ell \gg \lambda$, a pair of fronts fits inside each period of the potential thus supporting a single pulse at every cosine maximum. This is the foliated snaking regime and the resulting states are frequently known in the literature as soliton complexes. We show that the choices $\ell = 10$ and $\ell = 50$ are able to capture these two distinct regimes although m_1 must be sufficiently large to establish foliated snaking. In sufficiently shallow potentials we conjecture that classical snaking occurs always.

Turning to dynamics we show that gap solitons depin from the potential under sufficiently large phase gradient perturbations and capture this behavior with a strongly nonlinear theory. Through our theory of soliton depinning we were able to identify the two broad dynamical regimes (libration and rotation) that result from phase gradient perturbations. Specifically, the theory shows that the dynamics of the center of mass behaves like a pendulum. By extrapolating from the numerical simulations of symmetric perturbations we can conjecture that each front bounding the localized states has this pendulum-type behavior. Of particular interest is our observation of soliton fission, in which a depinned soliton radiates energy and breaks up into less energetic components that can then become trapped again.

The main natural extension of this work is to higher dimensions, cf. [44]. A significant literature already exists on localized snaking solutions in discrete and continuous models in two and three dimensions. To our knowledge the effects of the potential lengthscale have not been studied in these contexts and foliated snaking is likely to play an important role.

Further extension of this work to study of the effects of ℓ on gap solitons in higher gaps is also envisaged. These gap solitons are quite different than those in the semi-infinite gap studied here since there is no stable stationary front when $m_1 = 0$ out of which they can be constructed. Of course, the possibility that classical and foliated snaking may be differentiated in experiments in photonic systems is also exciting. Some work along these lines has been initiated in dissipative systems that also exhibit forced snaking [76] but we are not aware of any such work in optical systems.

7.6 Numerical methods

Linear stability calculations

Temporal stability calculations were performed by discretizing the linear eigenvalue problem using pseudo-spectral methods [147]. After discretization the block off-diagonal matrix eigenvalue problem for the eigenvalue σ was transformed to one of half the dimension for the eigenvalue σ^2.

As a pre-processing step for the stability calculations we transfer the ODE solutions to a uniform mesh by interpolation and then run a series of Newton iterations to increase the accuracy of the solution. Away from bifurcation points we do this using a Newton Conjugate

Gradient method with preconditioning as described in [160]. The solution is approximated at 1000 points with pseudo-spectral derivatives and the Newton iterations are run until $\|\mathcal{N}(u)\|_2 \leq 10^{-14}$. Despite the comments in [158] we observe failure of this method nearby fold bifurcations. At these points the Jacobian is rank-deficient and unchecked Newton steps along its null space typically lead to divergence. We remedy this by performing a singular value decomposition of the Jacobian at each Newton update step and subtract off the projection of the Newton update along the singular vectors whose singular value falls below some threshold. At degenerate folds we typically observe that more singular values fall below the threshold as the Newton updates proceed. This method eliminates any Newton descent along the selected directions. Thus in order to optimize the accuracy of the solution it is important not to subtract off projections until the associated singular value is small. The threshold for this procedure is sensitive to the number of points in the discretization and undoubtedly the accuracy of the conjugate gradient calculations. After appropriately tuning the threshold, we observe a typical convergence to $\|\mathcal{N}(u)\|_2 \leq 10^{-11}$ using this method.

Time evolution simulations

Time-stepping simulations are implemented with the split-step method Eq. (3.7). Details can be found in [160]. Because (3.7) corresponds to rotations in either real or Fourier space it preserves the L^2 norm and energy of the solution up to numerical errors. We observe good energy preservation for long simulation times.

Computation of the center of mass

In this section we detail the numerical implementation of the center of mass detection. A natural definition for the center of mass, $x = \alpha$, is

$$\alpha \equiv \frac{1}{||u||}\sqrt{\int_\Omega x u^2 \, dx}. \tag{7.7}$$

However, on periodic domains Eq. (7.7) is not straightforward to implement. This is because the weight x in Eq. (7.7) is not a periodic function. If the solution stretches across the boundary of the domain then the weight is incorrect. Specifically, Eq. (7.7) will give the correct center of mass on an interval but not on a circle. Solving the problem of properly weighting u to compute the center of mass on a circle is nontrivial since we only have access to a numerical sample of $u(x)$ and not the function itself, and of course we do not know α a priori. We therefore require a method that only uses integrals over $u(x)$.

We propose the following method to determine α. First we define the constants A and

B,

$$\begin{aligned}
A &= \int_\Omega \sin\left(\frac{2\pi x}{D}\right) u^2(x)\,dx \\
&= \cos\left(\frac{2\pi\alpha}{D}\right)\int_\Omega \sin\left(\frac{2\pi z}{D}\right) u^2(z-\alpha)\,dz - \sin\left(\frac{2\pi\alpha}{D}\right)\int_\Omega \cos\left(\frac{2\pi z}{D}\right) u^2(z-\alpha)\,dz \\
&\approx -\sin\left(\frac{2\pi\alpha}{D}\right)\int_\Omega \cos\left(\frac{2\pi z}{D}\right) u^2(z-\alpha)\,dz \\
B &= \int_\Omega \cos\left(\frac{2\pi x}{D}\right) u^2(x)\,dx \\
&= \cos\left(\frac{2\pi\alpha}{D}\right)\int_\Omega \cos\left(\frac{2\pi z}{D}\right) u^2(z-\alpha)\,dz + \sin\left(\frac{2\pi\alpha}{D}\right)\int_\Omega \sin\left(\frac{2\pi z}{D}\right) u^2(z-\alpha)\,dz \\
&\approx \cos\left(\frac{2\pi\alpha}{D}\right)\int_\Omega \cos\left(\frac{2\pi z}{D}\right) u^2(z-\alpha)\,dz\,,
\end{aligned}$$

where D is the domain length. To obtain these expressions we work in the center of mass frame and assume that the structure is approximately symmetric in this frame. This approximation is also inherent in the standard definition, Eq. (7.7). We define the location of the center of mass by

$$\alpha \equiv \frac{D}{2\pi}\arctan\left(-\frac{A}{B}\right). \tag{7.8}$$

This definition treats the interval $[0, D]$ as periodic and gives the correct weighting to solutions that span the boundary. We have found it to be much more accurate than Eq. (7.7).

Chapter 8

Impact and Outlook

The heart of this dissertation describes a mechanism by which spatially forced weakly subcritical systems support a family of localized states. This phenomenon occurs in a variety of physical systems both dissipative and not. In this final chapter we briefly place the contributions of this work within a broader view of the field and then focus on possible future research directions.

8.1 A broader context

The front propagation problem is an old one, some of the earliest work dating back to 1937 when Fisher published "The wave advance of advantageous species," and Kolmogorov, Petrovsky and Piskunov simultaneously published "A study of the diffusion equation with an increase in the amount of substance." From then on front propagation occupied a major area of research in a variety of disciplines. One important application was in the field of pattern formation where amplitude equations exhibiting front phenomena could be rigorously derived. Our work fits into this effort. Specifically, fronts in Eq. (1.1) were studied extensively in the 1980s and 90s but a full derivation of the exact front exhibited in chapter 4 was never completed. We reiterate moreover that since all systems which undergo a change from sub to supercriticality for appropriate parameters pass through the limit in which Eq. (1.1) is applicable our work is of wide appeal. We are aware of at least one case [105] in which the analytical expressions that we derived for the front speed (v_N) and trailing wave number (q_N) are in use for ongoing research.

One of the main applications of the exact front solution that we study in chapter 4 is the transition between pulled and pushed fronts for propagation into an unstable state. This topic remains a current area of research and much remains unknown [16, 17, 66]. Predictions based on the nonlinear marginal stability conjecture for front speeds were known in the case $a_1 = a_2 = 0$ [136] but we generalized them. In particular we showed that in some parameter regimes crossover to pulled fronts does not occur no matter how unstable the trivial state, and that in others the crossover occurs immediately when the trivial state destabilizes, i.e.

at $\mu = 0$. We also identified a series of behaviors including wave number resetting phase slips and chaotic fronts in Eq. (1.1) that are known in other models [133].

As part of our front selection analysis we also performed an explicit calculation of secondary front speeds. In performing this type of calculation the wave number k in the dispersion relation $\sigma(k)$ is promoted from real to complex and equations for the speed involve complex derivatives of σ. In the case considered here the dispersion relation is not analytic in k and has branch cuts which renders a straightforward analysis tremendously complicated. Instead our approach was to perform a homomorphic transformation of k eliminating the branch cuts and ultimately reducing the problem to intersections of polynomials. In this form we were able to clearly distinguish cases in which k is real and those where it is not, *analytically* as a function of parameters. Although this type of problem appears frequently these techniques are not in widespread use and it is more typical to use numerics. Our contribution shows that after reduction to polynomials significant understanding of the solution structure can be gained analytically despite not having explicit solutions for k.

Amplitude equation (1.1) is also the setting for the main results in this work concerning forced snaking. We show that homoclinic snaking occurs in second order systems that have spatial periodic parametric forcing. One of the main appeals of this result is that the system under consideration is strikingly minimal. We combine what is in effect a real-valued bistable reaction diffusion equation with the requirement that the state bistable with $u = 0$ be periodic. This second condition is enforced by promoting one of the coefficients of the equation to a periodic function of space. These ingredients are sufficient to support snaking solutions which generalizes the maxim "snaking requires oscillatory tails which only occur in fourth order systems." Here the precise meaning of "oscillatory tails" is that the state $u = 0$ have spatial eigenvalues with nonzero imaginary parts. Our result shows that this is not a strict requirement for snaking, since here the linearization of $u = 0$ is a second order Floquet problem, and that more care must be taken in non-autonomous problems. Because the form of the forcing in this work is a cosine the exact model can be written as a fourth order nonautonomous dynamical system, but snaking surely occurs in second order systems with more general types of forcing that preclude this simple reduction. As a result our discovery of *forced* snaking shows that snaking phenomena are indeed more generic and ubiquitous than previously thought.

A further ramification of our results concerning forced snaking is the theoretical validation of a number of experiments. Specifically, we reproduce the snaking behavior observed in [75, 76] and have set it in a more general context. We also show, with our work on foliated snaking, that the experimental parameters matter. Depending on the balance of system parameters very different snaking structures may appear, either forced or foliated. Moreover this balance can be tuned by adjusting the lengthscale of the imposed spatial forcing. To our knowledge foliated snaking has not been observed in experiments. In addition, the experimental observations of forced snaking in dissipative systems have not captured unstable states which play a crucial role in the bifurcation structure. Observation of unstable states might be achieved in future research by the application an appropriate control method as in the work of [153].

Finally, in the context of gap solitons our results provide new directions for future work. As noted in chapter 7 structures exhibiting snaking had been observed in the GPE prior to our work, though much less focus had been given to the 3-5 case and even less to the semi-infinite gap. Our main contributions in this area were first to provide a more complete bifurcation picture including the existence not only of a pair of snaking branches but also of the asymmetric rung states, and second to identify the regime of foliated snaking in the gap soliton context. We are aware of no other work identifying these solutions and their close relation to snaking states. A major consequence of our work is that such solutions should exist in all of the cases of snaking discovered previously whenever the forcing is on a sufficiently large length scale. As gap solitons have been thoroughly explored in higher dimensions this insight could spawn a plethora of interesting new research.

8.2 Extensions and new projects

Exact solutions

There are a variety of obvious extensions to our work in chapter 4 on exact solutions to Eq. (1.1). These begin with their existence and stability. Although we computed an exact solution and studied the parameter regimes in which it exists, the solution is not meaningful if the PDE initial value problem is not well posed. We outlined the known results about the well-posedness for Eq. (1.1), but a necessary condition has not be found in general. It is likely that such a bound on parameters is related to the existence conditions for the exact front and requirements determined here, like $\Gamma > 0$, might help to formulate the appropriate rigorous bounds. Moreover, in the regions where we know the problem to be ill posed one interpretation is that the asymptotic assumptions underlying the derivation of the amplitude equation have failed. Specifically the cubic and quintic terms are of the same order in such a scenario and higher order terms are needed in order to saturate. This suggests an avenue for going beyond the region $\Gamma > 0$ (or $a_1 < \frac{4}{\sqrt{3}}$ if $a_2 = 0$) by reformulating the asymptotics to include these higher order terms.

With respect to the stability of the exact front solution one component left out of our work is a study of point eigenvalues. Point spectra are known to exist in linearizations about front solutions and the non-normal linear operator obtained here when $a_2 \neq 0$ invalidates many classical results about stability that are known for the self-adjoint case. Such a study is difficult to carry out numerically in a traditional fashion because of the imposition of the trailing boundary condition behind the front and the segregation of the point and essential spectra. The correct method with which to carry out this analysis is via the computation of the Evans function [73, 89, 137]. The Evans function is a holomorphic function constructed in such a way that its roots occur at the locations of the point eigenvalues. Numerically the Evans function is computed by taking appropriate contour integrals around a region to the right of the imaginary axis in order to identify any unstable eigenvalues. This method is in widespread use for the study of the stability of traveling solutions to PDEs and integral equations [48, 73, 89, 137].

Another obvious extension of our work on the exact front solution is to compute the family of exact pulses also proposed by van Saarloos and Hohenberg [132]. As in the case of the front no analysis including (a_1, a_2) has been carried out to our knowledge. One reason that the pulse solution is less well known is the comment in [132] that the solution is unstable and thus of little dynamical significance.This situation might change when the (a_1, a_2) terms are included or by the presence of periodic forcing as done in this work. In fact, traveling pulse solutions have already made an appearance in our study of the dynamics of fronts. When $(a_1, a_2) = (\frac{9}{2}, 5)$ the front solution exhibits intermittent collapse which occurs in the amplitude of the state behind the front. This amplitude decay ceases near the leading edge of the front leaving a traveling pulse which persists for some time. An exact family to traveling pulses might inform our understanding of the dynamics in this situation and could provide insight into the propagation speed.

Forced snaking

Given the large number of parameters in Eq. (1.1) a number of avenues remain for future work. We have not investigated the effect of (a_1, a_2) on foliated snaking solutions. We know from (Fig. 4.2) that the heteroclinic front solution has a lengthscale that depends on (a_1, a_2) and becomes long in certain regimes. Because this heteroclinic is the base state from which snaking states are formed when $m_1 > 0$ it is natural to think that foliated snaking could be accessed by changing (a_1, a_2) rather than ℓ. This in addition to continuation of the known foliated snaking branches in (a_1, a_2) promises to involve much more complicated bifurcations.

In addition to stationary solutions there are multiple regimes in which the stability of solutions could be more thoroughly investigated. The most obvious extensions are to perform the type of Benjamin–Fier stability analysis on the forced snaking states with nonzero (a_1, a_2) as was performed for fronts. Beyond this, we have not systematically investigated the stability of foliated snaking states. Although we did verify that lumps are stable and spikes are not, additional interesting scenarios could occur. For m_0 beyond the right folds of the foliated snaking branches there is presumably depinning-like behavior but the region in which this can occur, i.e. to the left of the primary bifurcation, shrinks to zero as m_1 is increased. When this region vanishes the solutions would "depin" in a region where $u = 0$ is unstable and a competition between pushed depinning fronts and pulled fronts will occur.

A more basic topic on which we are currently working is the identification of the necessary bifurcations required in order to transition from forced to foliated snaking. The physical interpretation of increasing m_1 (adiabatically, say) is to deepen the wells of the applied potential which in the $\ell = 50$ case ultimately splits the snaking states into individual pulses. This process is of obvious interest to experimentalists who are focused on the control of such structures. In particular, we discuss in chapter 5 the collision of folds that precedes the foliated regime (Fig. 5.10) but many details remain missing. While chapter 5 is focused on the snaking branch that emerges for small m_1 it is not concerned with the origins of the lumps and spikes. Our work in progress on this topic reveals the situation to be significantly complex.

From a more theoretical perspective another important component of forced snaking that is not understood is the dynamical system phase-space picture. Homoclinic snaking in nonautonomous systems such as SHE has a well developed theoretical understanding. The creation of the large multiplicity of localized states is facilitated by the formation of a heteroclinic tangle [10, 68]. In the case of forced snaking a similar mechanism is likely at work but the problem is of a different form and does not obviously fit into existing theory due to the nonautonomous term, especially when the forcing is not a pure cosine. It could be interesting to generalize the existing theory to deal with this situation.

Relating to the idea of more general forcing functions is forced snaking when the forcing is quasi-periodic. Concretely this could be achieved by the forcing

$$\mu(x) = m_0 + m_1 \cos\left(\frac{2\pi x}{\ell}\right) + m_2 \cos\left(\alpha \frac{2\pi x}{\ell}\right)$$

where α is a real parameter. When α is chosen such that the two cosines are commensurate we expect to see a familiar form of forced snaking but when α is irrational the situation is much less clear. Indeed, even the linear problem with this type of quasi-periodic forcing is exceedingly complex [166]. This type of perturbation does not break reflection symmetry in the problem but would likely break reflection symmetry in many of the snaking solutions. This may significantly alter the stability of snaking states and the depinning process. This scenario can be realized by continuing the known forced snaking solutions in m_2 and as long as the states being continued are localized then one need not worry about the boundary conditions which would otherwise be subtle for generic α. This type of situation has no analog in classical SHE snaking.

Front propagation

The propagation of fronts into a nonhomogeneous unstable state is one of the most exciting extensions of this work. Many people have worked on this problem in the context of integral equations [27, 47] as well as reaction-diffusion equations [18, 19, 20, 21, 156] to name only a few. However, a number of interesting questions remain unanswered. One problem, posed by van Saarloos in [133], is to perform the linear spreading point calculation in periodic media. Although significant progress beyond this type of analysis has been made in the mathematical literature, few if any physics papers have tied this to real problems with numerical experiments. Moreover, a concise physical interpretation of the linear spreading point in a periodic framework is lacking. Specifically, an explanation of the role of band-gaps in the propagation of fronts remains unclear. From the gap soliton literature it is known that localized structures exist in the higher gaps. These could interfere with the front propagation process and have not been studied to our knowledge in the dissipative context. At an even more basic level the physical situation is obviously quite different in the homogenization limit, $\ell \to 0$, versus the WKB limit, $\ell \to \infty$, and it would be interesting to understand the physical effects of inhomogeneities in each case on front propagation and selection. Both of these limits are susceptible to asymptotic analysis so that a mix of numerical and analytical results could be compared.

Finally, one necessary component of the aforementioned research proposals is to compute branches of traveling fronts. This is simple for uniformly moving fronts but more complicated when the state left in the wake of the front is periodic and the front moves with a nonconstant speed. In this case one cannot eliminate time from the problem by changing frames and the setting of the downstream boundary condition is nontrivial. Work on continuation of this type of front is currently underway [105] and applications are widespread. A few that come to mind here are to continue the branches of pushed fronts from the subcritical regime where $m_0 < 0$ to $m_0 > 0$ along with the branch of pulled fronts emerging at $m_0 = 0$. Another application is to continue the branches of depinning fronts that were observed in the nongradient case with $a_2 = 1$ back into the interior of the pinning region.

Appendix A

The Benjamin-Feir Instability

This appendix is devoted to finding *all* solutions of Eq. (2.17) obtained from the dispersion relation for perturbations of nonlinear rotating wave solutions of Eq. (1.1). Because the marginally unstable wave number, q^*, is generically complex the dispersion relation can exhibit branch cuts and complicated dependence on the phase of the radicand. These properties render the task of solving the marginal stability equations analytically in their standard form intractable and their numerical solution unstable. In this section we instead transform these equations into polynomial equations and show that after appropriate transformations *all* the solutions lie along a unique elliptic curve. We thus provide an explicit parametrization of the solution curves and a numerically tractable route to computing the desired front speed. The entirety of the calculation is done in the stationary frame and we are particularly interested in the speed v_{BF} selected by secondary (Benjamin-Feir) instabilities.

A.1 Setup

Before analyzing the generic case, we note that there are two nongeneric situations that can occur, corresponding to $2g - f = 0$ and $g = 0$, respectively. When $g = 0$ the dispersion relation reads $\sigma = \pm\sqrt{-fq^2} - q^2$ and for each sign of the root there are four cases to consider depending on the sign of f and the quadrant of q. In each case we solve the marginal stability equations in the original variables to verify that q lies in a consistent quadrant. In the table below we take the positive root.

sgn(f)	quadrant of q	σ	solution of Eq. (2.17)
-1	1 , 4	$\sqrt{\lvert f\rvert}q - q^2$	$q^* = \frac{\sqrt{\lvert f\rvert}}{2}(1 \pm i)$
-1	2 , 3	$-\sqrt{\lvert f\rvert}q - q^2$	$q^* = \frac{\sqrt{\lvert f\rvert}}{2}(-1 \pm i)$
1	1 , 2	$-i\sqrt{\lvert f\rvert}q - q^2$	$q^* = 0$
1	3 , 4	$i\sqrt{\lvert f\rvert}q - q^2$	$q^* = 0$

As shown in the table, the first two cases are consistent while the second two are not. Since the case of the negative root is obtained by switching the dispersion relations and q values of rows $1 \leftrightarrow 2$ and $3 \leftrightarrow 4$, there is no consistent case and hence no solution for the branch with negative root. In the case $2g = f$ the dispersion relation is $\sigma = \pm|g| - g - q^2$ and the condition $\Re\left[\sigma'(q)\right] = 0$ implies $q_r = 0$ so that $q^* = i\sqrt{|g| - g}$.

In the general case ($f \neq 2g$, $g \neq 0$) we work in terms of the parameters $c = \frac{g}{2g-f}$, $d = \frac{1}{cg}$ and we define $\theta(q)$ via the relation $\sigma(q) = \frac{\theta(q)+c-1}{cd}$. We also introduce the shorthand notation $s_z \equiv \operatorname{sgn}(z)$. The condition (2.17) becomes

$$\Re\left[\theta'\right] = 0, \qquad -\Im\left[\theta'\right]\Im[q] = \Re\left[\theta\right] + c - 1, \qquad \Im[q] > 0, \tag{A.1}$$

along with the obvious requirement $\Re[\sigma] > 0$. With the introduced parameters and relation (4.9) we have

$$\theta = \pm s_g\sqrt{dq^2+1} - c\left(dq^2+1\right), \quad \theta' = \pm s_g\frac{dq}{\sqrt{dq^2+1}} - 2cdq.$$

To resolve the branches in $\sqrt{dq^2+1}$, consider the holomorphic substitution $q = \frac{2t}{\sqrt{|d|}(s_d - t^2)}$ which parametrizes both branches in t but double-counts the physically irrelevant point $q = 0$ at $t = 0$ and ∞. With this substitution the argument of the square roots becomes the square of $\frac{s_d+t^2}{s_d-t^2}$. Letting $t = x + iy$, where $x, y \in \mathbb{R}$, it becomes clear that x and y always appear squared in the relevant parts of Eq. (A.1). Thus we are free to choose their sign such that $\Im\left[\frac{s_d+t^2}{s_d-t^2}\right] > 0$. Eliminating the square roots produces

$$s_g\theta = \frac{\frac{1}{2}\frac{h+s_d}{h-s_d}\left(t^2+s_d\right)^2 \pm \left(1-t^4\right)}{\left(t^2-s_d\right)^2}, \qquad \frac{s_g\theta'}{\sqrt{|d|}} = \begin{cases} \frac{4t}{h-s_d}\frac{h+t^2}{1-t^4} & (+) \\ \frac{4s_d t}{h-s_d}\frac{1+ht^2}{1-t^4} & (-) \end{cases},$$

where h is a real variable defined by

$$h \equiv \frac{2\,|c| - s_d}{2\,|c|\,s_d + 1}.$$

Since the factor $\sqrt{|d|}$ cancels out in the equation for $\Im[\theta']$, the change of variables reduces a 4-parameter problem (q, f, g) into a 3-parameter problem (t, h) with eight cases depending on s_d and s_g and the sign of the root.

A.2 First condition

We are now prepared to begin resolving the condition $\Re\left[\theta'\right] = 0$ and focus first on the positive root. In the (t, h) variables this reduces to

$$\Re\left[\frac{t\left(h+t^2\right)}{1-t^4}\right] = 0. \tag{A.2}$$

We now proceed by clearing all denominators under the assumption that they do not vanish and return to nongeneric points like $t = \sqrt{i}$ later. Setting $t = x + iy$, relation (A.2) expands to

$$x\left\{h\left(x^4 - 2x^2y^2 - 3y^4 - 1\right) + \left(x^2 + y^2\right)^3 - x^2 + 3y^2\right\} = 0. \tag{A.3}$$

Note that the trivial condition $x = 0$ results in a purely imaginary t and this is the well-known solution with purely imaginary q [84]. In addition to this solution there is a set of solutions with nontrivial x and it is those solutions that we consider in what follows.

When $x \neq 0$ Eq. (A.3) is a polynomial in even powers of x and y. Introducing $u = x^2$ and $v = y^2$ we obtain

$$u = \frac{1}{4}\left(\frac{h - k^3}{hk - 1} + 3k\right) \tag{A.4}$$

with $k = u + v$. The case $h = \pm 1$ in which there are extra solutions $k = \pm 1$ is included in the set of nongeneric cases that are discussed at the beginning of this Appendix.

As for the negative root, the relation $\Re\left[\frac{t\left(1+ht^2\right)}{1-t^4}\right] = 0$ gives

$$x\left\{3y^4\left(hx^2 - 1\right) + y^2\left(3h\left(x^4 + 1\right) - 2x^2\right) + \left(x^4 - 1\right)\left(hx^2 + 1\right) + hy^6\right\} = 0.$$

Ignoring the case $x = 0$, the other factor may be written in terms of (u, k) as

$$u = \frac{1}{4}\left(\frac{hk^3 - 1}{h - k} + 3k\right).$$

From here we work in the (h, k) variables where k remains to be set by the second condition in Eq. (A.1).

A.3 Second condition

The second condition in Eq. (A.1) for the positive root can be written as

$$-\frac{8s_g}{h - s_d}\Im\left[\frac{t\left(h + t^2\right)}{1 - t^4}\right]\Im\left[\frac{t}{s_d - t^2}\right] = s_g\Re\left[\frac{\frac{1}{2}\frac{h+s_d}{h-s_d}\left(t^2 + s_d\right)^2 + \left(1 - t^4\right)}{\left(t^2 - s_d\right)^2}\right] + c - 1, \tag{A.5}$$

where c can be eliminated in favor of h. Depending on the signs s_d and s_g, there are four cases, each generating an equation in t and h. We proceed with each by clearing denominators and writing the expressions in the form of polynomials.

After writing relation (A.5) in the variables defined in Sec. A.2 and imposing the relation (A.4) we obtain the polynomial equation

$$\begin{aligned}\mathcal{P}(h, k) \equiv{} & \left(h^2 - 1\right)\left(k^2 + 1\right)^2\left(k - s_d\right)^2 \\ & + s_g(hk - 1)\left\{h\left(k^4 + 3\right)k - 3k^4 - 1 - 2s_d\left(k^3 + k\right)(hk - 1)\right\} = 0.\end{aligned} \tag{A.6}$$

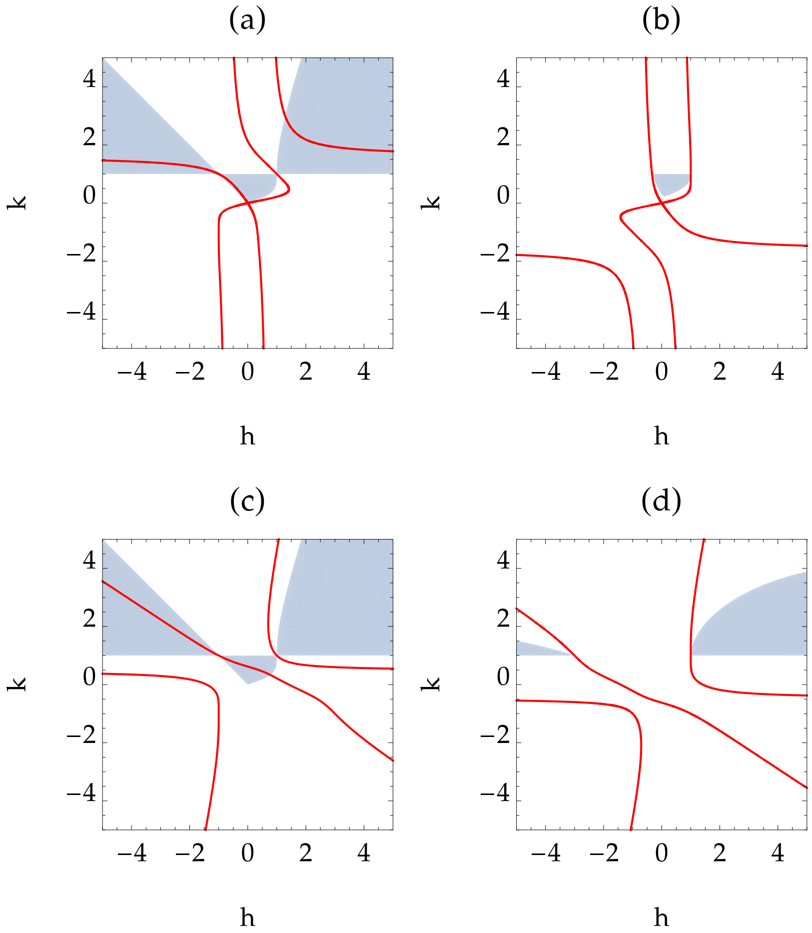

Figure A.1: Four cases of the $\Re[q] \neq 0$ generic solutions to the Benjamin-Feir stability equations for the positive root: (a) $g > 0, d > 0$ (b) $g > 0, d < 0$ (c) $g < 0, d > 0$ (d) $g < 0, d < 0$. Here the zero level-set of Eq. (A.6) is plotted in red and the region $u, v > 0$ and $\Im[\sigma] > 0$ is plotted in blue. The solutions correspond to the intersections of the red curve with the blue regions.

This equation must be solved along with constraints $u, v > 0$. The solution curves of different s_d and s_g are plotted in red in Fig. A.1 along with the region in which both $u, v > 0$ and $\Re[\sigma] > 0$ (also written in h, k variables) in blue. Intersections of the red curve with the blue regions correspond to secondary solutions of Eq. (2.17) in which q is not purely imaginary.

The polynomial equation $\mathcal{P} = 0$ can be transformed into a simpler form, the Weierstraß form. Since $\mathcal{P}$ is quadratic in h we write the equation in the form $(Ah + B)^2 = m(k)^2 n(k)$ where m is quadratic or cubic in k and n is quartic in k. We then define $h' = \frac{Ah+B}{m(k)}$ so the equation takes the form $(h')^2 = n(k)$. Using standard techniques to put the curve into Weierstraß form, we choose the point $k = 1$ and compute the quadratic $\ell(k)$ that is triply tangent to $\sqrt{n(k)}$. The quantity $\ell(k)$ has a second intersection with the original curve at k_c. We define

$$l = \frac{k-1}{h' - \ell(k)}, \qquad p = \frac{(k-1)(k-k_c)}{h' - \ell(k)},$$

which takes the original curve to an elliptic curve in (l, p). Subsequently, we take $L = A(p)l + B(p)$ choosing A, B so that the L^2 term has unit coefficient and the term linear in L vanishes. Next take $P = Cp + D$ where C, D are chosen to set the P^3 coefficient to 4 and the P^2 coefficient to 0. The resulting elliptic curve can be parametrized by the Weierstraß $\wp$-function. After a final rescaling of both L, P to clear denominators the first case $s_d = s_g = 1$ reduces to

$$L^2 = 4P^3 - 435P + 1081,$$

whose solutions are parametrized by a particular Weierstraß $\wp$-function with elliptic invariants $(g_1, g_3) = (435, 1081)$. In fact, all four cases of different (s_d, s_g) have solution curves that can be parametrized by the *same* Weierstraß $\wp$-function albeit in different variables. We thus provide an explicit description of the solution curves.

The second condition in Eq. (A.1) for the negative root can be written as

$$-\frac{8 s_g s_d}{h - s_d} \Im\left[\frac{t\left(1 + ht^2\right)}{1 - t^4}\right] \Im\left[\frac{t}{s_d - t^2}\right] = s_g \Re\left[\frac{\frac{1}{2}\frac{h+s_d}{h-s_d}\left(t^2 + s_d\right)^2 - \left(1 - t^4\right)}{\left(t^2 - s_d\right)^2}\right] + c - 1$$

and reduces to another polynomial equation,

$$\begin{aligned} \mathcal{P}(k,h) \equiv{} & \left(h^2 - 1\right)\left(k^2 + 1\right)^2 (k - s_d)^2 \\ & + s_g (h - k)\left\{3hk^4 + h - \left(k^4 + 3\right)k - 2 s_d \left(k^3 + k\right)(h - k)\right\} = 0. \end{aligned}$$

The solutions of this equation in each of the four cases are plotted in red in Fig. A.2. This case can also be reduced to the same Weierstraß $\wp$-function.

A.4 Speed

The analysis above shows that there is in general either one or two solutions to the marginal stability equations for the Benjamin-Feir instability. The solution with $q_r = 0$ is given in [84] and here we show that there is also a solution $q_r \neq 0$. The secondary solution with nontrivial wave number q_r only exists under certain conditions and never coexists with the $q_r = 0$ solution. For each pair s_g, s_d the values of h for which there is instability are restricted to the following intervals:

Parameters		Instability conditions	$q_r \neq 0$	$q_r = 0$
$d > 0$	$g > 0$	$h \in (-1, 0)$	all h	nowhere
$d > 0$	$g < 0$	$h \in (-1, 1)$	$h \in \left(-1, \frac{7}{9}\right)$	$h \in \left(\frac{7}{9}, 1\right)$
$d < 0$	$g > 0$	stable		
$d < 0$	$g < 0$	$h \in (-\infty, -1) \cup (1, \infty)$	nowhere	all h

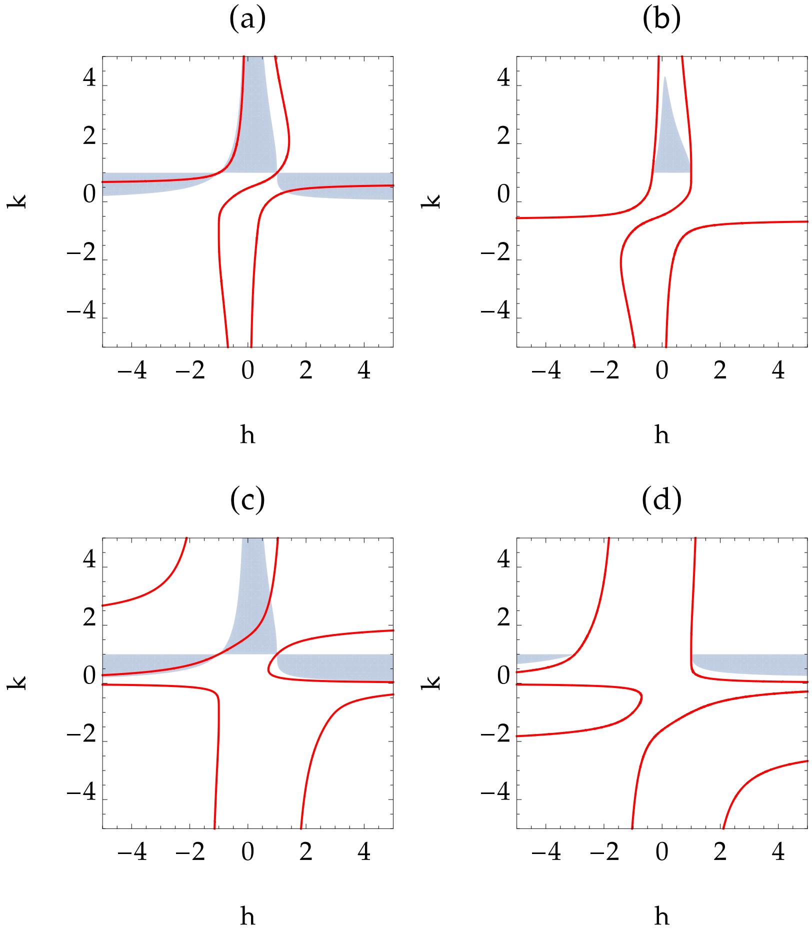

Figure A.2: Four cases of the $\Re[q] \neq 0$ generic solutions to the Benjamin-Feir stability equations for the negative root: (a) $g > 0, d > 0$ (b) $g > 0, d < 0$ (c) $g < 0, d > 0$ (d) $g < 0, d < 0$. Here the zero level-set of Eq. (A.6) is plotted in red and the region $u, v > 0$ and $\Im[\sigma] > 0$ is plotted in blue. The solutions correspond to the intersections of the red curve with the blue regions.

based on the instability requirements derived in [84]. The $q_r = 0$ speed was computed in [84] but can be written in h, d variables for the two relevant cases when $g < 0$:

$$v_{BF} = \begin{cases} \frac{\left(5-\sqrt{9h^2+2h-7}-3h\right)^{\frac{3}{2}}}{\sqrt{2d}(h+1)\left(\sqrt{h+1}-\sqrt{9h-7}\right)}, & d > 0, \\ \frac{\sqrt{(h-1)(9h+7)}s_{h+1}+3h+5}{\sqrt{(h-1)(9h+7)}s_{h+1}+1-h}\sqrt{\frac{\sqrt{(h-1)(9h+7)}s_{h+1}+3h+5}{2d(1-h)}}, & d < 0. \end{cases}$$

The speed for solutions with nonzero q_r may be written

$$v_{BF} = \begin{cases} \frac{8k(s_d h-1)}{(k^2+1)(h^2-1)}\sqrt{\frac{(hk-1)(h+k)}{|d|(k^2-1)}} & (+) \\ \frac{8k(h-s_d)}{(k^2+1)(h^2-1)}\sqrt{\frac{(k-h)(hk+1)}{|d|(k^2-1)}} & (-) \end{cases}.$$

The signs (±) correspond to the two different branches of the dispersion mentioned at the beginning of this section and k is to be evaluated on the curves of solutions obtained above. Once a pair (a_1, a_2) has been selected h and d are functions of μ only, although it is typically more convenient to plot the results in terms of h. When plotted in this fashion the h-values corresponding to $\mu = 0, \infty$ depend on a_1 and a_2.

To apply the above results we consider the instability of a rotating wave with wave number zero, as is observed in the wake of pulled fronts. Recall that these fronts exist along the entire line $a_1 = -a_2$ for all μ and at discrete values of μ off it. The expressions for f, g take the form

$$\begin{aligned} f &= \left(4 + a_2^2 - a_1^2\right) R^4 - 2R^2 \\ g &= 2\mu + R^2, \end{aligned}$$

where $R^2 = \frac{1}{2}\left(1 + \sqrt{4\mu + 1}\right)$ and thus $g > 0$. Based on the results above these are unstable to BF instability when $d > 0$ and the instability deposits a fixed nonzero wave number $q_r \neq 0$. With $\alpha \equiv a_2^2 - a_1^2$ the expression for c yields a relation between μ and h:

$$\mu = \frac{2(h-1)((\alpha-2)h+\alpha+2)}{((\alpha-4)h+\alpha+4)^2}.$$

Next, d can be written in terms of h by first passing to μ variables,

$$\sqrt{|d|} = \sqrt{\left|\frac{\alpha}{4\mu+1}\right|} = \left|\frac{\alpha+(\alpha-4)h+4}{\sqrt{\alpha}(h+1)}\right|.$$

It is now clear that with this parametrization $h = \frac{2+\alpha}{2-\alpha}$ corresponds to $\mu = 0$ and $h = \frac{4+\alpha}{4-\alpha}$ to $\mu = \infty$ and $v^\dagger$, v^* and v_{BF} can all be plotted in terms of h as in Fig. 4.12.

Appendix B

Nonlinear Selection Inequalities

In this section we determine the selection pattern dictated by the inequalities (2.18) governing the selection of the pushed front in Eq. (1.1), referred to as the nonlinear marginal stability criterion (NMS). By selection pattern we mean the intervals of $\mu \in [0, \infty)$ in which the pair of inequalities is either satisfied (N, nonlinear selection) or not (L, linear selection). The boundaries of these intervals, generically a set $\{\mu^\ddagger(a_1, a_2)\}$, occur when at least one of the inequalities becomes an equality and define the selection pattern (e.g. N–L–N or N–L...etc). In the original variables, the (a_1, a_2) dependence of the inequalities (2.18) is far from obvious and the expressions are manifestly unwieldy. Numerical examination of these inequalities in all three parameters is difficult to carry out, let alone visualize. To overcome this difficulty we focus only on determining possible selection patterns and not the explicit values $\{\mu^\ddagger(a_1, a_2)\}$; thus we seek general conditions on (a_1, a_2) independent of μ that are required for a given selection pattern.

B.1 Reduction of inequalities

To proceed we introduce changes of variables to show that (2.18) may be recast as a pair of quadratic inequalities. In order to determine which selection patterns are possible we reduce these to finite cases of inequalities that only depend on a_1, a_2 and not on μ. After sufficient simplification these logical statements can be verified analytically using a computer algebra system (Mathematica). We consider all possible selection patterns and show either that a particular pattern is not possible or provide a pair (a_1, a_2) for which it occurs.

We first determine which root of the Eqs. (4.6) is appropriate for NMS. The inequalities

(2.18) can be rewritten as

$$\frac{\sqrt{\Gamma}}{2\sqrt{3}}\frac{\Lambda-6}{\Delta} \pm \frac{\Gamma}{2\sqrt{3}\Delta}\sqrt{2\Lambda\left(1+s_\Delta\frac{\mu|\Delta|}{2\Lambda}\right)} > \sqrt{\mu}, \tag{B.1}$$

$$\frac{\sqrt{\Gamma}}{2\sqrt{3}}\frac{(5\Lambda-6)}{\Delta} \pm \frac{\Upsilon}{2\sqrt{3}\Delta}\sqrt{2\Lambda\left(1+s_\Delta\frac{\mu|\Delta|}{2\Lambda}\right)} > \sqrt{\mu}. \tag{B.2}$$

Here s_Δ denotes the sign of Δ. To apply the marginal stability criterion we select the sign ($\pm$) in the inequalities (B.1) and (B.2) corresponding to faster spatial decay rate and larger velocity and both must be positive at $\mu = 0$ [136]. In particular, in order for the front speed to be selected by NMS either

$$\Lambda - 6 \pm \sqrt{2\Gamma\Lambda} > 0, \qquad \sqrt{\Gamma}(5\Lambda-6) \pm \Upsilon\sqrt{2\Lambda} > 0, \qquad \Delta > 0$$

or

$$\Lambda - 6 \pm \sqrt{2\Gamma\Lambda} < 0, \qquad \sqrt{\Gamma}(5\Lambda-6) \pm \Upsilon\sqrt{2\Lambda} < 0, \qquad \Delta < 0 \tag{B.3}$$

must hold and the root with larger velocity and faster decay rate must be chosen. When $\Delta, \Upsilon > 0$ this always corresponds to the positive root, which always exists. When $\Delta > 0$ and $\Upsilon < 0$ the positive root always exists with positive velocity while the negative root has negative velocity whenever it exists. Thus the positive root is selected. For $\Delta < 0$ and $\Upsilon > 0$ both roots violate the conditions in Eq. (B.3). For $\Delta < 0$ and $\Upsilon < 0$ the positive root always satisfies the NMS conditions while the negative root never does. These results are summarized in Table B.1.

	$\Upsilon > 0$	$\Upsilon < 0$
$\Delta > 0$	$+$	$+$
$\Delta < 0$	NMS does not apply	$+^*$

Table B.1: The selected root of Eqs. (4.6) for nonlinear marginal stability near $\mu = 0$. The case $\Delta, \Upsilon < 0$, marked by $*$, is complicated at larger values of μ because the two decay rates and the corresponding velocities are oppositely ordered (see text).

It is further possible to show that when $\mu > 0$ both of the selections in the $\Delta > 0$ cases remain valid. When $\Delta < 0$ neither solution ever exists with positive velocity for $\Upsilon > 0$ while for $\Upsilon < 0$ the selection can be quite complicated. As shown in Fig. 4.5, for $5\Lambda - 6 < 0$ the negative sign solution exists for μ sufficiently large and this solution has positive velocity. In fact, it is easy to see from Eqs. (B.1) and (B.2) that when both solutions exist with positive velocity their decay rates and velocities will be oppositely ordered, $v_{N+} < v_{N-}$ and $\kappa_{N+} > \kappa_{N-}$. Because of this it is not clear that NMS applies in this μ range and which solution to choose if it does. We check whether either choice results in the selection of a nonlinear front according to the NMS inequalities.

We now proceed to reduce Eqs. (B.1) and (B.2) to polynomial inequalities. Because we consider $\mu > 0$ we define $\tilde{\mu} \equiv \frac{\mu|\Delta|}{2\Lambda}$ which is strictly positive and also the constants

$$b_1 = s_\Delta \frac{(\Lambda - 6)}{2\sqrt{3}} \sqrt{\frac{\Gamma}{2\Lambda|\Delta|}}, \quad b_2 = s_\Delta \frac{\Gamma}{2\sqrt{3|\Delta|}}, \quad b_3 = s_\Delta \frac{(5\Lambda - 6)}{2\sqrt{3}} \sqrt{\frac{\Gamma}{2\Lambda|\Delta|}}, \quad b_4 = s_\Delta \frac{\Upsilon}{2\sqrt{3|\Delta|}}$$

so that the pair of inequalities take the form $b_i \pm b_{i+1}\sqrt{1 + s_\Delta\tilde{\mu}} > \sqrt{\tilde{\mu}}$ for $i = 1, 2$. To eliminate the square roots we introduce a holomorphic substitution $\tilde{\mu} = f(t)$ with $t \in (0, 1)$ (see Table B.1) chosen to be bijective on the full domain $\tilde{\mu} \in [0, \infty)$ so that the arguments of both roots are squares of positive quantities. After this substitution each inequality reduces to an inequality quadratic in the parameter t.

s_Δ	$\tilde{\mu}$	$1 + s_\Delta\tilde{\mu}$	$\tilde{\mu}$−domain	$b_i \pm b_j\sqrt{1 + s_\Delta\tilde{\mu}} > \sqrt{\tilde{\mu}}$
1	$\frac{4t^2}{(1-t^2)^2}$	$\frac{(1+t^2)^2}{(1-t^2)^2}$	$\tilde{\mu} \in (0, \infty)$	$(b_j - b_i)t^2 - 2t + (b_i + b_j) > 0$
−1	$\frac{4t^2}{(1+t^2)^2}$	$\frac{(1-t^2)^2}{(1+t^2)^2}$	$\tilde{\mu} \in (0, 1)$	$(b_i \mp b_j)t^2 - 2t + (b_i \pm b_j) > 0$

Table B.2: Substitutions that eliminate both square roots in Eqs. (B.1) and (B.2). The root signs have been chosen to match s_Δ according to the relevant roots classified in Table B.1. The quantity $\tilde{\mu}$ is defined in the text. In both cases $t \in (0, 1)$.

At this point the question of selection can be reduced to one of solving quadratic equations in t in the interval $(0, 1)$. In the generic case, each of the inequalities Eqs. (B.1) and (B.2) loses validity at μ values for which an inequality becomes an equality, or the square root of the quadratic terms in Table B.1 becomes zero. That is, the intervals on which the selection is either N or L are separated by points at which at least one of the inequalities becomes an equality. The nongeneric case in which a double root occurs is of higher codimension and is dealt with separately. Thus we can determine selection patterns by tracking the roots obtained when Eq. (B.1) and Eq. (B.2) are *equalities*. Each of Eq. (B.1) and Eq. (B.2) corresponds to a single quadratic equation which may have 0, 1, or 2 roots in $(0, 1)$, so there are 19 possible arrangements of the roots each of which could be a different selection pattern. In what follows we show that the only possible selection regimes are N, L, and N–L. Thus the set $\{\mu^\ddagger(a_1, a_2)\}$ reduces to a single member where $\mu^\ddagger(a_1, a_2)$ is either 0 (L), finite (N–L) or ∞ (N).

To proceed we derive t-independent conditions on the coefficients of the quadratic equations that determine properties of their roots. We organize this discussion based on various properties of the root arrangements. To simplify the discussion we introduce two polynomials

$$\begin{aligned} h_1(t) &= \alpha t^2 - 2t + \beta, \\ h_2(t) &= \gamma t^2 - 2t + \delta \end{aligned} \tag{B.4}$$

to represent the two polynomials inherited from Eqs. (B.1) and (B.2). We assume $\beta > 0$ based on the qualification in [136] that NMS holds when the nonlinear velocity is positive at $\mu = 0$. Without loss of generality we also assume that Eq. (B.2) is satisfied at $m = 0$ because it is proportional to a_N^2 so $\delta > 0$. We use the standard logical notation for "AND", $A \wedge B$, to represent the condition that A and B are both true. Note that since the conditions generally depend on parameters, the joint condition $\wedge_i A_i$ is only false when it fails for *all* parameter values. Recall that both Γ, Λ are positive and the conditions $(\Gamma > 0) \wedge (\Upsilon > 0) \wedge (5\Lambda - 6 < 0)$ and $(\Gamma > 0) \wedge (\Upsilon < 0) \wedge (\Lambda - 6 > 0)$ are false.

B.2 Number of roots

In subcritical systems Eq. (2.18) is typically satisfied at $\mu = 0$, so if both equations (B.4) have an even number of roots the inequalities will also be satisfied for $\mu \to \infty$. This is unphysical since at a sufficiently large forcing the linear dynamics usually take over [136]. In order to translate this property to one of the quadratic roots consider h_1. If $h_1(0) > 0$ then the equation has an even number of roots in $(0, 1)$ provided $h_1(1) > 0$ (recall that we exclude the nongeneric case of double roots) or

$$\beta > 0 \quad \text{and} \quad \alpha - 2 + \beta > 0$$

with a similar statement for h_2. In order to distinguish between the polynomial having zero or two roots we also check the discriminant and the derivative at $t = 1$. If the polynomial has positive discriminant then it has two roots. If there are two roots, because both polynomials have derivative -2 at $t = 0$ then both roots are in $(0, 1)$ if and only if the derivative is positive at $t = 1$. These conditions (for two roots) are

$$\alpha\beta < 1 \quad \text{and} \quad \alpha > 1.$$

Applying this procedure to the equations from Table B.1 yields the conditions in Table B.2.

s_Δ	even # of roots	2 roots
1	$b_j > 1$ and $b_i > -b_j$	$b_j^2 - b_i^2 < 1$ and $b_j - b_i > 1$
-1	$b_i > 1$ and $b_i > -b_j$	$b_i^2 - b_j^2 < 1$ and $b_i - b_j > 1$

Table B.3: Conditions for each of Eqs. (B.1) and (B.2) to have an even number of points of equality. In the case $\Delta < 0$ the positive root was selected.

		$h_1(t)$		
		zero	one	two
$h_2(t)$	zero	$(-15, 16)$	$\left(3, \frac{9}{2}\right)$	impossible
	one	impossible	$(2, 2)$	$\left(0, \frac{1}{2}\right)$
	two	impossible	impossible	impossible

Table B.4: Summary of the possible numbers of roots for Δ, $\Upsilon > 0$. When the condition can be satisfied an example (a_1, a_2) for which this is possible is shown. All of the parameters except the zero-zero case satisfy the known condition sufficient for global existence of solutions to the Cauchy problem.

Case Δ, $\Upsilon > 0$

The conditions for an even number of roots are:

$$\left(\Gamma^2 > 12|\Delta|\right) \wedge \left(\Lambda - 6 > -\sqrt{2\Lambda\Gamma}\right), \qquad \left(\Upsilon^2 > 12|\Delta|\right) \wedge \left((5\Lambda - 6)\sqrt{\Gamma} > -\Upsilon\sqrt{2\Lambda}\right)$$

which can be true individually or both together. The conditions for two roots are:

$$\left(2\Lambda\Gamma^2 - (\Lambda - 6)^2\Gamma < 24\Delta\Lambda\right) \wedge \left(2\sqrt{3}\sqrt{2\Lambda\Delta} < \Gamma\sqrt{2\Lambda} - (\lambda - 6)\sqrt{\Gamma}\right), \tag{B.5}$$

$$\left(2\Lambda\Upsilon^2 - (5\Lambda - 6)^2\Gamma < 24\Delta\Lambda\right) \wedge \left(2\sqrt{3}\sqrt{2\Lambda\Delta} < \Upsilon\sqrt{2\Lambda} - (5\lambda - 6)\sqrt{\Gamma}\right). \tag{B.6}$$

The first of these Eq. (B.5) can be true or false but Eq. (B.6) is false for all parameters so h_1 always has 0 or 1 roots. A summary of all possible scenarios is provided in Table B.4 along with sample parameters when possible. These results rule out 12 of the possible 19 root arrangements.

Case $\Delta > 0$, $\Upsilon < 0$

The conditions for an even number of roots of h_1 are the same as those above but must now be checked along with $\Upsilon < 0$ instead. For h_2 it is easy to see that the condition $b_j > 1$ or $\Upsilon > 2\sqrt{3\Delta}$ fails and it therefore always has a single root. As before the allowed possibilities are summarized in Table B.5 and a total of 14 root configurations are ruled out.

Case $\Delta < 0$, $\Upsilon < 0$

In this section we only treat the positive root of Eqs. (B.1) and (B.2) and leave the case where both roots exist to Sec.B.5. The conditions for an even number of roots are

$$\left((\Lambda - 6)^2\Gamma > 24\Lambda|\Delta|\right) \wedge \left((\Lambda - 6)^2\Gamma > 2\Lambda\Gamma\right),$$

$$\left(-(5\Lambda - 6)\sqrt{\Gamma} > 2\sqrt{3}\sqrt{2\Lambda|\Delta|}\right) \wedge \left(-(5\Lambda - 6)\sqrt{\Gamma} > \Upsilon\sqrt{2\Lambda}\right),$$

		$h_1(t)$		
		zero	one	two
$h_2(t)$	zero	impossible	impossible	impossible
	one	impossible	$\left(2, \frac{1}{5}\right)$	$\left(-\frac{7}{4}, 0\right)$
	two	impossible	impossible	impossible

Table B.5: Summary of the possible numbers of roots for $\Delta > 0$, $\Upsilon < 0$. When the condition can be satisfied an example (a_1, a_2) for which this is possible is shown. All of the parameters satisfy the known condition sufficient for global existence of solutions to the Cauchy problem.

		$h_1(t)$		
		zero	one	two
$h_2(t)$	zero	impossible	impossible	impossible
	one	impossible	$\left(-2, \frac{1}{2}\right)$	$(-2, 1)$
	two	impossible	impossible	impossible

Table B.6: Summary of the possible numbers of roots for $\Delta < 0$, $\Upsilon < 0$. When the condition can be satisfied an example (a_1, a_2) for which this is possible is shown. None of the regimes fall in the known global existence region.

where we used the fact that $\Lambda - 6$ is negative in this regime to simplify the expressions. The latter set of inequalities is always false so h_2 always has a single root. The condition for two roots of h_1 is

$$\left((\Lambda - 6)^2\Gamma - 2\Lambda\Gamma^2 < 24\Lambda|\Delta|\right) \wedge \left(-(\Lambda - 6)\sqrt{\Gamma} + \Gamma\sqrt{2\Lambda} > 2\sqrt{3}\sqrt{2\Lambda|\Delta|}\right).$$

Checking the three remaining cases produces the results in Table B.6.

B.3 Root ordering

Next we derive conditions to determine the root ordering for the two polynomials. This dictates whether or not the selected velocity can jump discontinuously.

If selection of either L or N changes three times there will generically be a discontinuous jump in the selected velocity. The analysis in Sec. B.2 does not rule this out because in the case that h_1 has two roots and h_2 has one, both roots of h_1 may be smaller than that of h_2. Thus when the root of h_2 is encountered (as μ is increased) the predicted velocity will jump discontinuously. We assume that h_2 has a single root in the interval because the case in which both quadratics have two roots in $(0, 1)$ was ruled out in Sec. B.2. Another possible cause of discontinuity in the selected velocity occurs if Eq. (B.2) breaks first, before Eq. (B.1), since both inequalities are satisfied at $\mu = 0$. Given the previous results this can only occur in the case that h_2 has one root in $(0, 1)$ that is smaller than any of the roots of h_2 in the interval.

We now derive a condition that is implied by the two root orderings mentioned above, thus indicating whether or not they can occur. First, it is possible to show that $\delta > \beta > 0$ regardless of the parameter values. Because of this ordering it is clear that for either of the two properties mentioned above to occur, h_1 and h_2 must cross *and* the common value must be positive. In the former case t_{cross} is greater than both roots of h_1, and in the latter case t_{cross} is smaller than any roots of either polynomial. It is easy to see that the difference of the polynomials, $(h_2 - h_1)(t) = (\gamma - \alpha)t^2 + (\delta - \beta)$ has either zero roots or two roots of opposite signs. Since $h_2(0) > h_1(0)$ then the root of h_2 is smaller than those of h_1 if and only if $h_2 - h_1$ has a root $t_{cross} \in (0,1)$ such that $(h_2 - h_1)(t_{cross}) > 0$. These conditions are equivalent to the conditions

$$\begin{aligned} \gamma + \delta &< 2 && h_2 \text{ has one root in } (0,1) \\ \gamma - \alpha &< 0 && h_2 - h_1 \text{ has a root} \\ \delta - \beta &< \gamma - \alpha && t_{cross} \in (0,1) \\ (\gamma - \alpha)(\delta - \beta) + \delta - \beta &> 0 && (h_2 - h_1)(t_{cross}) > 0. \end{aligned}$$

We have verified that these conditions cannot be satisfied which shows that the selected velocity cannot suffer discontinuous jumps.

B.4 The case of double roots

Each double root in either of the quadratic inequalities generically drops the dimension of parameter space by one. In order for a double root to exist the discriminant must vanish, either $\alpha\beta = 1$ or $\gamma\delta = 1$. In each case these conditions factor,

$$\begin{aligned} (a_1 + a_2)\Delta &= 0, \\ (16 + (a_1 + a_2)(3a_1 + 11a_2))\,\Delta &= 0, \end{aligned}$$

and each case can be reduced to a 1-parameter space of solutions. It can be shown that $16 + (a_1 + a_2)(3a_1 + 11a_2) = 0$ is incompatible with the requirement $\Gamma > 0$, so the second case can be reduced further to $\Delta = 0$. Interestingly, if there are two double roots the solutions are still described by a single parameter specified by $\Delta = 0$. As mentioned in 4.2, when $\Delta = 0$ the Ansatz solutions that are used here cease to be valid and a different analysis has to be conducted using the appropriate solutions. We omit this step.

Excluding the case $\Delta = 0$ we analyze the root structure for a single double root of h_1. When $a_1 = -a_2$ then h_1 has a double root and all of the coefficients collapse to $h_1(t) = \sqrt{3}\left(t - \frac{1}{\sqrt{3}}\right)^2$, $h_2(t) = -2\left(t - \frac{1}{\sqrt{3}}\right)$. The roots are independent of parameters and coincide. This is the classic case that arises when $a_1 = a_2 = 0$ and hereby extends along the whole line $a_1 + a_2 = 0$.

B.5 The case Υ, $\Delta < 0$ with both solutions of the Ansatz

In this case the negative root solution to Eqs. (4.6) exists for $\mu \in \left(1 - \frac{\Gamma(5\Lambda-6)^2}{2\Lambda\Upsilon^2}, 1\right]$ and corresponds to a positive velocity. Although this solution does not exist at $\mu = 0$, this velocity can be compared to the linear prediction. Because we know that $\kappa_{N+} > \kappa_{N-}$ and $\kappa_{N-} = 0$ at $\mu = 1 - \frac{\Gamma(5\Lambda-6)^2}{2\Lambda\Upsilon^2}$ we focus on h_2 in order to see if Eq. (B.2) can ever be satisfied. First one can check that $\gamma + \delta < 2$, which means that h_2 is negative at 1. Since we know that h_2 is negative at $\mu = 1 - \frac{\Gamma(5\Lambda-6)^2}{2\Lambda\Upsilon^2}$ this means that it has either 0 or two roots. Then one can check that $\gamma\delta < 1$ (h_2 has roots) and $\gamma < 0$ (h_2 is positive between the roots) cannot both be satisfied. Thus the a_{N-} branch is never relevant.

Appendix C

Asymptotics for Oscillations of Gap Solitons

We perform an asymptotic analysis in the limit $0 < m_1 \ll 1$ in order to extract equations of motion for localized structures in Eq. (7.1). It is known that Eq. (7.2) has an exact front solution when $m_1 = 0$ for appropriate values of m_0. This front solution is translation-invariant and its reflection ($x \to -x$) is also a solution. Therefore the basic idea behind our method is to use a pair of these fronts to form a pulse solution. In the $m_1 = 0$ case such a pulse is not a stable solution but in the presence of the periodic potential the fronts are able to pin thereby stabilizing the structure. This technique has been used by a number of previous authors in order to study front dynamics and pinned states [47, 75].

Our Ansatz for a time-dependent solution to Eq. (7.1) is as follows,

$$\begin{aligned} A(x,t) &= e^{i\int \omega(t)dt + i\frac{\dot{\alpha}(t)}{2}(x-\alpha)} v(x,t) \\ v(x,t) &= aB\left(-\left[x - x_L\right]\right) B\left(x - x_R\right) + W(x,t) \\ x_L &= \alpha - \frac{L}{2} \\ x_R &= \alpha + \frac{L}{2}. \end{aligned} \tag{C.1}$$

Here a is a real constant and $aB(x)$ is the front solution to Eq. (7.2) when $m_1 = 0$; the correction W is assumed to be small. The two real-valued functions α and ω are selected in order that this Ansatz solve Eq. (7.1). The two fronts that bound the localized structure are located at $x = x_L$ and $x = x_R$ with $x = \alpha(t)$ representing the center of mass motion (i.e., the antisymmetric dynamics of the pulse). Thus L is the (fixed) pulse width.

In order to ensure that the Ansatz (C.1) satisfies Eq. (7.1) at leading order the two fronts must be placed sufficiently far apart. Although $u(x,t) = aB(x)$ is an exact solution to Eq. (7.1) when $m_1 = 0$, $\tilde{u}(x) = aB(x)B(-x + x_0)$ is not. On the other hand, there does exist an *exact* pulse solution that is exponentially close to $\tilde{u}$. The use of a pair of fronts rather than an exact pulse solution simplifies both the calculations that follow and their interpretation. The error incurred is exponentially small in L and we therefore assume that L is sufficiently large that it is negligible in what follows.

C.1 Asymptotic procedure

We begin the procedure by defining the scaling of the terms in Eq. (C.1). The dynamics that we capture occur on a slow time τ, $\tau = \epsilon t$, where $\epsilon \ll 1$ is a suitably defined small parameter. We work in the center of mass frame, $z = x - \alpha$, and adopt the following scaling for the phase and forcing:

$$\omega(\tau) = \frac{\omega_0}{\epsilon} + \omega_1(\tau) + \epsilon\omega_2(\tau)$$
$$m_1 = \epsilon^2\mu.$$

The resulting equation for $v(z,\tau)$ is

$$0 = i\epsilon v_\tau + \epsilon^2\left[\left(\frac{\dot{\alpha}}{2}\right)^2 - \frac{\ddot{\alpha}}{2}z + \mu\cos\left(\frac{2\pi(z+\alpha)}{\ell}\right)\right]v - (\omega_0 + \epsilon\omega_1 + \epsilon^2\omega_2)v + v_{zz} + |v|^2 v - |v|^4 v$$

and we expand v as follows:

$$v(x,t) = W_0(z) + \epsilon W_1(z,\tau) + \epsilon^2 W_2(z,\tau).$$

The lowest order equation is

$$0 = W_{0zz} - \left(\omega_0 - |W_0|^2 + |W_0|^4\right)W_0. \tag{C.2}$$

It follows that if $\omega_0 = \frac{3}{16}$ then Eq. (C.2) has the front solution

$$W_0(z) = \frac{\sqrt{3}}{2}\sqrt{\frac{1}{1+e^{\frac{\sqrt{3}}{2}z}}} \equiv \frac{\sqrt{3}}{2}B(z).$$

Using the fact that $\frac{\sqrt{3}}{2}B(-z)$ is also a solution, two of these fronts can be patched together to form the Ansatz as described above. Specifically we take

$$W_0(z) = \frac{\sqrt{3}}{2}B\left(-\left[z+\frac{L}{2}\right]\right)B\left(z-\frac{L}{2}\right) \equiv \frac{\sqrt{3}}{2}B_1(-z)B_2(z).$$

This solution is not exact but results in only a small error if L is large compared to the spatial decay rate of the front, $\frac{2}{\sqrt{3}}$.

Because the lowest order problem is nonlinear, all of the higher order problems involve a linear operator $\mathcal{L}$ that is based on this front. If $U = R(z) + iI(z)$ with R and I real-valued this operator diagonalizes. That is, $\mathcal{L}(U) = \mathcal{L}_0(R) + i\mathcal{L}_1(I)$, where

$$\mathcal{L}_0 = \partial_{zz} - \frac{3}{16} + 3W_0^2 - 5W_0^4$$
$$\mathcal{L}_1 = \partial_{zz} - \frac{3}{16} + W_0^2 - W_0^4.$$

The operator $\mathcal{L}$ is self-adjoint and has 3 approximate null eigenfunctions. This is normal for linearizations about pulse states. We report these in the notation (R, I). The eigenfunctions consist of a phase rotation mode, $n_0 = (0, W_0)$, plus two Goldstone-type modes $n_1 = (W_{0z}, 0) = \left(\frac{\sqrt{3}}{2}\left(-B_1'B_2 + B_1B_2'\right), 0\right)$ and $n_2 = \left(\frac{\sqrt{3}}{2}\left(B_1'B_2 + B_1B_2'\right), 0\right)$. The first of these, n_1, is the *true* Goldstone mode for the pulse and is antisymmetric with respect to its center $z = 0$. This mode is inherited from global translation symmetry. Also related to translation symmetry, the mode n_2 is symmetric about the pulse center reflecting the fact that for $L \gg 1$ the two fronts are independent and can translate freely in opposite directions. This mode arises only in the limit of large L, i.e., as a result of our lowest order approximation.

The $\mathcal{O}(\epsilon)$ equation is

$$0 = \mathcal{L}(W_1) - \omega_1 W_0.$$

To enforce the solvability condition for n_2 we must require $\omega_1 = 0$. Then we may also take $W_1 \equiv 0$. At second order we obtain,

$$0 = \mathcal{L}(W_2) + \left[\left(\frac{\dot{\alpha}}{2}\right)^2 - \frac{\ddot{\alpha}}{2}z + \mu\cos\left(\frac{2\pi(z+\alpha)}{\ell}\right) - \omega_2\right] W_0.$$

The two solvability conditions can be written

$$\begin{aligned} 0 &= -\frac{\ddot{\alpha}}{2} I_1 - \mu \sin\left(\frac{2\pi\alpha}{\ell}\right) I_3 \\ 0 &= \left[\left(\frac{\dot{\alpha}}{2}\right)^2 - \omega_2\right] I_2 + \mu\cos\left(\frac{2\pi\alpha}{\ell}\right) I_4 \end{aligned}$$

with the integrals I_k defined as follows,

$$\begin{aligned} I_1 &= \langle n_1, z\, W_0\rangle \\ I_2 &= \langle n_2, W_0\rangle \\ I_3 &= \left\langle n_1, \sin\left(\frac{2\pi z}{\ell}\right) W_0\right\rangle \\ I_4 &= \left\langle n_2, \cos\left(\frac{2\pi z}{\ell}\right) W_0\right\rangle. \end{aligned}$$

Here we have used the fact that W_0 and n_2 are even functions of z while n_1 is odd to simplify the expressions.

It follows that there are only four distinct integrals to calculate. To simplify the expressions we set $c = e^{-\frac{\sqrt{3}}{4}L}$, yielding the expressions

$$\begin{aligned}
I_1 &= \frac{3L}{8\left(c^2-1\right)} \\
I_2 &= \frac{6-3c^2\left(\sqrt{3}L+2\right)}{8\left(c^2-1\right)^2} \\
I_3 &= \frac{\sqrt{3}\pi^2 \operatorname{csch}\left(\frac{4\pi^2}{\sqrt{3}\ell}\right)\sin\left(\frac{\pi L}{\ell}\right)}{\ell(c^2-1)} \\
I_4 &= -\frac{\pi \operatorname{csch}\left(\frac{4\pi^2}{\sqrt{3}\ell}\right)}{2(c^2-1)}\left(\frac{3c^2\sin\left(\frac{\pi L}{\ell}\right)}{c^2-1}+\frac{2\sqrt{3}\pi\cos\left(\frac{\pi L}{\ell}\right)}{\ell}\right) \\
&\approx -\frac{\sqrt{3}\pi^2 \operatorname{csch}\left(\frac{4\pi^2}{\sqrt{3}\ell}\right)\cos\left(\frac{\pi L}{\ell}\right)}{\ell(c^2-1)} + \mathcal{O}(c).
\end{aligned}$$

To obtain these expressions we have used the substitution $s = e^{\frac{\sqrt{3}}{2}z}$ followed by contour integration.

The ODEs thus take the simpler form

$$\omega_2 = \frac{\dot{\alpha}^2}{4} + \frac{\lambda L}{4}\cos\left(\frac{\pi L}{\ell}\right)\cos\left(\frac{2\pi\alpha}{\ell}\right) \tag{C.3}$$

$$\ddot{\alpha} = -\lambda \sin\left(\frac{2\pi\alpha}{\ell}\right)\sin\left(\frac{\pi L}{\ell}\right), \tag{C.4}$$

where $\lambda = \frac{16\sqrt{3}\pi^2\mu}{3\ell L}\operatorname{csch}\left(\frac{4\pi^2}{\sqrt{3}\ell}\right)$. It is clear from these equations that ω is slaved to the dynamics of α.

Initial conditions for the oscillators can be derived by considering the time-independent problem. Instead of using the Ansatz (C.1) we seek an order-by-order expansion of the stationary localized snaking solutions. In this case α becomes time-independent and $\omega_2 \equiv 0$ but the asymptotics are otherwise unchanged. In particular since our structures are centered with respect to a cosine period we must have $\alpha = 0, \frac{\ell}{2}$; from the solvability conditions in Eqs. (C.3) and (C.4) it follows that we also require $L = k(\ell/2)$ with k an odd positive integer. For example, a localized state spanning 3 cosine wavelengths would have $L = 3\ell$ and $\alpha = 0$. Because the time-dependent calculation is designed to capture dynamics around perturbed stationary localized states we take $\alpha(t=0) = 0$ and $\dot{\alpha}(t=0) = 2\eta$ (the phase gradient perturbation) as initial conditions.

Before continuing to the solution of Eqs. (C.4) we first discuss the role of symmetries of the original system in the ODE dynamics. The original system described by Eq. (7.1) possesses at least three important continuous symmetries when $m_1 = 0$. These include spatial translation $u(x,t) \to u(x+y,t)$, phase rotation $u(x,t) \to u(x,t)e^{i\omega}$, and Galilean invariance $u(x,t) \to u(x+vt,t)e^{i\frac{v}{2}\left(x+\frac{v}{2}t\right)}$. The last of these suggests that solutions traveling at a uniform velocity are not translating but rather rotating (with angular frequency $\frac{v^2}{4}$) in a moving frame. The introduction of the cosine forcing in Eq. (7.1) formally breaks the spatial translation and Galilean symmetries but does not preclude the existence of states that travel with *nonuniform* velocity. Indeed, it is clear from the first terms of Eq. (C.3) that the Galilean structure persists for the *average* velocity of the solution. That is, if the center of mass velocity, $\dot{\alpha}$, has a nonzero time average v_{cm} then in the frame moving at this velocity the same structure has a zero average velocity but rotates in time with a frequency equal to $\frac{v_{cm}^2}{4}$.

C.2 ODE dynamics

We next discuss the dynamics of stationary localized states that are perturbed by a phase gradient. These states follow the dynamics of Eq. (C.4) where $L = k(\ell/2)$ for an odd integer k. Changing the variables (α,τ) to new variables called (x,t), where $\alpha = \frac{\ell}{2\pi}x$ and $t = \sqrt{\frac{\ell}{2\pi\lambda}}\tau$, puts the equation of motion in canonical form,

$$\ddot{x} + \sin(x) = 0, \tag{C.5}$$

and the motion reduces to that of a pendulum. There are thus two distinct dynamical regimes: libration and rotation. In the case of the solitons the libration regime corresponds to oscillations of the center of mass in space with zero mean speed while the rotation regime corresponds to propagation of solitons with nonzero mean speed. These regimes are distinguished by the value of the first integral of the equation of motion, the initial velocity, since the initial displacement is zero, $x(t=0)=0$. Integrating Eq. (C.5) once we obtain,

$$\frac{\dot{x}^2}{2} - \cos(x) = \frac{\dot{x}_0^2}{2} - 1.$$

The initial velocity can be translated back to the Ansatz variables by noticing that

$$\left.\frac{\partial x}{\partial \tau}\right|_{\tau=0} = 2\eta\sqrt{\frac{2\pi}{\ell\lambda}},$$

and is thus proportional to the magnitude of the "phase gradient" perturbation used in our simulations. Libration occurs when $0 < \dot{x}_0 < 2$ while rotation occurs when $\dot{x}_0 > 2$. Thus the critical transition at which solitons become "unbound" takes place at $\eta_c(\ell) = \sqrt{\frac{\lambda\ell}{2\pi}}$. In the specific cases considered here, $\ell = 10, 50$ and $\mu = 0.1$, we find $\eta_c(10) \approx \frac{0.387}{\sqrt{L}}$ and $\eta_c(50) \approx \frac{1.240}{\sqrt{L}}$.

The oscillation period in both the libration and rotation regimes may be computed in terms of elliptic integrals using standard techniques. Specifically, in the libration regime

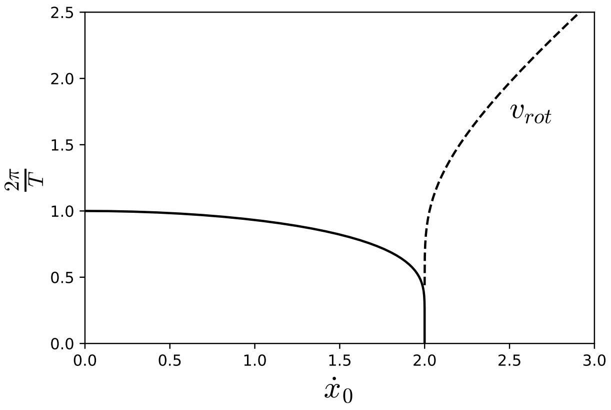

Figure C.1: The inverse periods of oscillation in the libration regime (solid line) and rotation regime (dashed line) as functions of the initial kinetic energy of the oscillator as measured by $\dot{x}_0$.

$(0 < \dot{x}_0 < 2)$ there is a maximum displacement $x_{max} = 2\arcsin\left(\frac{\dot{x}_0}{2}\right) < \pi$ so the period is

$$\tilde{T}_{lib} = 4\int_0^{x_{max}} \frac{dx}{\sqrt{\dot{x}_0^2 - 4\sin^2\left(\frac{x}{2}\right)}} = 4K\left(\frac{\dot{x}_0^2}{4}\right).$$

Here $K(x)$ is the complete elliptic integral of the first kind, $K(k) \equiv \int_0^{\frac{\pi}{2}} \frac{d\theta}{\sqrt{1-k\sin^2\theta}}$, and the tilde over $\tilde{T}_{lib}$ refers to the scaled time, τ. In the rotation regime $(\dot{x}_0 > 2)$ the period is defined as the time required to execute a single complete orbit,

$$\tilde{T}_{rot} = \int_0^{2\pi} \frac{dx}{\sqrt{\dot{x}_0^2 - 4\sin^2\left(\frac{x}{2}\right)}} = \frac{4}{\dot{x}_0}K\left(\frac{4}{\dot{x}_0^2}\right). \tag{C.6}$$

In the soliton context this period gives rise to the mean propagation velocity, $v_{rot} = \sqrt{\frac{\ell\lambda}{2\pi}}\frac{2\pi}{\tilde{T}_{rot}}$. In the frame moving at velocity v_{rot} the solution oscillates with period $T_{rot} = \sqrt{\frac{\ell}{2\pi\lambda}}\tilde{T}_{rot}$. The two periods computed here are plotted in Fig. C.1 as a function of $\dot{x}_0$.

Bibliography

[1] T. J. Alexander and Y. S. Kivshar. "Soliton complexes and flat-top nonlinear modes in optical lattices". In: *Appl. Phys. B* 82.2 (Feb. 2006), pp. 203–206.

[2] G. L. Alfimov, V. V. Konotop, and P. Pacciani. "Stationary localized modes of the quintic nonlinear Schrödinger equation with a periodic potential". In: *Phys. Rev. A* 75 (2 Feb. 2007), p. 023624.

[3] A. J. Archer et al. "Solidification in soft-core fluids: Disordered solids from fast solidification fronts". In: *Phys. Rev. E* 90 (4 Oct. 2014), p. 042404.

[4] F. Arecchi, S. Boccaletti, and P. Ramazza. "Pattern formation and competition in nonlinear optics". In: *Physics Reports* 318.1 (1999), pp. 1–83.

[5] D. G. Aronson and H. F. Weinberger. "Nonlinear diffusion in population genetics, combustion, and nerve pulse propagation". In: *Partial Differential Equations and Related Topics*. Ed. by J. A. Goldstein. Berlin, Heidelberg: Springer Berlin Heidelberg, 1975, pp. 5–49.

[6] D. Aronson and H. Weinberger. "Multidimensional nonlinear diffusion arising in population genetics". In: *Adv. Math.* 30.1 (1978), pp. 33–76.

[7] D. Avitabile and H. Schmidt. "Snakes and ladders in an inhomogeneous neural field model". In: *Physica D: Nonlinear Phenomena* 294 (2015), pp. 24–36.

[8] D. Avitabile et al. "To Snake or Not to Snake in the Planar Swift-Hohenberg Equation". In: *SIAM Journal on Applied Dynamical Systems* 9.3 (2010), pp. 704–733.

[9] C. Beaume, A. Bergeon, and E. Knobloch. "Homoclinic snaking of localized states in doubly diffusive convection". In: *Physics of Fluids* 23.9 (2011), p. 094102.

[10] M. Beck et al. "Snakes, Ladders, and Isolas of Localized Patterns". In: *SIAM Journal on Mathematical Analysis* 41.3 (2009), pp. 936–972.

[11] H. Bénard. "Les tourbillons cellulaires dans une nappe liquide". In: *Rev. Gen. Sci. Pures Appl.* 11 (1900), pp. 1261–1271.

[12] C. M. Bender and S. A. Orszag. *Advanced mathematical methods for scientists and engineers I: Asymptotic methods and perturbation theory.* Springer Science & Business Media, 2013.

[13] R. D. Benguria and M. C. Depassier. “Validity of the Linear Speed Selection Mechanism for Fronts of the Nonlinear Diffusion Equation”. In: *Phys. Rev. Lett.* 73 (16 Oct. 1994), pp. 2272–2274.

[14] R. D. Benguria and M. C. Depassier. “Variational characterization of the speed of propagation of fronts for the nonlinear diffusion equation”. In: *Commun. Math. Phys.* 175.1 (1996), pp. 221–227.

[15] E. Ben-Jacob et al. “Pattern propagation in nonlinear dissipative systems”. In: *Physica D: Nonlinear Phenomena* 14.3 (1985), pp. 348–364.

[16] H. Berestycki, J. Bouhours, and G. Chapuisat. “Front blocking and propagation in cylinders with varying cross section”. In: *Calculus of Variations and Partial Differential Equations* 55.3 (Apr. 2016), p. 44.

[17] H. Berestycki and J. Fang. “Forced waves of the Fisher-KPP equation in a shifting environment”. In: *Journal of Differential Equations* 264.3 (2018), pp. 2157–2183.

[18] H. Berestycki, F. Hamel, and L. Roques. “Analysis of the periodically fragmented environment model : I – Species persistence”. In: *Journal of Mathematical Biology* 51.1 (July 2005), pp. 75–113.

[19] H. Berestycki and F. Hamel. “Front propagation in periodic excitable media”. In: *Communications on Pure and Applied Mathematics* 55.8 (2002), pp. 949–1032.

[20] H. Berestycki, F. Hamel, and L. Roques. “Analysis of the periodically fragmented environment model: II–biological invasions and pulsating travelling fronts”. In: *Journal de Mathématiques Pures et Appliquées* 84.8 (2005), pp. 1101–1146.

[21] H. Berestycki, F. Hamel, and N. Nadirashvili. “The speed of propagation for KPP type problems. I: Periodic framework”. In: *Journal of The European Mathematical Society* 7.2 (2005), pp. 173–213.

[22] A. Bers. “Space-time evolution of plasma instabilities-absolute and convective”. In: *Basic Plasma Physics: Selected Chapters, Handbook of Plasma Physics, Volume 1.* Ed. by A. A. Galeev and R. N. Sudan. 1984, p. 451.

[23] Z. Birnbaum and B. A. Malomed. “Families of spatial solitons in a two-channel waveguide with the cubic-quintic nonlinearity”. In: *Phys. D (Amsterdam)* 237.24 (2008), pp. 3252–3262.

[24] C. de Boor and B. Swartz. “Collocation at Gaussian Points”. In: *SIAM Journal on Numerical Analysis* 10.4 (1973), pp. 582–606.

[25] U. Bortolozzo, M. G. Clerc, and S. Residori. “Local theory of the slanted homoclinic snaking bifurcation diagram”. In: *Phys. Rev. E* 78 (3 Sept. 2008), p. 036214.

[26] J. P. Boyd. *Chebyshev and Fourier spectral methods.* Courier Corporation, 2001.

[27] P. C. Bressloff. “From invasion to extinction in heterogeneous neural fields”. In: *The Journal of Mathematical Neuroscience* 2.1 (Mar. 2012), p. 6.

[28] L. Brevdo and T. J. Bridges. “Absolute and Convective Instabilities of Spatially Periodic Flows”. In: *Phil. Trans. R. Soc. A* 354.1710 (1996), pp. 1027–1064.

[29] J. Burke, S. M. Houghton, and E. Knobloch. “Swift-Hohenberg equation with broken reflection symmetry”. In: *Phys. Rev. E* 80 (3 Sept. 2009), p. 036202.

[30] J. R. Burke. *Localized states in driven dissipative systems.* University of California, Berkeley, 2008.

[31] J. Burke and J. H. P. Dawes. “Localized States in an Extended Swift-Hohenberg Equation”. In: *SIAM Journal on Applied Dynamical Systems* 11.1 (2012), pp. 261–284.

[32] J. Burke and E. Knobloch. “Homoclinic snaking: Structure and stability”. In: *Chaos* 17.3 (2007), p. 037102.

[33] J. Burke and E. Knobloch. “Localized states in the generalized Swift-Hohenberg equation”. In: *Phys. Rev. E* 73 (5 May 2006), p. 056211.

[34] J. Burke and E. Knobloch. “Snakes and ladders: Localized states in the Swift-Hohenberg equation”. In: *Physics Letters A* 360.6 (2007), pp. 681–688.

[35] C. G. Canuto et al. *Spectral methods: Fundamentals in single domains.* Springer, 2010.

[36] J. Carr. *Applications of centre manifold theory.* Vol. 35. Springer Science and Business Media, 2012.

[37] R. Carretero-González et al. “Multistable solitons in the cubic-quintic discrete nonlinear Schrödinger equation”. In: *Phys. D (Amsterdam)* 216.1 (2006), pp. 77–89.

[38] A. R. Champneys et al. “Homoclinic Snakes Bounded by a Saddle-Center Periodic Orbit”. In: *SIAM Journal on Applied Dynamical Systems* 11.4 (2012), pp. 1583–1613.

[39] A. Champneys. “Homoclinic orbits in reversible systems and their applications in mechanics, fluids and optics”. In: *Physica D: Nonlinear Phenomena* 112.1 (1998). Proceedings of the Workshop on Time-Reversal Symmetry in Dynamical Systems, pp. 158–186.

[40] S. Chapman and G. Kozyreff. “Exponential asymptotics of localised patterns and snaking bifurcation diagrams”. In: *Physica D: Nonlinear Phenomena* 238.3 (2009), pp. 319–354.

[41] Y. K. Chembo et al. “Theory and applications of the Lugiato-Lefever Equation”. In: *Euro. Phys. J. D* 71.11 (Nov. 2017), p. 299.

[42] Z. Chen, M. Segev, and D. N. Christodoulides. “Optical spatial solitons: historical overview and recent advances”. In: *Rep. Prog. Phys.* 75.8 (2012), p. 086401.

[43] J.-M. Chomaz. “Global instabilities in spatially developing flows: non-normality and nonlinearity”. In: *Annu. Rev. Fluid Mech.* 37.1 (2005), pp. 357–392.

[44] C. Chong et al. “Multistable solitons in higher-dimensional cubic-quintic nonlinear Schrö dinger lattices”. In: *Phys. D (Amsterdam)* 238.2 (2009), pp. 126–136.

[45] D. N. Christodoulides and R. I. Joseph. "Discrete self-focusing in nonlinear arrays of coupled waveguides". In: *Opt. Lett.* 13.9 (Sept. 1988), pp. 794–796.

[46] R. Conte and M. Musette. "Linearity inside nonlinearity: exact solutions to the complex Ginzburg-Landau equation". In: *Physica D: Nonlinear Phenomena* 69.1 (1993), pp. 1–17.

[47] S. Coombes and C. R. Laing. "Pulsating fronts in periodically modulated neural field models". In: *Phys. Rev. E* 83 (1 Jan. 2011), p. 011912.

[48] S. Coombes and M. R. Owen. "Evans Functions for Integral Neural Field Equations with Heaviside Firing Rate Function". In: *SIAM Journal on Applied Dynamical Systems* 3.4 (2004), pp. 574–600.

[49] A. Couairon and J.-M. Chomaz. "Absolute and convective instabilities, front velocities and global modes in nonlinear systems". In: *Physica D: Nonlinear Phenomena* 108.3 (Oct. 1997), pp. 236–276.

[50] M. C. Cross and P. C. Hohenberg. "Pattern formation outside of equilibrium". In: *Rev. Mod. Phys.* 65 (3 July 1993), pp. 851–1112.

[51] A. D. Dean et al. "Exponential asymptotics of homoclinic snaking". In: *Nonlinearity* 24.12 (2011), p. 3323.

[52] G. Dee and J. S. Langer. "Propagating Pattern Selection". In: *Phys. Rev. Lett.* 50 (6 Feb. 1983), pp. 383–386.

[53] J. E. Dennis Jr and R. B. Schnabel. *Numerical methods for unconstrained optimization and nonlinear equations*. Vol. 16. Siam, 1996.

[54] J. M. Dixon, J. A. Tuszynski, and P. A. Clarkson. *From Nonlinearity to Coherence: Universal Features of Nonlinear Behaviour in Many-Body Physics*. Clarendon, Oxford, 1997.

[55] E. Doedel et al. *AUTO-07P: continuation and bifurcation software for ordinary differential equations*. 2012.

[56] E. J. Doedel. "AUTO: A program for the automatic bifurcation analysis of autonomous systems". In: *Congr. Numer* 30 (1981), pp. 265–284.

[57] E. Doedel, H. B. Keller, and J. P. Kernevez. "Numerical analysis and control of bifurcation problems (I): bifurcation in finite dimensions". In: *International Journal of Bifurcation and Chaos* 01.03 (1991), pp. 493–520.

[58] E. Doedel, H. B. Keller, and J. P. Kernevez. "Numerical analysis and control of bifurcation problems (II): bifurcation in infinite dimensions". In: *International Journal of Bifurcation and Chaos* 01.04 (1991), pp. 745–772.

[59] A. Doelman and W. Eckhaus. "Periodic and quasi-periodic solutions of degenerate modulation equations". In: *Physica D: Nonlinear Phenomena* 53.2 (1991), pp. 249–266.

[60] J. Duan, P. Holmes, and E. S. Titi. “Global existence theory for a generalized Ginzburg-Landau equation”. In: *Nonlinearity* 5.6 (1992), p. 1303.

[61] J. Duan and P. Holmes. “Fronts, domain walls and pulses in a generalized Ginzburg-Landau equation”. In: *Proc. Edinburgh Math. Soc.* 38.1 (1995), pp. 77–97.

[62] J. Duan and P. Holmes. “On the cauchy problem of a generalized ginzburg-landau equation”. In: *Nonlinear Anal. Theor.* 22.8 (1994), pp. 1033–1040.

[63] U. Ebert and W. van Saarloos. “Front propagation into unstable states: universal algebraic convergence towards uniformly translating pulled fronts”. In: *Physica D: Nonlinear Phenomena* 146.1-4 (2000), pp. 1–99.

[64] W. Eckhaus and G. Iooss. “Strong selection or rejection of spatially periodic patterns in degenerate bifurcations”. In: *Physica D: Nonlinear Phenomena* 39.1 (1989), pp. 124–146.

[65] C. Elphick et al. “A simple global characterization for normal forms of singular vector fields”. In: *Physica D: Nonlinear Phenomena* 29.1 (1987), pp. 95–127.

[66] G. Faye, M. Holzer, and A. Scheel. “Linear spreading speeds from nonlinear resonant interaction”. In: *Nonlinearity* 30.6 (2017), p. 2403.

[67] W. J. Firth, L. Columbo, and T. Maggipinto. “On homoclinic snaking in optical systems”. In: *Chaos* 17.3 (2007), p. 037115.

[68] J. P. Gaivão and V. Gelfreich. “Splitting of separatrices for the Hamiltonian–Hopf bifurcation with the Swift–Hohenberg equation as an example”. In: *Nonlinearity* 24.3 (2011), p. 677.

[69] H. Gang et al. “Stochastic resonance without external periodic force”. In: *Phys. Rev. Lett.* 71 (6 Aug. 1993), pp. 807–810.

[70] L. Y. Glebsky and L. M. Lerman. “On small stationary localized solutions for the generalized 1-D Swift-Hohenberg equation”. In: *Chaos* 5.2 (1995), pp. 424–431.

[71] M. Haragus and G. Iooss. *Local bifurcations, center manifolds, and normal forms in infinite-dimensional dynamical systems.* Springer Science & Business Media, 2010.

[72] A. Hari and A. A. Nepomnyashchy. “Nonpotential effects in dynamics of fronts between convection patterns”. In: *Phys. Rev. E* 61 (5 May 2000), pp. 4835–4847.

[73] K. Harley et al. “Numerical computation of an Evans function for travelling waves”. In: *Mathematical Biosciences* 266 (2015), pp. 36–51.

[74] P. Hartman. *Ordinary Differential Equations.* Second. Society for Industrial and Applied Mathematics, 2002.

[75] F. Haudin et al. “Front dynamics and pinning-depinning phenomenon in spatially periodic media”. In: *Phys. Rev. E* 81 (5 May 2010), p. 056203.

[76] F. Haudin et al. “Homoclinic Snaking of Localized Patterns in a Spatially Forced System”. In: *Phys. Rev. Lett.* 107 (26 Dec. 2011), p. 264101.

[77] M. H. Holmes. *Introduction to perturbation methods*. Vol. 20. Springer Science & Business Media, 2012.

[78] R. B. Hoyle. "Zigzag and Eckhaus instabilities in a quintic-order nonvariational Ginzburg-Landau equation". In: *Phys. Rev. E* 58 (6 Dec. 1998), pp. 7315–7318.

[79] R. B. Hoyle. *Pattern formation: an introduction to methods*. Cambridge University Press, 2006.

[80] P. Huerre and P. A. Monkewitz. "Absolute and convective instabilities in free shear layers". In: *J. Fluid Mech.* 159 (1985), pp. 151–168.

[81] P. Huerre and P. A. Monkewitz. "Local and Global Instabilities in Spatially Developing Flows". In: *Annu. Rev. Fluid Mech.* 22.1 (1990), pp. 473–537.

[82] G. Iooss and M.-C. Pérouème. "Perturbed homoclinic solutions in reversible 1: 1 resonance vector fields". In: *J. Diff. Eqns* 102.1 (1993), pp. 62–88.

[83] D. W. Jordan and P. Smith. *Nonlinear ordinary differential equations: an introduction to dynamical systems*. Vol. 2. Oxford University Press, USA, 1999.

[84] H.-C. Kao and E. Knobloch. "Instabilities and dynamics of weakly subcritical patterns". In: *Math. Model. Nat. Phenom.* 8.5 (Sept. 2013). Ed. by L. Lerman et al., pp. 131–154.

[85] H.-C. Kao, C. Beaume, and E. Knobloch. "Spatial localization in heterogeneous systems". In: *Phys. Rev. E* 89 (1 Jan. 2014), p. 012903.

[86] H.-C. Kao and E. Knobloch. "Weakly subcritical stationary patterns: Eckhaus instability and homoclinic snaking". In: *Phys. Rev. E* 85 (2 Feb. 2012), p. 026211.

[87] T. Kapitula. "On the nonlinear stability of plane waves for the Ginzburg-Landau equation". In: *Comm. Pure Appl. Math.* 47.6 (1994), pp. 831–841.

[88] T. Kapitula. "Singular heteroclinic orbits for degenerate modulation equations". In: *Physica D: Nonlinear Phenomena* 82.1 (1995), pp. 36–59.

[89] T. Kapitula. "The Evans Function and Generalized Melnikov Integrals". In: *SIAM Journal on Mathematical Analysis* 30.2 (1999), pp. 273–297.

[90] T. Kapitula and K. Promislow. *Spectral and dynamical stability of nonlinear waves*. Vol. 457. Springer, 2013.

[91] Y. V. Kartashov, B. A. Malomed, and L. Torner. "Solitons in nonlinear lattices". In: *Rev. Mod. Phys.* 83 (1 Apr. 2011), pp. 247–305.

[92] Y. V. Kartashov, V. A. Vysloukh, and L. Torner. "Asymmetric soliton mobility in competing linear–nonlinear parity-time-symmetric lattices". In: *Opt. Lett.* 41.18 (Sept. 2016), pp. 4348–4351.

[93] Y. V. Kartashov, V. A. Vysloukh, and L. Torner. "Soliton modes, stability, and drift in optical lattices with spatially modulated nonlinearity". In: *Opt. Lett.* 33.15 (Aug. 2008), pp. 1747–1749.

[94] Y. V. Kartashov, V. A. Vysloukh, and L. Torner. “Soliton trains in photonic lattices”. In: *Opt. Express* 12.13 (June 2004), pp. 2831–2837.

[95] Y. S. Kivshar. “Self-localization in arrays of defocusing waveguides”. In: *Opt. Lett.* 18.14 (July 1993), pp. 1147–1149.

[96] P. P. Kizin, D. A. Zezyulin, and G. L. Alfimov. “Oscillatory instabilities of gap solitons in a repulsive Bose-Einstein condensate”. In: *Phys. D (Amsterdam)* 337 (2016), pp. 58–66.

[97] E. Knobloch and J. D. Luca. “Amplitude equations for travelling wave convection”. In: *Nonlinearity* 3.4 (1990), p. 975.

[98] E. Knobloch. “Spatial Localization in Dissipative Systems”. In: *Annual Review of Condensed Matter Physics* 6.1 (2015), pp. 325–359.

[99] R. Kuske and W. Eckhaus. “Pattern Formation in Systems with Slowly Varying Geometry”. In: *SIAM Journal on Applied Mathematics* 57.1 (1997), pp. 112–152.

[100] Y. A. Kuznetsov. *Elements of applied bifurcation theory.* Vol. 112. Springer Science & Business Media, 2013.

[101] B. L. Lawrence and G. I. Stegeman. “Two-dimensional bright spatial solitons stable over limited intensities and ring formation in polydiacetylene para-toluene sulfonate”. In: *Opt. Lett.* 23.8 (Apr. 1998), pp. 591–593.

[102] R. J. LeVeque. *Finite difference methods for ordinary and partial differential equations: steady-state and time-dependent problems.* Vol. 98. Siam, 2007.

[103] Y. Li et al. “Double symmetry breaking of solitons in one-dimensional virtual photonic crystals”. In: *Phys. Rev. A* 83 (5 May 2011), p. 053832.

[104] E. M. Lifshitz and L. P. Pitaevskii. *Physical Kinetics, Course of Theoretical Physics.* Vol. 10. New York: Pergamon, 1981.

[105] D. J. Lloyd. Private communication. 2018.

[106] D. J. B. Lloyd et al. “Homoclinic snaking near the surface instability of a polarisable fluid”. In: *Journal of Fluid Mechanics* 783 (2015), pp. 283–305.

[107] A. Maluckov, L. Had žievski, and B. A. Malomed. “Staggered and moving localized modes in dynamical lattices with the cubic-quintic nonlinearity”. In: *Phys. Rev. E* 77 (3 Mar. 2008), p. 036604.

[108] P. Marcq, H. Chaté, and R. Conte. “Exact solutions of the one-dimensional quintic complex Ginzburg-Landau equation”. In: *Physica D: Nonlinear Phenomena* 73.4 (1994), pp. 305–317.

[109] J. M. McSloy et al. “Computationally determined existence and stability of transverse structures. II. Multipeaked cavity solitons”. In: *Phys. Rev. E* 66 (4 Oct. 2002), p. 046606.

[110] H. Meinhardt. “Pattern formation in biology: a comparison of models and experiments”. In: *Reports on Progress in Physics* 55.6 (1992), p. 797.

[111] C. Mejía-Cortés, R. A. Vicencio, and B. A. Malomed. “Mobility of solitons in one-dimensional lattices with the cubic-quintic nonlinearity”. In: *Phys. Rev. E* 88 (5 Nov. 2013), p. 052901.

[112] T. R. O. Melvin et al. “Travelling solitary waves in the discrete Schrödinger equation with saturable nonlinearity: Existence, stability and dynamics”. In: *Phys. D (Amsterdam)* 237.4 (2008), pp. 551–567.

[113] I. Mercader et al. “Localized pinning states in closed containers: Homoclinic snaking without bistability”. In: *Phys. Rev. E* 80 (2 Aug. 2009), p. 025201.

[114] I. M. Merhasin et al. “Finite-band solitons in the Kronig-Penney model with the cubic-quintic nonlinearity”. In: *Phys. Rev. E* 71 (1 Jan. 2005), p. 016613.

[115] J. Nocedal and S. J. Wright. *Numerical Optimization.* second. Springer-Verlag New York, 2006.

[116] K. Nozaki and N. Bekki. “Exact solutions of the generalized Ginzburg-Landau equation”. In: *J. Phys. Soc. Jpn.* 53 (May 1984), p. 1581.

[117] K. Nozaki and N. Bekki. “Pattern selection and spatiotemporal transition to chaos in the Ginzburg-Landau equation”. In: *Phys. Rev. Lett.* 51 (24 Dec. 1983), pp. 2171–2174.

[118] K. Ogusu et al. “Linear and nonlinear optical properties of Ag–As–Se chalcogenide glasses forall-optical switching”. In: *Opt. Lett.* 29.3 (Feb. 2004), pp. 265–267.

[119] B. B. P. “Periodicheski deistvuyushchaya reaktsia i ee mekhanism [Periodically acting reaction and its mechanism]”. In: *Sbornik referatov po radiotsionnoi meditsine [Collection of abstracts on radiation medicine]* (1958), pp. 145–147.

[120] P. Parra-Rivas et al. “Interaction of solitons and the formation of bound states in the generalized Lugiato-Lefever equation”. In: *Euro. Phys. J. D* 71.7 (July 2017), p. 198.

[121] R. L. Pego and M. I. Weinstein. “Asymptotic stability of solitary waves”. In: *Commun. Math. Phys.* 164.2 (Aug. 1994), pp. 305–349.

[122] R. L. Pego and M. I. Weinstein. “On asymptotic stability of solitary waves”. In: *Phys. Lett. A* 162.3 (1992), pp. 263–268.

[123] D. E. Pelinovsky, A. A. Sukhorukov, and Y. S. Kivshar. “Bifurcations and stability of gap solitons in periodic potentials”. In: *Phys. Rev. E* 70 (3 Sept. 2004), p. 036618.

[124] D. Pelinovsky and G. Schneider. “Moving gap solitons in periodic potentials”. In: *Math. Meth. Appl. Sci.* 31.14 (2008), pp. 1739–1760.

[125] Y. Pomeau. “Front motion, metastability and subcritical bifurcations in hydrodynamics”. In: *Physica D: Nonlinear Phenomena* 23.1 (1986), pp. 3–11.

[126] B. C. Ponedel and E. Knobloch. “Forced snaking: Localized structures in the real Ginzburg-Landau equation with spatially periodic parametric forcing”. In: *Euro. Phys. J. Special Topics* 225.13 (2016), pp. 2549–2561.

[127] J. A. Powell, A. C. Newell, and C. K. R. T. Jones. “Competition between generic and nongeneric fronts in envelope equations”. In: *Phys. Rev. A* 44 (6 Sept. 1991), pp. 3636–3652.

[128] J. Prat, I. Mercader, and E. Knobloch. “The 1:2 mode interaction in Rayleigh-Bénard convection with and without Boussinesq symmetry”. In: *International Journal of Bifurcation and Chaos* 12.02 (2002), pp. 281–308.

[129] F. M. Richter. “Experiments on the stability of convection rolls in fluids whose viscosity depends on temperature”. In: *Journal of Fluid Mechanics* 89.3 (1978), pp. 553–560.

[130] R. Richter and I. V. Barashenkov. “Two-Dimensional Solitons on the Surface of Magnetic Fluids”. In: *Phys. Rev. Lett.* 94 (18 May 2005), p. 184503.

[131] R. D. Russell and J. Christiansen. “Adaptive Mesh Selection Strategies for Solving Boundary Value Problems”. In: *SIAM Journal on Numerical Analysis* 15.1 (1978), pp. 59–80.

[132] W. van Saarloos and P. C. Hohenberg. “Pulses and fronts in the complex Ginzburg-Landau equation near a subcritical bifurcation”. In: *Phys. Rev. Lett.* 64 (7 Feb. 1990), pp. 749–752.

[133] W. van Saarloos. “Front propagation into unstable states”. In: *Physics Reports* 386.2-6 (Nov. 2003), pp. 29–222.

[134] W. van Saarloos. “Front propagation into unstable states. II. Linear versus nonlinear marginal stability and rate of convergence”. In: *Phys. Rev. A* 39 (12 June 1989), pp. 6367–6390.

[135] W. van Saarloos. “Front propagation into unstable states: Marginal stability as a dynamical mechanism for velocity selection”. In: *Phys. Rev. A* 37.1 (1988), pp. 211–229.

[136] W. van Saarloos and P. C. Hohenberg. “Fronts, pulses, sources and sinks in generalized complex Ginzburg-Landau equations”. In: *Physica D: Nonlinear Phenomena* 56.4 (1992), pp. 303–367.

[137] B. Sandstede. “Chapter 18 - Stability of Travelling Waves”. In: *Handbook of Dynamical Systems*. Ed. by B. Fiedler. Vol. 2. Handbook of Dynamical Systems. Elsevier Science, 2002, pp. 983–1055.

[138] P. J. Schmid. “Nonmodal Stability Theory”. In: *Annu. Rev. Fluid Mech.* 39.1 (2007), pp. 129–162.

[139] A. Shepeleva. “Modulated modulations approach to the loss of stability of periodic solutions for the degenerate Ginzburg-Landau equation”. In: *Nonlinearity* 11.3 (1998), p. 409.

[140] J. A. Sherratt, A. S. Dagbovie, and F. M. Hilker. “A Mathematical Biologist’s Guide to Absolute and Convective Instability”. In: *Bull. Math. Biol.* 76.1 (2014), pp. 1–26.

[141] J. Sijbrand. “Properties of center manifolds”. In: *Transactions of the American Mathematical Society* 289.2 (1985), pp. 431–469.

[142] F. Smektala et al. “Non-linear optical properties of chalcogenide glasses measured by Z-scan”. In: *J. Non-Crystalline Solids* 274.1 (2000), pp. 232–237.

[143] J. Swift and P. C. Hohenberg. “Hydrodynamic fluctuations at the convective instability”. In: *Phys. Rev. A* 15 (1 Jan. 1977), pp. 319–328.

[144] C. Taylor and J. H. P. Dawes. “Snaking and isolas of localised states in bistable discrete lattices”. In: *Phys. Lett. A* 375.1 (2010), pp. 14–22.

[145] H. Tian et al. “Front and pulse solutions for the complex Ginzburg-Landau equation with higher-order terms”. In: *Phys. Rev. E* 66 (6 Dec. 2002), p. 066204.

[146] S. Tobias, M. Proctor, and E. Knobloch. “Convective and absolute instabilities of fluid flows in finite geometry”. In: *Physica D: Nonlinear Phenomena* 113.1 (1998), pp. 43–72.

[147] L. N. Trefethen. *Spectral methods in MATLAB*. Vol. 10. Siam, 2000.

[148] L. N. Trefethen and M. Embree. *Spectra and Pseudospectra: The Behavior of Nonnormal Matrices and Operators*. Princeton University Press, 2005.

[149] H. Uecker. “Stable Modulating Multipulse Solutions for Dissipative Systems with Resonant Spatially Periodic Forcing”. In: *Journal of Nonlinear Science* 11.2 (Apr. 2001), pp. 89–121.

[150] A. G. Vladimirov et al. “Two-dimensional clusters of solitary structures in driven optical cavities”. In: *Phys. Rev. E* 65 (4 Mar. 2002), p. 046606.

[151] J. Wang et al. “Lattice solitons supported by competing cubic-quintic nonlinearity”. In: *Phys. Lett. A* 339.1 (2005), pp. 74–82.

[152] S. Wiggins. *Introduction to applied nonlinear dynamical systems and chaos*. Vol. 2. Springer Science & Business Media, 2003.

[153] A. P. Willis et al. “Surfing the edge: using feedback control to find nonlinear solutions”. In: *Journal of Fluid Mechanics* 831 (2017), pp. 579–591.

[154] P. Woods and A. Champneys. “Heteroclinic tangles and homoclinic snaking in the unfolding of a degenerate reversible Hamiltonian-Hopf bifurcation”. In: *Physica D: Nonlinear Phenomena* 129.3 (1999), pp. 147–170.

[155] E. M. Wright et al. “Stable self-trapping and ring formation in polydiacetylene paratoluene sulfonate”. In: *Opt. Lett.* 20.24 (Dec. 1995), pp. 2481–2483.

[156] J. Xin. “Front Propagation in Heterogeneous Media”. In: *SIAM Review* 42.2 (2000), pp. 161–230.

[157] T. F. Xu et al. “Gap solitons and Bloch waves of interacting bosons in one-dimensional optical lattices: From the weak- to the strong-interaction limits”. In: *Phys. Rev. A* 83 (4 Apr. 2011), p. 043610.

[158] J. Yang. “Newton-conjugate-gradient methods for solitary wave computations”. In: *J. Comp. Phys.* 228.18 (2009), pp. 7007–7024.

[159] J. Yang. “No stability switching at saddle-node bifurcations of solitary waves in generalized nonlinear Schrödinger equations”. In: *Phys. Rev. E* 85 (3 Mar. 2012), p. 037602.

[160] J. Yang. *Nonlinear Waves in Integrable and Nonintegrable Systems.* SIAM, 2010.

[161] A. V. Yulin and A. R. Champneys. “Discrete Snaking: Multiple Cavity Solitons in Saturable Media”. In: *SIAM J. Appl. Dyn. Syst.* 9.2 (2010), pp. 391–431.

[162] C. Zhan et al. “Third- and fifth-order optical nonlinearities in a new stilbazolium derivative”. In: *J. Opt. Soc. Am. B* 19.3 (Mar. 2002), pp. 369–375.

[163] Y. Zhang, Z. Liang, and B. Wu. “Gap solitons and Bloch waves in nonlinear periodic systems”. In: *Phys. Rev. A* 80 (6 Dec. 2009), p. 063815.

[164] Y. Zhang and B. Wu. “Composition Relation between Gap Solitons and Bloch Waves in Nonlinear Periodic Systems”. In: *Phys. Rev. Lett.* 102 (9 Mar. 2009), p. 093905.

[165] J. Zhou et al. “Soliton control in optical lattices with periodic modulation of nonlinearity coefficient”. In: *Phys. Lett. A* 372.24 (2008), pp. 4395–4398.

[166] R. S. Zounes and R. H. Rand. “Transition Curves for the Quasi-Periodic Mathieu Equation”. In: *SIAM Journal on Applied Mathematics* 58.4 (1998), pp. 1094–1115.